UNIVERSITY OF READING

Department of Meteorology

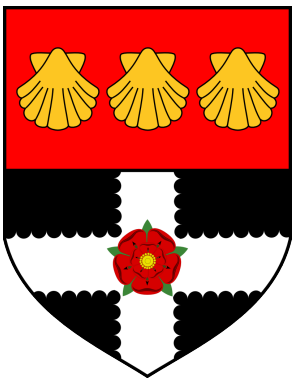

Observations and Characteristics of Updraught Structures using High Resolution Radar Observations

Liam Till

A thesis submitted for the degree of Doctor of Philosophy

July, 2021

Declaration

I confirm that this is my own work and the use of all material from other sources has been properly and fully acknowledged.

Liam Till

Abstract

This thesis presents new observations of updraught pulses ascending into deep convection over time. These were obtained using an improved scanning strategy and retrieval method for retrieving vertical velocity from the Chilbolton Advanced Meteorological Radar.

A vertical velocity retrieval algorithm was developed and tested on synthetic data and observations from prior campaigns. Vertical velocity is retrieved by comparing differences in Doppler velocities at a particular scale between pairs of measurements. Uncertainty was estimated to be less than 1.5 m s^{-1} on average with a 95th percentile of 2.4 m s^{-1}. Prior campaign data showed updraught structures evolving as discrete pulses or thermals noticed by studying consecutive scans. In this data multiple thermals were observed in convective cells with lifetimes mostly between 2 and 5 minutes with some up to 10 minutes. Thermals generally ascended less than 1.5 km in height and had diameters between 500 m and 2 km.

To provide information in three-dimensions with high spatial and temporal resolution, a new multi-scan scanning strategy was developed that primarily bracketed reflectivity cores. New scans of a particular deep convective cloud system provided detailed observations of much of the lifetime of three individual convective cells with approximately 2 minutes resolution. Dimensions of updraught and eddy dissipation rate structures were positively correlated and coherent in along-scan, cross-scan and perpendicular to scan directions and there were more smaller 'fragment' type structures. Individual convective cells developed over time as multiple ascending pulses, formed plume-like structures and an overshooting top. Pulses ascended ahead of differential reflectivity columns when located near the freezing level and into the cloud top with 30 dBZ echo top height with widths similar to reflectivity towers.

Acknowledgements

I would like to thank my supervisors: **Thorwald Stein**, **Peter Clark** and **Carol Halliwell** for their continued support throughout my PhD. I appreciate their patience and guidance, without it my work would not have been possible. I would also like to thank my monitoring committee: **Miguel Teixeira**, **Claire Ryder** and **Ellie Highwood** for their guidance and feedback on progress and support.

I am grateful for the staff at STFC for their help operating CAMRa and processing data which has been fundamental to this thesis. In particular **Chris Walden** and **Darcy Ladd** for when I needed to scan storms. I'm also thankful for the Radar Group weekly meetings, in which much interesting work was presented and for feedback on my work.

I would like to thank those on Lyle 5 for the many lunchtime chats with mentions to **Will Keat**, **Ewan Pinnington** and **Ben Courtier**. In particular, Will for the many walks, chats, rants and supportive friendship.

I am grateful to my parents, especially my mother for her support since the beginning of this journey which has taken many years to accomplish and for believing in me since the beginning. Without it, my journey into Meteorology would have never begun. I am also thankful for the support of my wife **Alyssa**, who has been there for me since my undergrad. Finally, our fluffy doggy **Toto** for his unconditional support and resting his head on my 'mouse hand' when I need to use it.

I am extremely grateful to you all for your support and understanding throughout my PhD.

Contents

Chapter 1

Introduction

Clouds are an important part of the energy transport process in the atmosphere, distributing heat and moisture throughout the atmosphere and coupling the boundary layer to the free atmosphere (Yang *et al.*, 2016). They have an impact on the radiation budget in terms of albedo and long wave radiation and come in a variety of different shapes and sizes, from high level wispy cirrus clouds to deep cumulonimbus clouds that produce severe weather in many parts of the world. Cumuli clouds ranging from small cumulus to cumulonimbus, amongst many other properties, are noted for having some of the strongest updraughts. Deep convective clouds with strong updraughts give rise to heavy precipitation and in some cases; strong winds, lightning, hail and tornadoes.

The traditional view of the life cycle of a convective cell undergoes three stages; cumulus stage, mature stage and the dissipating stage (Byers and Braham, 1949). The cumulus stage represents small to medium cumulus clouds where strong ascent is dominant. Significant precipitation during the cumulus stage is not likely. The cumulus stage can consist of multiple towers which can then merge to transition to the mature stage. Precipitation is usually associated with the mature stage. Ascending air, known as updraughts, and descending air, known as downdraughts, are present simultaneously at this stage.

Downdraughts can occur near cloud tops as dry environmental air is engulfed into the tops of cumuli, enhancing evaporative cooling as heat energy is used during the evaporation process and that evaporation more readily occurs into drier air, thus causing penetrating downdrafts. In the mature stages as the updraught intensifies due to pressure gradients and/or buoyancy, it reaches the tropopause and diverges horizontally forming the iconic anvil associated with thunderstorms. Downdraugths descend through the cloud and when severe can cause gust fronts. Once the downdraught

cuts off the updraught feeding air into the cloud, the dissipating stage begins. Downdraughts are further maintained as precipitation enhances negative buoyancy due to the supply of water being evaporated. In the dissipating stage downdraughts dominate and the cloud decays usually leaving the higher level ice cloud behind.

The World Climate Research Programme (WCRP) has set out a grand challenge to improve the understanding of clouds, circulations and climate sensitivity in climate models (Bony and Stevens, 2012). There is limited understanding of clouds and they are a major source of uncertainty in climate sensitivity and how they will respond to warming, modulate heating and their role in the large scale circulation (Bony and Stevens, 2012).

Donner *et al.* (2016) take the perspective that vertical velocities, updraughts on all scales, are among the keys to understanding and simulating climate forcing and that vertical velocity has had limited attention in climate models. Updraughts are crucial to understand because they are an important dynamic feature of clouds and are responsible for producing and maintaining clouds. Updraughts also impact microphysics by transporting cloud liquid and ice. Entrainment and mixing in parametrized convection are important controls on vertical velocity and have been shown to be related to climate sensitivity in general circulation models (Zhao, 2014). There are limited observational constraints for parametrization of entrainment and observations of vertical velocity which can effect microphysics and radiative properties (Jensen and Genio, 2006).

Due to the importance of updraught circulations and structures in convective clouds, their interactions with various processes within clouds and the continued research into modelling clouds and internal dynamics, updraughts remain a core focus of work in this thesis. This thesis aims to observe the two-dimensional and three-dimensional structures of updraughts and turbulence, investigate how such structures develop over time and determine characteristics at fine spatial scales in multiple developing convective cells.

1.1 Convection parametrization

As important as it is to understand how clouds impact the future climate and vice versa, it is critical to confidently simulate clouds to forecast them on shorter time scales. Weather forecasts that use a much smaller grid spacing can explicitly represent convection, compared to parametrized convection in climate models and global numerical models with larger grid spacing. Even though the grid resolution is greatly improved, problems remain with forecasting convection. Even models with small grid lengths still have a coarse grid when compared to the the typical size of a convective updraught and the internal processes occurring within convective clouds, known as the grey zone, thus causing evolution problems.

A majority of models use mass flux schemes which treat an ensemble of clouds in equilibrium (Arakawa and Jung, 2011). Convection becomes triggered once a parcel ascends, reaches its level of free convection, becomes unstable and ascends to the level of neutral buoyancy (Emanuel, 1994). The stability of a parcel depends on the thermodynamic structure of the atmosphere and the parcel. Some established schemes such as; Arakawa and Schubert (Arakawa and Schubert, 1974), Tiedtke (Tiedtke, 1989) and the Met Office large-scale model Gregory and Rowntree (Gregory and Rowntree, 1990) bulk scheme use entraining plumes.

A cumulus parametrizations purpose is to determine the feedback of the sub-grid effects from an ensemble of clouds on the large scale environment, without having to simulate individual clouds. To do this a closure is required using equations relating the statistics of the clouds to the large scale. Arakawa (2004) states two types of closures: (1) principal closure - which links the overall intensity of cumulus activity such as cloud base mass flux to the large scale process and (2) supplementary closures - which put constraints on cloud properties by large scale conditions using simplified cloud models or empirical data. Arakawa and Schubert (1974) obtains a closed system of equations relating the cumulus cloud ensemble to the large scale variables by using a quasi-equilibrium assumption. Tiedtke (1989) uses the large scale moisture convergence and supply of moisture by shallow convection providing moisture from surface evaporation to maintain penetrative and mid-level convection. Gregory and Rowntree (1990) closes

the mass flux scheme by asserting that a parcel's initial buoyancy is proportional to the initial convective mass flux.

Kain and Fritsch (1990) is another widely used scheme derived from the Fritsch and Chappell (1980) scheme where individual clouds are represented as entraining moist updraught and downdraught plumes in mesoscale numerical models. Fritsch and Chappell (1980) is based on the buoyant energy (convective available potential energy) available to a parcel, with a certain period of time available for the convection to remove that energy from the atmosphere, which regulates the convection in a mesoscale grid element, i.e deep convection. Kain and Fritsch (1990) modified the entraining plume model to use a two-way exchange of mass between clouds and the environment. A buoyancy sorting mechanism was used allowing partitions of mixtures of updraught and environmental air into entraining and detraining components. This introduced a physically realistic mechanism for estimating the rate of lateral detrainment at any level and the vertical profile of updraught mass flux can vary as a function of environmental conditions.

A recent study by Gu *et al.* (2020a) of the bulk mass flux formulation for shallow and deep convection found that a bulk mass flux approximation fails to represent contributions that arise from inter-object (updraught to updraught) and intra-object (updraught to cloud) variability. The correct magnitudes and vertical distributions of turbulent heat and water fluxes for the same time cannot be captured (Gu *et al.*, 2020a). By partitioning vertical velocity into the mean velocities of the 'core' and 'cloak', that is the strong and weak parts of the updraughts, vertical velocity is decomposed into different types of drafts. Gu *et al.* (2020a) found this method to significantly improve the representation of vertical transport in a simple bulk transport equation, improving the vertical distribution and magnitude of heat and water fluxes using a mass flux approximation for shallow and deep convection. This indicates the importance of predicting vertical velocities in different parts of clouds and the variability of vertical velocities in updraughts and thus the need for a better understanding of different types, or structures, of updraughts and pressure drag, not only in the cloud centre but also off the central axis.

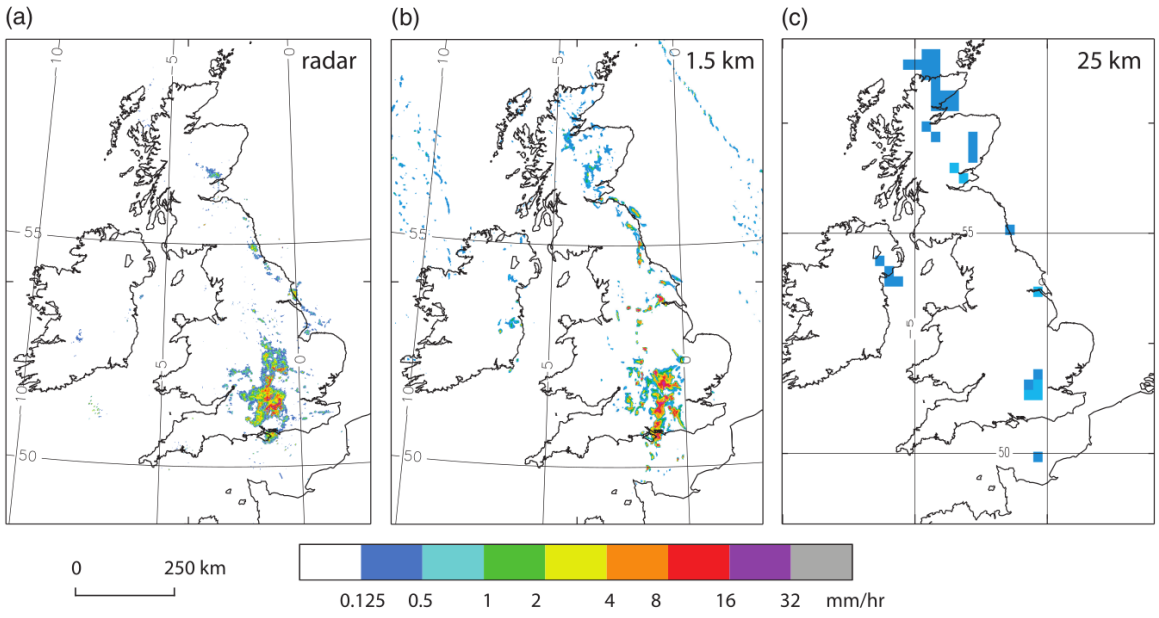

Figure 1.1: Comparison of a Mesoscale Convective System (MCS) over the UK in (a) rain rate derived at 1 km from radar observations, (b) UK Variable Resolution (UKV) 9 hour lead time forecast at 1.5 km grid spacing and (c) global 25 km grid spacing 12 hour lead time forecast. Colour bar indicates rain rate in mm/hr. Taken from Clark *et al.* (2016).

The UK Variable Resolution (UKV) forecast model developed and used by the Met Office runs with a 1.5 km horizontal grid spacing over the UK domain. Even though rainfall features look realistic compared to radar observations as shown by comparing Figure 1.1(a) to 1.1(b) from the UKV convection permitting model, the model cannot produce the initial convective plume and thus initiates convection at the wrong time (Clark *et al.*, 2016). This is most likely due to the grid length of the model compared to the typical sizes of convective plumes that initiate in the atmosphere. Kilometre scale grid lengths are most likely larger than some smaller scale convective plumes. Showers are usually under-resolved leading to evolution on the wrong scales (Clark *et al.*, 2016), leading to issues with representing rainfall rates in models with large grid spacing such as seen in Figure 1.1(c) from a global model using a convective parametrization. Lean *et al.* (2008) also reported large peaks in rainfall rates and fewer too large cells and at a grid spacing of 1 km too many small cells were found.

Similarly, Hanley *et al.* (2015) found that the UKV produced cells that are too in-

tense, too far apart and did not have enough light rain. A 200 m grid length produced the right number of large cells when simulating showers but when simulating deep clouds, the storms were not large enough. It is not just the horizontal resolution that changes the characteristics of cell evolution but there are smaller scale parametrizations such as turbulence that can also have an impact. For multiple grid lengths, decreasing the mixing length, which is the scale that small-scale (sub-grid) mixing and microphysical processes happen, leads to convection initiating sooner (Hanley *et al.*, 2015).

Nicol *et al.* (2015) found that the horizontal scale of updraughts decreased with grid length. At sub-kilometre grid lengths the horizontal scale of updraughts was determined by mixing length. Nicol *et al.* (2015) suggest that a mixing length of 40 m at very high horizontal resolution (sub-kilometre grid spacing) could be used to obtain updraughts at the correct horizontal scale. Realistically, it is currently computationally expensive to run daily forecasts at sub-kilometre grid spacing. Parametrization of entrainment could be one source of incorrect evolution (Stirling and Stratton, 2012), highlighting the importance to learn more from observations about the internal processes occurring in convection.

Stein *et al.* (2015) compared radar observations with the Met Office Unified Model using various horizontal grid spacing. Storms in the 1.5 km grid length simulation produced structures that were 1.5 - 2 times wider compared to radar observations. As grid spacing was decreased, down to 100 m, convergence of storm width was found. Clouds were categorised into shallow, intermediate and deep structures. Narrowing storm structures were produced with decreasing grid spacing. Both the 100 m and 200 m simulations represented the median structure of convective cores well. This could imply that the representation of convective storms converges at the 200 m grid length.

1.2 Updraughts in deep convection

The buoyantly-driven vertical motion associated with convective clouds is central to their dynamics and strongly influences their microphysics and hence precipitation and

lightning production. Updraughts are fundamental for the growth and maintenance of convection throughout its lifetime. Once clouds are developed, updraughts can distribute momentum, mass and moisture throughout the vertical. Updraughts also distribute ice particles and liquid water drops aiding the formation of precipitation and the growth of ice in clouds. Thus they are also fundamental for the production of lightning by separating ice particles into different regions of the cloud.

Correlations between differential reflectivity (ZDR) column strength, updraught strength and surface reflectivity have been shown to exist in a small sample of severe storms with tornadoes in Oklahoma (Picca and Ryzhkov, 2010). ZDR is the ratio between horizontal and vertical radar reflectivity and large values indicate large oblate hydrometeors, see chapter 2 for a full definition. ZDR strength was shown to be time lagged with reflectivity increasing in low levels of cloud with peak lag correlations up to 0.8 with three of four cases exhibiting a strong signal supporting the hypothesis that a maturing ZDR column is indicative of an intensifying updraught (Picca and Ryzhkov, 2010). This increase in updraught intensity could result in larger hail over the next 20 - 30 minutes. Increases in the horizontal and/or vertical extent of ZDR column above the 0°C level were positively correlated with an increase in low level reflectivity at 10 - 30 minute lag times (Picca and Ryzhkov, 2010). This implied that the increasing ZDR column volume preceded an intensification of surface precipitation.

In simulations of deep convection using the Hebrew University Cloud Model (HUCM) with ZDR columns in, the life cycle of ZDR columns was investigated (Kumjian *et al.*, 2014). Updraughts greater than 10 m s^{-1} were required for ZDR columns to exist and that updraught maxima was almost always located above the ZDR column, as shown by the green contours overlapping with the magenta contour and reflectivity for various output times in Figure 1.2. Snyder *et al.* (2015) also simulated ZDR columns using HUCM and found similar results of updraught location, intensity and location of ZDR column height to Kumjian *et al.* (2014). Updraughts were in excess of 10 m s^{-1}, located above and to the side of the ZDR column and changes in updraught maximum velocity tended to be seen after changes in ZDR column height. The simulations also showed that developing and mature updraughts with

vertical velocity greater than 10 m s^{-1} and below 4 km height were associated with perturbations of enhanced ZDR (Snyder *et al.*, 2015).

Similar to Picca and Ryzhkov (2010), Kumjian *et al.* (2014) found that the 1 dB ZDR column height and maximum updraught velocity had a lag correlation peaking at 0.65 with a lag time of 2 minutes. Maximum vertical velocity and the 20 dBZ echo top height had a peak correlation of 0.73 with a lag time of 0 minutes. 1 dB ZDR column height and maximum reflectivity at the surface had a peak correlation of 0.83 with a lag time of 14 minutes and finally the 1 dB ZDR column height and maximum amount of hail at the surface had a correlation of 0.89 with a lag time of 13 minutes. Once updraught cores weakened and ascended, ZDR columns began to decay. Large hail mass aloft that begins as frozen raindrops that are lofted in the ZDR column can fall to the ground, reducing the depth of the ZDR column and increasing surface reflectivity. This is because there is increased depletion of super-cooled water by the hailstones collecting droplets as they fall or because updraughts weaken (Kumjian *et al.*, 2014). If updraughts weaken by decreased inflow temperature, then it can be expected that ZDR columns will become shallower as the lower regions of updraughts weaken, changes in the depth of ZDR columns may be seen before the maximum updraught intensity changes because the lower part of the updraught weakens before the buoyancy is reduced in the core of the updraught (maximum updraught velocity) (Kumjian *et al.*, 2014).

Given updraughts interact with cloud dynamics and microphysics, and that many factors can effect the intensity and size of updraughts, it is important to understand characteristics of updraughts. Equation 1.1 shows updraught speed is controlled by; (1) local vertical pressure gradient, (2) buoyancy due to virtual temperature anomalies, pressure anomalies and liquid/frozen water loading, (3) turbulent Reynolds stresses and (4) viscous dissipation (Cotton *et al.*, 2011). In equation 1.1 ρ_0 = surface air density, $p^{'}$ = perturbation pressure, θ_0 = surface potential temperature, $\theta_v^{'}$ = virtual potential temperature perturbation, c_v = specific heat capacity at constant volume, c_p = specific heat capacity at constant pressure and $r_w^{'}$ = mixing ratio for water.

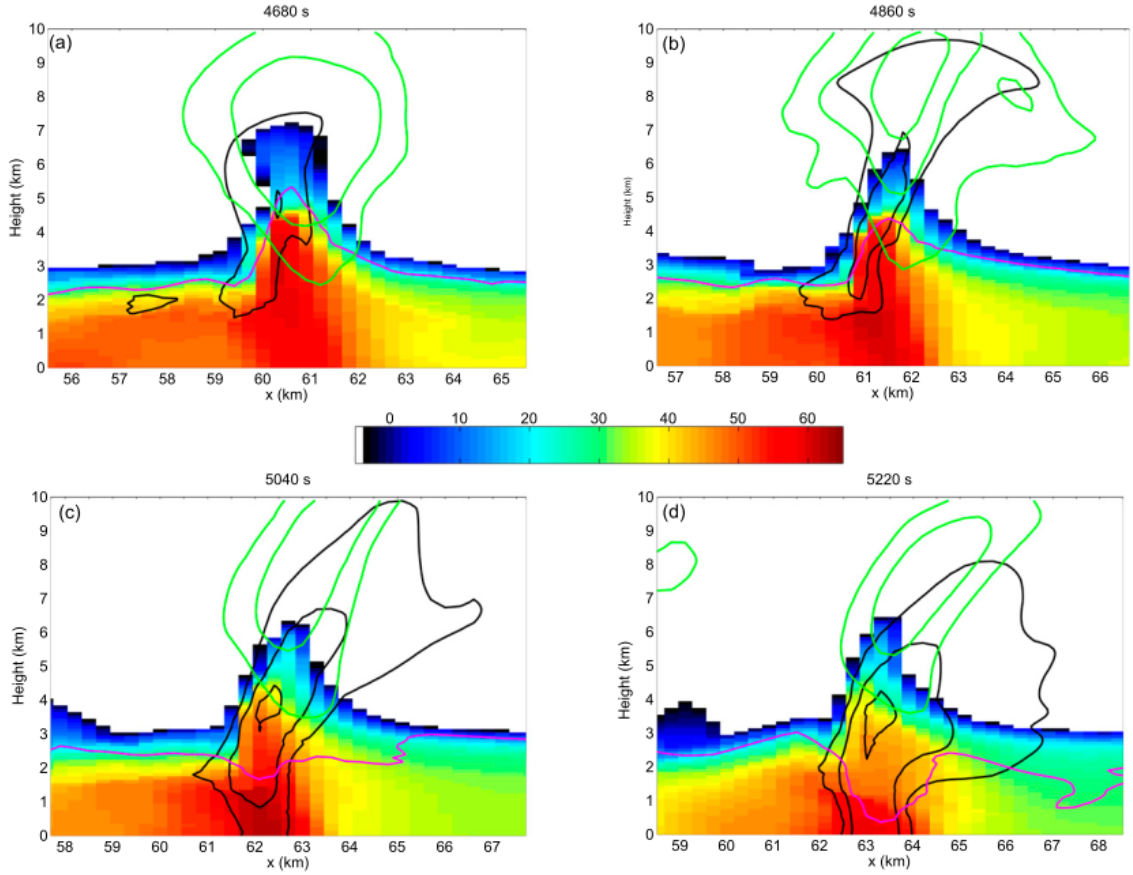

Figure 1.2: Reflectivity from rain only with updraught speed contoured at 10, 20 and 30 m s^{-1} (green), total differential reflectivity (magenta is 1.5 dB) and reflectivity from hail (black for 50, 60 and 70 dBZ) for a simulated storm at (a) 4680, (b) 4860, (c) 5040 and (d) 5220 s. Colour bar shows reflectivity in dBZ. Taken from Kumjian *et al.* (2014).

$$\frac{d\overline{w}}{dt} = \underbrace{-\frac{1}{\rho_0}\frac{\partial p'}{\partial z}}_{(1)} + \underbrace{(\frac{\theta'_v}{\theta_0} - \frac{c_v}{c_p}\frac{p'}{\rho_0} - r'_w)g}_{(2)} - \underbrace{\frac{1}{\rho_0}\frac{\partial}{\partial}(\rho_0\overline{w''u''})}_{(3)} + \underbrace{viscous \quad terms}_{(4)} \tag{1.1}$$

In-situ measurements from aircraft of each of the terms in equation 1.1 would be difficult over a large number of updraught samples. It is less difficult to measure the speed and size of updraughts themselves rather than the quantities controlling an updraughts characteristics. Updraughts have been observed using wind profilers, single and dual Doppler radars and in-situ measurements using aircraft. Aircraft take measurements of updraughts using gust probes and inertial navigation systems. Aircraft can also

make in-situ measurements of microphysics such as liquid water content (LWC) using Forward Scattering Spectrometer Probes (FSSP).

The Global Atmospheric Research Program Atlantic Tropical Experiment (GATE) project measured updraughts in convective cells using aircraft (LeMone and Zipser, 1980). Vertical velocity was measured as the wind velocity relative to the aircraft minus the vertical velocity of the aircraft relative to earth. Statistics were collected on updraughts and downdraughts from hundreds of flight legs. LeMone and Zipser (1980) found that diameters, average vertical velocity and maximum vertical velocity magnitude and mass flux are approximately log-normally distributed, downdraught cores were smaller and weaker than updraughts and in the middle troposphere only 10% of updraught cores had diameters greater than 2 km and mean vertical velocity greater than 5 m s^{-1}.

Over land, updraughts have been observed in the Florida Area Cumulus Experiment (FACE) campaign (Keller and Sax, 1981) using aircraft with vertical velocity measurements taken using an inertial navigation system. Keller and Sax (1981) found updraught growth can pass through remnants of a dissipating older tower and contained particles suitable for the Hallet-Mossop (Hallett and Mossop, 1974) ice splintering process to occur. Some observations had large amounts of ice crystals in active updraughts and some did not when updraughts were located in stagnant regions, where the updraught region was nearly ice free.

In hailstorms observed with aircraft during National Hail Research Experiment (NHRE) (Musil *et al.*, 1973; Sand, 1976), hail consistently occurred near updraught edges and larger hail was found in stronger updraughts. Sand (1976) found that major updraughts were not in high reflectivity regions and are not always in the weaker echo region ahead of the high reflectivity region. Most updraughts were found well ahead of the high reflectivity region in areas of new development. Observations also found that high concentrations of liquid cloud droplets were rarely observed in high reflectivity regions but were in updraught regions. Well defined coherent updraught structures surrounded by downdraughts on each side were observed by Kollias *et al.* (2001) using a wind profiler.

Multiple Doppler radars and wind profilers have been used to retrieve three-dimensional wind profiles using variational methods (Gao *et al.*, 2006; Kumar *et al.*, 2016; North *et al.*, 2017). Variational retrieval methods require observations from multiple Doppler radars and retrieve wind fields by minimising a cost function. Such a cost function is constrained either using strong constraints where all analysed and retrieved variables exactly satisfy a chosen model of the field or weak constraints where the variables do not exactly satisfy the constraining equations, leaving a residual. Some equations used in the cost function are; mass continuity, equation of Doppler velocity relating to the horizontal wind components and azimuthal scanning angle, conservation of reflectivity and vorticity equations. Background fields such as atmospheric soundings can also be used as additional information in the cost function. The difference between the observations and the model variables are minimised to retrieve the three-dimensional wind field, using a choice of gradient function until convergence is obtained. Using single Doppler radars, updraughts have been retrieved using integration methods (Ray *et al.*, 1980; Protat and Zawadzki, 1999) and later contiguous structures in vertical velocity were retrieved by Nicol *et al.* (2015) using an updated version of the integration technique. Vertical velocity retrievals have not been limited to research campaigns,

Bousquet *et al.* (2008) used a large operational radar network for multiple Doppler retrieval in France. Although care should be taken with vertical velocity estimates from Doppler radar measurements due to the various assumptions of the retrieval method. Variational approaches tend to be more robust than integration techniques as errors can be minimised. Assumptions such as; density profiles, boundary conditions, neglecting velocity components and constraints placed on the retrieval method will introduce errors and reduce the accuracy of the estimates.

A drawback of aircraft measurements is that they cannot sample stronger convective cores due to safety concerns and only sample over limited spatial and time scales. During the Convective Precipitation Experiment (COPE) (Leon *et al.*, 2016), High Plains Cumulus Campaign (HiCu) (Damiani *et al.*, 2006) and the Ice in Clouds Experiment-Tropical (ICE-T) (Yang *et al.*, 2016) many convective clouds were inves-

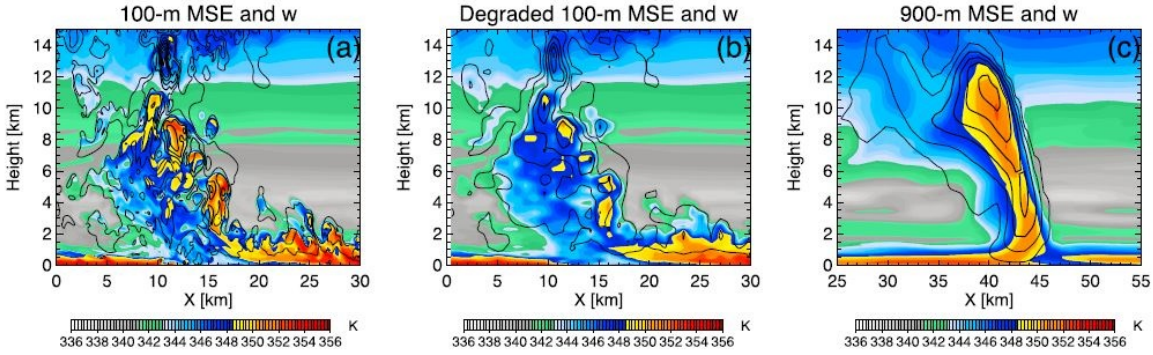

Figure 1.3: Vertical cross sections through updraughts from DHARMA-2M simulations showing moist static energy (filled contours) and vertical velocity (w) (black contours). (a) 100 m grid spacing, (b) 100 m grid spacing degraded to 900 m grid spacing and (c) 900 m grid spacing. Taken from Varble *et al.* (2014).

tigated. Statistics of vertical velocity and air mass flux showed that (1) updraughts expand and vertical velocity weakens with height, (2) updraughts expand and vertical velocity can strengthen with height, (3) updraughts split into multiple updraughts and (4) updraughts merged into one updraught. In these campaigns, peak vertical velocity was observed at higher levels and mostly within 2 km of cloud top (Yang *et al.*, 2016). It was found that weak and moderate vertical velocities contributed more to mass transport.

Yuter and Houze (1995) used radar observations of deep convection and found that later in the storm life cycle, most updraught area and upward mass transport was at the mid and upper levels. The area of weak vertical velocities increased in the horizontal as updraught intensity decreased. Yuter and Houze (1995) proposed that updraughts evolved as a series of parcels or bubbles. The increased mass transport is then associated with an aggregation of bubbles in the mid-levels. Bubbles can slow down due to; dilution of buoyancy by entrainment (Yuter and Houze, 1995; Peters *et al.*, 2019), enhancement of the downward directed dynamic pressure gradient force increasing drag (Morrison and Peters, 2018), dilution of vertical momentum reducing ascent rates, and in environments with vertical wind shear thermals follow a slantwise path reducing effective buoyancy and ascent rates (Peters *et al.*, 2019). Once thermals have slowed down and production in the lower levels has decreased, bubbles can spread out horizontally congregating in the mid and upper levels, depositing mass over a

horizontal region.

Updraughts in shallow cumulus clouds (depths less than 3 km) in Florida were observed using aircraft observations to evolve as pulsating bubbles ascending through the cloud (French *et al.*, 1999) rather than a persistent column. Similarly, Damiani *et al.* (2006) observed updraughts exhibiting cycles of vigorous growth followed by quiescence producing pulsating behaviour. Taylor *et al.* (2016) encountered several small pockets of updraughts from aircraft measurements as well as two distinct updraught regions during COPE. Hogan *et al.* (2008) used high resolution radar data to investigate mass and momentum fluxes in cumulonimbus clouds. The authors suggest that from the observations there was support for the hypothesis that updraughts form in a sequence of 'bubbles'.

High resolution, $O(100$ m) grid spacing, simulations of convection have shown vertical velocity taking the form of a 'thermal chain' compared to column-like vertical velocity at 1 km grid spacing (Varble *et al.*, 2014). Figure 1.3 shows an example vertical cross sections through updraughts from the Distributed Hydrodynamic-Aerosol-Radiation-Microphysics Application model (DHARMA). The 900 m grid spacing in Figure 1.3(c) shows updraughts being represented as a singular column, compared to the 100 m grid spacing in Figure 1.3(a) where updraughts take the form of a 'thermal chain' with separate fragments of updraught rising. When the 100 m grid spacing output is degraded to 900 m grid spacing (Figure 1.3(b)), the individual fragments of updraught are smoothed out. Hernandez-Deckers and Sherwood (2016) used numerical simulations to investigate thermals in cumulus clouds and the authors suggest that treating entrainment using transient thermals cloud provide a more physical approach for simulations. Yano (2014) suggests it may be easier to recognise convection consisting as an ensemble of thermals rather than a quasi-steady plume.

1.3 Thermals in deep convection

1.3.1 Laboratory experiments

Attempts to understand cumulus convection often focused on simple, conceptual models. Scorer and Ludlam (1953) introduced 'bubble theory' using a series of photographs of growing cumulus clouds. The photographs showed several thermals rising as turrets ascended, suggesting the theory that a bubble rises, shedding its outer skin in a wake until it becomes exhausted and spreads out. Scorer (1957) associated these discrete bubbles with 'thermals' discussed by glider pilots.

An example of a thermal studied in a water tank is shown in Figure 1.4. This thermal was created by releasing a dense fluid into a tank and photographing it as it descended. The wake of the thermal consisted of a mixture of thermal air and the surrounding environmental air. Scorer and Ludlam (1953) proposed that thermals transport heat upwards and can coagulate into larger thermals through wakes of prior thermals that engulf succeeding thermals. This implies that with increasing height, thermal radius will increase as they join together into a larger thermal. Thus thermals in lower regions of the cloud would be smaller. The amalgamation of thermals would produce an increase in mass in the upper regions of clouds. The cauliflower appearance of clouds could be considered a visualisation of an ensemble of bubbles.

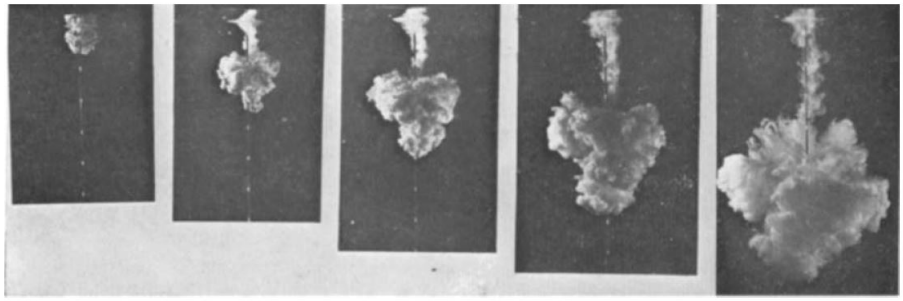

Figure 1.4: Photos of the shape of a thermal created by releasing a fluid into a tank. The shape of the thermal persists whilst the volume increases. Taken from Scorer (1957).

Woodward (1959) used laboratory experiments to suggest it is unlikely that thermals immediately become detached from the ground. They leave the ground as a

column or intermittent plume and then eventually become isolated. In his seminal paper, Turner (1969) discussed the structure of 'thermals' along with 'plumes' and 'starting plumes'. Turbulent plumes had a sharp boundary between the buoyant fluid and the surroundings and as they rose their width increased via entrainment. Woodward (1959) showed that the mean motion inside a thermal was like a flattened Hill's spherical vortex at any given height. There is upwards motion at the centre and descent near the edges. As the size of the thermal increased the velocity distribution remained similar. There was a sharp boundary between the turbulent buoyant thermal fluid and the environment.

Starting plumes have characteristics of both plumes and thermals. A plume-like flow is produced from a steady source of buoyancy. Similar to the plume, the flow pattern remains similar and increases with size behind the head, at the head the flow is like a thermal (Turner, 1969). The thermal top travels at about half the velocity at the centre of the plume at a given height (Turner, 1969). Similarly for a thermal alone, Woodward (1959) found that the thermal cap rose at a rate that is half that the thermal centre was rising at.

Figure 1.5 shows a schematic of a thermal indicating the buoyancy in shading, orientation of vertical acceleration on the left and theoretical vertical velocity profile on the right. This schematic depicts the typical shape of a thermal with the thermal head/core rising due to buoyancy forcing. An associated toroidal circulation is shown by the black arrows. The pressure perturbation due to buoyancy forcing and the pressure perturbation due to dynamic (hydrostatic) forcing acts towards the centre.

Figure 1.6 shows the results from laboratory measurements of the right-hand side only of an isolated thermal. Buoyant fluid is shown shaded, vertical velocity by solid lines and radial velocity by dashed lines are expressed as multiples of the vertical velocity of the thermal cap. Comparing Figure 1.6 with Figure 1.5 of an ideal thermal structure shows that the thermals from the Woodward (1959) laboratory experiments had the ideal flow patterns of thermals. The shaded region shows the right side of the filament structure of the thermal head descending and curling into the thermal centre. Negative vertical velocity is present in the filament and as the fluid enters a region of

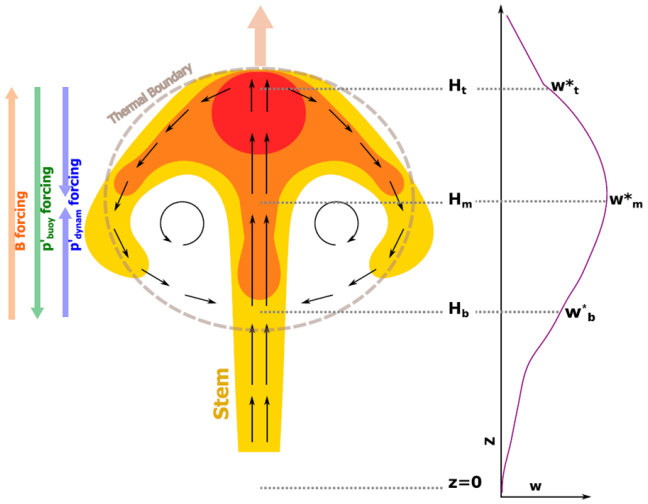

Figure 1.5: Schematic of a rising moist thermal. Shading shows buoyancy and air flow shown by black arrows. (left) Orientation of vertical accelerations in thermal. (right) Theoretical vertical velocity profile through core of thermal. W_b^*, W_m^* and W_t^* are the vertical velocities at the bottom H_b, middle H_m and top H_t. Taken from Morrison and Peters (2018).

positive vertical velocity it begins to curl around. The vertical velocity flow pattern also shows the increase in vertical velocity towards the thermal head, as indicated by Figure 1.5. Similarly, in Woodward (1959) their Figures 3 - 5 (not shown here) show the flow patterns of particles, and that 50 - 70% of particles entered the thermal at the front, before maximum radius was obtained. Remaining particles entered at the rear of the thermal, pushed outwards and then brought towards the centre as shown by the toroidal circulation.

Scorer (1957) found that wider thermals had more wake and they moved slower. A vortex ring structure was also observed and later confirmed by Woodward (1959) using a glider as well as laboratory experiments (discussed above). It was suggested that a thermal is not immediately detached from the ground but rises as a column or intermittent plume then becomes detached and isolated as its radius increases as it rises.

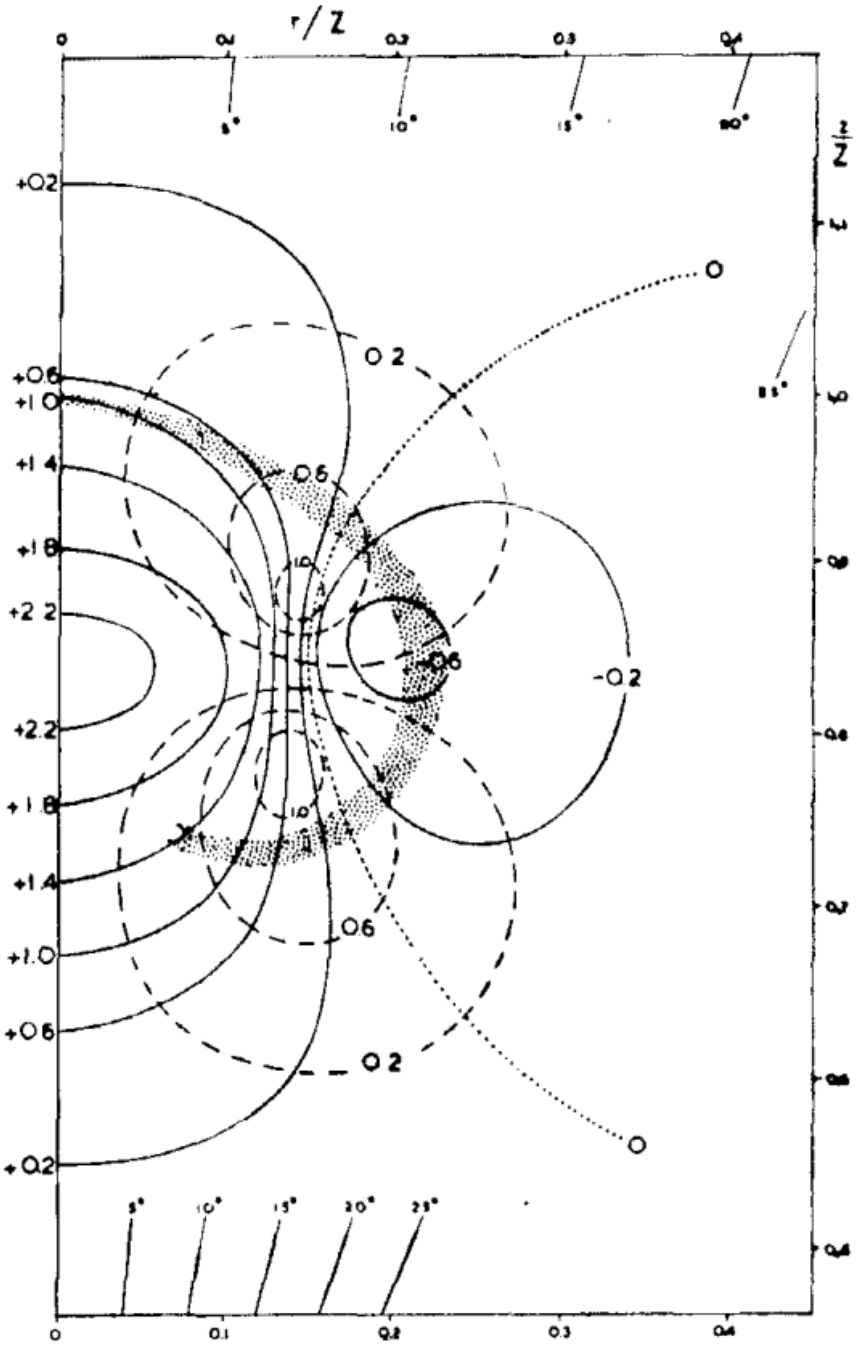

Figure 1.6: Distribution of velocity in and around an isolated thermal. Only the right hand side of the thermal is shown. Outline of the buoyant fluid is shaded. Vertical velocity (solid lines) and radial velocity (dashed lines) are expressed as multiples of the vertical velocity of the thermal cap. Taken from Woodward (1959).

1.3.2 Numerical simulations

Thermal circulations were simulated in a two-dimensional simulation of a small non-precipitating cumulus cloud (Klaassen and Clark, 1985) and three dimensional model

(Carpenter *et al.*, 1998). More recently entrainment of successive thermals in simulations of cumulus congestus (Moser and Lasher-Trapp, 2017), entrainment in individual convective clouds using thermals (Hannah, 2017), deep convection (Sherwood *et al.*, 2013), axis-symmetric model of thermal ascent rate in moist deep convection (Morrison and Peters, 2018) and thermal chains in idealised simulations of cumulus updraughts (Morrison *et al.*, 2020; Peters *et al.*, 2020) have been studied.

If the thermal-like nature of updraughts has been known about since the 1950's, it raises the question; why have most parametrizations represented updraughts using plumes rather than thermals? A parametrizations purpose is to determine the feedback of the sub-grid processes on the large scale environment. Given the sub-grid processes cannot be explicitly represented, the parametrizations represent the effect of the process and its impact of the large scale variables in the numerical model. With grid lengths over the last few decades remaining on the order of 10s of kilometre scale for operational forecasting, there was no requirement to attempt to simulate individual clouds. Improvements in computing power led to the usage of ensembles of plumes used in convective parametrizations. The interaction and impact of thermals in moist convection has recently and is currently being investigated using numerical simulations (Morrison, 2019; Whitall, 2019) and with grid spacing reaching the same scale as the clouds themselves (in the grey zone), observations of updraughts and in-cloud dynamics at fine scales are needed to understand in-cloud dynamical and turbulent behaviour.

Due to the transient nature of thermals, this means that the properties they can transport, their circulations and interactions can also be transient which can have impact on cloud evolution. Thermals have been found to impact entrainment (Blyth *et al.*, 1988) and transport hydrometeors (Damiani *et al.*, 2006). Figure 1.7a shows a schematic of an ascending thermal in a cumulus cloud and how the undilute core can continue to rise. Air entrained into the surface erodes the thermal and a turbulent wake exists to the rear of the thermal.

Simulations of a cumulus cloud in Florida shown in Figure 1.7b shows very similar results to Figure 1.7a. A cloud was simulated in a high resolution model, a thermal was seen to rise at different time snapshots shown in the panels. The contours show cloud

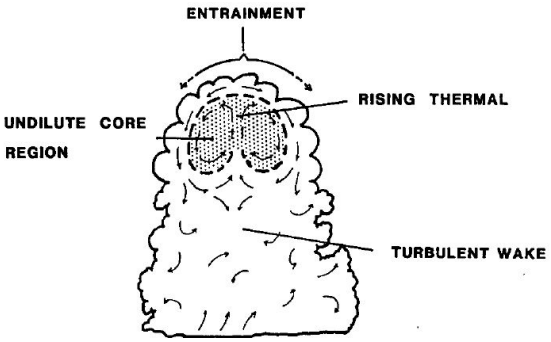

(a)

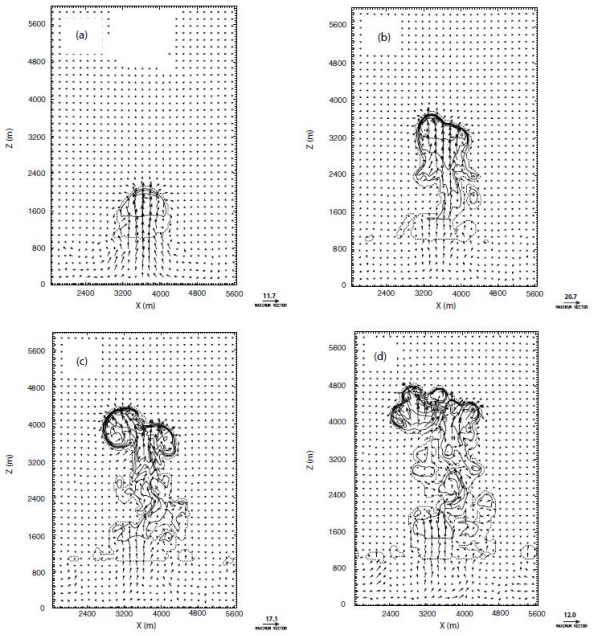

(b)

Figure 1.7: (a) Diagram of a cumulus cloud showing a shedding thermal that has ascended through the cloud. Entrainment into the surface of the thermal erodes the inner core. The undilute inner core rises until eroded near cloud top. Arrows indicate turbulent wake behind thermal. Taken from Blyth *et al.* (1988). (b) Simulation of cumulus clouds in Florida for different times from the Straka atmospheric model. Contours show cloud liquid water content (1 g m^{-3} intervals) and quivers show air motion in the plane of the cross section. Taken from Blyth *et al.* (2005).

liquid water and the arrows show the air motion. A thermal head was seen ascending with a turbulent wake left behind. As the thermal rose it had a similar shape to that of a starting plume. As time progressed this structure broke down, leaving no continuous feeding of cloud top from the surface and a thermal type structure in the cloud top. Sherwood *et al.* (2013) used simulations of congestus clouds, and found that deepening occurred in a sequence of multiple thermals with each successive thermal reaching higher than its predecessor.

Moser and Lasher-Trapp (2017) suggest that thermals can rejuvenate updraughts increasing the maximum vertical velocity thus increasing the cloud top height and proposed that this could cause a shallow to deep transition. In high resolution simulations by Hernandez-Deckers and Sherwood (2016) thermals were tracked using an adapted version of the tracking method presented in Sherwood *et al.* (2013). Hernandez-Deckers

and Sherwood (2016) found that tracked thermals contribute ≈18% to the total mass flux. Even though this seems small the authors suggest there are indications that the thermals are representative of most of the updraught activity. Updraughts that were not captured by the method were found to be very small or very slow thermals. Hernandez-Deckers and Sherwood (2016) found no evidence of coherent vertical updraught plumes in simulations.

Sherwood *et al.* (2013) suggest that the net buoyancy and drag from in-mixing and stagnant air may be smaller than what has previously been assumed in many parcel models. Entrainment rates were found to be on order of 2 - 3 km^{-1} but the drag caused by this mixing was very small, resulting in the thermal accelerating. Momentum budget calculations throughout thermal lifetimes showed that there was a near balance between buoyancy and nonhydrostatic forces. Individual drag forces found in the simulations were comparable to or smaller than the ratio of thermal ascent to lifetime. This showed that thermals were not strongly damped. Sherwood *et al.* (2013) termed these thermals as 'slippery' because there was no drag the thermal can slip through the atmosphere, thus buoyancy is dominant causing acceleration. This is similar to a Hill's vortex (Hill, 1894), in which the vorticity confinement leads to a symmetric dynamic pressure field above and below the vortex and hence no pressure drag.

In contrast, Romps and Charn (2015) propose the dominant balance is between drag and buoyancy. The authors integrated the vertical momentum equation to calculate a time series of cloud-top heights using the thermodynamic variables inside identified thermals. The authors do this using (1) only buoyancy, (2) only the pressure perturbation gradient acceleration and (3) the sum of both (1) and (2). By comparing to the actual cloud top height, results showed that the balance was between buoyancy and perturbation pressure forces, and that drag did play a role on thermals. Using buoyancy alone would mean that thermals would accelerate upward much more quickly than the true observed ascent. This is termed the 'sticky' thermal, because the thermal is experiencing drag forces from the perturbation pressure gradient force. This result was achieved whilst still neglecting entrainment and detrainment.

Morrison and Peters (2018) examined the pressure forces using high resolution sim-

ulations and found that the perturbation pressure gradient force does counter the perturbation buoyancy force. Therefore, thermals were found to be 'sticky' in agreement with Romps and Charn (2015) and Romps and Öktem (2015). Thus, the sticky behaviour is dissimilar from a Hill's vortex, which experiences no drag.

Gu *et al.* (2020b) studied how the pressure drag of a cloud ensemble relates to that of a single cloud to successive thermals in shallow cumulus. Gu *et al.* (2020b) also found that the dynamical pressure drag in the vertical velocity budget was dominant and that the thermodynamic pressure perturbation is considered to be important along the updraught central axis. In the cloud layer, buoyancy is a major source and is mostly offset by pressure drag. For clouds with lifetimes longer than 5 minutes the pressure drag always increased with height in the cloud layer. Local oscillations in the pressure gradients in the vertical were found. A single cloud was analysed and multiple maxima of vertical velocity and buoyancy were found in the vertical, indicating the cloud was composed of multiple rising thermals (Gu *et al.*, 2020b). Local minima of pressure perturbations were found lower in the cloud but stronger in magnitude than their counterparts on the up-shear side of the cloud. These were due to downdrafts associated with the cloud top circulation. These pressure perturbations mean that the pressure gradient force had couplets of negative and positive tendencies, located off the central axis due to vertical wind shear. The dynamic pressure gradient was present because the spatial distribution of local extremes of pressure perturbation, which themselves are due to flow structures of thermals (Gu *et al.*, 2020b). These successively rising thermals in the vertical lead to multiple minima of pressure perturbations. Even though there are oscillations, the overall pressure drag increased with height because it was enhanced by horizontal vorticity as thermals ascended, and the horizontal vorticity was increased by baroclinic generation. The vorticity was a source for dynamic pressure drag (Gu *et al.*, 2020b).

1.3.3 Observations

Thermals have also been observed in shallow cumulus clouds (Blyth *et al.*, 1988; French *et al.*, 1999; Blyth *et al.*, 2005) and cumulus congestus (Battan, 1975; Damiani *et al.*,

2006; Damiani and Vali, 2007). Figure 1.8 shows toroidal circulations observed with a Doppler cloud radar mounted on the Wyoming King Air aircraft in clouds over Wyoming (Damiani *et al.*, 2006). Multiple counter rotating vortex pairs were observed at multiple times indicating thermals in the cloud, with an example highlighted.

Melnikov and Zrnic (2017) used a Next Generation Radar (NEXRAD) in Oklahoma to observe the evolution of thermals in the boundary layer. The sensitivity of the radar was enhanced to increase the detectability of weak echoes. The enhanced detectability and oversampling of radar scans in elevation allowed the collection of dual polarization variables at high resolution. The evolution of thermals was characterised in measurements of differential reflectivity, which is the ratio of the horizontal and vertical echoes. The rise rate and width of thermals were estimated from vertical scans. Thermal top rise rates of 1.5 - 3.7 m s^{-1} and widths of 1 - 3 km were found. The thermals reached heights of 2 - 4 km, where low level cumulus clouds formed but did not deepen to precipitating clouds. Melnikov and Zrnic (2017) suggest that storm initiation could be estimated from areas that have the most intense thermals and that this strategy could possibly identify areas that have enhanced potential for convective storm initiation.

In observations of thermals in the boundary layer using echoes returned by insects (Melnikov and Zrnic, 2017) or in observations of shallow cumulus clouds that are not precipitating (French *et al.*, 1999), it seems reasonable to use the reflectivity and differential reflectivity to measure growth pulses. At the early stages of cloud development, reflectivity is low due to small particle sizes and therefore the reflectivity signal is not dominated by large liquid drops due to reflectivity being proportional to the 6th power of the the particle size (D^6). Insects and small cloud droplets can trace out the motion of the air at small wavelengths. Prior observations of deeper clouds in the congestus stage or extending to the tropopause and that were precipitating have used measurements of Doppler velocity to inspect the air motion in clouds. The usage of the Doppler velocity field seems reasonable given it is not proportional to D^6, and as seen in radar scans of deep convection, reflectivity does not provide the same insight into the in-cloud motions that Doppler velocity measurements do.

Doppler velocity measures the motion of the particles towards and away from the

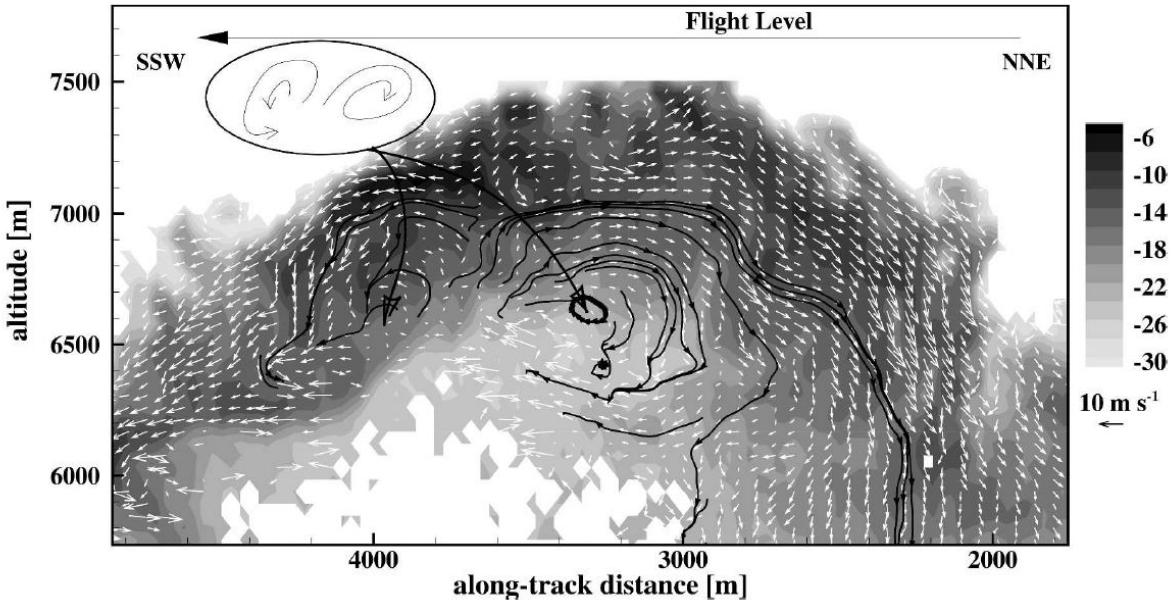

Figure 1.8: Radar scan of growing cumulus cloud showing vertical beam reflectivity (dBZ) and arrows show two dimensional velocity field in cloud. Solid lines are streamlines. Black circles highlights region of vortical circulation deemed to be a thermal. Observations taken from the Wyoming King Air aircraft of a cloud in Wyoming. Taken from Damiani *et al.* (2006).

radar, but animations also highlight 'blobs' of air rising in Doppler velocity measurements and complex dynamics. Furthermore, Doppler measurements provide the variance on the mean Doppler velocity, which is also useful for measuring turbulent air motion. Thus, it is reasonable to use Doppler velocity measurements, a direct measure of air motion in clouds, rather than reflectivity measurements that do not clearly show in-cloud motion when observing deep precipitating clouds. Significant in-cloud dynamics can be occurring whilst clouds have quiescent cloud tops and this is not seen in observations of reflectivity which usually shows columns of heavy rain. This was the case in measurements by Yuter and Houze (1995) where observations of deep convective clouds using S (3 GHz) and X (10 GHz) band ground based radar were used.

Blyth and Latham (1993) used aircraft observations and found that clouds go through several stages of growth and decay, with each growth gradually increasing in height. French *et al.* (1999) determined that in cumulus clouds the growth and decay of pulses can be tied to entrainment and detrainment. Vertical velocity and LWC observed using aircraft in Florida cumulus clouds, up to 4 km deep, indicated

thermal behaviour. These measurements also matched transects taken through numerical simulations of thermals for the observed cases (Blyth *et al.*, 2005). The aircraft observations of cumulus congestus clouds found a strong updraught across most of the cloud with weak downdrafts at cloud edge. Updraught size and strength were found to increase with altitude. Two connected thermals in different stages of development were found but it was suggested the two thermals could also be a single thermal that had forked into two (Blyth *et al.*, 2005).

Damiani *et al.* (2006) used 95 GHz radar mounted on aircraft to take single and dual Doppler measurements of in-cloud motion in a non-precipitating cloud and Hogan *et al.* (2008) retrieved vertical velocity from Doppler velocity measurements in deep convection and noted updraughts developing as pulses. Finally, features in reflectivity are expected to move with hydrometeors, which are being advected by the movement or flow of air in clouds. Observations show that reflectivity features can be uniform over distances on the order of kilometres and that fine scale dynamical features can be hard to discern from reflectivity fields. Such uniformity can also occur in Doppler velocity fields, but observations clearly show fine scale dynamical features developing in Doppler velocity measurements that are not visible in reflectivity measurements of deep convection. This would make it hard to track features in reflectivity, but development of fine scale dynamical features can be tracked in Doppler velocity measurements.

Entrainment is a vital processes because entrainment of environmental air can dilute updraughts and affect the growth and decay of clouds. The main focus of many observational and numerical studies is entrainment. Thermals can be modified by entrainment and can modify spatial charge distributions (Moser and Lasher-Trapp, 2017). Aircraft observations showed cumulus clouds entrain from all levels of the environment as the aircraft descended where entrainment is through the front cap and the rear in the wake of the thermal (Blyth *et al.*, 1988). Thermals can moisten the environment so that successive thermals can rise to greater heights.

Hydrometeor transport can affect the production of precipitation and the microphysics in clouds. Observations and numerical simulations can be used to investigate these characteristics, behaviour and interactions of thermals with other processes in

cumulus clouds. Blyth and Latham (1993) investigated ice production and precipitation development in cumulus cloud in New Mexico, US using the King Air aircraft. Cloud continuously developed in place over mountains allowing multiple aircraft penetrations to take place through cloud tops every 5 minutes. The authors found that ice first formed in updraughts or downdraughts, there were more ice particles observed in the clouds than prior studies suggest should exist due to only primary ice nucleation. Therefore the Hallett-Mossop process of ice splintering during the riming process (Hallett and Mossop, 1974) was likely to be occurring to account for the high concentrations of ice measured. The largest graupel particles were observed in regions of fewer total number of particles, maybe due to particle sorting. Graupel embryos were introduced into new turrets that ascended through the cloud and ice had a long time to grow into graupel embryo sizes. The authors suggest that the ice particles are transported to the general level of cloud top by updraughts if produced at lower levels by the Hallett-Mossop process and downdraughts if produced at higher levels.

For the Hallett-Mossop process to be responsible for the ice development in the New Mexico thunderstorms, because of the large concentrations of ice, some process must be occurring below. Keller and Sax (1981) suggest that large concentrations of ice particles in observations of Florida cumulus clouds with splinters were also produced via the Hallett-Mossop process. For this process to operate, the required particles for the Hallett-Mossop process are provided by a multiple thermal mechanism, providing particles from lower regions of cloud and the vertical transport of splinters (Blyth and Latham, 1993).

Romps and Öktem (2015) used stereo photogrammetry, utilising two synchronised cameras, to measure the three-dimensional position of ascending cloud thermals. This technique can measure the size and speed of cloud thermals, particularly applied to observed clouds in Florida. The importance of drag was investigated in the momentum equation for the observed cloud thermals. Romps and Öktem (2015) found that via two methods: (1) combining three pieces of information on the ascent speed, radii of thermals and the vertical momentum equation and (2) buoyancy of thermals measured in-situ and large-eddy simulations (LES), to show a drag co-efficient of approximately

1 was required for measurements from the stereo photogrammetry to match the known buoyancy from previous in-situ measurements and LES. Thus, concluding that the 'sticky' thermal hypothesis holds, because drag was present and acting on thermals in the observations.

1.3.4 Equations describing thermal motion and properties

In this subsection equations describing the basic motion and properties of a thermal are derived. A thermal is assumed to be in an environment that is stationary, homogeneous and dry. The environment outside of the thermal (subscript o) has properties; density ρ_o, pressure P_o and potential temperature θ_o. A thermal (subscript i) has vertical velocity w, density ρ_i, pressure P_i, potential temperature θ_i, volume V, radius R and cloud liquid water q. The volume change is related to the current volume plus some source and sink terms. These terms are the volume entrained and detrained in and out the thermal respectively

$$(\rho V)_{t+\Delta T} = (\rho V)_i + (\rho V)_{in} - (\rho V)_{out}, \tag{1.2}$$

which can be discritized and variables for the environment and thermal are substituted in

$$\frac{(\rho V)_{t+\Delta T} - (\rho V)_i}{\Delta t} = \frac{\rho_o \delta V_{ent}}{\Delta t} - \frac{\rho_i \delta V_{detr}}{\Delta t}, \tag{1.3}$$

where V_{ent} is the air entrained into the thermal from the environment and V_{detr} is the air detrained from the thermal into the environment. The volume can also change due to thermodynamic effects such as change in temperature causing expansion and contraction

$$\frac{\partial \rho_i V}{\partial t} = \frac{\rho_o \partial V_{ent}}{\partial t} - \frac{\rho_i \partial V_{detr}}{\partial t} + thermodynamics, \tag{1.4}$$

which are not considered at this stage. The motion of the thermal is described by the vertical momentum equation

$$\frac{Dw}{Dt} = \frac{-1}{\rho_i}\frac{\partial P_i}{\partial z} - g - F, \tag{1.5}$$

where $\frac{\partial P_i}{\partial z}$ is the pressure gradient force on the thermal, g is gravity and F is a sink term. The environment the thermal resides in is assumed to be in hydrostatic balance, given by equation 1.6.

$$\frac{\partial \overline{P_o}}{\partial z} = -\overline{\rho_o} g. \tag{1.6}$$

The Lagrangian derivative $\frac{Dw}{Dt}$ can be decomposed into its Eulerian and advective components for an incompressible fluid, given by equation 1.7.

$$\frac{Dw}{Dt} = \frac{\partial w}{\partial t} + \vec{u} \cdot \nabla w. \tag{1.7}$$

Assuming that the pressure in the thermal rapidly adjusts to the environment $P_i = P_o$ then $\frac{\partial P_i}{\partial z} = \frac{\partial \overline{P_o}}{\partial z}$. For the thermal

$$\frac{\partial w}{\partial t} = -\frac{1}{\rho_i}(-\overline{\rho_o} g) - \vec{u} \cdot \nabla w - g - F, \tag{1.8}$$

$$\frac{\partial w}{\partial t} = g(\frac{\overline{\rho_o} - \rho_i}{\rho_i}) - \vec{u} \cdot \nabla w - F. \tag{1.9}$$

The total density is decomposed into its mean ($\overline{\rho_i}$) and perturbation ($\rho_i^{'}$) components $\rho_i = \overline{\rho_i} + \rho_i^{'}$. Substituting this into equation 1.9 gives

$$\frac{\partial w}{\partial t} = g(\frac{\overline{\rho_o} - (\overline{\rho_i} + \rho_i^{'})}{\overline{\rho_i} + \rho_i^{'}}) - \vec{u} \cdot \nabla w - F, \tag{1.10}$$

due to the pressure adjustment $\rho_i = \overline{\rho_o}$, and given that usually $\overline{\rho_i} >> \rho_i^{'}$

$$\frac{\partial w}{\partial t} = \underbrace{-g\,(\frac{\rho_i^{'}}{\overline{\rho_i}})}_{\mathrm{B}} - \vec{u} \cdot \nabla w - F, \tag{1.11}$$

where B is the buoyancy.

The vertical momentum equation found by integrating a differential equation for the vertical acceleration of a cumulus tower (Simpson and Wiggert, 1969) is used in some studies, for example Gu *et al.* (2020b). This equation can be applied to a cloud tower being idealised as a jet, buoyant plume or thermal with internal vortical circulations. Using the chain rule $\frac{\partial w}{\partial t} = \frac{\partial w}{\partial z}\frac{\partial z}{\partial t}$, and that $\frac{\partial z}{\partial t} = w$ then $\frac{\partial w}{\partial z}w = \frac{\partial}{\partial z}\frac{1}{2}w^2$. Equation 1.11 is modified and a virtual mass coefficient (γ) is introduced as Simpson and Wiggert (1969) found thermals were ascending too quickly. The virtual mass coefficient arose from Turner (1969) suggesting thermals continually swallowed the turbulent boundary layer so that the drag coefficient (C_D) should be zero. Therefore the virtual mass coefficient accounts for thermals pushing air outside of and ahead of the thermal around the rising thermal. γ reduces rise rates whilst giving slightly higher cloud top heights with the same buoyancy (Simpson and Wiggert, 1969). Furthermore, velocity can change due to entrainment (ϵ) and detrainment (δ) of air with different properties

$$\frac{\partial}{\partial z}(\frac{w^2}{2}) = \frac{-gB}{1+\gamma} - F + \epsilon - \delta. \tag{1.12}$$

Simpson and Wiggert (1969) hypothesised the entrainment relationship $\epsilon - \delta = \frac{1}{M}\frac{dM}{dz} = \frac{9}{32}\frac{K_2}{R_i}$ where entrainment is inversely proportional to the updraught dimension. R_i is the radius of the updraught, M is the mass and K_2 is the entrainment coefficient. Simpson and Wiggert (1969) arrive at Equation 1.13 by applying the Levine (1959) rise rate equation, in which the full derivation can be found. R_i for cumulus towers can be prescribed, Simpson and Wiggert (1969) determined R_i for cumulus towers empirically from photographs or aircraft penetrations.

$$\frac{\partial}{\partial z}(\frac{w^2}{2}) = \frac{gB}{1+\gamma} - \frac{3}{8}(\frac{3}{4}K_2 + C_d)\frac{w^2}{R_i} \tag{1.13}$$

The liquid water content (q) inside the thermal is modified by entrainment, detrainment, condensation and evaporation

$$\frac{\partial q}{\partial t} = \epsilon - \delta + condensation - evaporation. \tag{1.14}$$

From above $\epsilon - \delta = \frac{1}{M}\frac{dM}{dz} = \frac{9}{32}\frac{K_2}{R_i}$. The change of liquid water content (q) assuming pseudo-adiabatic processes is then given by

$$\frac{\partial q}{\partial t} = \frac{9}{32}\frac{K_2}{R_i} + \frac{c_p T}{L}(\frac{dT}{T} - \frac{kdP}{P}), \tag{1.15}$$

Where T is the temperature, P is the pressure, c_p is the specific heat capacity at constant pressure, L is the latent heat of vaporisation.

Equation 1.15 can be expressed in terms of potential temperature (θ_i) because it is a conserved quantity. Using the relationship between θ and T of $\theta = T(\frac{P_0}{P})^{\frac{R}{c_p}}$, by applying a logarithmic transform and differentiating $dln(\theta) = \frac{dT}{T} - \frac{kdP}{P}$, where $k = \frac{R}{c_p}$. Equation 1.15 becomes

$$\frac{\partial q}{\partial t} = \frac{9}{32}\frac{K_2}{R_i} + \frac{c_p T}{L}(\frac{dln(\theta_i)}{dt}), \tag{1.16}$$

and using the Exner pressure $\pi = (\frac{P}{P_0})^k$ and that $\frac{T}{T_0} = (\frac{P}{P_0})^k$, now $T = \pi\theta$. Equation 1.16 becomes

$$\frac{\partial q}{\partial t} = \frac{9}{32}\frac{K_2}{R_i} + \frac{c_p \pi\theta_i}{L}(\frac{d\theta_i}{\theta_i dt}). \tag{1.17}$$

Finally $\frac{\partial q}{\partial t}$ is given by

$$\frac{\partial q}{\partial t} = \frac{9K_2}{32R_i} + \frac{c_p \pi}{L}\frac{d\theta_i}{dt}. \tag{1.18}$$

The potential temperature of the thermal is found by re-arranging equation 1.18 to arrive at a similar result as that derived in Levine (1959)

$$\frac{\partial \theta_i}{\partial t} = \frac{L}{\pi c_p}\left(-\frac{9K_2}{32R_i} + \frac{\partial q}{\partial t}\right). \tag{1.19}$$

These equations provide a simple model for describing the basic properties of a thermal. Further complex equations have been derived explaining the theoretical behaviour and properties of thermals and can be used to model thermals to compare to large eddy simulations (Morrison and Peters, 2018; Morrison *et al.*, 2020; Peters *et al.*,

2020).

1.3.5 Vortical circulation

The vortical circulation (or toroidal in 3D) associated with thermals forms an important topic of discussion in the literature. This circulation, as discussed above, has been observed in laboratory experiments, is commonly seen in numerical simulations and has been seen in limited observations. Many studies use the vortical circulation as a definition of a thermal, inspect the local pressure perturbations associated with circulations and discuss relationships to entrainment.

Many numerical studies initiate convection by adding a rising thermal or bubble such as warm moist bubble as a Gaussian perturbation in the numerical domain. Such a Gaussian has a defined width usually on the order of a few hundred metres or 1 - 4 km and temperature perturbations of around 1 - 2 K. Of the studies discussed above, convection was initiated by; Klaassen and Clark (1985) induced a rising thermal originating in a heated boundary layer, Carpenter *et al.* (1998) added a Gaussian mountain to act as an elevated convection initiating heat source, Sherwood *et al.* (2013) using diurnally varying heating at a central portion of the surface for a given horizontal extent, Moser and Lasher-Trapp (2017) used a Gaussian heating function in the centre of the domain, Romps and Charn (2015) and Gu *et al.* (2020b) used a radiative convective equilibrium sounding, Varble *et al.* (2014) used initial conditions from an idealised oceanic lower boundary, Hernandez-Deckers and Sherwood (2018) used random perturbations at the surface and Blyth *et al.* (2005); Hannah (2017); Morrison (2017); Morrison and Peters (2018); Peters *et al.* (2019); Morrison *et al.* (2020); Peters *et al.* (2020) added a bubble (Gaussian). If a blob of buoyant air rises, it can develop vortical circulations.

Given thermals are a region of more buoyant, less dense air compared to the surroundings a the thermal is ascending in the atmosphere, the Richardson number determines the stability of ascending thermals or parcels and whether turbulence will exist due to the vertical stability and vertical wind shear. The Richardson (Ri) number is given by

$$Ri = \frac{g}{\theta} \frac{\frac{\partial \theta}{\partial z}}{(\frac{\partial u}{\partial z})^2}, \tag{1.20}$$

where θ is the potential temperature, g is gravity, $\frac{\partial \theta}{\partial z}$ is the vertical gradient of potential temperature (vertical stability) and $(\frac{\partial u}{dz})^2$ is the vertical wind shear. When the environmental lapse rate is greater than the dry adiabatic lapse rate, the atmosphere is unstable. In an unstable atmosphere a displaced parcel, a thermal, will accelerate upwards in the direction of its displacement. When Ri is less than the critical Richardson number (Ri_c), generally taken to be $\approx$0.25, or Ri becomes negative which occurs in cases of buoyant (static) instability ($\frac{\partial \theta}{\partial z} < 0$ i.e the environment is absolutely unstable) or either the vertical wind shear is large then turbulence will exist. In cases of strongly negative Ri number, convection predominates and there is strong vertical motion characteristic of an unstable atmosphere.

The relative vorticity (ξ) is found by taking the curl of the velocity field

$$\xi = \nabla \times \vec{u} = (\frac{\partial w}{\partial y} - \frac{\partial v}{\partial z})\hat{i} + (\frac{\partial u}{\partial z} - \frac{\partial w}{\partial x})\hat{j} + (\frac{\partial v}{\partial x} - \frac{\partial u}{\partial y})\hat{k}, \tag{1.21}$$

where $\hat{i}$, $\hat{j}$ and $\hat{k}$ denote the x, y an z components respectively. u, v and w are the velocity components in the x, y and z directions respectively. The rate of change of the absolute vorticity is given by

$$\frac{D\zeta}{Dt} = -\nabla(\frac{1}{\rho}) \times \nabla p + (\zeta \cdot \nabla)\vec{u} - \zeta(\nabla \cdot \vec{u}) + \nu \nabla^2 \xi, \tag{1.22}$$

where ζ is the absolute vorticity, ν is the viscosity, $-\nabla(\frac{1}{\rho}) \times \nabla p$ is the baroclinic production term, $(\zeta \cdot \nabla)\vec{u}$ is the stretching and tilting term, $\zeta(\nabla \cdot \vec{u})$ is the expansion term and $\nu \nabla^2 \xi$ represents the change in vorticity due to viscosity.

Due to the local maxima of buoyancy associated with a thermal, an upwards directed buoyant pressure gradient force is present. This creates a dynamic low pressure below the thermal and high pressure above the thermal, inducing divergence above the thermal and convergence below, resulting in the typical thermal flow pattern. Peters

et al. (2019) and Morrison and Peters (2018) simulate the pressure patterns due to buoyancy and dynamical forcing in detail.

Thus for simulations that induce convection using a warm bubble, vortical circulations can be expected due to the baroclinic production term in the vorticity equation (equation 1.22) because of the density difference between the thermal and the environment. The stretching term may play a role if a thermal stretches as it accelerates upwards. Limited observations provided some evidence of vortical circulations in clouds (Blyth *et al.*, 1988, 2005; Damiani *et al.*, 2006), therefore observing such circulations with developing updraught pulses could provide some insight into the development of updraughts structures at fine spatial scales and how these features interact with cloud development.

1.4 Thermal chains

To understand convection there are three conceptual models; the steady state plume, rising thermals and the starting plume. Steady state plumes are assumed to be a continuous column of rising fluid with lateral entrainment occurring along the edge. Plumes greatly reduce the complexity of theoretical equations used to understand deep convection. With thermals, deep convection is assumed to be composed of discrete pulses of rising positive buoyancy anomalies that resemble spherical vortices. Entrainment is primarily accomplished by organised toroidal flow structures that occur on the scale of the thermal itself. Starting plumes have a plume body and a thermal head, therefore characteristics of both. Each models updraughts very different in the way they behave, such as entraining air and not one individual model can fully explain moist convection.

Throughout this thesis the terminology updraughts, updraught pulses, thermals and thermal chains is encountered. Updraughts are defined as a large contiguous structure of vertical velocity lasting on the order of minutes and longer, usually conceptualised as plumes. Updraught pulses are defined synonymous to thermals (defined above) as short lived small buoyant structures with a vertical velocity maxima and toroidal or vortical circulations. The term thermal is also applied to identify individual vertical

velocity maxima with vortical circulations that are associated with thermal chains. Thermal chains used by Morrison *et al.* (2020) and Peters *et al.* (2020) are smaller in size shorter lived structures of vertical velocity identified as a local intensification, or pulse of vertical velocity that is chained to a larger updraught structure, such as that shown in Figure 1.9. Larger updraught structures can also consist of multiple smaller updraught pulses or thermal structures, individually or as chains.

Updraughts that evolve as a sequence of successive rising thermals with each thermal having its own circulation could have implications for the properties of the air entrained in clouds and into later thermals. Damiani *et al.* (2006) found that thermals could influence precipitation efficiency and Blyth and Latham (1993) found that thermals could contribute to the rapid glaciation of clouds. Morrison *et al.* (2020) and Peters *et al.* (2020) investigated why the thermal chain or plume structure occurs in clouds. It is important to understand why thermal chains may be favoured as an updraught structure under certain conditions. Morrison *et al.* (2020) derived theoretical equations describing thermal behaviour, buoyancy and vertical velocity to produce an axis-symmetric model. Updraught widths and relative humidity were prescribed to represent wide and narrow updraughts and moist and drier environments. Constant values of 42.5% were used for dry environments and 85% for moist environments above 1.5 km height. Radii between 400 m and 2 km were used as initial thermal radii. Each relative humidity was tested at a fixed width and each width was used as a starting width for a fixed relative humidity.

Morrison *et al.* (2020) found that isolated thermals can transition to thermal chains then to plume-like structures when updraughts are wide and moist in clouds. With wider updraughts the structure resembled starting plumes, with a primary thermal at the head and a plume-like body, as discussed by Turner (1969). For narrow and dry updraughts, the structure tended to be more isolated and thermal-like. Updraughts can contain thermals and vortices with a variety of sizes, ranging from the scale of the updraught down to the Kolmogorov micro-scale, the scale at which eddies dissipate into heat. This means there are circulations with the largest having horizontal scales similar to the cloud and in models these can be considered explicitly. The smallest

circulations are turbulent eddies, and these turbulent eddies must be parametrized in model since no meteorological model is able to resolve them. Thermal circulations within moist updraughts tended to retain an approximate constant radius and spherical shape as they ascended through clouds, as long as thermals started positively buoyant. For thermals that had radii greater than 1 km and became negatively buoyant, their radii increased rapidly as they ascended (Morrison *et al.*, 2020).

The transition between the isolated thermal and the plume regime can be represented by the thermal chain structure. Thermal chains were favoured over the starting plume structures over a wide range of conditions in the axis-symmetric simulations (Morrison *et al.*, 2020). Thermal chains were more dominant in moist convection, determined to be from the close coupling between dynamic entrainment, that is entrainment near the base of the thermal due to the vortical circulation, and the enhanced mixing of dry environmental air causing a reduction in buoyancy (Morrison *et al.*, 2020).

Peters *et al.* (2020) further investigated why thermal chains are a common mode of cumulus convection and what mechanisms determine whether updraughts have this structure using a cloud model to simulate thermals of various radii to compare to axis-symmetric simulations. In their simulations buoyant updraughts ascended and rapidly developed vortical circulations in the primary thermal, as expected when a warm bubble is released in a model. The inward circulation associated with the vortical circulation locally enhanced entrainment of environmental air. If the environment was dry this leads to a local reduction of buoyancy relative to other regions where the dynamic entrainment was not locally enhanced. The buoyancy structure, which was modified by entrainment, then modified the flow and leads to a breakdown of updraughts into successive rising thermals, thermal chains as shown in Figure 1.9(a) and (c) for narrow updraughts. For wider updraughts in dry environments shown in Figure 1.9(e), individual thermals are less distinct but local regions of vertical velocity maxima can still be seen.

Peters *et al.* (2020) hypothesised that thermal chains are prevalent as the middle troposphere becomes drier, all else being equal. Convective structures became more plume-like in a comparatively moist middle tropospheric environment as shown in

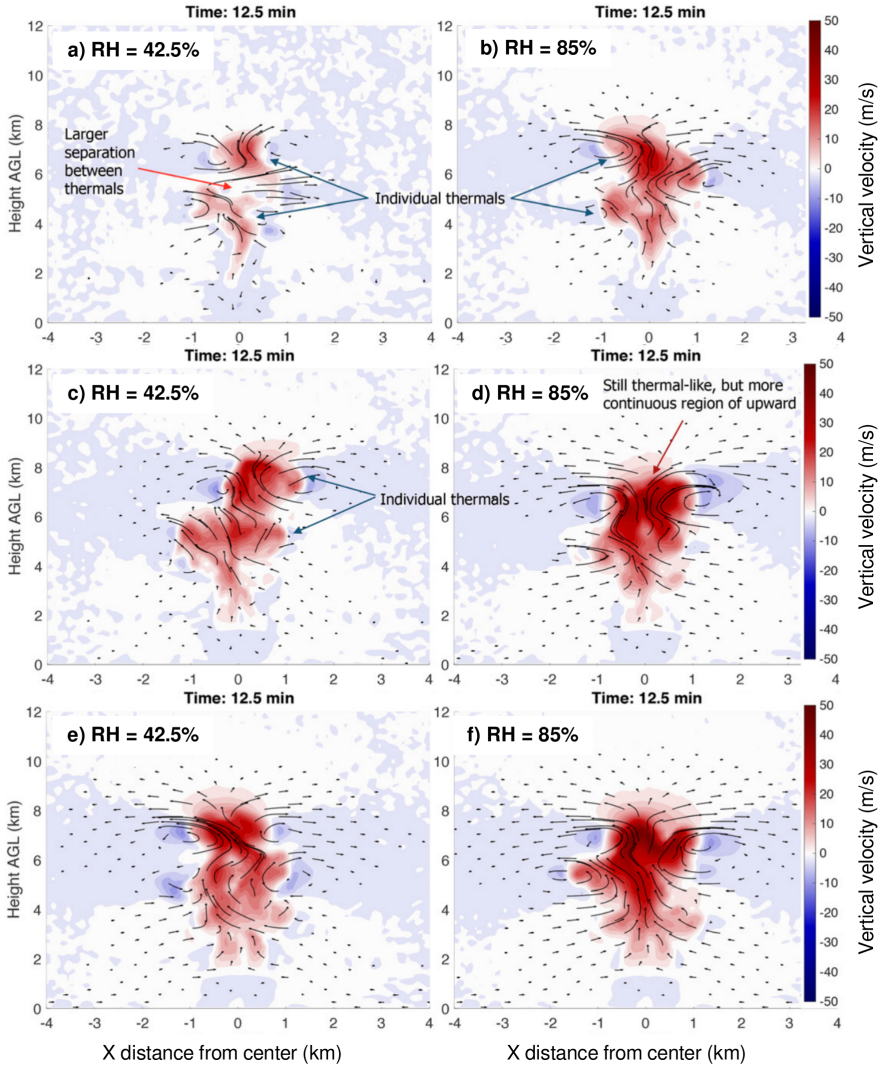

Figure 1.9: Vertical cross sections along the x-axis from 3D simulation model output at 12.5 min of vertical velocity from (shading, m/s) and flow vectors (black arrows with an initial bubble radius (R) of (a) 1000 m and relative humidity (RH) of 42.5%, (b) 85%. R of (c) 1500 m and RH of 42.5%, (d) 85% and an R of (e) 2000 m and RH of 42.5% and (f) RH of 85%. Results from model output at 12.5 min. Taken from Peters *et al.* (2020).

Figure 1.9(b) and (d) for narrow updraughts but individual thermals can still be seen. Figure 1.9(f) shows that with wide updraughts individual thermals are not distinct and the updraught resembles a starting plume. This was suggested to be because of the dependence of entrainment driven dilution on cloud radius, where narrower clouds are hypothesised to be more thermal-like and wider clouds are more plume-like. Entrainment of dry air can reduce condensation rates and increase evaporation rates, thus causing a breakdown of the updraught into a succession of rising thermals.

Therefore entrainment of dry air was essential for the development of thermal chain type structures (Peters *et al.*, 2020).

In this study the authors defined a thermal object to have vertical velocity greater than 3 m s^{-1}. Clouds that had radii between 400 - 1000 m contained isolated thermals and clouds with radii greater than 800 m tended to have updraughts resembling starting plumes over the first 15 - 20 minutes during simulations. In simulations, thermal radii was almost constant with height in dry atmospheres up to about 7 km. After 7 km, thermal radii increased with height. In moist atmospheres, thermal radii increased and after 7 km rapidly increased. The thermal size increase near the end of a thermal ascent is related to the deformation of the thermal as they reached levels of neutral buoyancy in the clouds. Therefore they become negatively buoyant and their shape can deform. This was consistent with the axis-symmetric simulations in Morrison *et al.* (2020).

Peters *et al.* (2020) hypothesise that turbulence can promote breakdown of initial thermals that are large into smaller distinct vortical circulations, but these were not investigated in any further detail. Simulations contained multiple distinct thermal objects, and they were not vertically aligned and it was suggested turbulence could induce horizontal drift.

In Morrison *et al.* (2020) turbulence was provided by adding random temperature perturbations with a maximum amplitude of 1 K below 2 km height to the initial conditions and the Smagorinsky subgrid-scale turbulence scheme was used. The authors suggest that turbulence is not critical for explaining the occurrence of thermal chains, but individual thermal circulations were more distinct in the 3D turbulent moist simulations, than in simulations with no turbulence and that were axis-symmetric. Although, one may consider a thermal itself a form of turbulence. Clearly, this points to the need to investigate interactions between updraught structures and turbulence.

1.4.1 Thermal ascent

There appears to be some discontinuity in the literature on whether thermals ascend successively with new thermals forming below their predecessor, or if a starting plume type updraught breaks up forming chains of thermals therefore are not entirely new

entities or whether thermals originate higher and higher. In some studies a single thermal was used to initiate convection so these cannot be discussed in this context (Hannah, 2017; Morrison and Peters, 2018).

Blyth *et al.* (2005) simulated one thermal for a cloud, but there was a hint of a second thermal forming near the base as the first thermal was near cloud top. The authors note that an observed cloud could contain two connected thermals in different stages of development or a single thermal had bifurcated. Model simulations indicated the latter when comparing the simulated cloud to that observed by aircraft. But most often, clouds did appear to contain more than one thermal in different stages of development. An example of this structure is shown in Figure 1.7b. Carpenter *et al.* (1998) noted the pulsating nature of convection in their simulations with about a 30 minute or less pulsation time. It was not possible to discern whether these pulses were from individual thermals. Successive rising thermals were present in simulations by Gu *et al.* (2020b) and sequences of multiple thermals each reaching higher than the last were determined to cause cloud deepening in simulations by Sherwood *et al.* (2013).

Hernandez-Deckers and Sherwood (2016) found that as convection deepens thermals originated higher up and are larger and rise faster, rather than originating lower, regardless of cloud depth. Morrison (2017) found pulse-like behaviour of updraughts in simulations that were thermal-like and driven by dynamic entrainment. This structure of updraughts is further investigated in Morrison *et al.* (2020) and Peters *et al.* (2020), as discussed above where updraught flow above levels of locally reduced buoyancy separate from below, leading to a breakdown of the updraught into successive discrete thermals, termed the thermal chain. The thermal chain structure poses a different model to those where new thermals are originating from below or higher up in clouds. A similar thermal chain structure was found by Varble *et al.* (2014) and is shown in Figure 1.3, where updraughts with vertical velocity greater than 10 m s^{-1} change from resembling plumes in ≈1 km grid spacing simulations to bubble-like cores of shedding thermals in ≈100 m simulations. These structures appear to rise in successive discrete regions of high vertical velocity.

Ideally observations would provide insight into the development of strong up-

draughts in convective clouds. Observations of thermals in the boundary layer that later formed shallow cumulus found that plumes of air consisted of two or three close thermals, seen in the radar reflectivity field (Melnikov and Zrnic, 2017). Pulses of growth with subsequent bubbles ascended through remnants of earlier bubbles which indicated evidence of multiple bubble behaviour in shallow cumulus (French *et al.*, 1999). The authors note that while their work can reinforce bubble theory, the focus was on individual bubbles rather than multiple bubbles ascending, and that the growth and decay of such individual bubbles was similar to that found in Klaassen and Clark (1985).

Further aircraft observations by Blyth *et al.* (1988) and Blyth and Latham (1993) found multi-thermal behaviour. Blyth *et al.* (1988) found shedding thermal behaviour in clouds observed with aircraft. The authors claim that each thermal was not a simple single thermal, but had pulsating nature with alternating sequences of growth during repeated aircraft penetrations of clouds. Growth occurred on the upshear side of clouds and decayed on the downshear side and it was likely that some more vigorous clouds had a persistent updraught that behaved like a starting plume. A diagram of their model can be seen in Figure 1.7a, where organised vortical circulations exist around the updraught core. Thus far, observations have been limited to shallow non-precipitating cumulus or deep convective clouds that are limited in sample via aircraft.

Yuter and Houze (1995) observed deep convection with multiple radars, and proposed a 'particle fountain' model where parcels have a range of initial buoyancy and experience different entrainment. Only 'lucky' parcels reach the cloud top, and this model accounts for the transition of a convective cloud to the stratiform phase. This study treated updraughts as behaving like a buoyant bubble, or population of bubbles. Observations of moderately deep cumulus (depths $\approx$3 km) by Damiani *et al.* (2006) noted multi-thermal systems, with pulsating nature. There were alternating sequences of updraught during repeated aircraft penetrations. Vigorous updraughts were often followed by relative quiescence and then again followed by renewed updraughts. It should be noted that Damiani *et al.* (2006) focused on individual thermals and thus no results on the multi-thermal aspect of clouds were presented but only noted visually.

More recent observations of deep convection observed cloud tops and found thermal pulses from the growth of cloud tops using cameras (Romps and Öktem, 2015).

Observations of a thunderstorm in New Mexico using multiple Doppler radars found that the central cell behaved like an isolated bubble or thermal, where the bubble was elongated vertically and transient with the presence of vortical motions (Raymond and Blyth, 1989). Concentrations of positive and negative vorticity indicate vortex ring characteristics of thermals and that the bubble may have ascended with little entrainment (Raymond and Blyth, 1989). Finally, vertical velocity retrieved from observations tracking a precipitating deep convective cloud supported the notion that updraughts form in a sequence of bubbles (Hogan *et al.*, 2008), similar to the updraught behaviour proposed by Yuter and Houze (1995).

It seems that isolated pulses of buoyancy that rise in clouds (originating higher or lower than their predecessors) and larger updraught structures that breakup into smaller structures with pulses of growth are both termed thermals, with the larger ascent region with local vertical velocity maxima being more chain like. At what stage in a clouds lifetime these different updraught structures occur, or whether they can both occur at the same time and how they are developing in time in deep convection and interacting with the cloud and microphysics is not fully understood. Whilst many properties of thermals in numerical simulations have been derived and some limited observations of thermals with vortical circulations or updraught pulse growth (assumed to be thermals ascending) has been observed, no study has investigated the development of updraught pulse structures in deep convection developing over time, observed in multiple convective cells and to determine properties of and how thermals are interacting in deep clouds, with turbulence and microphysics. This can be achieved using a series of high resolution large eddy simulations or detailed observations of in-cloud dynamics. This thesis aims to do the latter using high resolution observations.

1.5 Thesis Outline

Updraughts evolving as a sequence of pulses or thermals have been suggested in studies, discussed above and in the following chapters, in observations from aircraft, radar, cameras and in numerical simulations. With higher resolution observations and numerical simulations, at order 100 m grid spacing, thermals, thermal chains and bubble type updraughts are seen. A larger updraught can be broken down into smaller objects, compared to updraughts at grid spacing larger than 1 km. There may be larger vertical velocity regions but these may evolve as a pulse/series of thermals.

Given limited observations of updraught structures at fine scales and development in time in deep precipitating convective clouds. The lack of consensus in the literature using numerical simulations on whether updraught structures develop as a series of successive thermals with each new thermal originating higher or lower than its predecessor, or whether an updraught has a starting plume structure that breaks down to form the thermal chain structure due to dynamic entrainment, this thesis aims to:

1. Observe thermals or updraught pulse structures in observations of precipitating deep convection, specifically focusing on investigating the time and spatial evolution.

2. Estimate thermal characteristics in precipitating deep convective clouds using high resolution radar observations.

3. Expand upon the aircraft observations using in-situ measurements and mounted cloud radar that were limited in space and time and cannot track large spatial regions of cloud from a fixed perspective, for example those of Damiani *et al.* (2006), and discuss the multi-thermal nature in deep clouds with low bases hinted at by Hogan *et al.* (2008).

4. Observe updraught pulses using new 3D radar scans of cloud to determine what such structures look like at fine spatial scales and how they develop in time.

5. Determine interactions between updraught pulses, polarimetric radar signals and turbulence (derived using eddy dissipation rate) using 3D radar scans.

In chapter 2 the scanning strategy used to obtain data is discussed and the radar data used in this thesis is presented. In chapter 3, a conventional method for retrieving vertical velocity using Doppler velocity measurements from ground based radar is investigated and associated caveats are discussed. Chapter 4 presents an alternative method for retrieving vertical velocity from Doppler velocity measurements that is not subject to the caveats with the method discussed in chapter 3. An analysis of this method on ideal test cases is shown and a method and analysis for deriving the uncertainty on vertical velocity estimates is discussed. Chapter 5 details the thermal tracking algorithm, sensitivity to thresholds and presents results of thermal characteristics such as number per cloud cell, lifetime, diameter and vertical displacement. In chapter 6 a new scanning strategy is proposed to improve observations of convective cells and updraughts in clouds. This scanning strategy is applied to a case study of deep convection from which further updraught properties are derived and analysis of the development of updraught pulses is presented. Finally, chapter 7 concludes the work in this thesis, discusses limitations and suggests some improvements for future work into observing dynamical structures in deep convection at fine scales.

Chapter 2

Data

2.1 Doppler radar

Weather radar is a critical component for monitoring the current weather. The most common use of a weather radar is to observe rainfall and Doppler winds. In the UK and much of Europe, rainfall products from the radar network are mostly used operationally. Only recently has Doppler capability become available on the UK radar network. In the US, as well as rainfall products, Doppler wind observations are commonly used which provide useful information for the severe weather experienced throughout the continental US. A product the general public are familiar with are rainfall maps showing location and intensity. Rainfall rate can be calculated from the received reflectivity (Z_H).

Radars emit pulses of electromagnetic radiation in either the horizontal *or* vertical plane (single polarisation) or the horizontal *and* vertical plane (dual polarisation). Waves are emitted at a certain wavelength, upon interacting with a target, meteorological or not, a certain amount of radiation is back-scattered to the receiver on the radar. The received power tells us information on the size and number density of the particles in a sampling volume and their range from the radar.

There are various wavelengths radars can use and different wavelengths can result in different scattering regimes. The most common regime is the Rayleigh scattering regime where the wavelength is much greater than the particle diameter ($\lambda \gg$ D). Operational radar networks are generally C-band operating with a wavelength of 3 cm. Radar variables such as reflectivity are commonly displayed as horizontal scans known as Plan Position Indicators (PPI's). PPI's are scans taken at fixed elevation whilst scanning in azimuth. Vertical scans known as Range-Height Indicator (RHI's), which

scan in elevation at fixed azimuths are mostly used in research.

2.1.1 Reflectivity

For observing rainfall, reflectivity is calculated from the back-scattered power. The radar reflectivity factor per unit volume (Z_H) is given by

$$Z_H = \int_0^\infty |K|^2 N(D) D^6 dD, \tag{2.1}$$

where $|K|^2$ = dielectric factor (approximately 0.93 for water and 0.192 for ice), N(D) = drop size distribution (DSD) and D^6 = the 6th power of the particle diameter. Z_H is expressed in units of mm^6 m^{-3}. Natural rain DSD's are described by a gamma distribution (Ulbrich, 1983)

$$N(D) = N_0 D^\mu \exp\left[-\frac{(3.67+\mu)}{D_0} D\right], \tag{2.2}$$

where D = the equivalent spherical drop diameter, N_0 = the intercept parameter, D_0 = median volume drop diameter and μ = the dispersion parameter, which is a measure of the spectrum shape. The equivalent reflectivity factor (Z_h) has logarithmic units of dBZ and is given by

$$Z_h[dBZ] = 10 log_{10}(Z_H[mm^6 m^{-3}]). \tag{2.3}$$

Thunderstorm cores generally have reflectivity upwards of 40 dBZ for example and Z_H is proportional to D^6 such that larger drops have higher reflectivity, as shown by equation 2.1.

2.1.2 Differential reflectivity

Using dual polarisation, pulses are emitted and received in the vertical and horizontal plane. Using both horizontal and vertical pulses yields additional information about the particle shape. Polarised waves are either emitted alternating or simultaneously.

For the radar data used in this thesis, the pulses are emitted alternating and the radar receives both co-polar and cross-polar returns. Co-polar returns are signals received in the same plane as the emitted signal, horizontal emission and horizontal receive for example and cross-polar are signals received in the orthogonal plane, horizontal emission and vertical receive for example. Differential reflectivity is defined as the ratio of the radar horizontal (H) and vertical (V) reflectivity factors from both polarisation's (in logarithmic units)

$$Z_{DR}[dB] = 10log_{10}\frac{Z_H}{Z_V}. \tag{2.4}$$

Differential reflectivity thus measures the shape and alignment of particles and is independent of number concentration. When H is larger than V, differential reflectivity is positive. This occurs for oblate rain drops, which are larger along their horizontal axis, and ice crystals aligned with their major axis in the horizontal plane. Spherical hydrometeors such as large hail will have differential reflectivity ≈0 dB, as will small spherical liquid droplets. High differential reflectivity values above the freezing level are usually used as an indicator of strong updraughts, known as differential reflectivity columns, as super-cooled large liquid droplets are lofted above the freezing layer resulting in a larger signal in the horizontal plane.

2.1.3 Doppler velocity

Some radars are able to detect the Doppler shift due to the along-beam movement of the reflectors (particles). The phase of the returned signal is compared to the transmitted signal to derive the velocity of particle motion towards or away from the radar parallel to the emitted beam. The phase shift is given by

$$\frac{d\phi}{dt} = \frac{4\pi V_D}{\lambda}, \tag{2.5}$$

where ϕ = phase of the wave, V_D = velocity and λ = wavelength of emitted wave. Equation 2.5 is re-arranged to calculate V_D giving

$$V_D = \frac{\lambda}{4\pi}\frac{d\phi}{dt}. \tag{2.6}$$

V_D represents the velocity of a single particle in a radar volume. There are many particles within a sampled radar volume with various back-scatter cross-sections each having a different velocity. Therefore the mean Doppler velocity $\overline{V_D}$ is estimated from the sampled volume using many pairs of radar pulses.

2.1.4 Spectrum width

When measuring the mean Doppler velocity, the radar spends a certain amount of time on a target volume emitting pulses, known as the dwell time. The dwell time is given by the pulse pairs divided by the pulse repetition frequency (PRF). Within this dwell time there are variations in the Doppler velocity, hence the mean is taken. The variability in the Doppler velocity is known as the variance in the Doppler velocity spectrum, or spectrum width (σ_v) and has units m s^{-1}.

Spectrum width is estimated from the rate of decorrelation of the phase of each pulse during the sampling time. Assuming the Doppler spectrum is Gaussian, the correlation between pulse pairs is (Doviak and Zrnic, 1984)

$$\rho(T_s) = \exp\left[-8(\frac{\sigma_v \pi T_s}{\lambda})^2\right], \tag{2.7}$$

where λ = radar wavelength, $\rho(t)$ is the correlation coefficient and T_s is the spacing between pulses. Equation 2.7 shows pulses decorrelate with $exp(-T_s^2)$. Re-arranging equation 2.7 yields the equation used to estimate σ_v

$$\sigma_v[ms^{-1}] = \frac{\lambda}{2\sqrt{2}\pi T_s}[-ln(\rho)]^{1/2}. \tag{2.8}$$

The turbulent component of σ_v can be isolated and expressed as the eddy dissipation rate (Feist *et al.*, 2019). This method allows turbulence to be retrieved in radar scans of convective clouds where σ_v is measured. This retrieval is not derived in this thesis, but a full derivation with application to convection scanned with the radar used in this

thesis is provided in Feist *et al.* (2019) and further retrievals are presented in Chapter 6.

2.1.5 Chilbolton Advanced Meteorological Radar (CAMRa)

The radar data used in this thesis was from the Chilbolton Advanced Meteorological Radar (CAMRa), a 10 cm S-band (3 GHz) research radar located in Chilbolton, Hampshire, UK shown in Figure 2.1. CAMRa has a large dish size of 25 m making it the worlds largest fully steerable radar. The narrow beamwidth of 0.28° (Goddard *et al.*, 1994) provided by the large radar antenna yields a vertical resolution of ≈250 m and ≈500 m at 50 km and 100 km range respectively. The narrow beamwidth means that CAMRa has a much higher spatial resolution compared to the operational radars in the UK of 1° beamwidth. The native range resolution is 75 m which can be averaged over 4 gates to yield a 300 m resolution. CAMRa has dual-polarisation and Doppler capabilities, which make it ideal for research of internal dynamics of deep convection. At 1 km range with a 300 m range resolution the sensitivity of CAMRa is -36.7 dB and with a 75 m range resolution is -39.7 dB. The reported system noise due to instrumentation is 5.5 dB (Chris Walden, personal communication) and the noise in Doppler measurements due to turbulence is discussed in chapter 4.

The specifications of CAMRa are given in table 2.1 and further details can be found in Goddard *et al.* (1994).

2.2 Data processing

Radial velocity data were provided by the Chilbolton facility where quality control was performed that included Doppler velocity unfolding, calibration and removal of system noise and atmospheric noise. Reflectivity in linear units (mm^6 m^{-3}) and velocity were linearly interpolated (Warren and Protat, 2019) using super sampling anti-aliasing (Macura, 2019) from the native radial-elevation grid to Cartesian x-z grid. Interpolation resulted in a final grid length of 100 m horizontally and 50 m vertically, with 50 m by 25 m intermediate grid lengths. Interpolated reflectivity values were then converted

Figure 2.1: A photo of the CAMRa dish located in Chilbolton, Southern England, UK.

back to log units of dBZ. Doppler winds, spectrum width and differential reflectivity were similarly interpolated to a Cartesian grid using super sampling anti-aliasing.

2.2.1 RHI scanning strategy

The scanning strategy generally used to carry out RHI scans of deep convection are consecutive RHI's throughout certain or multiple regions of clouds, using an alternating up-down-up-down pattern. This strategy targeting reflectivity cores was used for the Dynamical and Microphysical Evolution of Convective Storms (DYMECS) (Stein *et al.*, 2015) and the 28th July 2000 (Gatwick) (Hogan *et al.*, 2008) cases. The strategy takes consecutive RHI scans through the assumed reflectivity core of a cloud by using the

Parameter	Value
Frequency	3.0765 GHz
Wavelength	9.75 cm
Transmit power	600 kW peak pulse
Number of pulses per ray	64 and 128
Half power beamwidth	0.28°
System noise figure	5.5 dB
Maximum unambiguous velocity	14.9 m s^{-1}
Maximum unambiguous range	246 km
PRF	610 Hz
Range resolution	75 m (300 m over 4 gates)
Pulse width	0.5 μ s
Sensitivity at 1 km range	-36.7 dBZ
Maximum azimuthal scan velocity	2° s^{-1}
Maximum elevation scan velocity	1° s^{-1}
Minimum detectable signal	-5 dBZ at 90 km range

Table 2.1: Specification of the CAMRa radar used in this thesis.

maximum reflectivity as a proxy for updraught location. This scanning pattern is depicted in Figure 2.2 showing a scan upwards with increasing elevation (left) and a scan downwards with decreasing elevation (right) through the reflectivity core marked by a red 'x' separated by time $T + \tau$. Using such a scanning strategy yields pairs of scans as shown in Figure 2.3. Vertical velocity can be retrieved for each upwards (red arrows) and downwards (blue arrows) scan pairs separated by time T. The strategy either assumes a cloud is stationary during a sequence of RHI scans, or it estimates a motion vector to advect clouds and estimate location which is used to change the azimuth between consecutive RHI's.

During DYMECS, RHI scans were taken in an automated sequence using storm tracking and an automated scanning scheduler. The tracking algorithm ingests the Met Office operational radar network composite every 5 minutes to track storms. Storm tracking is based on rain rate and storm area that are used to threshold rainfall features in the rainfall field. The tracking software calculates and stores information about the detected storms such as storm size, velocity vectors, rain rate, location (azimuth and range) and age. It updates the scanning location by advecting the core location using calculated motion vectors from pairs of composite radar images (Stein *et al.*, 2015). This information is then fed to the scanning scheduler provided on the Chilbolton

facility computer system. The scan scheduler uses the rainfall rate and storm area to prioritise storms for scanning and issues scan sequence commands to CAMRa for automatic radar scanning based on the required scanning strategy. During DYMECS sets of RHI scans and PPI scans were taken as the scheduler cycled through the top 3 priority storms. As discussed in chapter 5, this type of strategy is not optimal for observing long time series of a selected storms and especially for tracking thermals in time and space in evolving convective clouds.

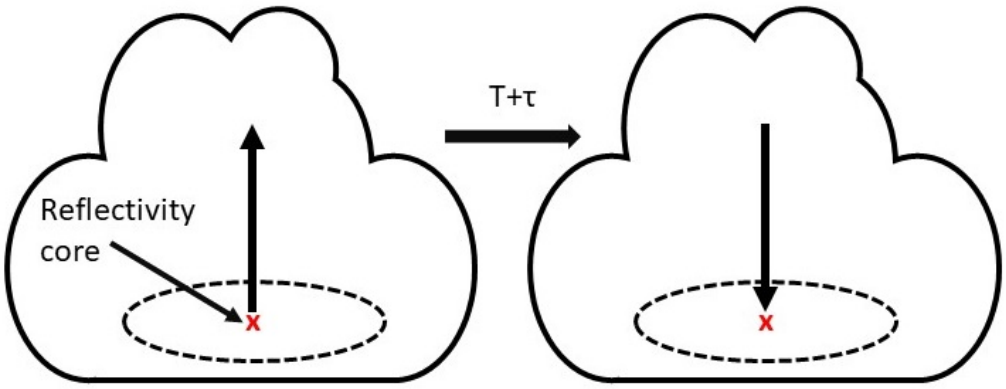

Figure 2.2: Diagram showing the continuous RHI scan strategy. An updraught (dashed) moves with its core 'x' whilst consecutive upwards and downwards RHI scans (vertical arrows) are taken separated by time $T + \tau$.

2.3 DYMECS case study: 25th August 2012

The Dynamical and Microphysical Evolution of Convective Storms (DYMECS) (Stein *et al.*, 2015) provided RHI scans with high resolution in the vertical using a 0.4° s^{-1} elevation scanning rate. Using 64 pulses per ray (32 pulse pairs) yielded a resolution of ≈34 m at 50 km range and ≈70 m at 100 km range. A velocity estimate every 0.04° was obtained which is given by $\frac{64}{PRF(610Hz)} \approx 0.11$ s x 0.4° $s^{-1} = 0.04°$. This data was collected using CAMRa in 2011 and 2012 over 40 days where multiple convective clouds were scanned in southern England, UK. In DYMECS the continuous RHI scan strategy was used to scan reflectivity maxima using the tracking detailed in section 2.2.1 and Figure 2.2. Most data from this campaign scanned storms for around 2

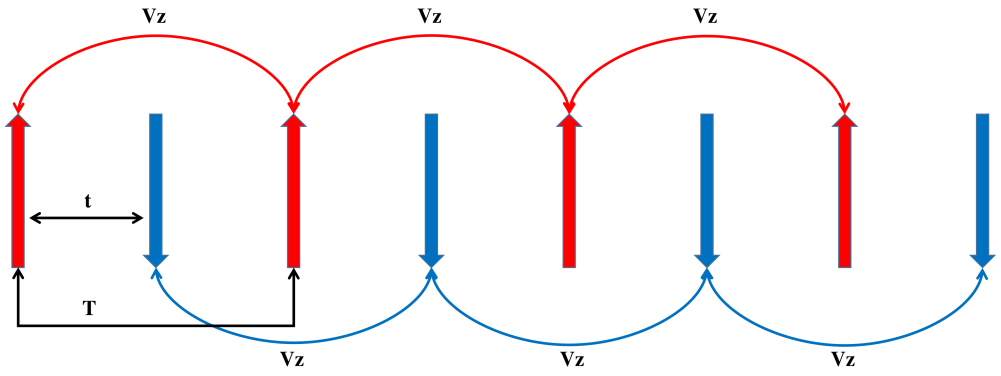

Figure 2.3: Arrows indicating sequences of scans for consecutive RHI scans. Upwards scans indicated by red arrows and downwards scans indicated by blue arrows. Vertical velocity (V_z) is derived from pairs of upwards scans (red) and downwards scans (blue). Consecutive scans are separated by time t and each pair of upward or downward scans are separated by time T. Both T and t are determined by the duration of each scan which is dependant upon the elevation scanning velocity and the time required to change azimuth when the reflectivity core location is updated.

minutes obtaining 4 RHI's. Data from DYMECS was averaged to 300 m in range which reduces noise in the measurements, although the native range resolution of the radar is 75 m.

The objective of DYMECS was to collect a large dataset of convective clouds to statistically investigate the morphology and evolution of clouds. The radar observations were used in conjunction with high resolution Met Office Unified Model simulations at various resolutions. However, given that all other cases consisted of scans of cloud lasting only around 2 minutes and hence comprising of 4 RHI's, only one cloud case from the DYMECS campaign was suitable for the purpose of tracking thermals. The case used in this thesis from the DYMECS campaign is from the 25th August 2012 where a deep cloud was scanned for around 15 minutes at the same azimuth angle. This case provided enough scans to track thermals in the Doppler velocity data and estimate thermal characteristics presented in Chapter 5.

The Met Office synoptic chart for 1200 UTC on 25th August 2012 is shown in Figure 2.4. A low pressure system was situated over England with a trough located behind an occluded front which moved eastward across the UK.

The 00Z 25th August 2012 atmospheric sounding from Herstmonceux, UK (125

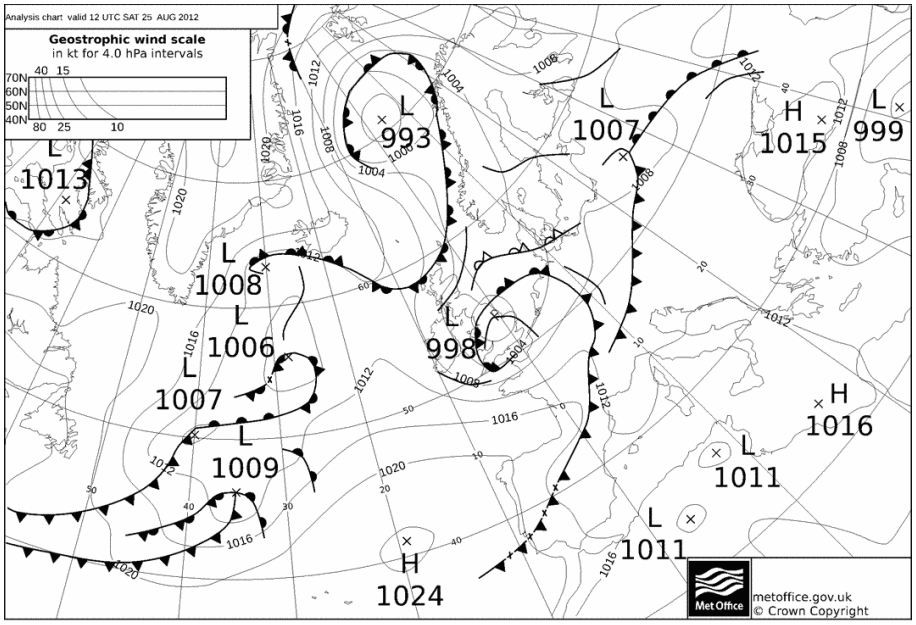

Figure 2.4: Met Office synoptic chart for 12 UTC on 25th August 2012 showing a low pressure system located over central and southern UK.

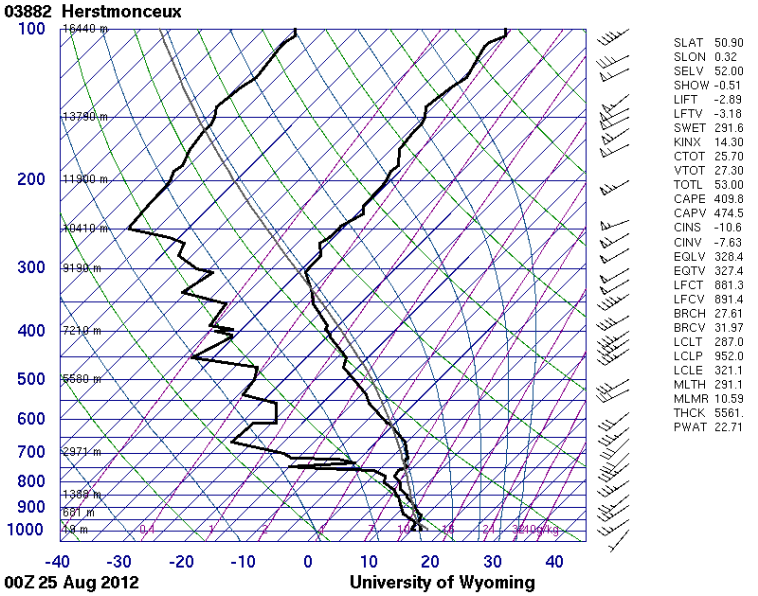

Figure 2.5: 00Z 25 August 2012 atmospheric sounding at Herstmonceux, UK. Provided by University of Wyoming. Temperature and dew point shown in solid black and projected parcel ascent shown in grey. Wind flags are shown on the right using 5 knot intervals.

km south-west of Chilbolton) is shown in Figure 2.5. The temperature profile shows that the tropopause was at about 300 hPa and the wind profile shows that there were strong upper level winds associated with the jet stream flowing north eastwards.

There was slight wind veering in the low levels indicating some weak directional wind shear. At 00Z the convective available potential energy (CAPE) was 409 J kg^{-1} K^{-1} which most likely increased accounting for the adjustment of the temperature and dew point profiles to represent the day time values, providing suitable CAPE required for convective development.

Convection formed over southern England with scattered storms becoming more organised into the afternoon. An example of the composite rainfall image from the operational radar network used to track storms is shown in Figure 2.6 at around the time the RHI scans were taken with the cloud system of interest highlighted by the white square box. Clouds reached up to 10 km depth with reflectivity exceeding 50 dBZ.

2.4 Gatwick case study: 28th July 2000

Deep convection over Gatwick, UK was scanned multiple times throughout the day on 28th July 2000 with the longest period of consecutive RHI scans of up to 30 minutes. The consecutive RHI scan strategy was also used in this case, with only a few individual PPI scans interspersed in sets of RHI scans. Scans maintained almost the same azimuth angle, generally within 1° azimuth of each other because the storm did not deviate much from the line-of-sight. Measurements were obtained with a 0.5° s^{-1} elevation scanning rate. With 64 pulses per ray, a vertical resolution of ≈44 m at 50 km range and ≈87 m at 100 km range was obtained.

The Met Office synoptic chart for 0000 UTC on 28th July 2000 is shown in Figure 2.7. Two low pressure centres were situated around the UK, one in the Atlantic and one off the east coast of Scotland, UK in the North Sea. High pressure was to the south of the UK. A trough extended north to south over Ireland and moved east. Convection formed in the afternoon with cloud top heights reaching up to 10 km and radar reflectivities exceeding 50 dBZ. Unfortunately the composite rainfall images from the operational radar network are not available for this case. The 12Z 28th July 2000 Herstmonceux, UK atmospheric sounding is shown in Figure 2.8. The sounding showed

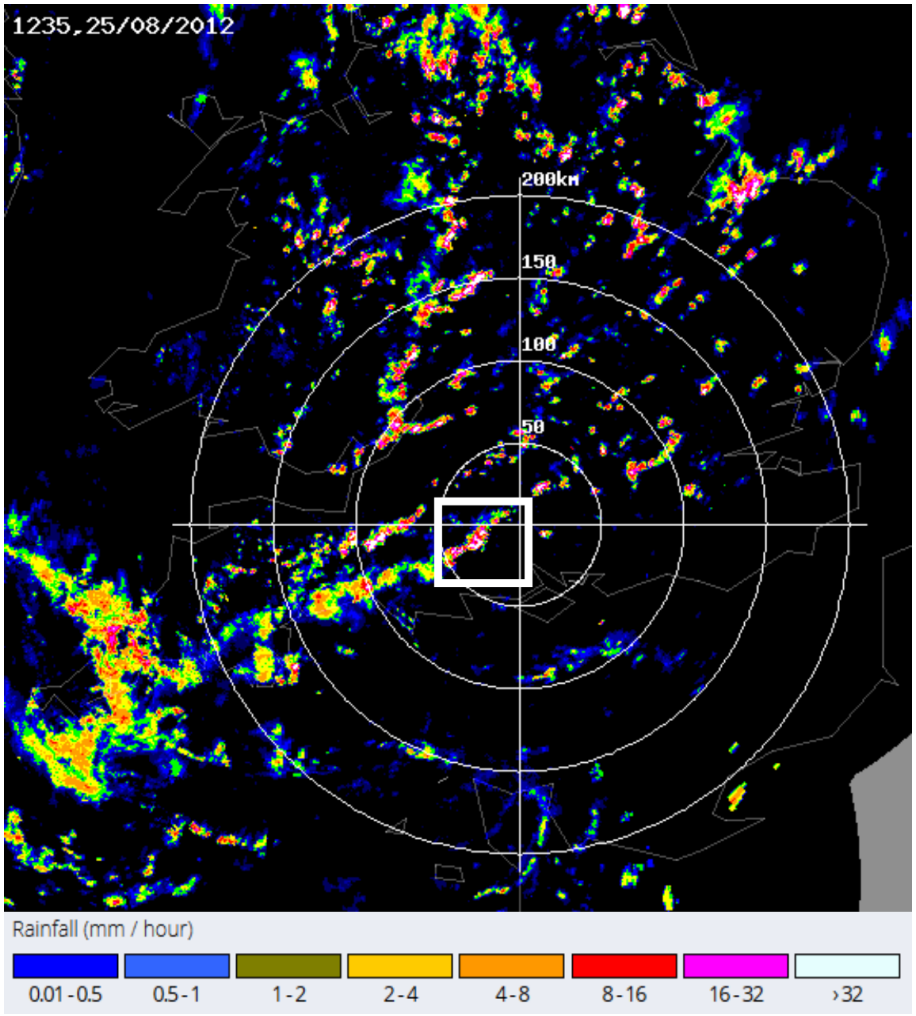

Figure 2.6: Composite rainfall radar from the operational radar network for 1235 UTC on 25th August 2012. Centred on Chilbolton with 50 km range circles. Cloud system scanned during DYMECS highlighted by white square box.

that there was a moderate amount of convective available potential energy present, estimated to be around 875 J kg^{-1} K^{-1}. The environmental temperature shown by the solid black line indicates the tropopause was near 250 hPa. Upper level and mid-level winds were weak, as shown by the wind flags, with little vertical wind shear. The synoptic environment and sounding supported convection that organised into a line, which was scanned with the CAMRa radar and are the radar scans used in this thesis.

Table 2.2 shows the scan dates and times, number of cells where a convective cell was defined as a region enclosed by the 30 dBZ contour and the total number of thermals identified in all cells for the DYMECS and Gatwick cases.

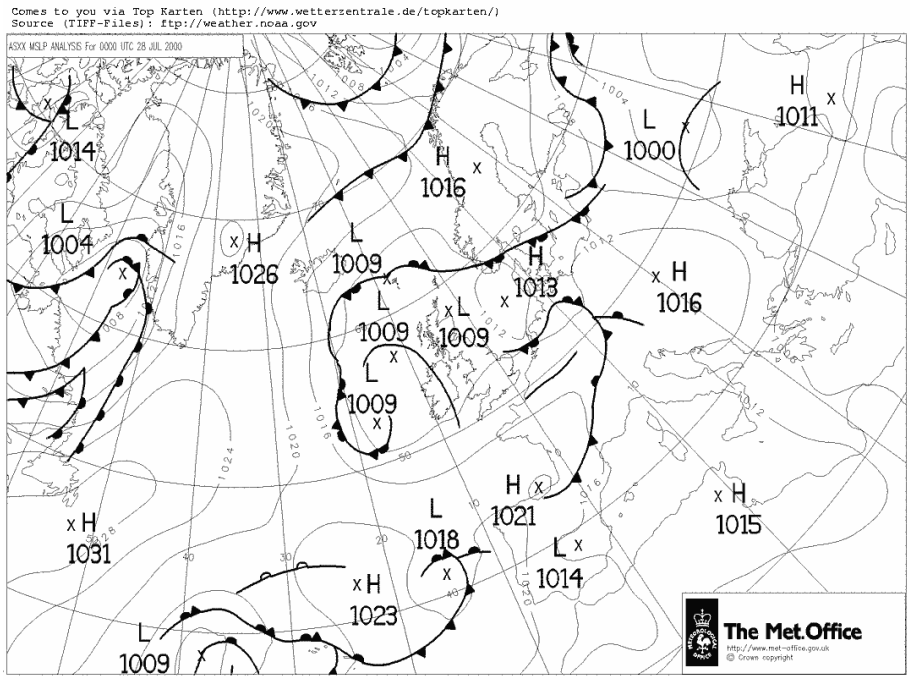

Figure 2.7: Met Office synoptic chart for 00 UTC on 28th July 2000. Provided by Met Office and wetterzentrale.de.

2.5 24th September 2019 case study

Data was collected using a new scanning strategy, to be described in chapter 6. The 24th September was characterised by a complex low pressure system sitting to the west of the UK in the Atlantic as shown in Figure 2.9. Associated with this low pressure system were multiple fronts. An upper warm front had passed over the UK the day before, an occluded front was passing over the southern UK during the early hours of the 24th September 2019 and this was followed by a cold front that was occluding. With this system tropical maritime and polar maritime air would be drawn into the south of the UK, situated in the left exit region of the jet stream. Multiple surface troughs were located behind the cold front and combined with an upper level trough at 500 hPa this synoptic setup provided suitable synoptic forcing for ascent.

Upper level forcing was further seen in the atmospheric sounding taken at 12Z on 24th September 2019 from Camborne, UK in Figure 2.10. Camborne is approximately 360 km south-west of the location of the scanned storms. A strong upper level jet

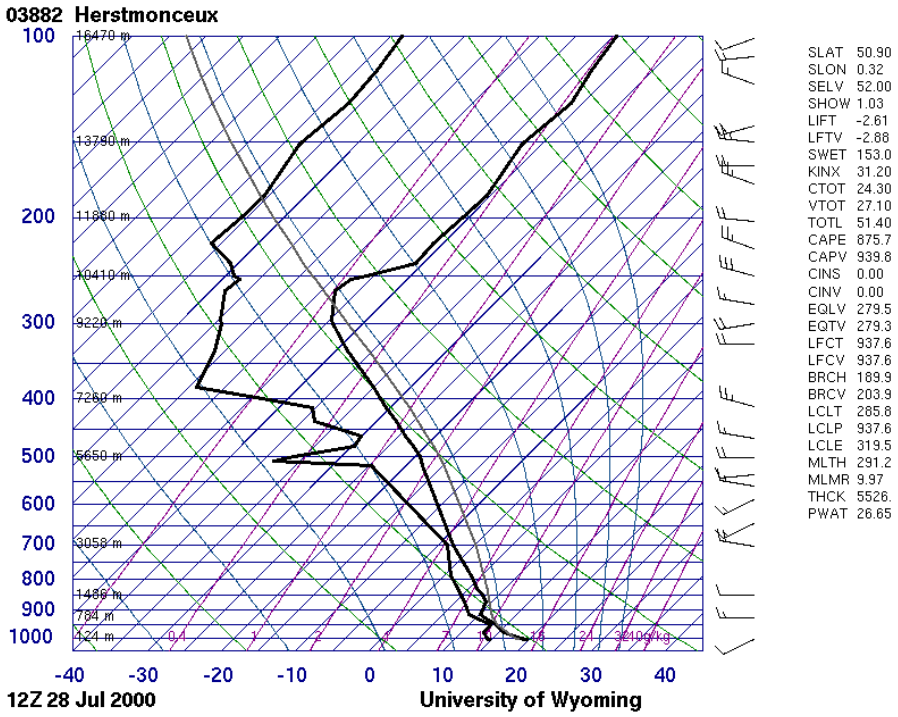

Figure 2.8: Atmospheric sounding for 12Z on 28th July 2000 from Herstmonceux, UK. Provided by University of Wyoming. Temperature and dew point shown in solid black and projected parcel ascent shown in grey. Wind flags are shown on the right using 5 knot intervals.

was present over the southern UK heading due east. The southern UK would be situated in the left exit region of the upper level jet and an upper level trough at 500 hPa travelled over southern UK. The wind profile from the sounding indicated weak vertical wind shear from near the surface to around 3 km height shown by the wind flags veering. The combination of upper and mid-level divergence and surface level convergence provided by the synoptic scale setup produced a favourable environment for convection. If wind shear increased during the afternoon this would also support organised convective development. The tropopause was located around 300-250 hPa indicated by the increase in temperature. The temperature and dew point profiles on the sounding in Figure 2.10 may not be representative of the values later in the afternoon at the location of the radar scans. The surface temperature and dew points were modified to those reported by a surface observation from a Met Office station in London, UK. The reported surface temperature was 20°C and dew point was 14°C. This allowed an estimated parcel ascent for a 50 hPa deep mixed layer to be calculated.

Table 2.2: Case date, time of first and last scan, number of cells and total number of thermals identified in all cells.

Case Date	Scan Period	N Cells	Total Thermals
28 July 2000	15:02-15:06	1	1
28 July 2000	15:09-15:15	1	1
28 July 2000	15:19-15:31	1	1
28 July 2000	15:47-16:00	1	5
28 July 2000	16:05-16:17	3	11
28 July 2000	16:23-16:51	4	21
25 August 2012	12:31-12:48	3	10

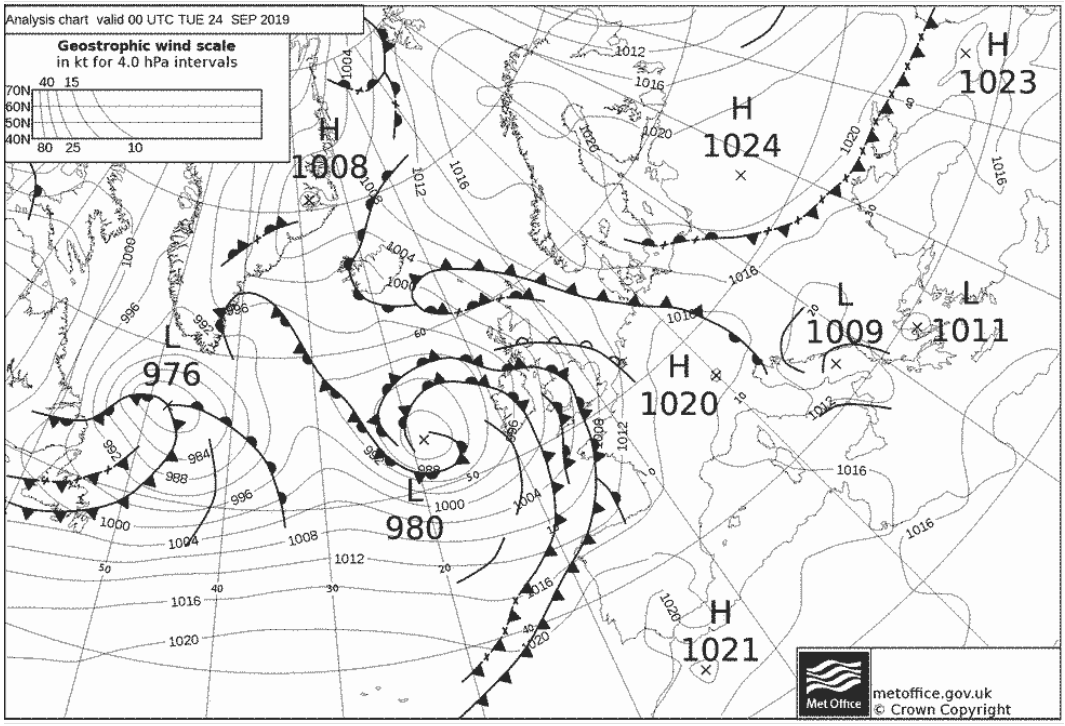

Figure 2.9: Mean sea level pressure chart for 24th September 2019. Provided by the Met Office.

The calculated lifting condensation level (LCL) and level of free convection (LFC) was 740 m, CAPE was 914 J K Kg $^{-1}$, equilibrium level (EL) was 8.8 km and the maximum parcel level (MPL), which is the level a parcel can reach before exhausting all of its upward momentum after it becomes neutrally buoyant at the EL, was 11 km.

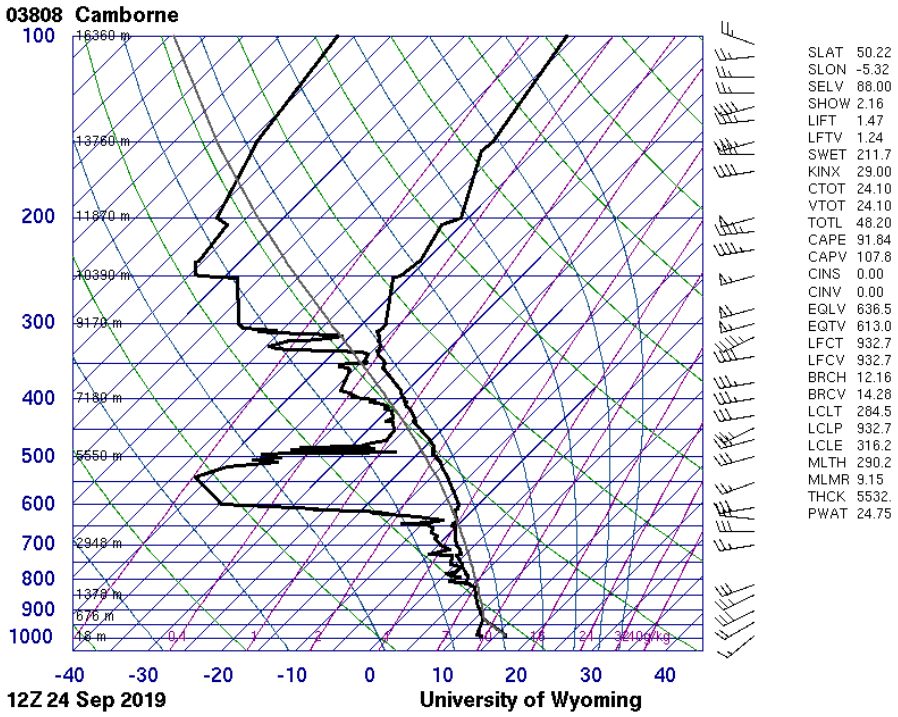

Figure 2.10: Atmospheric sounding for Camborne, UK at 12Z 24th September 2019. Provided by University of Wyoming. Temperature and dew point shown in solid black and projected parcel ascent shown in grey. Wind flags are shown on the right using 5 knot intervals.

Figure 2.11 shows the radar composite from the Met Office operational radar network at 15:00 UTC on 24th September 2019. This is around the time that scanning of the clouds for this case started. Larger scale precipitation can be seen to the north and south-west with some embedded convection. A line of intense rainfall with convective cells was located due north of Chilbolton over 100 km away. The clouds scanned for this case were associated with the line of convection due east between 50 and 100 km range circles towards London, UK, shown by the white square box.

2.6 Estimation of system motion

It was useful to estimate the velocity of the clouds in order to remove the overall bias in horizontal displacement of air parcels between scans and focus on the cloud-relative motion. Since interest focused on thermal identification within a single cell, analysis was performed in a system-relative framework. Horizontal displacement of

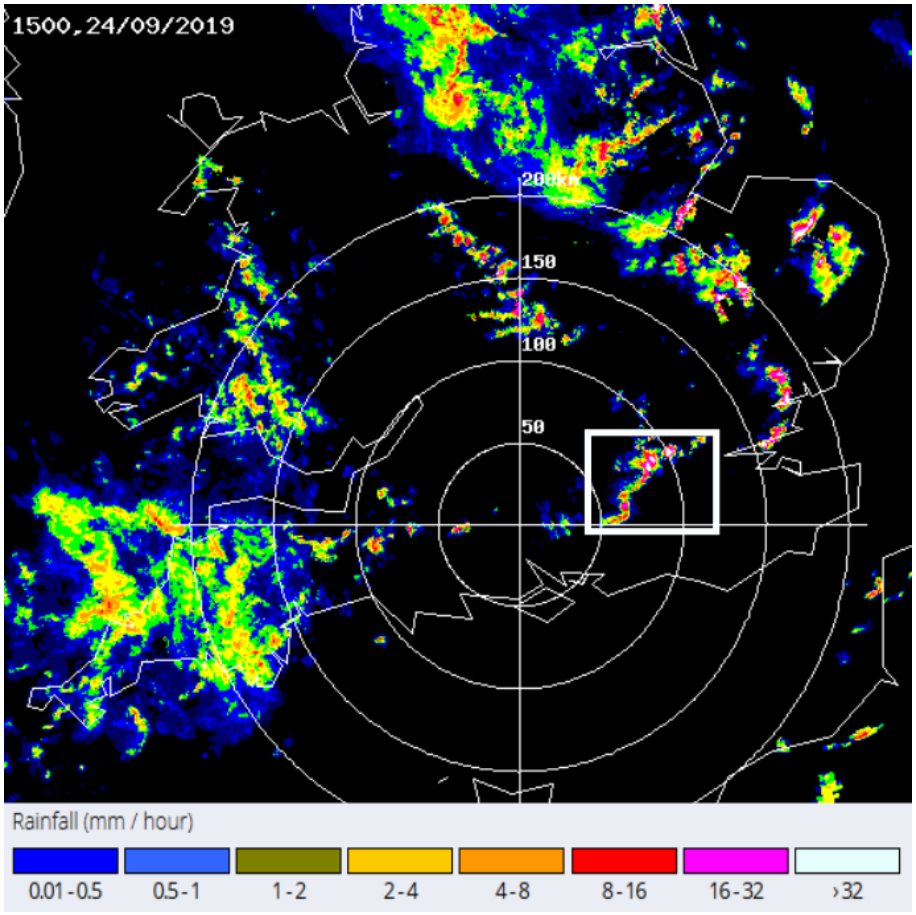

Figure 2.11: UK composite radar image at 15:00 UTC on 24th September 2019. Centred on Chilbolton Observatory with 50 km range circles. Cloud system of interest highlighted by white square box.

a cell between scans was removed using the mean Doppler wind of the cloud. As clouds were tracked in the DYMECS and Gatwick cases an alternating up-down-up-down scanning pattern was used, as discussed above. The finite time between rays in scans introduced a systematic relative positional error, exacerbated by the alternate up-down-up-down scanning strategy. The positional error due to the time between rays was removed using the time difference between each individual ray to a reference time, the first ray in the first scan, multiplied by the mean Doppler wind. Only the mean advection was considered in this displacement. System-relative motions are more detectable in animations by the human observer, providing a useful subjective check on the technique. This horizontal correction technique was facilitated by transforming the data to a Cartesian grid.

Although radar scans from 24th September 019 did not suffer from the positional error due to the up-down-up-down scanning pattern, they were also corrected using the processes described above to produce a Lagrangian framework.

2.7 Summary

This chapter has introduced the CAMRa radar that collected data in previous campaigns and new data which are both used thesis. The specification and parameters used when scanning with CAMRa to collect data were detailed. Reflectivity, Doppler velocity, differential reflectivity and spectrum width which are the radar measurements used in this thesis were discussed along with details of how they are used. The DYMECS and Gatwick cases were detailed from which data are later used in this thesis. New data that were acquired for this thesis from the 24th September 2019 was discussed and the large scale synoptic, vertical atmospheric profiles and network radar data were discussed for each case to give background information of the atmospheric environments of the clouds that were scanned. Displacement of radar data using a Galilean transformation that facilitated further data processing, vertical velocity retrieval and thermal tracking was discussed.

Chapter 3

Updraught retrievals

3.1 Introduction

Vertical velocity can be retrieved from observations of Doppler velocity using single or multiple Doppler radars. Some examples using variational methods (Gao *et al.*, 2006; North *et al.*, 2017; Kumar *et al.*, 2016), which require three independent sets of data to provide three degrees of freedom for a full wind field retrieval were discussed in chapter 1. Along with Doppler velocity measurements providing a component of velocity, the continuity equation can provide a second constraint and a third constraint can be provided by further assumptions or another independent source of data, for example another radar from a different viewing angle, atmospheric soundings or wind profilers. Using a single Doppler radar providing only one measurement of Doppler velocity along the beam, vertical velocity can be retrieved using integration methods (Ray *et al.*, 1980; Protat and Zawadzki, 1999; Nicol *et al.*, 2015).

This chapter discusses the Nicol *et al.* (2015) single Doppler radar retrieval method for vertical velocities, its assumptions and limitations and whether it is applicable to track thermals as transient vertical velocity signals retrieved using this method in a small sample of clouds.

3.2 Single Doppler radar vertical velocity retrievals

Vertical velocity can be estimated from single Doppler velocity observations by integrating the mass continuity equation (Ray *et al.*, 1980; Protat and Zawadzki, 1999; Nicol *et al.*, 2015). In this section the ground-up and top-down integration calculations are derived, which are then used in a weighted estimate of vertical velocity

at each observation grid point following the Nicol *et al.* (2015) method. To use this method, upper and/or lower boundary conditions must be applied. The upper vertical velocity boundary condition can be assumed or measured with other instrumentation. The upper vertical velocity boundary condition is assumed to be 0 m s^{-1} here, and the lower boundary condition at the ground is 0 m s^{-1}, these boundary conditions are commonly applied (Protat and Zawadzki, 1999; Nicol *et al.*, 2015). Furthermore, a vertical profile of density must also be assumed, to do this the barometric equation is used with starting values of standard temperature and pressure to create a vertical density profile.

Matejka and Bartels (1998) did a comprehensive study of eight methods for calculating vertical velocity in a column investigating boundary conditions, input data and associated errors. The eight methods tested were:

1. Deduction using hydrometeor fall speed and vertical air velocity by estimating vertical velocity as the sum of the hydrometeor fall speed and vertical air velocity.

2. Upward integration from a lower vertical velocity boundary condition by integrating the anelastic continuity equation upwards from a given (usually 0 m s^{-1}) vertical velocity boundary condition.

3. Downward integration from an upper vertical velocity boundary condition by integrating the anelastic continuity equation downwards from a given (usually 0 m s^{-1}) vertical velocity boundary condition.

4. Downward integration from an upper hydrometeor boundary condition by integrating the anelastic continuity equation downwards but the boundary condition at the top of the column is given by hydrometeor information as in method 1.

5. Variational solution between lower and upper vertical velocity boundary conditions by using a variational adjustment to remove divergence bias error when using the integration methods.

6. Variational solution between a lower vertical velocity boundary condition and an upper hydrometeor boundary condition by using a variational adjustment as

above but the boundary condition at the top of the column is given by hydrometeor information as in method 1.

7. Complete variational column solution with no constraints, similar to Ray *et al.* (1980) method by applying method 1 and the anelastic continuity equation concurrently throughout the column.

8. Complete variation column solution with lower vertical velocity boundary condition is the same as method 7 but applying a lower vertical velocity boundary condition.

Each test showed how the methods responded to data error, systematic bias and random errors. By deriving analytical expressions for the errors of each method or using a Monte Carlo approach, idealised errors were calculated in a column allowing the root mean square error of the vertical velocity at each point in a column to be compared across methods. Errors are investigated using error space diagrams where the x-axis is given by the variance of method 1 divided by the variance of divergence and the y-axis is given by the variance of the vertical velocity boundary condition divided by the variance of divergence (Matejka and Bartels, 1998). The variance of method 1 and the boundary conditions varied from 0.1 to 10 m s $^{-1}$ and the variance of divergence varied from 10^{-3} to 10^{-5} s^{-1}.

Across the error space diagrams, methods (3), (5), (7), (8) and (4) (when the error non-randomness is high) performed best out of the 8 methods. These methods were determined to be the best because the variance of the vertical velocity in the column was less than 1.25 m s $^{-1}$ for each method. Methods (1) and (6) performed slightly poorer and method (2) performed the worst. Methods that performed poorly had larger variance of the vertical velocity in the column, hence vertical velocity profiles were less consistent throughout the column.

3.2.1 Ground-up integration

Starting with the anelastic mass continuity equation and assuming that the cross-beam divergence ($\frac{\partial V_y}{\partial y}$) is negligible

$$\frac{\partial \rho V_x}{\partial x} + \frac{\partial \rho V_z}{\partial z} = 0. \tag{3.1}$$

Horizontal gradients in density (ρ) are zero, thus giving

$$\frac{\partial V_x}{\partial x} + \frac{\partial V_z}{\partial z} + \frac{V_z}{\rho}\frac{\partial \rho}{\partial z} = 0. \tag{3.2}$$

Defining the horizontal velocity V_x to be at level i and the vertical velocity V_z to be at half levels $i + \frac{1}{2}$ and $i - \frac{1}{2}$. Equation 3.2 becomes

$$\rho_i \frac{\partial V_{x,i}}{\partial x} + \frac{\rho_{i+\frac{1}{2}} V_{z,i+\frac{1}{2}} - \rho_{i-\frac{1}{2}} V_{z,i-\frac{1}{2}}}{z_{i+\frac{1}{2}} - z_{i-\frac{1}{2}}} = 0. \tag{3.3}$$

Letting $z_{i+\frac{1}{2}} - z_{i-\frac{1}{2}} = \delta z_i$ and $\rho_i = \frac{\rho_{i+\frac{1}{2}} + \rho_{i-\frac{1}{2}}}{2}$ and re-arranging to isolate $V_{z,i+\frac{1}{2}}$ yields

$$V_{z,i+\frac{1}{2}} = \frac{\rho_{i-\frac{1}{2}}}{\rho_{i+\frac{1}{2}}} V_{z,i-\frac{1}{2}} - \frac{\rho_{i+\frac{1}{2}} + \rho_{i-\frac{1}{2}}}{2\rho_{i+\frac{1}{2}}} \delta z_i \frac{\partial V_{x,i}}{\partial x}. \tag{3.4}$$

3.2.2 Top-down integration

Similarly, integration can be calculated downwards by defining V_x to be at level $N - i$ where N is the number of vertical levels and V_z to be at levels $N - i + \frac{1}{2}$ and $N - i - \frac{1}{2}$

$$\rho_{N-i} \frac{\partial V_{x,N-i}}{\partial x} + \frac{\rho_{N-i+\frac{1}{2}} V_{z,N-i+\frac{1}{2}} - \rho_{N-i-\frac{1}{2}} V_{z,N-i-\frac{1}{2}}}{z_{N-i+\frac{1}{2}} - z_{N-i-\frac{1}{2}}} = 0. \tag{3.5}$$

Letting $z_{N-i+\frac{1}{2}} - z_{N-i-\frac{1}{2}} = \delta z_{N-i}$ and $\rho_{N-i} = \frac{\rho_{N-i+\frac{1}{2}} + \rho_{N-i-\frac{1}{2}}}{2}$ and re-arranging to isolate $V_{z,N-i-\frac{1}{2}}$ yields

$$V_{z,N-i-\frac{1}{2}} = \frac{\rho_{N-i+\frac{1}{2}}}{\rho_{N-i-\frac{1}{2}}} V_{z,N-i+\frac{1}{2}} + \frac{\rho_{N-i+\frac{1}{2}} + \rho_{N-i-\frac{1}{2}}}{2\rho_{N-i-\frac{1}{2}}} \delta z_{N-i} \frac{\partial V_{x,N-i}}{\partial x}. \tag{3.6}$$

3.2.3 Weighted vertical velocity

Errors in the horizontal divergence can be amplified when integrating upwards due to the decrease in air density with height and that integration begins when density is largest at the bottom (Ray *et al.*, 1980), but integrating downwards dampens errors. By integrating only one way it is hard to match both boundary conditions. Final vertical velocity can be estimated by taking the error weighted average of the ground-up and top-down retrievals. A linear weighting was proposed by Protat and Zawadzki (1999) based on the distance from the upper and lower boundaries but an error-weighting was found to further improve retrievals (Nicol *et al.*, 2015). The error weighted approach, weights each integration based on its expected errors due to the propagation of errors with height throughout the column being integrated. Nicol *et al.* (2015) found that this method yielded expected vertical velocity errors ≈25% less than the linear average approach.

The estimated error at each height is given by

$$\sigma_i = \sqrt{(\frac{\sigma_{i-1}\rho_{i-1}}{\rho_i})^2 + \sigma_0^2}, \tag{3.7}$$

where σ_i is the error and an initial error (σ_0) of 0.1 was specified (Nicol *et al.*, 2015). Equation 3.7 is iterated upwards and downwards for each vertical grid point i. Weighting coefficients (ω) are applied to the ground-up and top-down retrievals where ω_{up} and ω_{down} are given by

$$\omega_{up} = \frac{\sigma_{down}^2}{\sigma_{down}^2 + \sigma_{up}^2}, \tag{3.8}$$

$$\omega_{down} = \frac{\sigma_{up}^2}{\sigma_{down}^2 + \sigma_{up}^2}, \tag{3.9}$$

where σ_{up}^2 and σ_{down}^2 are the errors for the upwards and downwards integration's respectively. Finally, retrieved vertical velocity at a point i is given by

$$V_{z,i} = \omega_{up,i} V_{z,up,i} + \omega_{down,i} V_{z,down,i}. \tag{3.10}$$

3.3 Limitations of retrieval method

Updraught strength and width will have uncertainty associated with it due to 1) the missing velocity component in the mass continuity equation (Nicol *et al.*, 2015) and 2) the assumption that radar scans were carried out through the updraught core. To study the impact of scan displacement from updraught core, a cylindrically symmetric idealised updraught field with a maximum updraught velocity of 2 m s^{-1} was used. Radial winds were derived from an idealised flow assuming a radar beam of constant width parallel to the x-axis at each 500 m in the y and z directions. The Nicol *et al.* (2015) updraught retrieval, as detailed above, was applied to these synthetic radial winds.

Starting with a horizontal u and v wind field given by equations 3.11 and 3.12 (shown by arrows in Figure 3.1)

$$u = -re^{(-r^2/r_w^2)}cos(\theta), \tag{3.11}$$

$$v = -re^{(-r^2/r_w^2)}sin(\theta), \tag{3.12}$$

where r is the range from the radar to the centre of the synthetic updraught, r_w is the updraught width and θ is the azimuth angle between the positive x-axis and Doppler velocity.

The Doppler velocity is given by

$$V_D = ucos(\theta) + vsin(\theta)., \tag{3.13}$$

and is shown in Figure 3.1 by filled contours overlaid on the u and v field. The radar is assumed to be in the centre of the domain ($0r_w$, $0r_w$) and $r_w = 4$ grid points.

From a Cartesian co-ordinate system the range can be calculated as follows: $r = \sqrt{x^2 + y^2}$, where x and y are the 2D Cartesian co-ordinates. θ can be calculated by $\theta = arctan(\frac{y}{x})$. The cosine and sine of θ can also be represented in terms of x and y

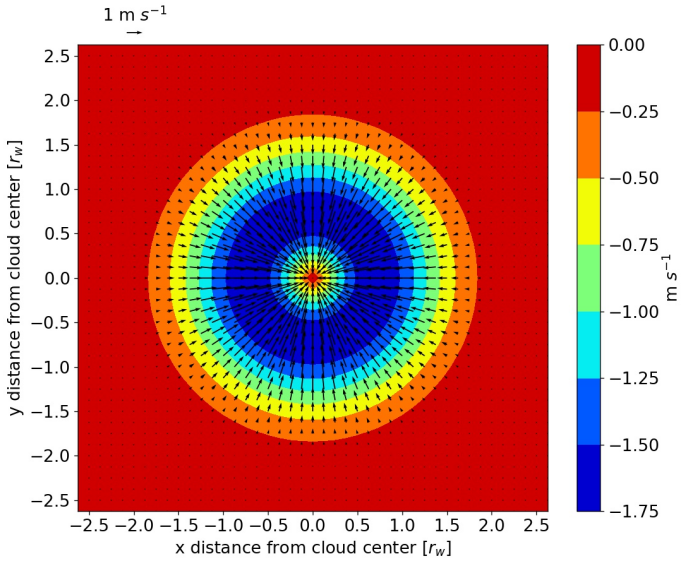

Figure 3.1: Cylindrically symmetric updraught with converging wind field to representing an idealised synthetic updraught. Quivers represent u and v vectors and filled contours are Doppler velocity assuming radar was in centre of domain. Distance is given in terms of cloud width r_w.

given by; $cos(\theta) = \frac{x}{r} = \frac{x}{\sqrt{x^2+y^2}}$ and $sin(\theta) = \frac{y}{r} = \frac{y}{\sqrt{x^2+y^2}}$ respectively.

From the u and v wind field, vertical velocity (w) must be calculated that is consistent with mass continuity given by

$$\frac{\partial u}{\partial x} + \frac{\partial v}{\partial y} + \frac{\partial w}{\partial z} = 0, \tag{3.14}$$

where this version of the mass conservation equation is for incompressible flow (i.e. it assumed that the density is constant). Expressing u in terms of x and v in terms of y, then differentiating equations 3.11 and 3.12 gives the horizontal components of divergence in equation 3.14 (shown in Figure 3.3) which results in

$$\frac{\partial w}{\partial z} = -2e^{-(x^2+y^2)/r_w^2}\left(\frac{x^2}{r_w^2} + \frac{y^2}{r_w^2} - 1\right). \tag{3.15}$$

The calculated divergence in the x and y direction is shown in Figure 3.2. This is estimated by taking the difference along the x or y axis and dividing by the difference in x or y co-ordinates for u and v respectively.

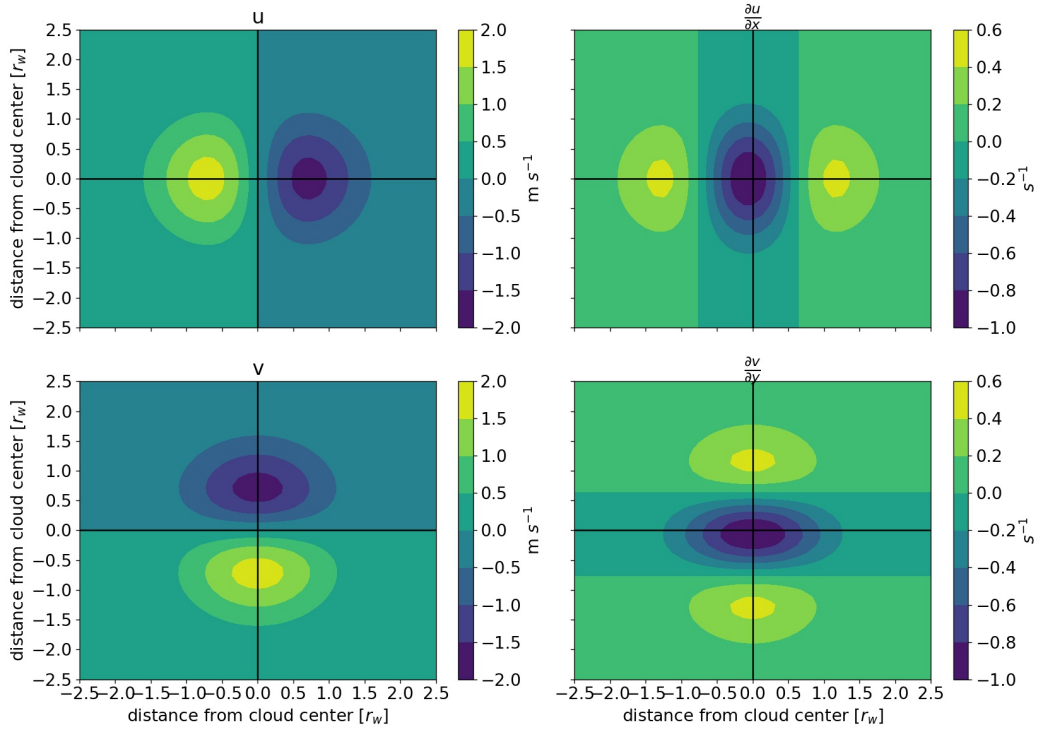

Figure 3.2: u (top left), v (bottom left) both in m s^{-1} filled contours, $\frac{\partial u}{\partial x}$ divergence (top right) and $\frac{\partial v}{\partial y}$ divergence (bottom right) both in s^{-1} filled contours. Solid black lines mark centre of domain.

The analytical (real) vertical velocity profile was calculated by taking the value of $\frac{\partial w}{\partial z}$ at a point and multiplying it by a function defining the vertical profile. In this case such a function was given by equation 3.16 and shown in Figure 3.4. This function was bound to 0 at cloud edges and was 1 at the cloud centre.

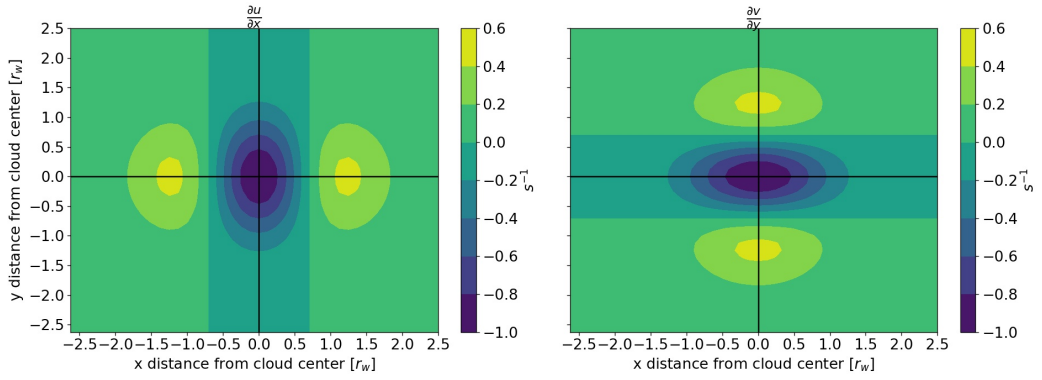

Figure 3.3: $\frac{\partial u}{\partial x}$ (left) and $\frac{\partial v}{\partial y}$ (right) analytical divergences in s^{-1} filled contours.

$$f(z) = \frac{4z}{z_{max}}(1 - \frac{z}{z_{max}}). \tag{3.16}$$

The final true vertical velocity profile is given by equation 3.17

$$w = f(z)(-2e^{-(x^2+y^2)/r_w^2}(\frac{x^2}{r_w^2} + \frac{y^2}{r_w^2} - 1)). \tag{3.17}$$

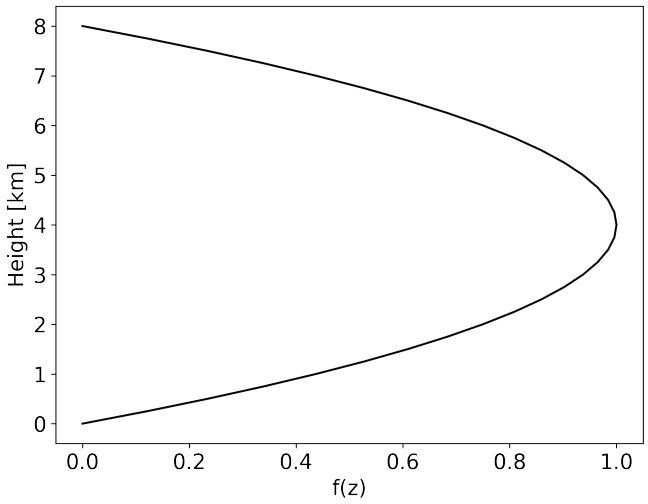

Figure 3.4: Function applied to 2D $\frac{\partial w}{\partial z}$ field to produce a w profile through cloud.

The pattern in Figure 3.3 required further scaling to obtain vertical velocities that increase in magnitude with height until the cloud centre and then decrease in magnitude until the cloud top, convergence must be present in the bottom half of the cloud and divergence in the top half. Therefore divergence profiles are obtained by defining a function that was dependent on height shown in Figure 3.5 and multiplying the divergence by this function. Divergence was integrated using the vertical velocity retrieval algorithm described above, ignoring air density by setting the vertical density profile to 1, dz = 0.25 km for a cloud depth z_{max} of 8 km. A weighted vertical velocity profile was obtained that was quadratic with zero boundary conditions. Vertical profiles were normalised by (z_{max}) so they were bound between -1 and 1. Retrieved vertical velocity using only the $\frac{\partial u}{\partial x}$ component of divergence (as done in Nicol *et al.* (2015)) and the real vertical velocity are shown in Figure 3.6.

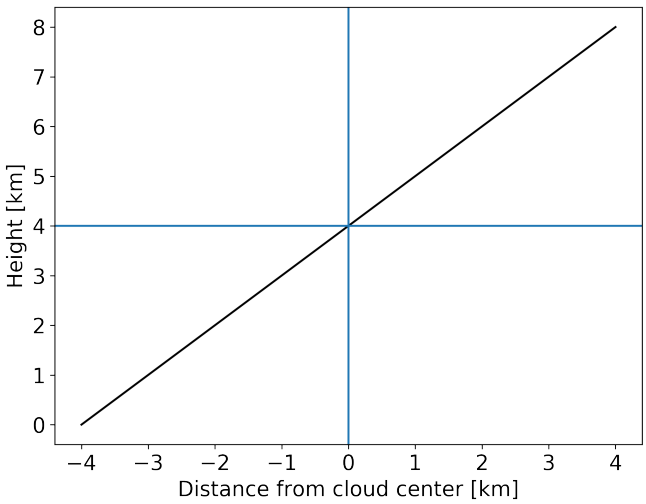

Figure 3.5: Linear scaling function applied to 2D divergence field to produce convergence in the bottom half of the cloud and divergence in the top half of the cloud.

Updraught core strength was underestimated by 50% compared to the real updraught, this was also shown statistically by Nicol *et al.* (2015) using model data and is shown in Figure 3.6. For a cylindrically symmetric updraught, with a beam going through the core, the cross-beam divergence equals the along-beam divergence. Thus by only using one divergence component, a factor of 2 error in vertical velocity is expected. To account for this error, Nicol *et al.* (2015) assumed $\frac{\partial w}{\partial z} = -2\frac{\partial u}{\partial x}$ and that scans were through the core. The error is largest at the core and decreases away from the core.

Updraught width was underestimated by 20% when scanning through the core, further adding to the error in updraught properties derived with this method. If radar scans are not aligned with the updraught core, which cannot be guaranteed, updraught width can still be underestimated as shown in Figure 3.7. The error in updraught width estimate decreased to 0 near the edge of the updraught, but then updraught width was overestimated when calculating updraught profiles using the $\frac{\partial u}{\partial x}$ component of divergence only. This is further shown in Figure 3.8 because the updraught estimate was more elongated and 'bean' shaped compared to the real updraught, which would contain both components of divergence. This is caused by the structure of the $\frac{\partial u}{\partial x}$ field. The combination of updraught width and strength underestimation due to the retrieval

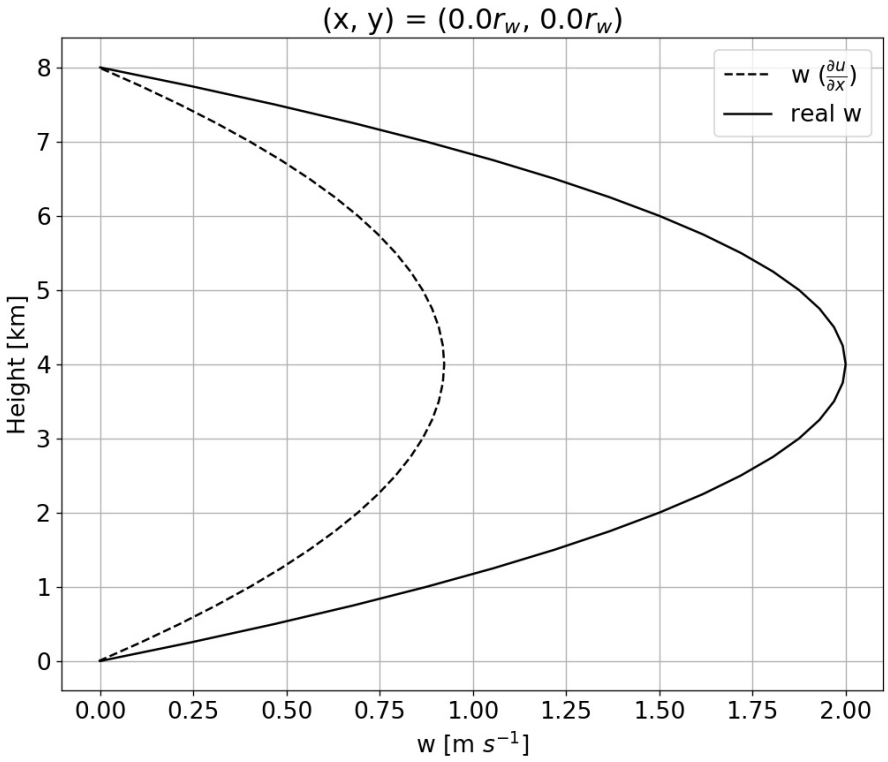

Figure 3.6: Retrieved vertical velocity using only the $\frac{\partial u}{\partial x}$ component of divergence (dashed black) and the real vertical velocity (solid black). Vertical profiles taken at updraught core (0.0r_w, 0.0r_w).

method and updraught core location uncertainty means that the updraught core may have been missed in observations and its true width and strength cannot be obtained using the single Doppler retrieval technique.

Due to these caveats, this retrieval method would not be suitable to estimate vertical velocity and apply object tracking to a small number of clouds to investigate updraught structures this thesis is focused on.

3.4 Particle fall speed correction

To derive estimates of particle fall speeds for different hydrometeors, the reflectivity weighted hydrometeor fall velocity (Feist *et al.*, 2019) was used and is given by

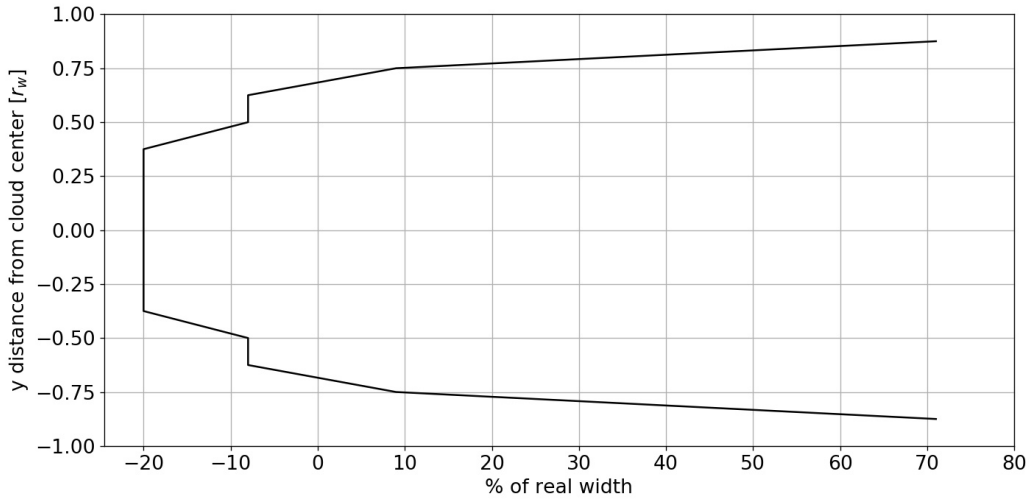

Figure 3.7: Width of retrieved vertical velocity using only the $\frac{\partial u}{\partial x}$ component of divergence as a percentage of the real vertical velocity width with distance from the core.

$$\overline{W_j}^2 = (\frac{\int_0^\infty V_j(D) M_j(D)^2 n_j(D) dD}{\int_0^\infty M_j(D)^2 n_j(D) dD})^2, \tag{3.18}$$

where V = velocity, D = drop diameter (melted for ice aggregates), subscript j corresponds to hydrometeor type. $V_j(D) = p_j D^{q_j}$ is the terminal velocity-diameter relationship, $M_j(D) = a_j D^{b_j}$ is the mass-diameter relationship and $n_j(D) = N_{0_j} \exp -\lambda_j D$ is the particle size distribution (DSD) assuming each hydrometeor type can be approximated by an exponential distribution (Marshall and Palmer, 1948), where λ_j is the slope parameter. An expression relating λ_j to radar reflectivity is given by $\lambda_j = (\frac{R_j a_j^2 N_{0_j} \Gamma(1+2b_j)}{Z_j})^{\frac{1}{1+2b_j}}$ (Stein *et al.*, 2014), which provides a way for relating radar reflectivity to terminal velocity ($\overline{W_j} - Z_j$ relationship) after terminal velocity has been related to λ_j by the velocity-lambda ($\overline{W_j} - \lambda_j$) relationship. Values of p, q, a, b and N_0 are taken from table 1 in Feist *et al.* (2019).

Taking the $\sqrt{(3.18)}$ yields the reflectivity weighted mean of the distribution of hydrometeor fall velocity. Assuming a radar volume contains the same hydrometeor type then ρ, $|K^2|$, p, q, a, b, N_0 and R are constant for a particular hydrometeor type j, taken from table 1 in Feist *et al.* (2019). Using the equation for λ_j with values of $R = 3.65 \times 10^{12}$, a = 523.6, $N_{0_j} = 8 \times 10^6$ and $\Gamma(1 + 2b_j) = 720$ for rain gives

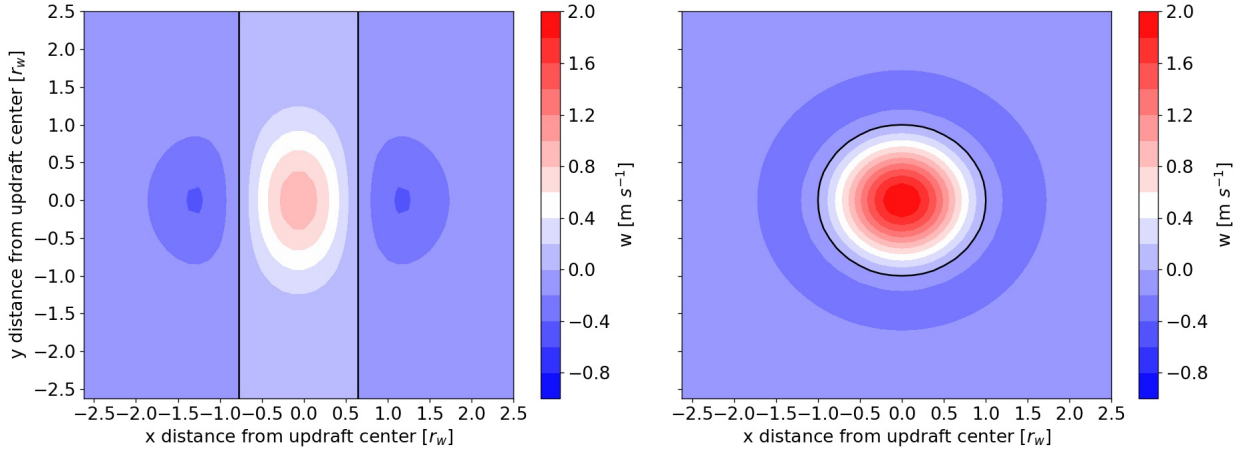

Figure 3.8: Retrieved updraught using $\frac{\partial u}{\partial x}$ component of divergence (left) and real updraught (right) at height of peak updraught velocity (4 km). Black contour represents 0 m s^{-1} vertical velocity bounding the updraught core.

$$\lambda_{rain} = 2.20 \times 10^{-3} Z^{\frac{67}{700}}, \tag{3.19}$$

the velocity-lambda relationship for rain is given by (full derivation not shown)

$$\overline{W} = 1401.78 \lambda^{-0.67}, \tag{3.20}$$

now substituting (3.19) into (3.20)

$$\overline{W}_{rain} = 3.08 Z^{\frac{67}{700}}. \tag{3.21}$$

Similarly for aggregates with values of p = 8.34, q = 0.31, a = 0.0444, b = 2.1, $N_{0_j} = 6.8 \times 10^6$ and R = 8.12×10^{11} gives

$$\overline{W}_{aggregates} = 0.063 Z^{\frac{67}{542}}. \tag{3.22}$$

Finally, for hail with values of p = 142.6, q = 0.50, a = 480.1, b = 3, $N_{0_j} = 1.2 \times 10^4$ and R = 8.12×10^{11} gives

$$\overline{W}_{hail} = 7.04 Z^{\frac{1}{14}}. \tag{3.23}$$

Equations 3.21, 3.22 and 3.23 relate the observed reflectivity to the estimated hydrometeor fallspeed for a given hydrometeor type observed at vertical incidence. The component of $\overline{W}_j$ affecting the radial (Doppler) velocity (V_r) at radar elevation angle (ϕ) is given by $\overline{W}_j \sin(\phi)$.

Finally the fall speed contribution to the Doppler velocity along the beam is given by

$$\tilde{V}_r = V_r - \overline{W_j} \sin(\phi). \tag{3.24}$$

Hail observed at 60 dBZ will contribute 4.9 m s^{-1} to the radial velocity if observed at a 15° elevation angle. Given that cloud top heights were around 8 km, any cloud observed beyond 30 km range would be scanned at shallower elevation angles, and the contribution from hail to fall speeds would be small. Aggregates are not corrected for given there contribution are always negligible. Corrections for the terminal velocity of rain were not required given they are negligible with range from the radar at low elevation scanning angles (≤15°). At these angles precipitation fall speed does not usually have a significant component in the Doppler velocity. Thus, corrections to the Doppler velocity for the Nicol *et al.* (2015) retrieval method were not required.

3.5 Summary

This chapter reviewed the Nicol *et al.* (2015) vertical velocity retrieval method to determine whether it was suitable for application to vertical velocity retrievals in this thesis. The Nicol *et al.* (2015) assumes the cross-beam divergence is the same as the along-beam divergence and that scans are taken through the updraught core. The uncertainty in the core location, missing component of divergence, density profile assumption and errors in vertical velocity and new results presented in this chapter have shown that updraught width can be underestimated when updraught fields are retrieved using the integration Nicol *et al.* (2015).

Given updraught structures are a core factor of study in this thesis, the Nicol *et al.*

(2015) is not suitable for studying updraught structures in this thesis. Furthermore, corrections for hydrometeor fall speed to the Doppler velocity would have to be applied when using the Nicol *et al.* (2015) method. Thus, by using an alternative method the need to apply further corrections to the Doppler velocity field, which themselves can contain errors, is avoided. Furthermore. this method would not be suitable to estimate vertical velocity in clouds from which object tracking can be applied to identify transient updraught structures and estimate updraught properties on small sample sizes in individual clouds, investigated later in this thesis.

The Nicol *et al.* (2015) method was primarily designed and applied as a statistical method, using 'random' beam directions over many clouds, providing a large sample size, such that the discussed limitations and errors are reduced when sampled over many updraught cores. Such a large data set is not used in this thesis, resulting in the Nicol *et al.* (2015) method being unsuitable to vertical velocity retrievals in individual clouds or a small number of clouds.

Therefore work pursuing the Nicol *et al.* (2015) retrieval route method was terminated. An alternate vertical velocity retrieval and thermal tracking algorithm is described in chapter 4.

Chapter 4

Vertical velocity retrieval and analysis

4.1 Motivation

There is no single observational system that can directly measure the full 3D wind field within convective systems. To gain an understanding of the dynamics on the scale of storms and their internal dynamics, measurements of each wind component are necessary. Wind field measurements are also very useful to initialise numerical models. With access to multiple Doppler radars and other independent observations, 3D wind profiles can be retrieved using variational methods (Gao *et al.*, 2006; North *et al.*, 2017). In reality, access to such systems is unlikely in an operational environment and limited to research campaigns. Horizontal and vertical velocities can be retrieved from a single Doppler radar but have limitations associated with retrievals.

Single Doppler radars can only observe horizontal winds in the along-beam direction, restricting information to a small section of cloud. Horizontal velocities are commonly retrieved using the Velocity-Azimuth Display (VAD) method (Browning and Wexler, 1968). By scanning a full (usually) 360° in azimuth at a fixed elevation angle and repeating this process at many elevation angles, a vertical profile (VAD) of horizontal wind and direction above the radar location can be obtained. One method of retrieving vertical velocities from a single radar was explored in chapter 3 along with limitations.

In this thesis, vertical velocity in convective clouds was retrieved by building on the method of Hogan *et al.* (2008) by correlating Doppler velocity features in pairs of RHI radar scans. This method, detailed below, does not require assumptions of mass continuity, air density or variational constraints and is not subject to the errors discussed in chapter 3 associated with the integration method. Instead, it derives the

vertical velocity from displacement of features observed to be ascending in Doppler velocity measurements. These features, visible in animations, clearly show complex larger scale and small scale bubble type motion within convective clouds. Vertical velocity retrieved using this method enabled the application of object tracking to track ascending features in clouds, i.e various updraught structures, from which properties can be derived and development in time can be observed.

4.2 Vertical velocity retrieval

Radar observations of convective clouds show small scale features in the Doppler velocity field that move coherently, as if carried along with a mean flow. These velocity features are more clearly identifiable from scan to scan than features in reflectivity fields. A key characteristic of thermals that can be observed with radar is the velocity signature, i.e the variance at relatively small scales. Doppler velocity features have been observed to move with the flow (Hogan *et al.*, 2008). Thus, the wind field retrieval is based on the method presented in Hogan *et al.* (2008).

The Hogan *et al.* (2008) method used RHI scans that were separated by a short interval that continuously scanned convective clouds using the alternating up-down-up-down pattern. Regions of 2 km width by 1° elevation at each grid point in pairs of the raw (polar) Doppler velocity measurements were compared using a cost function. This allowed vertical displacement (dz) to be estimated by finding the 'best' minimum from the three lowest cost minima. Horizontal displacement (dx) was estimated by using the area averaged mean Doppler velocity in the 2 km by 1° elevation region. A final pass comparing dz to neighbours was performed to ensure consistency. The final field was then smoothed to a coarser resolution of 2 km by 1 km compared to the original radar resolution.

In this thesis a similar scale was used based on visual inspection of ascending features in Doppler velocity data and maximum reported radii of thermals from the literature ($\approx$1 km). Secondly, the original data must be able to resolve the scale, allowing more than 4 observations in range (300 m) and more than 2 beam widths within the search

domain out to 100 km range from the radar. This requirement leads to a search window of 2 km in width by 1 km in height, similar to Hogan *et al.* (2008). Furthermore, before retrieving vertical velocity the radar data was interpolated to a Cartesian grid. A Cartesian grid was introduced because a horizontal displacement was applied to the radar observations to displace scans to a uniform reference time, resulting in a Galilean transformation. This reference frame was the first scan taken in a sequence. It is useful to remove the overall bias in horizontal displacement of air parcels between scans and focus on the cloud-relative motion. This allowed vertical velocity retrieval in a system-relative framework. Finally, tracking of thermal objects was easier to carry out on a fixed Cartesian grid.

The procedure detailed below to retrieve in-cloud wind fields is shown by Figure 4.1. The following steps are executed to retrieve in-cloud motion vectors:

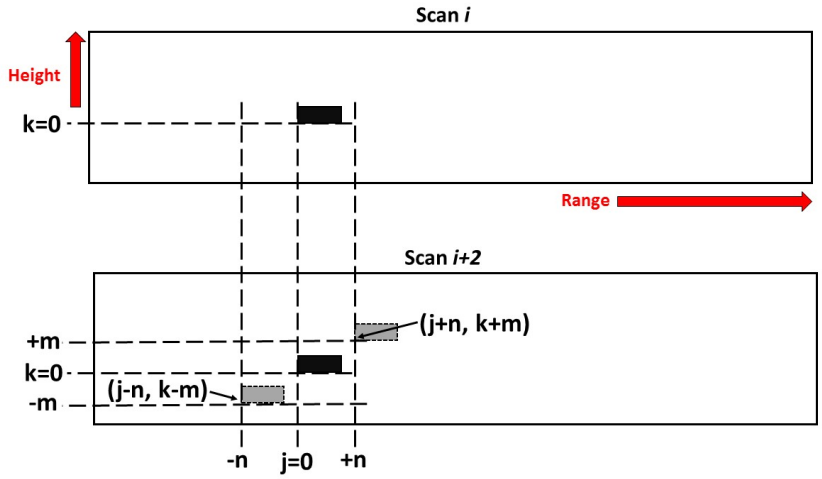

Figure 4.1: Diagram showing the vertical velocity retrieval process searching for similar features by iterating for k in (-m, +m) at displacement j (-n, +n) in scan $i+2$ (grey box). Cost values were calculated between the grey box in scan $i+2$ and black box in scan i for each grid point in range and height.

1. Determine two alternate scans to track with (denoted i and $i+2$), that is, two that scanned with increasing elevation or with decreasing elevation so that individual rays are separated by the same time due to the constant scanning speed (≈60 s for Gatwick clouds and ≈120 s for the DYMECS cloud).

2. In scan i, a box was centred on a point of interest (j, k), then in scan $i + 2$,

a search box was displaced horizontally by $n = n_0$. n_0 was estimated from the Doppler velocity local to (j, k) and provided an estimate of where features were expected to have moved horizontally. For example, a feature in the black box moved to be in the grey box ($j + n_0$, $k + m$) in Figure 4.1.

3. A search box was iterated vertically between -m and +m (grey box), shown in Figure 4.1. Cost values were calculated for each displacement. A box in scan i was only selected if it had complete valid data, thus retrieval to the cloud edges was not possible. The top 3 cost minima were stored at this step.

4. The cost value from the top 3 minima that corresponded to the smallest displacement (equalling a velocity nearest to 0 m s^{-1}) was selected as a first guess.

5. A second pass on all retrievals was performed which compared the estimated velocity vector ($\vec{v} = \sqrt{u^2 + w^2}$) where u is given by n_0 and w (estimated vertical velocity) from step 4, to the mean velocity vector of the neighbours. If the estimated velocity vector was > 1 m s^{-1}, the vertical velocity that yielded the smallest difference in velocity vectors between the neighbours and the current grid point was selected from the potential 3 estimates found in step 4.

6. A final pass was performed over all points which compared the velocity vector to the mean velocity vector of the neighbours of the current grid point. If the difference was > 5 m s^{-1} then the displacement was replaced with the neighbour mean.

7. Step 1 was repeated for each set of scans and for each range and height grid point in the Doppler velocity data.

Differences between Hogan *et al.* (2008) and the algorithm presented here are:

1. A two-step process has been applied. Firstly the Galilean transformation of the entire cloud and secondly a mean displacement for each search window.

2. A first guess was used by selecting the cost value corresponding to the smallest displacement.

3. Uncertainty was estimated for each vertical velocity retrieval.

4. No final smoothing reducing the resolution was applied.

4.2.1 Horizontal search

As part of the vertical velocity algorithm, searching for features in the horizontal was tested to account for slantwise movement. This in turn would produce a horizontal velocity field retrieval for clouds, based on the horizontal patterns in Doppler velocity. Ideally the retrieved horizontal velocity would closely match the observed Doppler velocity. This would imply that the search algorithm had correctly identified features moving in the horizontal. Even though radar scans were corrected horizontally to be in a Lagrangian framework, and that animations of Doppler velocity show clear patterns of features moving vertically, horizontal searching was still tested to determine it's impact on in-cloud motion vectors and if in-cloud horizontal motion was retrievable after the Galilean transformation.

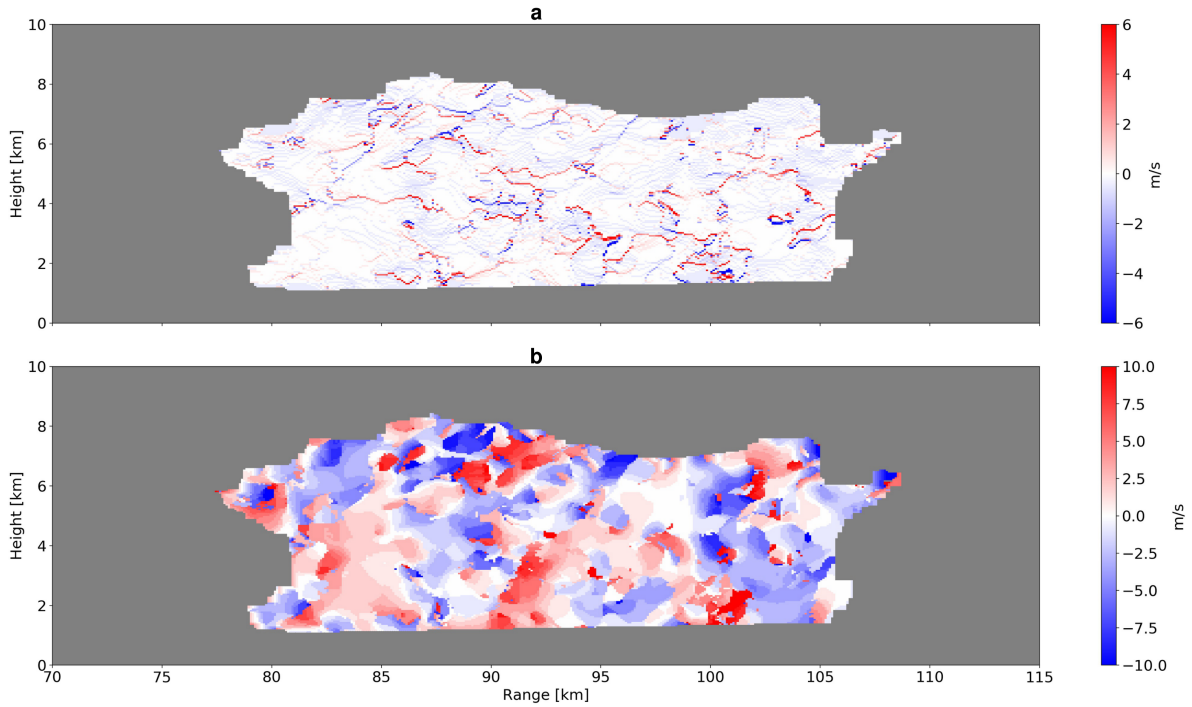

Figure 4.2: (a) Example of gradients in vertical velocity when retrieved without Doppler adjustment and (b) example of estimated horizontal velocity retrieved using horizontal search. Data from 15:11 on 24th September 2019.

To compare, n_0 which estimates the column to search in was calculated using the Doppler velocity local to the region or grid point currently being retrieved. If the flow was towards the radar at a given point, yielding a Doppler velocity (V_D) of -5 m s^{-1} for example in scan i. Then in scan $i + 2$, due to this flow, air from that point of interest was expected to have moved by $dx = V_D * dt$ between scans, where dt is the time difference between scans. For example if $dt = 100$ s, then $dx = -5 * 100 = -500$ m, 500 m towards the radar. Therefore, to estimate the column that the vertical search was initiated in, the horizontal grid point index for the corresponding displacement is given by

$$dx_{index} = \frac{V_D * dt}{\Delta x}, \tag{4.1}$$

where Δx is the horizontal grid resolution in metres. For a horizontal grid resolution of $\Delta x = 100$ m, for the example above the estimated index displacement dx_{index} would be $\frac{-500}{100} = -5$. This means that the algorithm will search in the column 5 grid points to the left in scan $i+2$ given this is where the corresponding pattern is expected to be. A dx_{index} of 0 would indicate that there is no adjustment. For non integer estimates, these are converted to integers to be able to work with the code. This means that the margin of error on estimated column selection is 100 m.

Figure 4.2(a) shows the gradient in vertical velocity retrieved without Doppler adjustment and by allowing a horizontal search and (b) estimated horizontal velocity from horizontal search. Figure 4.3(a) shows the gradient in vertical velocity retrieved with Doppler adjustment, using the area mean Doppler velocity (n_0), (b) estimated horizontal velocity from the Doppler adjustment (n_0) and (c) observed Doppler velocity. Figure 4.2(b) shows that the estimated horizontal velocity retrieved by allowing a search window in the horizontal did not match the observed Doppler velocity field features in Figure 4.3(c). Some larger scale features were retrieved but the estimated field showed some incorrect velocity magnitudes in some regions.

Figure 4.3(b) and shows that the estimated Doppler velocity used in the Doppler adjustment, calculated as the area mean Doppler velocity matched the observations in Figure 4.3(c). This was expected given the observed Doppler velocity was used to

calculate the estimate. This shows that the search for a feature will be initiated in the expected location given by dx_{index} and not in the opposite direction, which could occur prior to this adjustment by letting a search occur in the horizontal solely without using the observed Doppler velocity. This was most likely due to the Doppler velocity field having been transformed to a fixed horizontal view point. Therefore, features in Doppler velocity tend not to move horizontally as they would without the Galilean transformation to a fixed Cartesian grid but show significant development of features vertically. This makes it difficult for the search algorithm to match patterns in the horizontal, but in-cloud horizontal motion was sufficiently provided by the Doppler velocity.

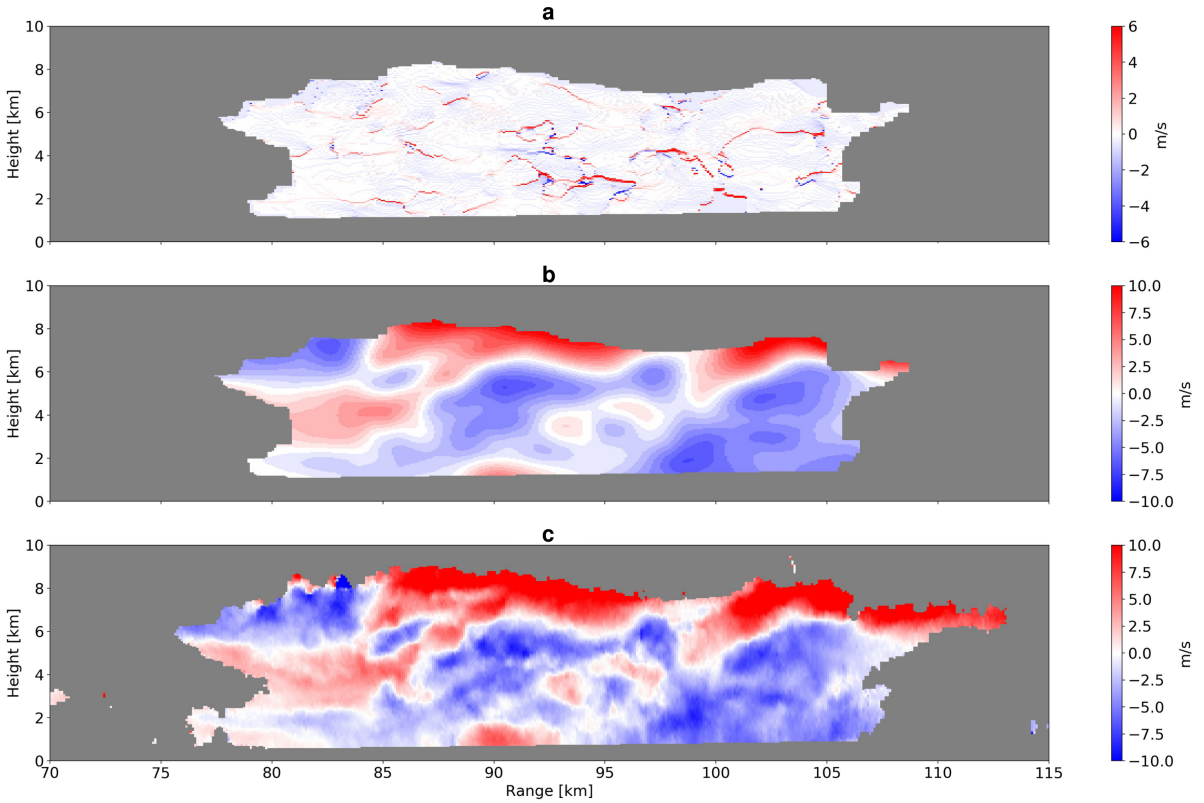

Figure 4.3: (a) Example of gradients in vertical velocity when retrieved with Doppler adjustment, (b) example of estimated horizontal velocity, the area mean Doppler velocity, from Doppler adjustment and (c) observed Doppler velocity. Data from 15:11 on 24th September 2019.

Examples of vertical velocity gradients retrieved without Doppler adjustment are shown in Figure 4.2(a) and with Doppler adjustment in Figure 4.3(a). Comparing the

two examples, and others not shown, upon visual inspection there were less vertical gradients in the vertical velocity field in Figure 4.3(a) than in Figure 4.2(a) which indicated a more consistent field. The retrieved vertical velocity field was consistent with vertical motion observed visually in the Doppler velocity but most importantly had a consistent field in adjacent scans in space (not shown) and time compared to retrievals without the Doppler adjustment. An example of a pair of vertical velocity retrievals for two adjacent time periods is shown in Figure 4.4(a) and (b). The consistency of the vertical velocity retrievals in a scan compared to its prior and the next scan, and to scans adjacent in space (those done using the bracket scanning strategy discussed in chapter 6 section 6.3), increased confidence in the retrieval. Consistency in vertical velocity fields in space and time is further shown in chapter 6 using composites of vertical velocity from the multiple scans taken using the bracket scan strategy.

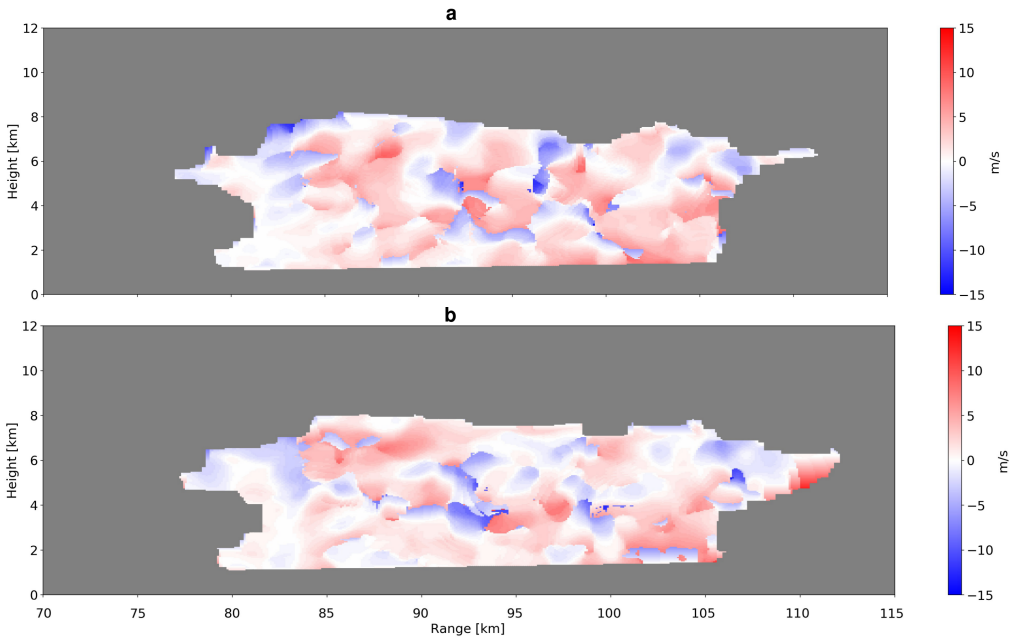

Figure 4.4: Example of vertical velocity retrieved for two adjacent time periods for two scans from the 24th September 2019 scans through the assumed reflectivity core.

Finally, by searching in the expected column, the cost map in Figure 4.5 reduced to a vertical profile only, as shown by the curve in the left panel. This results in comparison of the lowest 3 cost minima in the vertical column only.

4.2.2 Cost function minimisation

A cost function (J) was defined as in Hogan *et al.* (2008), as the mean absolute difference between the values of horizontal velocity (V) in the first scan i and the second scan $i + 2$ and was given by

$$J_{j,k} = \sum_{p=n,q=-m}^{m} W_{p,q}|V^{i+2}_{j+p,k+q} - V^{i}_{j,k}| / \sum_{p=n,q=-m}^{m} W_{p,q}, \tag{4.2}$$

where W is a Gaussian weighting decreasing from 1 in the centre, resulting in more weight being given to values in the centre than at the corners. A maximum vertical velocity of up to 25 m s^{-1} was allowed to be retrieved. Therefore, the iteration limits of q varied per set of scans, as the time difference between scans varied.

An example cost map for a selected grid point is shown in Figure 4.5. Local cost minima (black dots) and the top 3 minimum cost values (red crosses) are shown in the right panel. The left panel shows an example of the vertical profile of cost values for a grid point of interest indicated by the dashed black line in the right panel. On the cost curve in the left panel the minimum and local turning points are identified by the red stars. Blue circles indicate the half way points used to calculate the uncertainty. The turning points are found by iterating along the cost curve away from a selected minimum. The halfway points are calculated by finding the distance halfway between the turning points and a chosen minimum. These calculations and uncertainty estimates are discussed further below and were used to estimate uncertainty on vertical velocity by using the structure of the cost curve and uncertainty in Doppler velocity measurements.

4.3 Testing cost and correlation methods for vertical velocity retrieval

In this section results testing the robustness of the vertical velocity retrieval are presented. Vertical velocity retrievals can be subject to error from noise in radar mea-

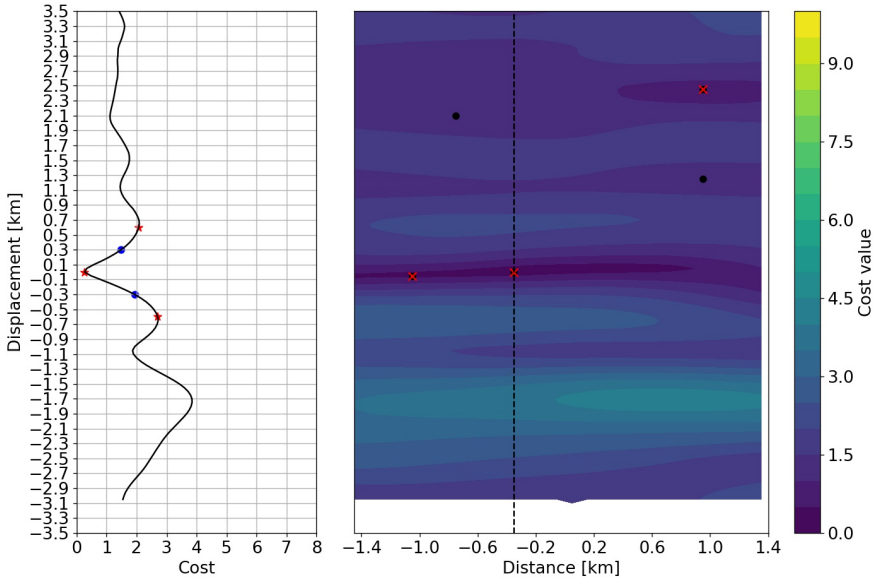

Figure 4.5: (left) Vertical profile of cost values for column shown by dashed black line in right panel going through minimum cost shown by red 'x'. Red stars mark the minimum cost in column and the local turning points. Blue circles indicate the halfway points between the minimum and turning points. (right) Cost map for a select grid point showing how the cost values change in 2D space. Black dots are local minima and red 'x' are the top 3 minima. Grid spacing for this example was 50 m in the vertical and 100 m in the horizontal.

surements. Uncertainty on vertical velocity retrievals can also be due to the grid scale being a similar order of magnitude to the features of interest, that is the patterns being searched for in Doppler velocity. An analysis was done testing two methods of retrieving displacement, from which velocity is derived; (1) using correlation and (2) using a cost function defined as the mean absolute difference and weighting data in a search box ($cost_1$ herein) (Hogan *et al.*, 2008). Each test case was compared to a high resolution true solution to determine the robustness of each method.

For this analysis only steps 1 - 3 from section 4.2 $cost_1$ were followed because the test cases are highly idealised. The minimum cost value was selected to calculate displacement to determine which method performed best without the final passes and if selection of a cost minima functioned as expected. Steps 4 - 7 of the retrieval process were included in retrievals on observations to account for optimal selection of minimum cost value and consistency in the field required with real data. Correlation (r) was calculated between the current box of interest in the current velocity field (t)

and the search box in the velocity field forward in time ($t = 2$) by using equation 4.3.

$$r = \frac{\sum_{i=1}^{n}(V_z^t - \overline{V_z^t})(V_z^{t=2} - \overline{V_z^{t=2}})}{\sqrt{\sum_{i=1}^{n}(V_z^t - \overline{V_z^t})^2}\sqrt{\sum_{i=1}^{n}(V_z^{t=2} - \overline{V_z^{t=2}})^2}} \tag{4.3}$$

Where V_z^t are the vertical velocity values in the current box of interest (t), $V_z^{t=2}$ are the velocity values in the search box forward in time ($t = 2$) and n is the number of velocity values in the search box.

Idealised thermals were represented in a vertical column as a Gaussian signal with magnitude 10 centred at 3 km height and 3 km range on a 6 km x 6 km grid on a background field of 0. Multiple test cases using ideal thermals of different sizes were displaced vertically, with and without random noise applied and background noise provided by a stationary object. The tracking methods were first run on a high resolution case without noise to determine the 'true' response of each method. Thermals were displaced by a fixed vertical displacement of 250 m for an arbitrary time corresponding to 100 s. This meant that the true thermal vertical velocity was 2.5 m s^{-1}. A displacement of 500 m should correspond to the minimum cost value and the maximum correlation when using alternate pairs of signals (t = 0 and t = 2). Similarly, using consecutive pairs of signals (t = 0 and t = 1) a displacement of 250 m was expected given thermals were manually displaced 250 m.

In the test cases, down-sampling was applied to the 25 m vertical by 50 m horizontal grid to yield a 250 m vertical and 500 m horizontal grid, except the reference case. The retrieval method was applied using a search window size of 2 km, i.e how far to look, such that 4 km deep profiles of cost values were obtained. A search box was iterated in the vertical direction only in the column the thermal was located. In the case of real data, the search was initiated at every grid point, in these test cases searching was only initiated in the column of interest beginning at the bottom of the grid (0 km height). A search box size of 1 km height and 2 km width was used as this was the same as used with real data. Figures of cost and correlation curves shown in the sub-sections below are vertical profiles of the cost and correlation values from the grid point centred on the thermal maximum signal (3 km height and 3 km range) at t = 0. Therefore, a

curve peaking at 500 m displacement indicated that the object was correctly located 500 m above is prior location.

4.3.1 Reference thermal

A reference thermal was tested with a grid spacing of 25 m in the vertical. The thermal was represented as a Gaussian peak with a standard deviation of 100 m in width and was displaced by 250 m between consecutive scans.

The Gaussian curve that represents a thermal is shown in Figure 4.6, where the magnitude of the Gaussian was set at 10 and did not change over time. The $cost_1$ function (Figure 4.7(left)) shows the minimum cost value found between corresponding fields with a peak at 500 m. This showed that the cost function correctly identified the displacement between corresponding fields. The shape of the curve was also expected with local maxima in cost value directly above and below the minimum cost value. These local maxima are caused when the cost function was being calculated between the full Gaussian in scan i and part of a Gaussian in scan $i+2$. Thus, when they are subtracted negative values are obtained, but these are taken to be absolute then summed causing a larger number. Figure 4.7(right) shows the correlation values which matched well with $cost_1$ values, where maximum correlation of 1 was at 500 m displacement. The correlation was also a Gaussian which was expected as the correlation increased to find the matching spatial pattern and then decreased as the window moved past the best matching pattern. The symmetry of the functions was expected for this reference case.

The high resolution thermal was down-sampled to a grid resolution that was 10 times coarser than the fine grid spacing, that is 250 m in the vertical and 500 m in the horizontal. Down-sampling by averaging the high resolution grid points that are within a coarse resolution grid box has the effect of (1) mimicking in simple terms how the radar would sample an average volume by averaging multiple higher resolution samples and (2) dramatically dampen the amplitude of a thermal that is on the order of the grid resolution. The down-sampling of the thermal in Figure 4.6 yielded the Gaussian in Figure 4.8.

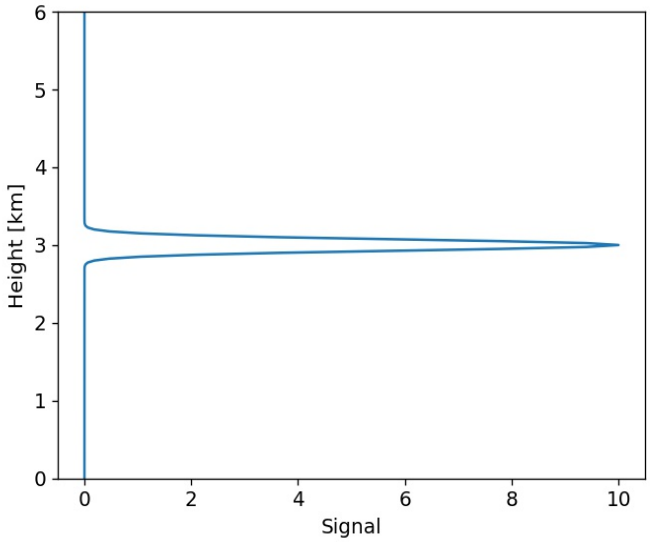

Figure 4.6: Example of a thermal on the high resolution grid (25 m x 50 m grid spacing) showing the Gaussian signal with magnitude 10 centred at 3 km height with standard deviation of 100 m.

Figure 4.8 clearly shows the expected decrease in amplitude and the coarser representation of a Gaussian curve. This is expected to not have an effect on the tracking given there was still a peak that was clearly evident against the uniform background field. Even though the amplitude was low in magnitude, the tracking methods should still be able to track a single peak moving.

Figure 4.9 for $cost_1$ (left) shows the correct displacement of the thermal of 500 m. The correlation values are shown in Figure 4.9 (right). For both methods, a correct displacement of 500 m was identified. The bias in vertical velocity of the thermal centroid in this case would be 0 m s^{-1} given the correct displacement was identified. The root mean square error (RMSE) of vertical velocity between this case and the truth was 0.8 m s^{-1} for $cost_1$ and 1.1 m s^{-1} for the correlation method. RMSE is given by

$$RMSE = \sqrt{(\sum_{i=1}^{n} \frac{(V_z^{true} - V_z)^2}{n})}, \tag{4.4}$$

where V_z^{true} is the true vertical velocity in the column of the thermal from the high

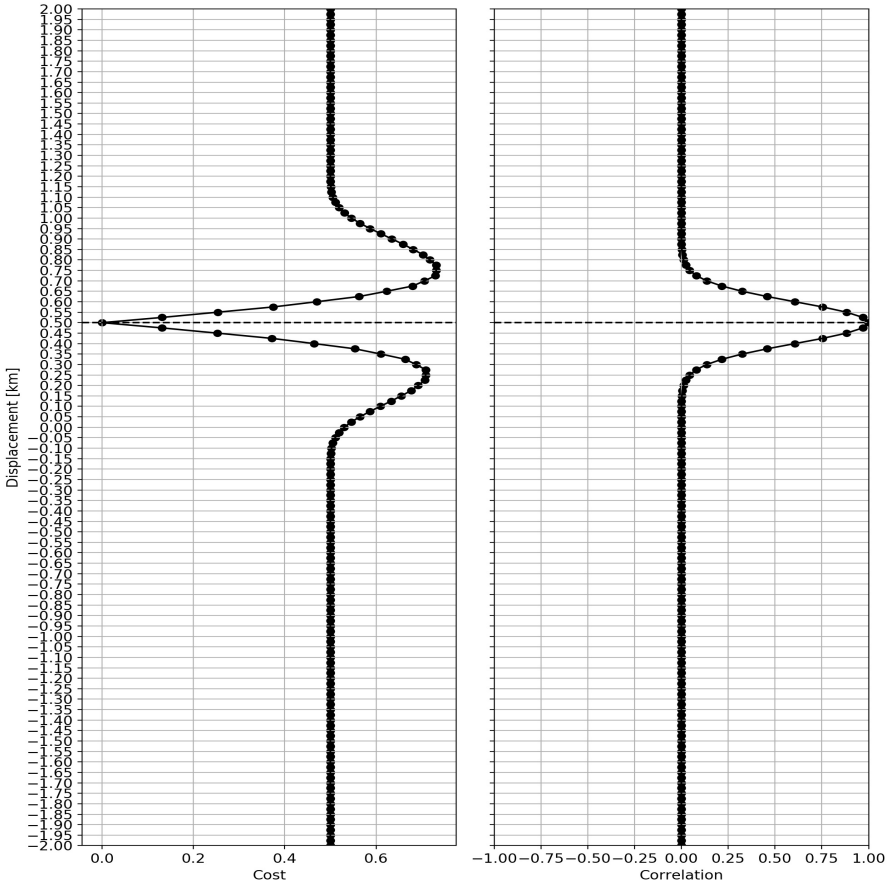

Figure 4.7: Vertical profile of mean absolute difference cost ($cost_1$) (left) and correlation values (right) selected from centre of thermal. Peaks identify found displacement for corresponding pair of synthetic thermals. Black dashed lines indicates expected 500 m displacement.

resolution reference thermal. V_z is the vertical velocity in the column of the thermal for each test case and n is the number of velocity values in the column. RMSE of vertical velocity was then determined for the column of the thermal for each of the test cases discussed in this section.

Having a displacement that matches the grid resolution neatly raises the question of what happens if the displacement is irregular, i.e does not fit neatly onto the grid length? To asses this impact using the ideal test case on the coarse grid, the thermal was displaced 200 m between scans. Therefore the true cost minimum will be a peak at 400 m. On the coarse grid this will result in a peak at 500 m, given the grid spacing. To deal with irregular displacements on a coarse grid, a Lagrange interpolation was tested and aimed to improve displacement estimates. Ideal test cases showed that this

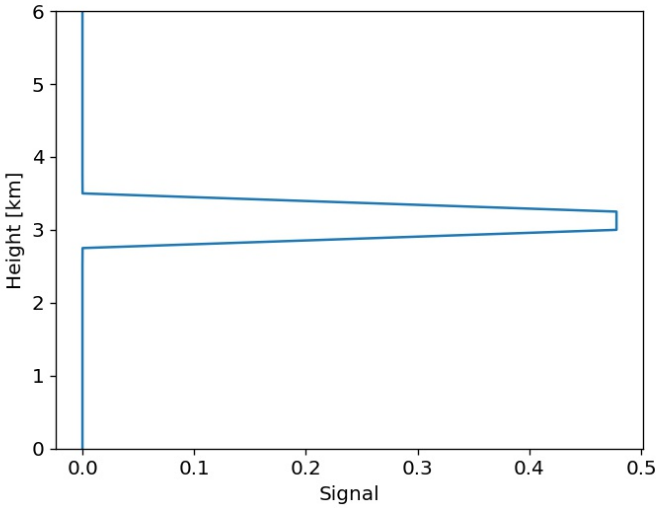

Figure 4.8: Down-sampled (250 m x 500 m grid spacing) thermal with standard deviation of 100 m to coarse grid.

method correctly identified the displacement when thermals were displaced non whole grid box values. This is shown in Figure 4.10 which shows the cost values (blue line) for an ideal thermal on a coarse grid. A Lagrange polynomial (green dashed line) was created using the minimum cost value and the points either side (grey crosses). The minimum of the Lagrange curve fit yielded the new estimated displacement (red star) of 410 m, which is close to the expected value. Figure 4.10 shows that the Lagrange interpolation improved displacement estimates for coarse grids. In this thesis the Lagrange polynomial to improve displacement estimates due to coarse grids was not used, given the observational data was significantly high enough resolution. The Lagrange polynomial is further discussed in section 4.4 and was used as part of an algorithm to estimate the uncertainty on vertical velocity retrievals.

4.3.2 Thermal with random noise of 1 standard deviation

Testing signals with added noise is important to determine if a signal can be extracted from a noisy signal and at what point the retrieval process may fail. In observations thermal signals most likely will not be as distinct as in these ideal cases, therefore adding random noise can provide some insight into how the retrieval may work with

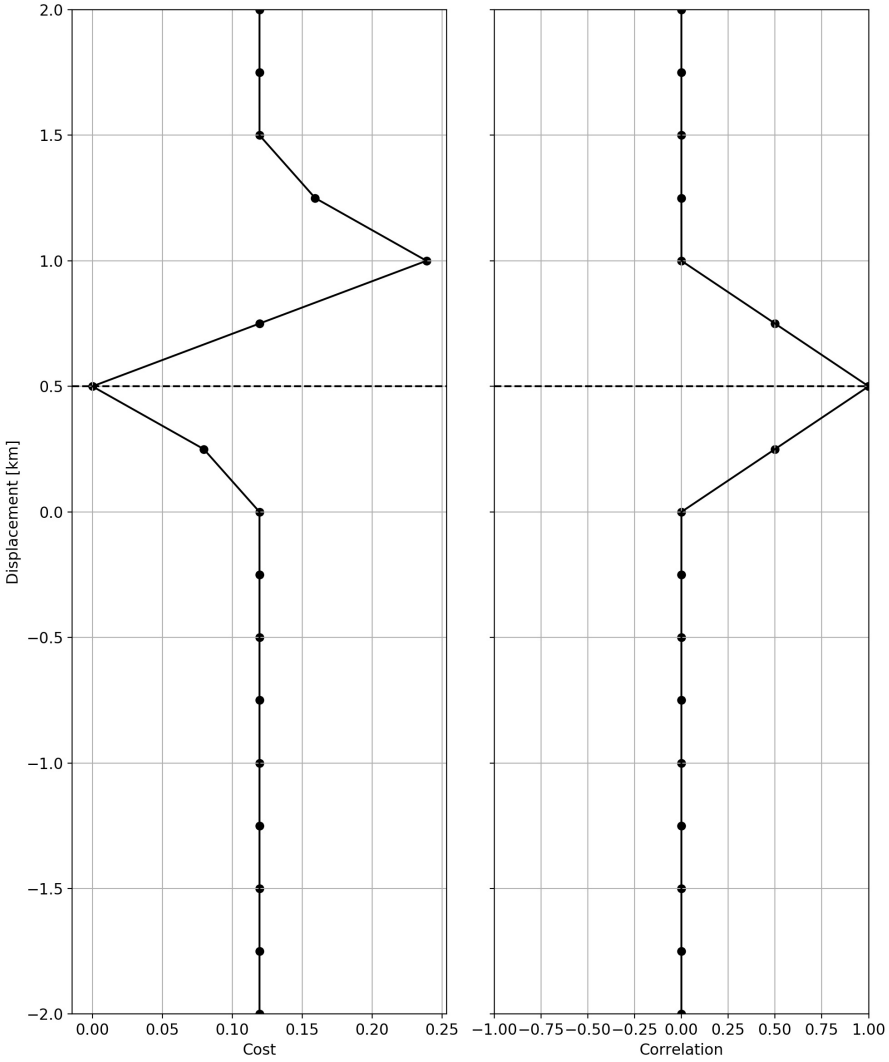

Figure 4.9: As in Figure 4.7 but for the downgraded thermal.

observations.

To test the limitations of the algorithm given the radar measurements, various idealised thermals sampled on a 500 m grid were studied. The assumption is that at coarse resolutions, narrower or weaker pulses may not be captured. This test gives an indication of the scale and intensity of features that can be tracked. Thermals were moved with background noise added that was sampled from a Gaussian distribution with a mean of 0 and standard deviations (SD) of 1 and 2 in separate cases. Noise was also added in the form of an additional broader updraught feature that a thermal may propagate within to determine if the tracking methods still suitably tracked the thermal of interest.

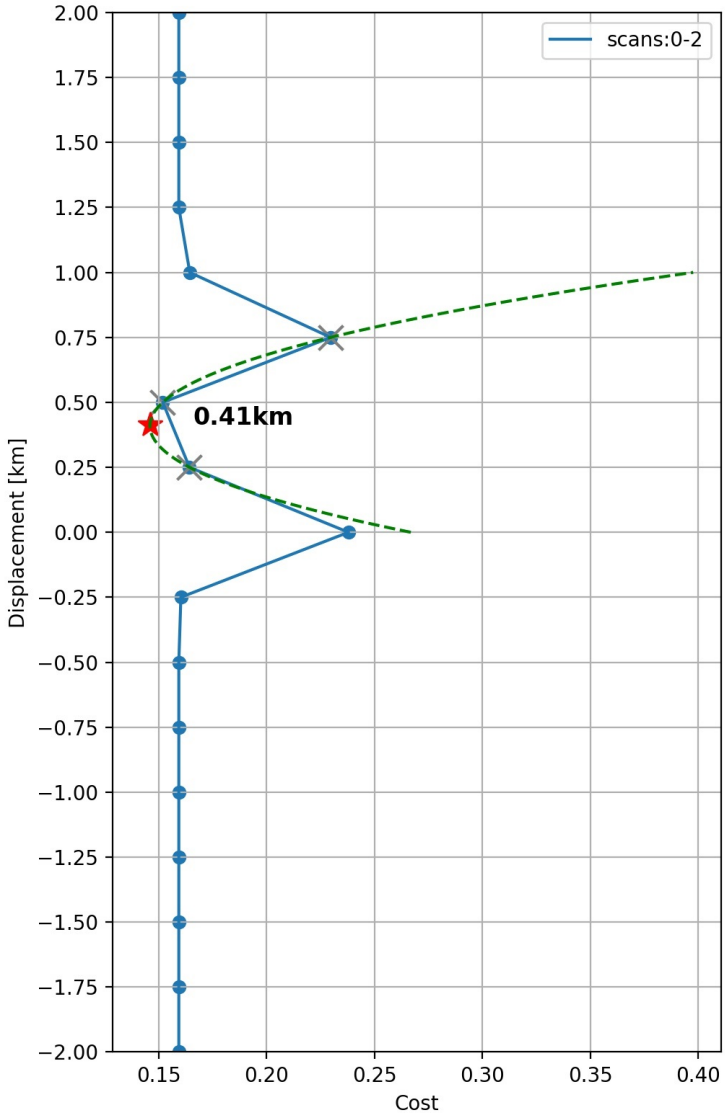

Figure 4.10: Figure showing the cost curve (blue) and the Lagrange interpolation (green dashed). Cost curve shows estimated displacement at 0.5 km. The 3 points used to produce the Lagrange polynomial (grey crosses) and the minimum of the Lagrange curve (red star) yields an updated displacement of 0.41 km.

The same thermal as in Figure 4.6 was used with added random noise sampled from a normal distribution with a mean of 0 and standard deviation of 1, shown in Figure 4.11a. A distinct peak was seen protruding from the noisy background and was easily identifiable. When down-sampled to the 250 m by 500 m grid, shown in Figure 4.11b a distinct peak was still seen over the noisy background. Again the magnitude was dampened but a peak was still visible. There were other smaller amplitude peaks and troughs which may impact the tracking methods if they reach magnitudes similar to

the signal.

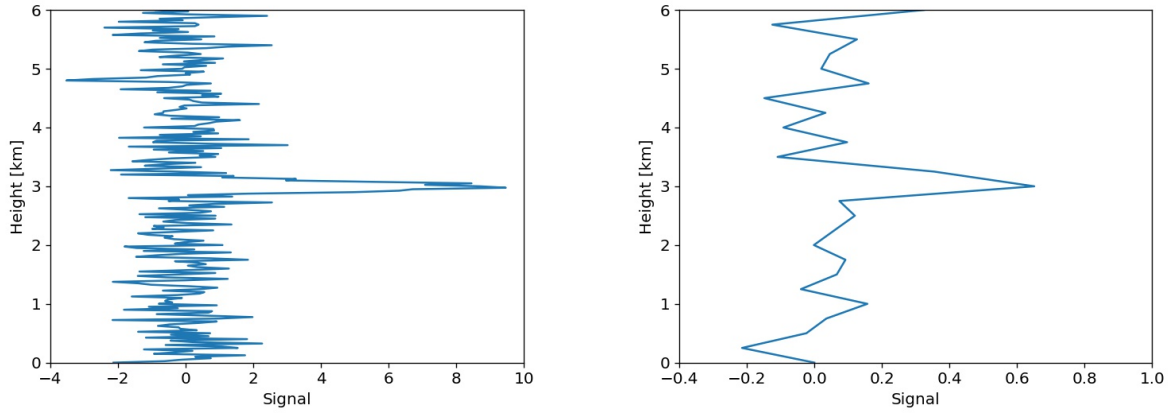

(a) (b)

Figure 4.11: (a) High resolution Gaussian with peak showing the core of the thermal against the background noise. (b) Down-sampled Gaussian on the coarse grid. Peak still identifies thermal core. Background random noise sampled from Gaussian with a mean of 0 and SD of 1.

Figure 4.12 for $cost_1$ (left) and correlation (right) both show good identification (low cost value, high correlation) at 500 m displacement with the expected variation in cost values due to noise and the increase in cost either side of the minimum as seen in the reference thermal. Both methods correctly identified the displacement of the thermal when there was background noise that had smaller magnitude to the thermal and had varying widths of peaks and troughs. The vertical velocity bias for both methods of the thermal centroid in this case was 0 m s^{-1}. The RMSE of the velocity field retrieved using the correlation method is 11.3 m s^{-1} and 10.5 m s^{-1} with $cost_1$.

4.3.3 Thermal with random noise of 2 standard deviations

This case is the same as above but the random noise has a standard deviation of 2, increasing the amount of noise that can affect the signal being tracked. Figure 4.13a shows the increase in noise which was close to effectively drowning out the main signal. A peak could be seen but there were also many other peaks and troughs that the methods will attempt identify, causing problems in identifying the correct peak. Figure 4.13b shows the field down-sampled to the coarse grid. It can be seen there

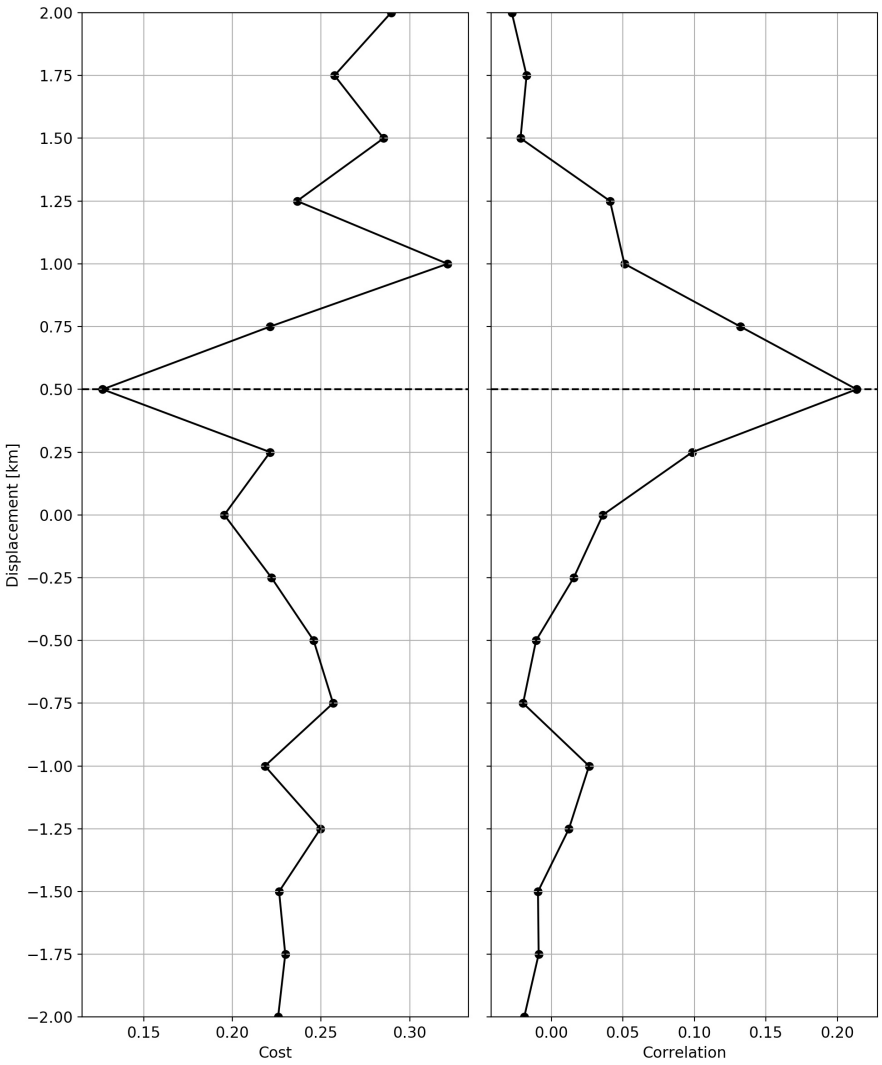

Figure 4.12: Vertical profile of mean absolute difference cost $cost_1$ (left) and correlation (right) functions selected from centre of thermal. Sampled from thermal with background noise with mean of 0 and SD of 1 downgraded to coarse grid. Peaks identify found displacement for corresponding pair of synthetic thermals. Black dashed lines indicates expected 500 m displacement.

were peaks that are of similar magnitude to the main peak and with varying widths. It is expected from looking at the field that the methods may find it difficult to identify the correct peak with this amount of noise.

Figure 4.14 $cost_1$ (left) and correlation (right) show that both methods were still able to retrieve the correct displacement which resulted in a bias of 0 m s^{-1} for the thermal centroid velocity. Visually, there appeared to be more structure in the shape of the peaks and troughs in the $cost_1$ profile which is discussed in section 4.4 for

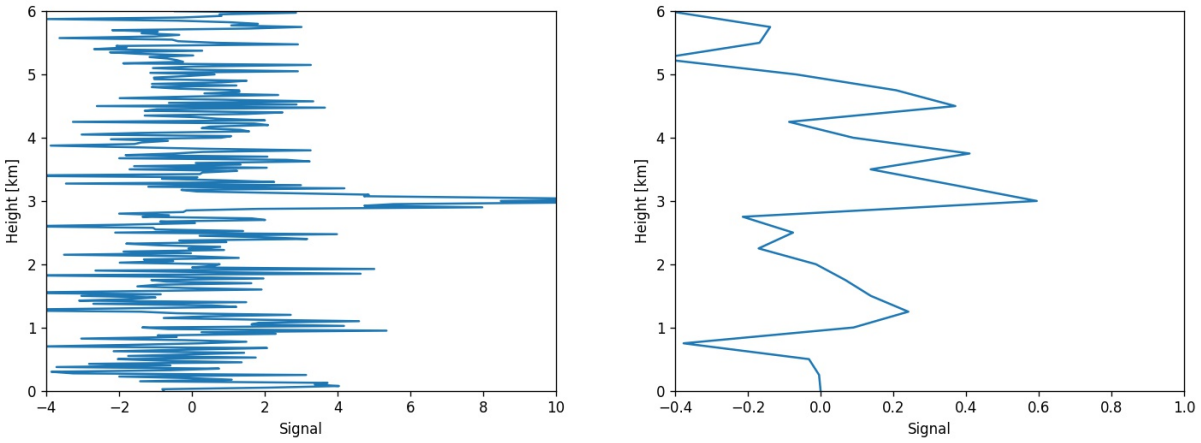

(a) (b)

Figure 4.13: (a) High resolution thermal in the vertical with peak showing core of thermal over background noise. (b) Down-sampled thermal where peak is harder to identify against background noise. Background noise sampled from a Gaussian distribution with mean of 0 and SD of 2.

calculating uncertainty in vertical velocity retrievals. The RMSE for the correlation method was 10.6 m s^{-1} and for the $cost_1$ method was 9.7 m s^{-1}. This indicated that the $cost_1$ method retrieved a vertical velocity field closer to the truth than the correlation method. Further tests using this case specification were run and multiple peaks were identified in the cost and correlation functions. Nevertheless, in this case the basic step of selecting the minimum cost behaved as expected. When multiple peaks occur, the further steps discussed in section 4.2 provide a route to attempt to select the most suitable cost minima and mitigate incorrect cost minima selection.

In cases where the noise level was high resulting in a low signal-to-noise ratio in cloudy regions, i.e near cloud edges, or noise in measurements of Doppler velocity due to turbulence, an uncertainty associated with the retrieved vertical velocity can be estimated. The noise due to the instrument system is 5.5 dB (Chris Walden, personal communication) which is low compared to the signal in active convection regions which is generally on the order of 20 dB. Signals of order 20 dB and greater result in a high signal-to-noise ratio where it is not expected that significant noise levels exist, which would cause difficulties with the retrieval algorithm. These test cases represent a worst case scenario.

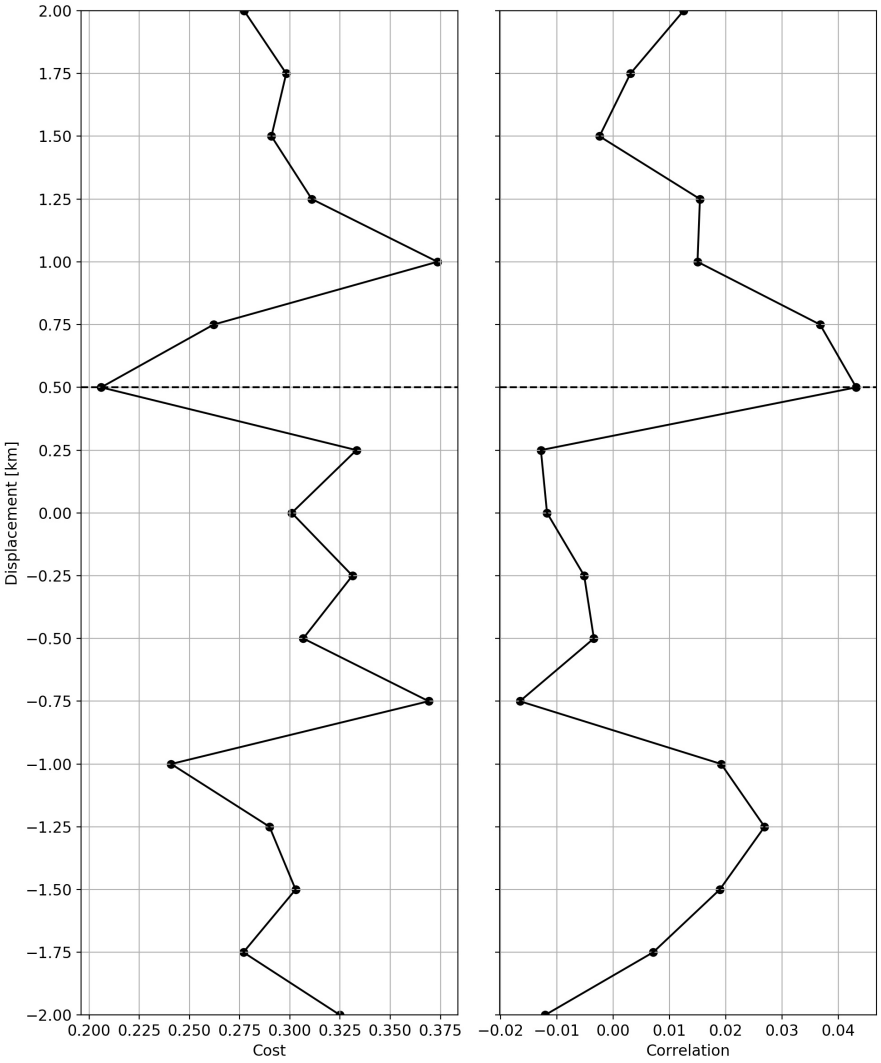

Figure 4.14: Vertical profile of mean absolute difference cost ($cost_1$) (left) and correlation (right) functions selected from centre of thermal. Sampled from thermal with background noise with mean of 0 and SD of 2 downgraded to coarse grid. Peaks identify found displacement for corresponding pair of synthetic thermals. Black dashed lines indicates expected 500 m displacement.

4.3.4 Thermal embedded in a large stationary feature

This case tests the methods ability to track a thermal that ascends within a stationary feature that extends through the domain in the vertical, a broad Gaussian. This is equivalent to a thermal/updraught pulse/velocity maxima rising in an environment that has near uniform background vertical velocities/steady updraught, shown in Figure 4.15a. When down-sampled in Figure 4.15b, magnitudes decrease but a narrow peak of the thermal was still visible on the background broad Gaussian. The signal at

t + 2 is shown in grey in both Figure 4.15a and 4.15b.

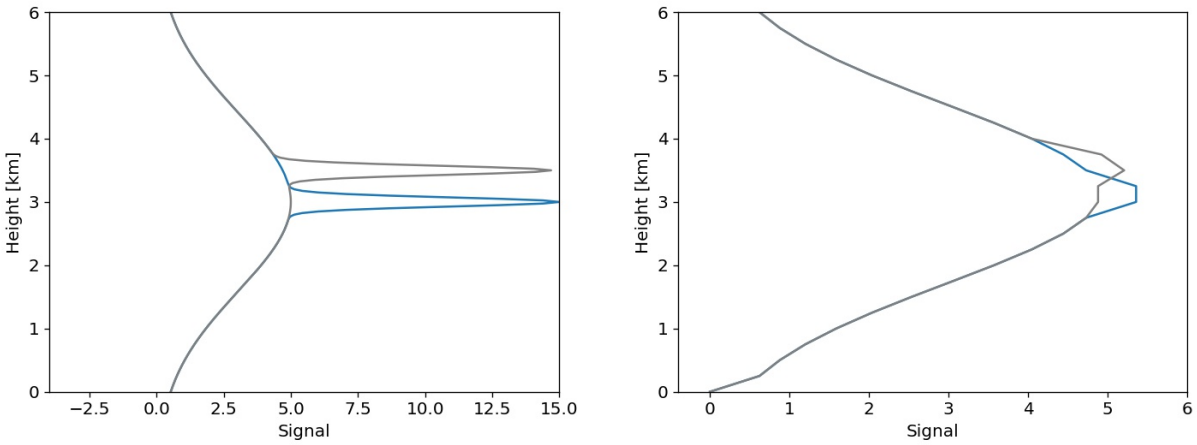

(a) (b)

Figure 4.15: (a) High resolution Gaussian with stationary background field. (b) Down-sampled Gaussian showing thermal peak harder to identify against background field. Signal at t + 2 is shown in grey.

$cost_1$ in Figure 4.16 (left) had a minimum cost at a displacement of 0 m. The correlation function did not have a distinct peak but it could be argued that by taking the mid-point between 250 m and 500 m (where the curve flattens) resulted in a 375 m displacement estimate. Again, the further passes on the cost function would help to identify the correct minima. Furthermore, the correlation function had an RMSE of 13.3 m s^{-1} and the $cost_1$ function had an RMSE of 4.7 m s^{-1}. This showed that the cost function retrieved a vertical velocity field closer to the truth than the correlation method. A high resolution test (not shown) found that $cost_1$ correctly identified the 500 m displacement indicated by a distinct peak. A second shallow peak was also identified at 0 m displacement. The correlation method did not yield a distinct peak at 500 m displacement but two very shallow peaks at 500 m and 0 m displacement were found. The two peaks are presumably one for the small thermal and one for the large updraught. The distinct peak in $cost_1$ located at the correct displacement indicated that $cost_1$ identified the thermal structure more distinctly than the correlation method. The RMSE values for this test were also similar with the RMSE of $cost_1$ being lower.

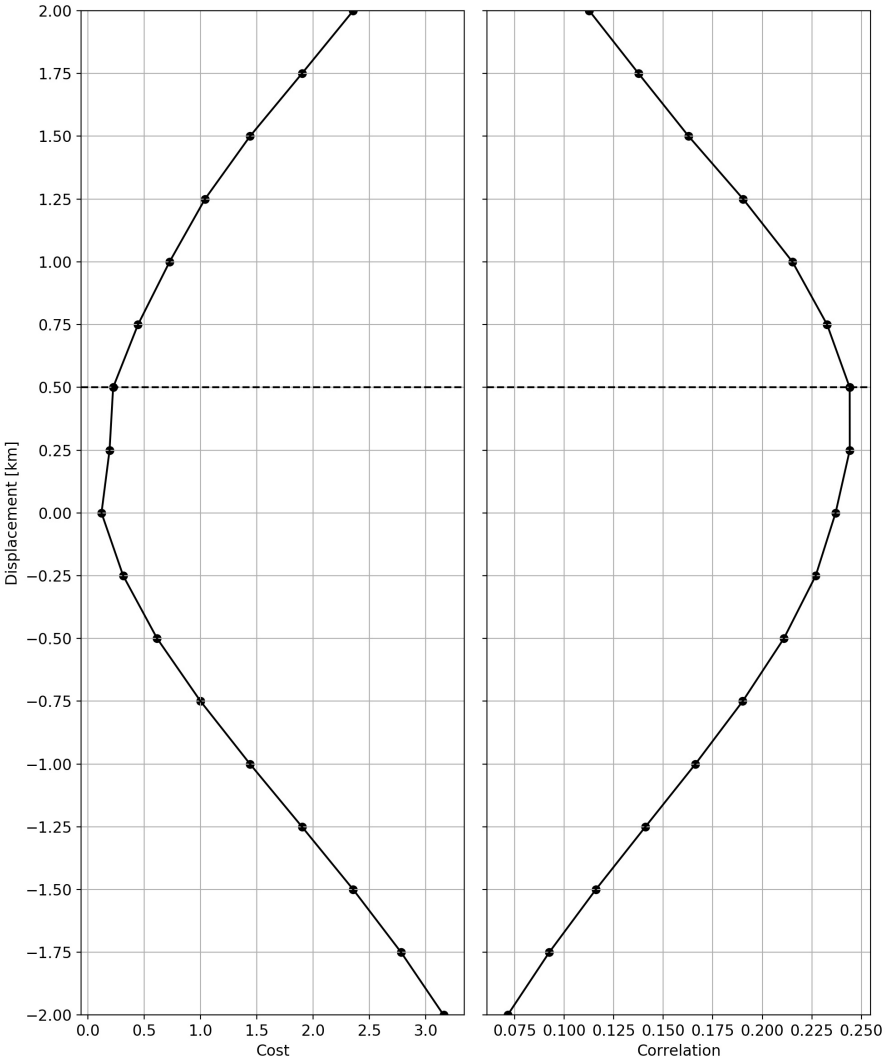

Figure 4.16: Vertical profile of mean absolute difference cost ($cost_1$) (left) and correlation (right) functions selected from centre of thermal. Thermal located within larger stationary updraught downgraded to coarse grid. Peaks identify found displacement for corresponding pair of synthetic thermals. Black dashed lines indicates expected 500 m displacement.

4.4 Estimating the uncertainty on Doppler velocity measurements

Uncertainty on vertical velocity retrievals can be due to (1) measurement error from turbulence in the measurement volume of the radar, (2) uncertainty due to the resolution of the radar, (3) the vertical velocity retrieval method on a gridded field and (4) system noise, determined to be negligible and is removed by processing (Chris Walden,

personal communication). In this section uncertainty estimates for Doppler velocity are discussed and a method for estimating uncertainty on the vertical velocity retrievals is derived. The uncertainty on the Doppler velocity is given by the variance on the mean Doppler velocity (Doviak and Zrnic, 1984), shown by equation 4.7. To do this, the signal-to-noise ratio must be estimated at each grid point to determine which form of equation will be used to calculate the variance on the mean Doppler velocity.

To investigate noise in observations, an example of a radar scan from the DYMECS case was used from 12:31 on 25th August 2012. The reflectivity for this time is shown in Figure 4.17(a). The red line indicates a transect through signal at 3 km height and the black line a transect through noise at 12 km height. 3 km height was chosen as it is assumed to be the height at which it is expected there to be a consistent retrieval of signal from within convective clouds. 12 km height was chosen for the noise level given no signal from clouds is expected at this height in the UK. Figure 4.17(b) shows the values of signal along the 3 km height transect in cloud (red circles) and noise (black circles) along the 12 km height transect. Figure 4.17(c) shows the noise (black crosses) at 12 km height compared to the estimated noise ($Noise_{est}$) (grey crosses) using the noise value reported for CAMRa at 1 km range of -36.7 dBZ (Chris Walden, personal communication) and multiplying by the range (R) squared, given by equation 4.5 in linear units. The match between the measured and estimated noise value shows that using the estimated noise values in calculations is suitable.

$$Noise_{est} = 10^{\left(\frac{-36.7}{10}\right)} R^2 \tag{4.5}$$

Reflectivity was converted into linear units (Z_{lin}) of mm^6 m^{-3}, along with the noise (Z_N) for each range. Signal-to-noise ratio (SNR) in logarithmic units can be calculated using equation 4.6 at each point in clouds. SNR estimates were further used in uncertainty calculations and are discussed below.

$$SNR = 10log_{10}\Big(\frac{Z_{lin}}{Z_N}\Big). \tag{4.6}$$

The full equation for the variance on the Doppler velocity ($var(\hat{v})$) is (Doviak and

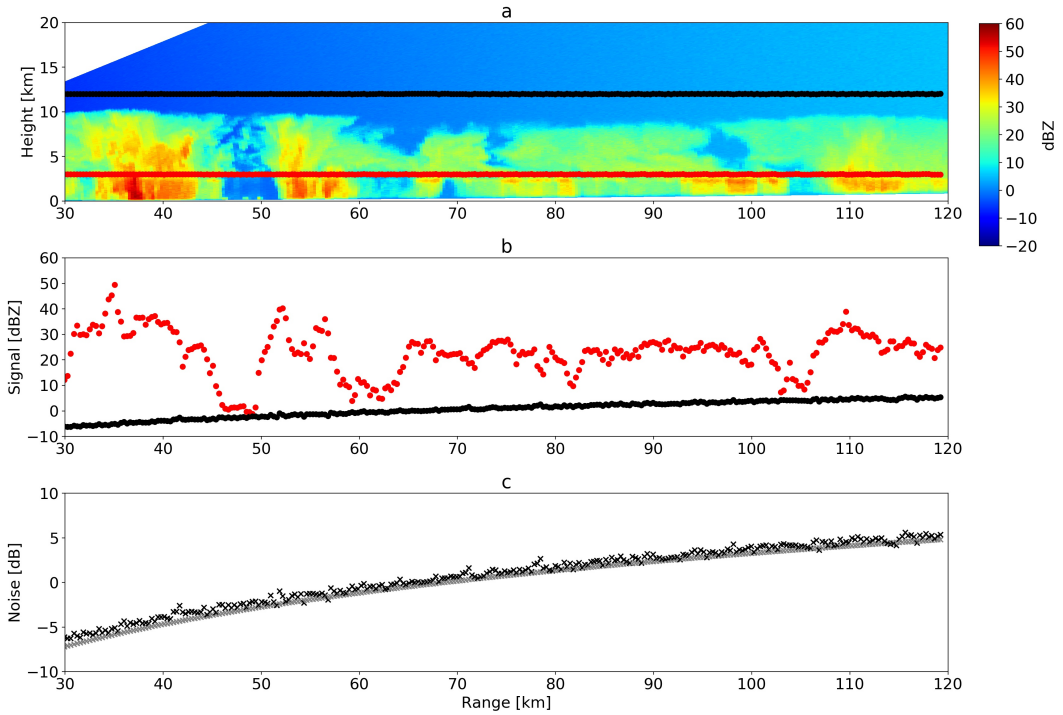

Figure 4.17: a) Example of reflectivity, b) transects of signal at 3 km height (red circles) and observed noise at 12 km height (black circles) in log units of dBZ and c) observed noise at 12 km height (black crosses) and estimated noise using equation 4.5 (grey crosses) in log units. Data from 25th August 2012 at 12:31.

Zrnic, 1984):

$$var(\hat{v}) = \lambda^2[32\pi^2 T_s^2 \rho^2(T_s)]^{-1}\{M^{-2}[1-\rho^2(T_s)] \sum_{m=-(M-1)}^{M-1} \rho^2(mT)(M-|m|) + N^2/MS^2 + (2N/MS)[1+\rho(2T_s)(1/M-1)\delta_{T-T_s,0}]\}, \quad (4.7)$$

where λ is the wavelength, T is the pulse pair separation, T_s is the spacing between pulses, ρ is the normalised signal correlation given by $\rho(mT_s) = exp[-8(\pi\sigma_v mT_s/\lambda)^2]$, σ_v is the spectrum width, σ_{vn} is the normalised spectrum width, N/S is the reciprocal of the SNR and M is the number of sample pairs. The variable m in $\rho(mT_s)$ is iterated between -M and +M solely in equation 4.7.

Equation 4.7 can be approximated when the sum can be replaced with an integral assuming a Gaussian spectrum (Doviak and Zrnic, 1984) and is given by equation

4.8 (DZ: 6.22a). Herein 'DZ: 6.22a', 'DZ: 6.22b' and 'DZ: 6.23' refer to the equation numbers used in (Doviak and Zrnic, 1984) where 'DZ' refers to *Doviak and Zrnic*.

$$var(\hat{v}) \approx \lambda^2[32M\pi^2T_s^2\rho^2(T_s)]^{-1}[[1-\rho^2(T_s)]T_s/2\sigma_{vn}T\sqrt{\pi} + N^2/S^2 + (2N/S)[1-\rho(2T_s)\delta_{T-T_s,0}]. \quad (4.8)$$

Furthermore, when sample pairs are independent (DZ: 6.22b):

$$var(\hat{v}) \approx \lambda^2[32M\pi^2T_s^2\rho^2(T_s)]^{-1}[(1+\frac{N}{S})^2 - \rho^2(T_s)]/\rho^2(T_s). \quad (4.9)$$

For large SNR, contiguous pairs and a large number of sample pairs the uncertainty can be estimated by a simplified equation of $var(\hat{v})$ (Doviak and Zrnic, 1984) (DZ: 6.23):

$$var(\hat{v}) \approx \sigma_v\lambda/(8MT_s\sqrt{\pi}), \quad (4.10)$$

where σ_v, λ, M and T_s are as defined above. For CAMRa, with contiguous sample pairs $T_s = T = \frac{1}{610Hz}$, $\lambda = 9.75$ cm and M is given below as it varies by case.

Equations 4.8 (DZ: 6.22a), 4.9 (DZ: 6.22b) and 4.10 (DZ: 6.23) for SNR between -5 and 30 with increments of 5 are shown in Figure 4.18 for a range of spectrum width values. Values for the variables in the equations are defined by the specifications of CAMRa detailed in table 2.1 and using M = 64 as defined in the DYMECS and Gatwick cases. Figure 4.18 shows that the SNR must be at least 20 dB for equation 4.10 (DZ: 6.23) approximations to hold across the range of σ_v of 1 m s^{-1} to approximately 4 m s^{-1}. σ_v values exceeding 4 - 5 m s^{-1} are not common and a large portion of the σ_v distribution lies between 1 - 4 m s^{-1} for the data used in this thesis (not shown).

Given that equation 4.7 can be approximated due to a Gaussian spectrum, in regions of cloud where the SNR is less than 20 dB equation 4.8 (DZ: 6.22a) can be used to estimate $var(\hat{v})$. This implies that at each grid point SNR must be calculated to determine which form of equation to use. In regions with large SNR (SNR > 20 dB) and

for data with narrow spectrum widths and contiguous pulse pairs, equation 4.10 (DZ: 6.23) can be used to estimate $var(\hat{v})$. Given these assumptions are met for CAMRa and the data used in this thesis, there was no need to use the full $var(\hat{v})$ equation given by equation 4.7. The relevant equations to use stated above were determined by the SNR regime given that equation 4.8 accounts for noise in low SNR regions.

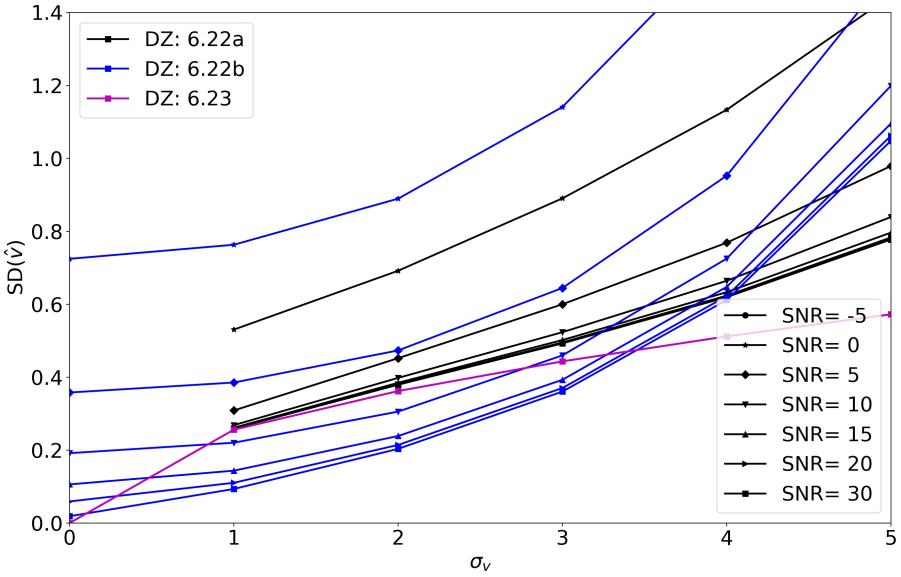

Figure 4.18: Comparison of $var(\hat{v})$ expressed as the standard deviation SD($\hat{v}$) as in Doviak and Zrnic (1984) for equations 4.8 (DZ: 6.22a) in solid black, 4.9 (DZ: 6.22b) in solid blue and 4.10 (DZ: 6.23) in solid purple. Spectrum width (σ_v) is shown on the x-axis. Values for CAMRa are used as detailed in table 2.1 with M = 64 (as in DYMECS and Gatwick). SNR in dB between -5 and 30 with an increment of 5 are used shown by the symbols in the legend.

Figure 4.19 shows (a) reflectivity, (b) SNR, (c) spectrum width (σ_v) and (d) $var(\hat{v})$ for the same scan in Figure 4.17(a) with the range extended to 120 km. Panel (c) shows the observed spectrum width that was used to calculate $var(\hat{v})$ in panel (d). This shows that regions of high spectrum width generally match with regions of high $var(\hat{v})$. In regions where SNR was greater than 20 dB, equation 4.10 (DZ: 6.23) was used and equation 4.8 (DZ: 6.22a) otherwise, as shown by the white contour in panel (d). The calculation of SNR and $var(\hat{v})$ was done at each grid point using M = 64 in the DYMECS and Gatwick cases and M = 128 for the 2019 case.

$var(\hat{v})$ is important to know combined with low SNR on the cloud edges indicating

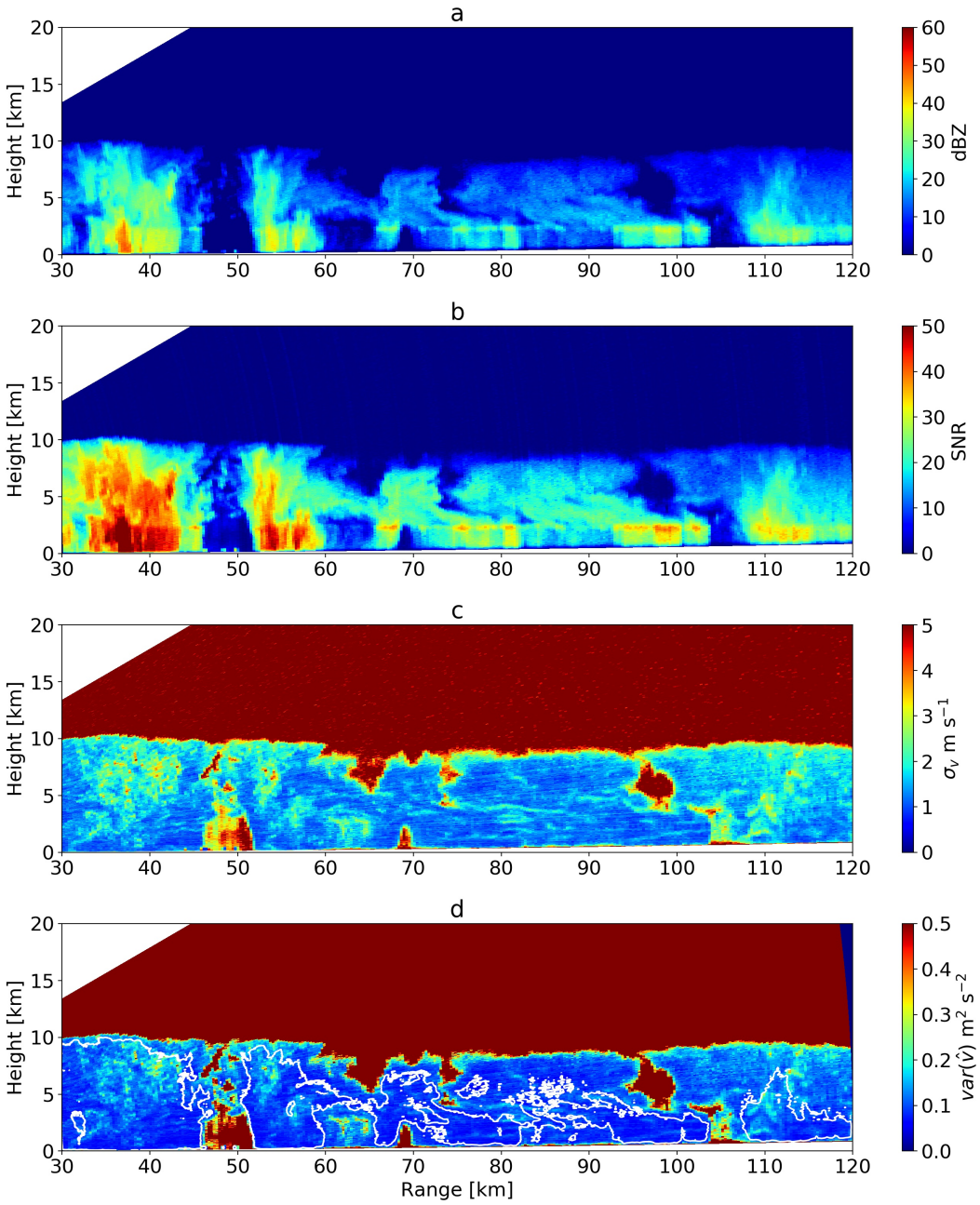

Figure 4.19: a) Example of reflectivity, b) SNR [dB], c) spectrum width (σ_v) and d) $var(\hat{v})$ for the same scan in Figure 4.17(a). Solid white contour in (d) is the SNR = 20 dB line.

that these regions are noisy. This type of scenario was investigated in the noisy thermal simulations in the previous section. Therefore it is expected that the retrieval algorithm may struggle in regions of very low SNR. Hence the requirement to estimate the uncertainty on the vertical velocity retrieval using information of SNR and uncertainty in the Doppler velocity measurement, this is discussed further below.

4.4.1 Finding the minimum cost function using Lagrange polynomials

Once the uncertainty in the Doppler velocity measurements has been estimated, this information can be used to determine the extent it may affect the vertical velocity retrieval. By fitting a Lagrange polynomial to the cost curve about the local minima, it is possible to use this to estimate uncertainty and to update vertical displacement estimates on coarse grids, if required. In this thesis the grid spacing is significantly fine enough that there was no need to update vertical displacement estimates using the Lagrange method. Therefore, the Lagrange polynomial was used for the sole purpose of estimating uncertainty on vertical velocity retrievals.

Suppose a set of vertical co-ordinate points at z_i with i = 1, 2, 3, cost function values C_i where C_2 is the local minimum. A degree 2 polynomial is fitted by

$$C(z) = \sum_i L_i(x) C_i, \tag{4.11}$$

where

$$L_i(x) = \prod_{j \neq i} \frac{z - z_j}{z_i - z_j} \tag{4.12}$$

The denominator above is constant so it is convenient to write

$$\sum_i \prod_{j \neq i} (z - z_j) w_i C_i, \tag{4.13}$$

where

$$w_i = (\prod_{j \neq i} (z_i - z_j))^{-1} \tag{4.14}$$

$C(z)$ can be differentiated to find the minimum

$$\frac{dC(z)}{dz} = 2z \sum_i w_i C_i - \sum_i \sum_{j \neq i} z_j w_i C_i, \tag{4.15}$$

at the minimum $z = z_m$, and $\frac{dC(z)}{dz} = 0$

$$2z_m \sum_i w_i C_i - \sum_i \sum_{j \neq i} z_j w_i C_i = 0 \Rightarrow z_m = \frac{\sum_i \sum_{j \neq i} z_j w_i C_i}{2 \sum_i w_i C_i}. \tag{4.16}$$

4.4.2 Uncertainty in determining the position of a minimum

Suppose each C_i has an uncertainty ϵ_i. For small δC_k, a Taylor expansion can be used to estimate z_m

$$z_m = z_m(\{C_k\}) + \sum_k \left. \frac{\partial z_m}{\partial C_k} \right|_{C_k} \delta C_k, \tag{4.17}$$

then the error in z_m is

$$\delta z_m \approx \sum_k \left. \frac{\partial z_m}{\partial C_k} \right|_{C_k} \delta C_k. \tag{4.18}$$

The partial derivative of z_m with respect to C_k is given by taking the derivative of equation 4.16

$$\frac{\partial z_m}{\partial C_k} = \frac{\sum_{j \neq k} z_j w_k}{2 \sum_i w_i C_i} - \frac{\sum_i \sum_{j \neq i} z_j w_i C_i}{(2 \sum_i w_i C_i)^2} 2 w_k = \frac{\sum_{j \neq k} z_j w_k}{2 \sum_i w_i C_i} - z_m \frac{w_k}{\sum_i w_i C_i}, \tag{4.19}$$

therefore

$$\delta z_m \approx \sum_k \left[\frac{\sum_{j \neq k} z_j w_k}{2 \sum_i w_i C_i} - z_m \frac{w_k}{\sum_i w_i C_i} \right] \delta C_k. \tag{4.20}$$

Note that $\sum_{j \neq k} z_m w_k = 2 z_m w_k$, thus

$$\delta z_m \approx \sum_k \left[\frac{\sum_{j \neq k} z_j^{'} w_k}{2 \sum_i w_i C_i} \right] \delta C_k, \tag{4.21}$$

where $z_j^{'} = z_j - z_m$. Assuming uncorrelated equal errors ($\langle (\epsilon_1 - \epsilon_3)^2 \rangle = 2 \langle \epsilon^2 \rangle$)

$$\langle \delta z_m^2 \rangle \approx \sum_k \left[\frac{\sum_{j \neq k} z_j^{'} w_k}{2 \sum_i w_i C_i} \right]^2 \langle \epsilon^2 \rangle = \sum_k \left[\sum_{j \neq k} z_j^{'} w_k \right]^2 \frac{\langle \epsilon^2 \rangle}{2 (C^* - C)^2}. \tag{4.22}$$

Equation 4.23 is reached from equation 4.22 assuming a symmetric cost curve (as shown by Figure 4.20) where $z_1 = -\Delta$, $z_2 = 0$ and $z_3 = \Delta$ with $w_1 = (2\Delta^2)^{-1}$, $w_2 = -(\Delta^2)^{-1}$ and $w_3 = (2\Delta^2) - 1$. With $C_1 = C_3 = C^*$ and $C_2 = C$. Then

$$\begin{aligned}\langle \delta z_m^2 \rangle &\approx \left\{ \left[\frac{\Delta}{2\Delta^2} \right]^2 + \left[-\frac{\Delta}{2\Delta^2} \right]^2 \right\} \frac{\langle \epsilon^2 \rangle}{\left[2(\frac{C^*}{2\Delta^2} - \frac{C}{\Delta^2} + \frac{C^*}{2\Delta^2}) \right]^2}, \\ &= \frac{1}{2\Delta^2} \frac{\langle \epsilon^2 \rangle}{\left[2(\frac{C^* - C}{\Delta^2}) \right]^2}, \\ &= \frac{1}{2} \frac{\langle \epsilon^2 \rangle \Delta^2}{[2(C^* - C)]^2},\end{aligned}$$

therefore

$$\sqrt{\langle \delta z_m^2 \rangle} = \frac{\sqrt{\langle \epsilon^2 \rangle} \Delta}{2\sqrt{2}(C^* - C)}. \tag{4.23}$$

This shows that the bigger the ratio of the peak of the cost curve $(C^* - C)$ to the uncertainty in the signal of Doppler velocity, where $\langle \epsilon^2 \rangle = var(v)$, the smaller the error in the location of the minimum cost.

The largest uncertainty in a cost minimum occurs when $(C^* - C)$ is as small as possible whilst being close enough to be on the quadratic curve, and the width of the cost curve (Δ) about the local minima is large. The following steps are followed to obtain Δ and $(C^* - C)$ and is illustrated in Figure 4.20 at each grid point:

1. Find the nearest local maxima either side of the local minima (if none found, find the first significant change in slope) by iterating away from the local minima. This yields the 3 points marked by the red stars in Figure 4.20.

2. Find the midpoints in z (height co-ordinate) between the minimum and the maxima, shown by blue circles in Figure 4.20.

3. Find the cost value C at these points. Then $\Delta = 0.5(\Delta z_1 + \Delta z_2)$ is calculated along with the corresponding $C^* - C = 0.5(\Delta C_1 + \Delta C_2)$.

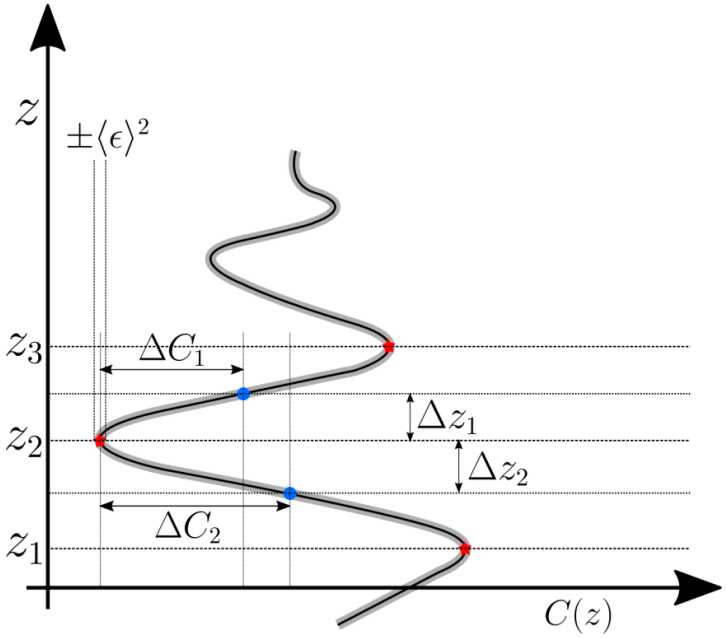

Figure 4.20: Idealised cost function (solid black), uncertainty $\pm\langle\epsilon\rangle^2$ (grey shading), local minimum and maxima (red stars) located at z_2, z_3 and z_1 respectively. Mid-points (blue circles) are distanced between local minimum and maxima by (ΔC_1, Δz_1) and (ΔC_2, Δz_2).

4.4.3 Example of vertical velocity uncertainty retrievals for a cloud from the DYMECS case

An example of the vertical velocity field and uncertainty in vertical velocity (δV_z) is shown in Figure 4.21. In this example and further examples (not shown) the vertical velocity uncertainty in the interior of the cloud was seen to be mostly $\leq$ 2 m s^{-1}. Larger vertical velocity uncertainties occur on the edges of the cloud and near cloud tops where SNR is low and $var(\hat{v})$ is high. Some larger vertical velocity uncertainties can also be seen within the cloud indicating uncertainty in the cost curve. Given these larger values are at the edges, they are not of concern for tracking thermals within the interior of clouds. Furthermore, vertical velocity was not retrieved to the cloud edge due to the search box size.

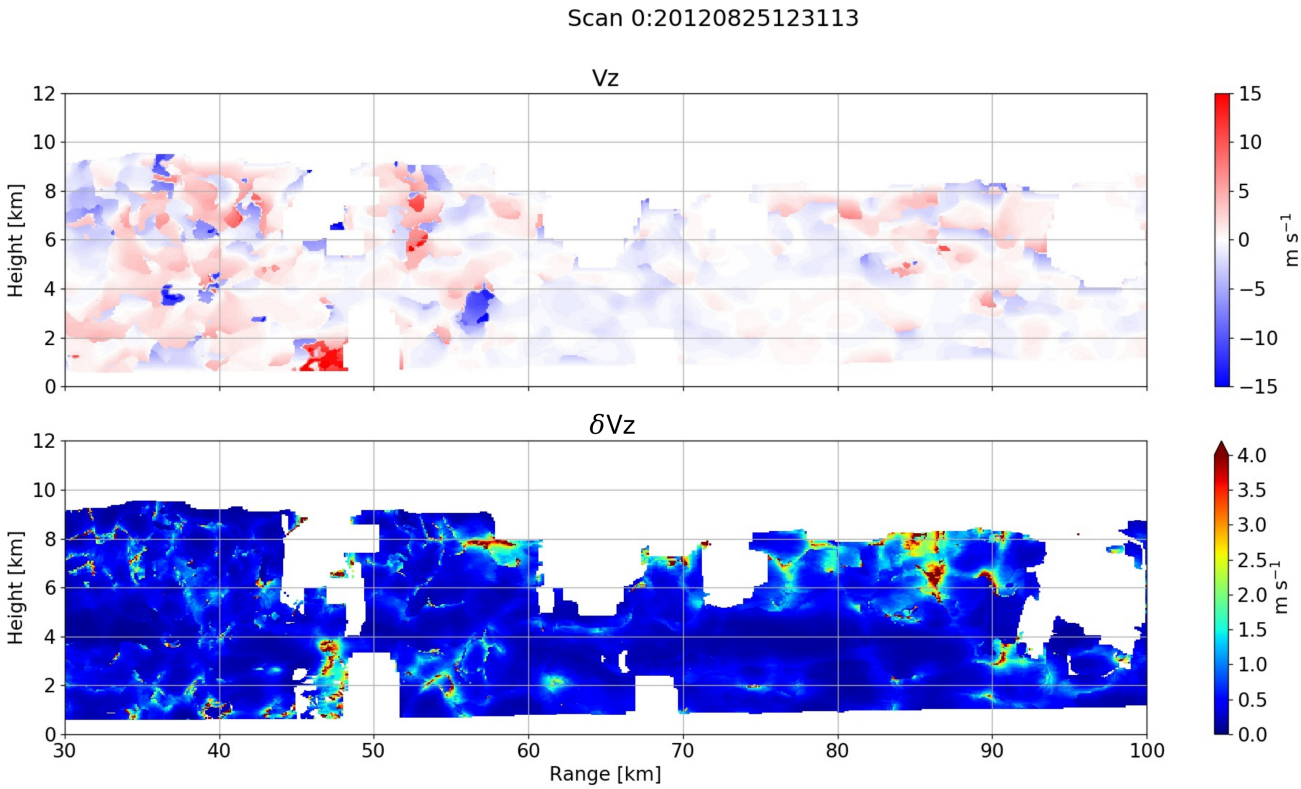

Figure 4.21: Example of vertical velocity (V_z) retrieval (top) and uncertainty on vertical velocity (δV_z) (bottom). Data from 25th August 2012 at 12:31.

4.4.4 Statistics of uncertainty on vertical velocity retrievals

The mean, median, 95th percentile and 99th percentile of estimated uncertainty (δV_z) and $var\hat{(}v)$ are shown in table 4.1 for the DYMECS and 2019 cases. Unfortunately spectrum width data was not available for the Gatwick cases. To be able to estimate uncertainty, the median value of $var(\hat{v})$ from the DYMECS case was used as a fixed value and δV_z was calculated using the cost curves at each grid point in the Gatwick cases. Due to using this fixed value, the uncertainty statistics are not shown in table 4.1. To asses whether the uncertainty in the Gatwick cases was similar to those in the DYMECS and 2019 cases, the statistics of the parameters used to calculate uncertainty are compared in table 4.2.

Table 4.2 shows that the statistics of $C^* - C$ for the DYMECS and Gatwick cases were very similar. The statistics for Δ were also similar but generally values were larger in the DYMECS case. Based on the statistics of the parameters used in the δV_z

calculation, uncertainties in the Gatwick cases most likely had similar statistics and therefore similar uncertainty on retrieved vertical velocity to those in the DYMECS case. The statistics of $C^* - C$ for the 2019 case were larger in value indicating more peaked cost curves. This may be due to the change in radar parameters such as the range gate resolution being finer than in the Gatwick and DYMECS cases or that features were more clearly identifiable in the 2019 case. The statistics of Δ for 2019 were similar to Gatwick and DYMECS cases, which may be due to the same beam width resolution which is fixed for CAMRa.

Table 4.1: Table of the mean, median, 95th percentile and 99th percentile $\hat{var(v)}$ and uncertainty on vertical velocity for the DYMECS and 24th Septemper 2019 cases.

Case	$\hat{var(v)}$ [m^2 s^{-2}]				Uncertainty [m s^{-1}]			
	Mean	Median	95th %ile	99th %ile	Mean	Median	90th %ile	95th %ile
DYMECS (25 August 2012)	0.11	0.09	0.15	0.21	1.56	0.65	1.86	2.82
24th September 2019	0.07	0.06	0.1	0.12	1.21	0.49	1.58	2.44

Uncertainty statistics for the DYMECS and 2019 cases show that the median uncertainty was less than 1 m s^{-1} and that the 95th percentile uncertainty was less than the 4 m s^{-1} vertical velocity threshold used to identify significant upwards motion, discussed in chapter 5. To compare, the $\hat{var(v)}$ statistics are different, mostly due to the change in pulse pairs between the DYMECS and 2019 cases. In the 2019 case, the higher number of pulse pairs allowed lower values of spectrum width to be measured, therefore impacting $\hat{var(v)}$.

Table 4.2: Table of the mean, median, 95th percentile and 99th percentile of $C^* - C$ and Δ for the Gatwick, DYMECS and 24th September 2019 cases.

Case	$C^* - C$ [m s^{-1}]				Δ [m]			
	Mean	Median	95th %ile	99th %ile	Mean	Median	90th %ile	95th %ile
Gatwick (28 July 2000)	0.68	0.54	1.4	1.79	398.05	375	637.5	750
DYMECS (25 August 2012)	0.66	0.52	1.37	1.7	463.48	400	825	1000
24th September 2019	1.24	0.88	2.68	3.68	515.25	475	875	1000

Figure 4.22 shows box plots of uncertainty for different vertical velocity intervals. Uncertainty was binned by vertical velocity into 2 m s^{-1} intervals between -20 and 20 m s^{-1} and a 6 m s^{-1} interval was used at velocities less than -20 m s^{-1} and greater than 20 m s^{-1} due to small sample sizes. This shows how the uncertainty statistics varied for different vertical velocity intervals. Figure 4.22 shows that generally the distribution of

uncertainties was less than 4 m s^{-1} up to vertical velocities greater than 14 m s^{-1}. The uncertainty tended to be larger for vertical velocities greater than 14 m s^{-1} as shown by the wider box plots. Due to the low samples numbers, vertical velocities greater than 14 m s^{-1} did not occur often in clouds observed used in this thesis and may not be consistent features in time so are not of concern for the object tracking applied at later stages.

Faster vertical velocities may occur in other cloud observations, for example long lived severe convection or supercells. If required the uncertainty can be used to identify these regions, but on average the uncertainty was low throughout a large range of vertical velocities. Most updraughts were occurring between vertical velocities greater than 0 m s^{-1} and less than 12 m s^{-1}, with significant updraughts mostly between 4 and 8 m s^{-1}. The upper whisker and 95th percentile in these velocity ranges was less than 4 m s^{-1} but can be up to 3 m s^{-1}. In cases where the uncertainty of vertical velocity is large such that is exceeds the 95th percentile, then updraught regions may not correctly be identified due to the uncertainty. On average the uncertainty was less than 1 m s^{-1} and the upper quartile was less than 2 m s^{-1}.

Similarly to Figure 4.22, box plots for the 24th September 2019 case are shown in Figure 4.23. Generally the 95th and 99th percentiles of uncertainty were lower than in the DYMECS case and the distribution of uncertainty for each vertical velocity range was similar, with a reduction in uncertainty for velocities greater than 14 m s^{-1}. Comparing the two cases the mean and quartiles for each velocity range were very similar, but notably the 95th percentile in the range of vertical motion of interest between 2 and 8 m s^{-1} was less than or equal to 2 m s^{-1}. In the 2 and 8 m s^{-1} vertical velocity range the uncertainty IQR and whiskers were tighter than in the DYMECS case with a mean uncertainty of around 1 m s^{-1}, indicating lower spread and convergence to lower uncertainty values. Therefore, uncertainty in the 24th September 2019 case was not substantially high and was small enough to not have a significant impact on updraught identification.

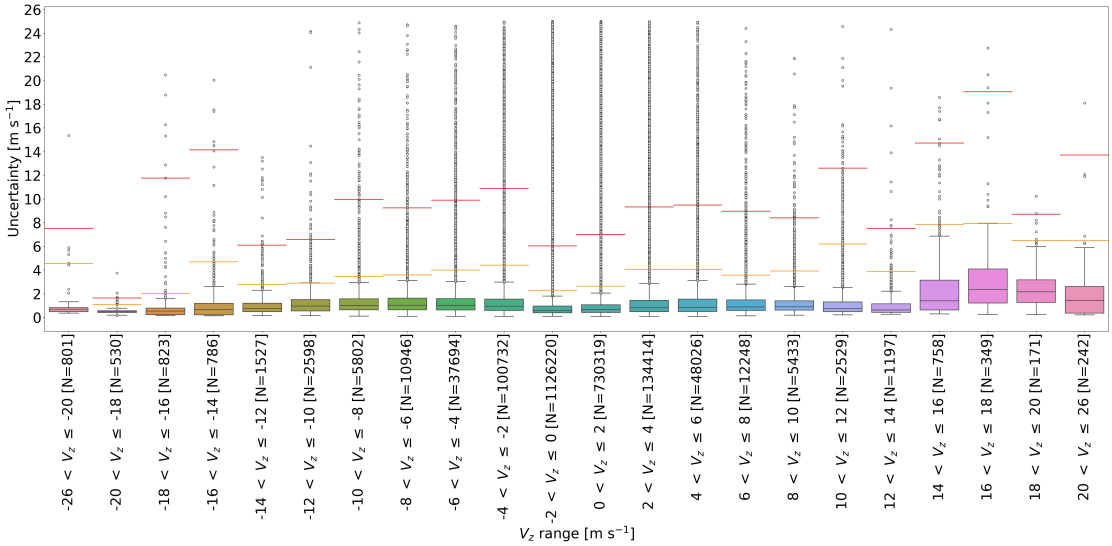

Figure 4.22: Box plots showing the uncertainty for multiple vertical velocity bins for the DYMECS case. Bin size between -20 and 20 m s^{-1} is 2 m s^{-1} intervals and bin size less than -20 m s^{-1} and greater than 20 m s^{-1} is 6 m s^{-1} due to sample size. Boxes show mean, 25th (Q_1) and 75th (Q_3) percentiles and the lower whisker is Q_1-1.5IQR and the upper whisker is Q_3+1.5IQR, where IQR is the interquartile range. Outliers are shown as grey circles. The 95th percentile is shown by orange lines and the 99th percentile is shown by red lines. N shows the number of grid points in each given range.

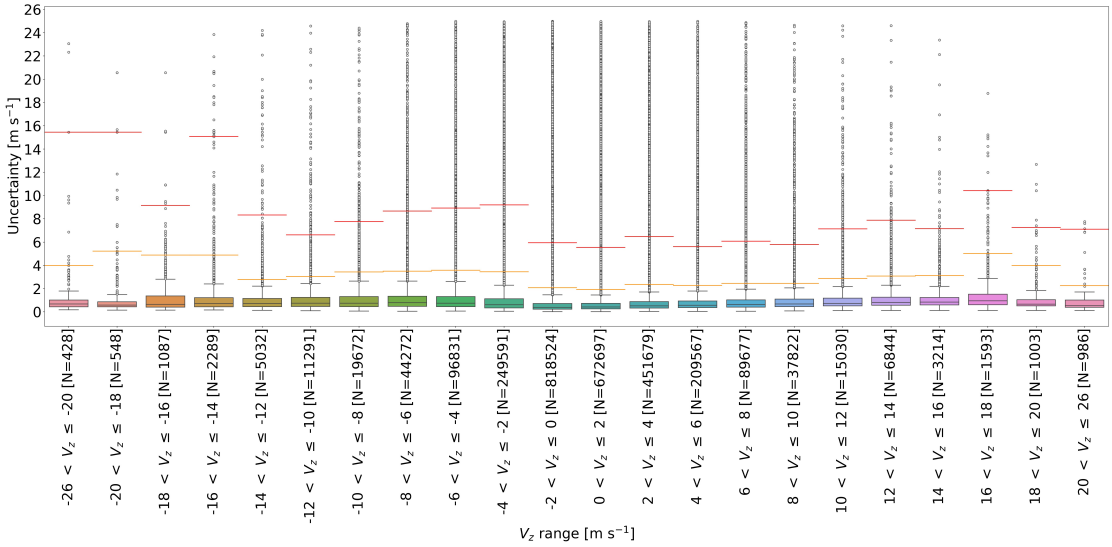

Figure 4.23: As in Figure 4.22 but for the 24th September 2019 case.

4.5 Summary

In this chapter a method was described for retrieving vertical velocity from pairs of radar scans taken using a vertical scanning strategy. The method determines where

air parcels are expected to have travelled horizontally in succeeding scans, calculates a cost function from a vertical search at each grid point between a pair of radar scans and then determines the optimal cost value. Vertical velocity can be estimated from the location of the optimal cost value and the time between scans. To determine if the cost function was a suitable method, the cost function and a correlation method were tested on ideal thermal objects in various scenarios. It was determined that the cost function performed best at identifying the correct displacement of idealised thermals in pairs of scans determined by cost curve structure, bias and RMSE.

A method for determining the uncertainty on vertical velocity retrievals was derived and tested. The uncertainty in the radar measurement due to signal-to-noise ratio and turbulence was found to be small when away from cloud edges. In all cases the statistics of vertical velocity uncertainty indicated that the uncertainty was not significantly larger than the updraught magnitudes of interest (vertical velocities greater than 4 m s^{-1}), given the upper quartiles of around 2 m s^{-1} and 95th percentiles of around 3 m s^{-1}. Across the range of updraught magnitudes of interest uncertainty was generally small (less than 1 m s^{-1}) on average, which is considered to be within an acceptable margin of error given strong updraughts will still be identified by thresholds with an average uncertainty of less than 1 m s^{-1}. Statistics of the parameters used to calculate uncertainty were also similar across cases, further indicating that uncertainty was similar and that confidence can be given to the method applied across a range of cases.

Chapter 5

Measuring properties of thermals in deep convection

5.1 Introduction

It is important to study the vertical velocity in convective clouds because different vertical velocity flow patterns can impact cloud dynamics and microphysics differently, such as thermals potentially transporting hydrometeors (Damiani *et al.*, 2006). Scorer and Ludlam (1953) suggested that thermals can transport heat upwards and that individual thermals can coagulate into larger thermals through the wakes of prior thermals. The toroidal circulation, vortical circulations in three-dimensions such as those associated with a ring vortex, that is associated with thermal flow can entrain air and therefore thermals can impact entrainment in clouds (Blyth *et al.*, 1988).

Moser and Lasher-Trapp (2017) used numerical simulations to study entrainment of successive thermals in cumulus congestus and also found that successive thermals can modify spatial charge distributions. In growing tropical congestus clouds Sherwood *et al.* (2013) simulated successive thermals to suggest the 'slippery' thermal hypothesis that drag forces acting on thermals are not important. High resolution simulations have showed that updraughts can develop as a succession of thermals (Varble *et al.*, 2014; Morrison *et al.*, 2020; Peters *et al.*, 2020), termed the thermal chain under certain conditions. Thermal flow patterns are different from that of a coherent vertical plume of air. Therefore, updraughts occurring as successive thermals or as pulses of growth could impact cloud development and transport of particles in clouds.

Some observations of shallow cumulus clouds have shown that they evolve through a series of pulses or ascending thermals. French *et al.* (1999) used a ground based radar

and an airborne 95 GHz Doppler radar to observe multiple thermals producing pulsating growth in cumulus clouds (cloud tops below 3 km) in Florida, defining thermals as a pulsation of reflectivity echo that ascended, causing growth in echo top height. The authors defined a reflectivity flux by multiplying the vertical velocity with the reflectivity factor. They found that near levels of maximum reflectivity flux, there was a strong correlation between vertical velocity and reflectivity factor. This indicated that high reflectivity factors are co-located with updraught cores. Vertical cross-sections of reflectively showed multiple growth pulses of reflectivity ascending over a clouds lifetime. As individual thermals ascended further, the correlation between vertical velocity and reflectivity factor decreased (French *et al.*, 1999). These pulses lasted about 10 - 15 minutes and only one was present at a time. During the growth phase the strongest reflectivity was in the updraught due to scattering by cloud droplets. During the decay phase high reflectivity factor was found in the downdraught, likely due to larger drops. These clouds were non-precipitating, except for one where drizzle was noted during later aircraft penetrations.

Battan (1975) observed a severe hailstorm with a vertically pointing X-band (3 cm) Doppler radar. Updraught velocity was estimated using a relationship between the mean Doppler velocity in still air which yields the same reflectivity as observed and the observed mean Doppler velocity. Time-height plots showed updraughts in excess of 18 m s^{-1}, assuming hydrometeors were raindrops, and that updraughts occurred mostly in the upper parts of the thunderstorm. A pattern of updraughts was observed to resemble rising plumes of bubbles, with regions of slowly sinking air between them. Battan (1975) also found that inside updraught cores the Doppler variance was small, but outside updraught cores it was large. Updraughts were not laminar but composed of several large eddies with diameters 1 - 2 km. Battan (1975) speculated that rapid hail growth could occur within volumes of rising air and that successive passages through series of ascending volumes could account for the growth of large hailstones.

As discussed in chapter 1, a characteristic of a thermal is its toroidal circulation which was observed in early laboratory experiments. To further investigate thermals in convective clouds, Damiani *et al.* (2006) used the toroidal circulation property of

thermals to track them. The toroidal circulation is a better signal than reflectivity to attempt to observe given this circulation is a unique flow pattern, which can be seen in velocity and vorticity fields from numerical simulations and in velocity fields from dual Doppler radar observations. Examples of such patterns in laboratory, numerical simulations and observations were presented in chapter 1.

Damiani *et al.* (2006) used a 95 GHz dual-Doppler radar mounted on the King Air aircraft. Transects were taken through newly developing cloud turrets to measure velocities with cloud bases ≈5 km above mean sea level and depths of 2 - 3 km. Antennas were pointed sideways, side-forward, down-forward, upward and downward. The dual side and dual down layout allowed the retrieval of 2D velocities in the horizontal. Vertically pointing antennas allowed the vertical velocity to be retrieved. A significant number of studies have focused on shallow or growing convection up to the congestus stage with clouds depths between 2 - 5 km, hence the use of aircraft combined with radar to observe the clouds. Observations of thermals in shallow convection and cumulus congestus using high resolution cloud radar successfully derived thermal characteristics for short lived cumulus clouds. Observations of precipitating deep convection reaching the tropopause, with low cloud bases using ground based radar have suggested thermals are present in such clouds (Yuter and Houze, 1995; Hogan *et al.*, 2008) and that updraughts evolve through a series of pulses. Whilst limited in number, Yuter and Houze (1995) and Hogan *et al.* (2008) suggested that updraughts were developing as pulses.

Observations of thermals in shallow cumulus and cumulus congestus have shown thermal mean vertical velocity to be 5 m s^{-1}, have a 2 km ascent distance and with average diameters between 500 m - 1 km (Damiani *et al.*, 2006). Both Damiani *et al.* (2006) and French *et al.* (1999) found 2 - 3 thermal events per cloud, lasting around 2 - 15 minutes each. In the 41 cases of single and/or dual Doppler radar scans studied by Damiani *et al.* (2006), 24 of such cases supported thermals. In the cases that thermals were not identified, a clear pattern of toroidal circulation was not detected. This could be due to the radar sensitivity not being able to detect weaker thermal patterns exhibited in radar signals, attenuation in the cloud due to the short wavelength of

the cloud radar (95 GHz = 0.3 cm), clouds not supporting thermals at this stage of lifetime, or the aircraft penetrated a region of cloud that did not contain thermals.

Sherwood *et al.* (2013) used simulations of convective clouds growing in a typical tropical environment. They found origin heights of thermals to be around 2 - 3 km, with rising rates of 4 - 5 m s^{-1}, lifetimes of 8 - 10 minutes and reaching heights of 4.5 - 5.5 km. Simulations showed thermal flow features eventually occurring in the upper troposphere and dominating the lower levels. Thermals showed little net mass growth with height, maintaining a characteristic scale of about 2 km. Idealised simulations of convection driven by surface fluxes by Hernandez-Deckers and Sherwood (2016) showed thermals to be slightly elongated downwards with peak vertical velocity just above the centre, assuming a spherical shape. The elongated shape was largest at the beginning of thermals lifetime then decreased. This was interpreted to be linked to the acceleration of the thermal. Characteristics derived from these simulations found that ascent rate was between 2 - 4 m s^{-1} with an average life of 4 - 5 minutes. Thermals travelled on average 500 - 700 m vertically and had radii between 250 m - 1.1 km. They began their ascent at heights between 3.2 - 5.3 km, which then decreased after previous thermals had risen and convection deepened. Net entrainment calculations found that thermals had little net entrainment or detrainment thus stayed approximately the same size through their ascent.

Morrison *et al.* (2020) used an axis-symmetric model of updraughts and Peters *et al.* (2020) used the Cloud Model 1 (Bryan and Fritsch, 2002) to run idealised simulations of convection to investigate thermal-chain structures in updraughts. The authors note that they neglected the possible influence of the modification of the environment due to thermals, which may change the properties of the air of the succeeding thermals and that this could precondition the environment and promote later development of deep convection, the shallow to deep transition. This is due to vertical velocity detraining air and moistening the atmosphere.

Results presented in this chapter add to the the observations of updraughts developing as pulses or thermals in long lived precipitating deep convection extending in depth to the tropopause using a ground based scanning Doppler radar, allowing the

evolution of such features to be tracked in time from a fixed perspective. This measurement technique allows observations of thermal structures in deep convection over large temporal and spatial scales, not previously observed or possible to investigate in studies such as Yuter and Houze (1995), Damiani *et al.* (2006) and Hogan *et al.* (2008) with limitations discussed in chapter 1. Furthermore, this chapter adds estimates of thermal characteristics in observations of deep convection, not previously discussed in the literature. Thermals were tracked for a period of time, a large number for their entire lifetime duration, from which their genesis and termination was estimated as well as their size and speed. Given the many studies using numerical simulations to describe the behaviour and physics of thermals in clouds, observations of thermal characteristics could provide some validity to the characteristics of thermals in numerical models.

In this chapter estimates of thermal properties derived using Chilbolton radar observations from the Gatwick storm (Hogan *et al.*, 2008) and the DYMECS campaign (Stein *et al.*, 2015) are explored, including:

1. Number of thermals per cloud.
2. Distance travelled.
3. Location of origin and termination height.
4. Size of thermals.

5.2 Thermal identification and tracking

5.2.1 Existing methods applied to observations of shallow cumulus and numerical simulations

Tracking thermals in observations is difficult as it requires high resolution (≈100 m) and high frequency (≈2 minutes) measurements to capture the somewhat physically small and short lived pulses. There is a longer history of tracking thermals in model

simulations, including simulations of deep convection. This can inform thermal tracking practices for observations.

In shallow cumulus clouds thermal features have been tracked by identifying changes in maximum echo top height signals from cloud radar (French *et al.*, 1999). This is possible because the maximum height of the echo top signal increases over time when a cloud is growing vertically, leading to ascend of echo top height. This behaviour is not seen so clearly in deep convection with strong reflectivity cores. Deep convective clouds near the mature stage of cloud evolution that have strong reflectivity echoes at S-band and echo tops being somewhat stable in height do not exhibit the same echo top evolution seen in earlier growing phases. Observations of deep convection show that whilst there is significant dynamic development occurring in the internal of the cloud its echo top height generally remains stable. Therefore the effect of thermals on echo top height are not so visible or cause an increase in echo top height once a cloud is mature and has reached the tropopause, with a quiescent anvil cloud. On some occasions strong updraughts are observed to impact echo top height in deep convection, these occurrences are seen as overshooting tops, where the echo top height overshoots the tropopause.

Wind fields can be used from model simulations and observations to identify thermals and track them (Blyth *et al.*, 2005; Damiani *et al.*, 2006; Peters *et al.*, 2019) for example. This requires more than one wind component be present by using multiple radars or aircraft measurements for observations. From wind fields, vorticity can be calculated and used to identify and track thermals that have a toroidal circulation associated with them (Damiani and Vali, 2007).

Tracking algorithms that allow properties of thermals to be estimated were derived by Sherwood *et al.* (2013) and expanded upon by Hernandez-Deckers and Sherwood (2016). Sherwood *et al.* (2013) tracked the location of peak vertical velocity at each time step. A 60 s output time was used in model simulations. Coarse 2D runs had a 500 m horizontal grid spacing and fine 2D runs had a 125 m grid spacing. Coarse 3D runs had a 250 m horizontal grid spacing and fine 3D runs had a 250 m grid spacing. All simulations had a vertical grid spacing of 100 m. Peak vertical velocity points were

found to rise at approximately a constant rate, thus forward projection of the height of peak vertical velocity location was done using a linear estimate $z_{thermal}$ = Wt + b. The slope W provides the ascent rate, t is time and b is the origin height (z_0). Thermal radius was determined by expanding a volume around the maximum velocity until the average vertical velocity inside the enclosed volume matched the ascent rate W. This method yielded good results when applied to numerical simulations. An example of an identified thermal using this method is shown in Figure 5.1. Vorticity colouring shows the toroidal circulation associated with the identified thermal. The maximum updraught velocity is shown by the black 'x' and the centre of the thermal is shown by the red '+'. The thermal boundary, assumed to be a circle is shown by the black circle, enclosing the region deemed to be an identified thermal.

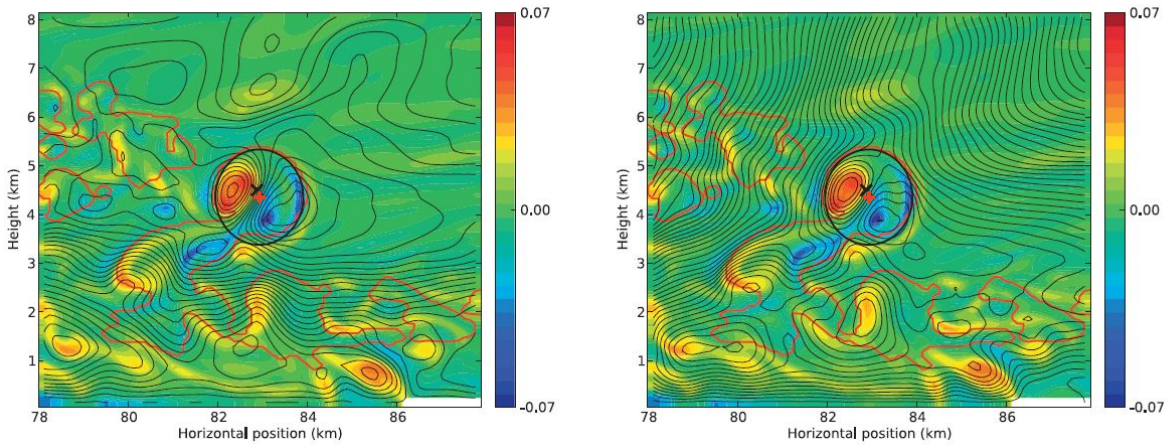

Figure 5.1: Snapshot of thermals from a high resolution simulation. Colour shows vorticity (s^{-1}), black contours show streamlines in reference from (a) fixed and (b) moving with the thermal. Black 'x' is the maximum vertical velocity and red '+' is the estimated centre of thermal. Thermal boundary is shown by black circle. Taken from Sherwood *et al.* (2013).

Hernandez-Deckers and Sherwood (2016) expanded on this method by also using pressure, temperature and water content fields. A vertical velocity threshold of 0.8 m s^{-1} and a 500 m minimum distance between objects was used. Clusters of local maxima were determined to be the same thermal. The next and previous local vertical velocity maxima (w_{max}) were estimated using the linear estimate from Sherwood *et al.* (2013), but in this method acceleration was taken into account by considering points that were ± 1.5dt(w_{max}) away, where dt is the output time (60 s). Model time steps for

the 3 models ran were significantly shorter than the output time, with two simulations having a time step of 0.5 s and one with a time step of 0.33 s.

Hernandez-Deckers and Sherwood (2016) used a 65 m grid length which was smaller than the model grid length used by Sherwood *et al.* (2013). w_{max} points were only clustered together if each w_{max} point had a corresponding point in the next and previous time steps, then only clusters with at least 3 points were retained. Thermal trajectories were then smoothed by fitting a second or third order polynomial. This method provided some improvements for tracking thermals than the Sherwood *et al.* (2013) method by allowing acceleration and velocity components to be estimated. An example of identified thermals (black circles) in the vertical velocity field from high resolution simulations using the Weather Research and Forecasting model (WRF) are shown in Figure 5.2. The total mass flux (ϕ) and thermal mass flux (ϕ_{th}) are shown on the right.

The toroidal circulation associated with thermals would provide an ideal way to track objects using this distinct circulation as a signature. Such a method can be applied when multiple measurements of Doppler velocity are made, such as in Damiani *et al.* (2006), allowing fine scale vortical structures to be clearly observed using each wind component. The range resolution used in Damiani *et al.* (2006) is significantly finer, between 30 - 45 m, than that of CAMRa at all ranges and the usage of multiple radars allowed observation of fine scale vortices. Even though the beamwidth of the radars was 0.5°, the maximum measurement range was 3 km, yielding a 26 m vertical resolution.

Such retrieval of fine scale vortices may not be possible with CAMRa due to the range resolution and beamwidth getting larger with range up to the order of hundreds of metres with observations between 30 and 120 km from the radar. With CAMRa, only the along beam velocity is observed and the vertical velocity is retrieved. Therefore the potential to measure any toroidal circulations is not possible, but vortical circulations could be observed in the along beam direction. These circulations may not be captured or may be distorted in deep convection by shear (Peters *et al.*, 2019). If a vortical circulation is aligned with the radar beam such that the flow from the top/bottom will have components towards and/or away from the radar and the retrieved vertical

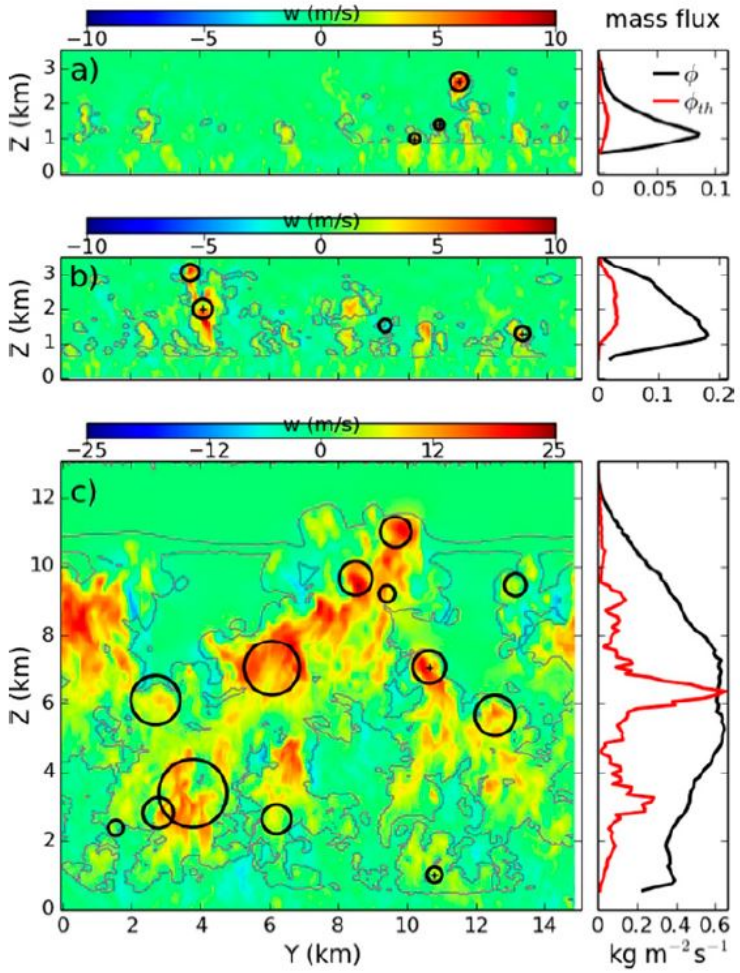

Figure 5.2: Snapshot of thermals identified in the vertical velocity field from high resolution model simulations. Cross-sections are along the Y axis at (a) X = 30, (b) X = 28.5 and (c) X= 25.6 km. Thermals are identified by black circle. (right) Total (ϕ; solid black line) and thermal (ϕ_{th}; solid red line) mass flux vertical profiles. Taken from Hernandez-Deckers and Sherwood (2016).

velocity is strongest in the stem or in the upward branch of the vortex, then a vortical circulation pattern may be seen.

The methods applied to numerical simulations by Sherwood *et al.* (2013) and Hernandez-Deckers and Sherwood (2016) yields good results with numerical fields. Due to noise in retrieved vertical velocity from observations, and as observed by eye the peak vertical velocity can fluctuate in space with increasing time difference between observations. Thus, these methods were not used in this thesis, but they inform certain choices of the thermal tracking presented in this chapter.

5.2.2 Method applied to Chilbolton radar observations

The uncertainty analysis and the tests of the algorithm for retrieving vertical velocity of idealised thermals have built confidence in its application to the radar observations. Due to the possibility of observing a toroidal circulation not being possible and observing vortical circulations along the beam being unknown but the fact that strong vertical velocity occurs in (1) updraughts and (2) the centre or near the top thermals as depicted by conceptual diagrams of thermals and in numerical simulations of thermals. Vertical velocity was used to define persistent ascending objects and a thermal object identification and tracking algorithm was applied.

The vertical velocity retrieval produces a field of displacement vectors interpreted as a flow velocity. Well-defined, persistent objects with substantial vertical velocity were of particular interest. A vertical velocity threshold of 4 m s^{-1} was applied to define objects. This velocity threshold was chosen given it is larger than the median and 95th percentile of vertical velocity uncertainty discussed in chapter 4. Furthermore, this threshold falls within the range of reported average velocities of thermals between 3 - 5 m s^{-1} (Damiani *et al.*, 2006; Sherwood *et al.*, 2013; Hernandez-Deckers and Sherwood, 2016) and that used by Peters *et al.* (2019) of 3 m s^{-1} to identify thermals in sheared and non-sheared environments.

Using a threshold will define a contiguous region of vertical velocity to track, in contrast to a peak or pixel as used by Sherwood *et al.* (2013). As discussed above, thermal objects are expected to be a contiguous 'blob' of vertical velocity ascending within a cloud. Such that, defining a vertical velocity threshold will define objects which can be tracked in consecutive vertical velocity retrievals. A minimum area threshold of at least 0.04 km^2 was applied. For the chosen grid resolution of 50 m x 100 m = 5000 m^2 (0.005 km^{-2}), objects are at least $\frac{0.04km^{-2}}{0.005km^{-2}} = 8$ grid points. This area threshold was based on minimum radii from previous studies. where reported radii of thermals were generally between 200 m to 1 km (Damiani *et al.*, 2006; Sherwood *et al.*, 2013; Hernandez-Deckers and Sherwood, 2016). An estimated minimum threshold is 0.12 km^2 (200 m radius assuming a circle), which would clearly be captured by the selected threshold of 0.04 km^2.

The search box used in this thesis and by Hogan *et al.* (2008) of 2 km width and 1 km depth also encompass the possible range of sizes of thermals. For an object to be identified it had to be present in at least 2 scans, which corresponds to a lifetime of at least 2 minutes. Identified objects were then tracked using the algorithm described in Stein *et al.* (2014). In summary, the algorithm compares distributions of area overlaps of objects between two times. An example of vertical velocity retrieval, upward motion shown in red and downwards motion shown in blue is shown in Figure 5.4(c) for 12:34, 12:35 and 12:37 on the 25th August 2012. Identified updraught pulses are indicated by letters and dashed black contours. Updraughts 'B', 'C', 'D' and 'E' were identified to be ascending in the cloud between 12:34 and 12:37 near the 30 dBZ (solid black) reflectivity contour and updraught 'E' ascended ahead of the 30 dBZ contour.

To more accurately determine lifetime and number of thermals it was useful to account for objects that split and merge. This allowed lifetime to be attached to the correct object and the correct number of objects to be counted. Furthermore, this provided extra information on object characteristics. Additional steps were taken to handle splitting and merging objects as shown in Figure 5.3a. Objects that underwent splits and/or mergers were identified as 'complex', otherwise were identified as 'simple'.

Object splitting was determined by checking if multiple objects identified at the current time step overlapped with an object from the previous time step, if so, this would indicate that the object had split in the intermediate time into multiple objects. Object merging was determined conversely to splitting, by checking if multiple objects at the previous time step overlapped with a single object at the current time step. Events were recorded as 'complex' and the contributing object labels were logged and tracked. Following Figure 5.3b, the 'path' of each object's interaction was tracked. A merging thermal ended at the merging event and began at the start of the parent thermal with the longest lifetime before the merge, shown by 'X' and 'S' respectively in Figure 5.3b. The parent thermal, that existed prior to merging had a longer lifetime and did not terminate at a merging event. A splitting thermal began at 'C' and ended at 'X', shown in Figure 5.3b. The lifetime of a splitting thermal was measured from the start of the parent thermal that the split occurred from ('S') to the split thermals

termination ('X'). A complex event led to multiple thermals, i.e. a complex split with one split, will count as 2 thermals, the child and the parent. This allowed the impact of a split or merge on lifetime to be taken into account (Plant, 2009).

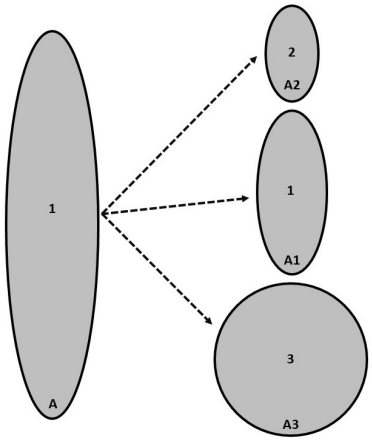

(a)

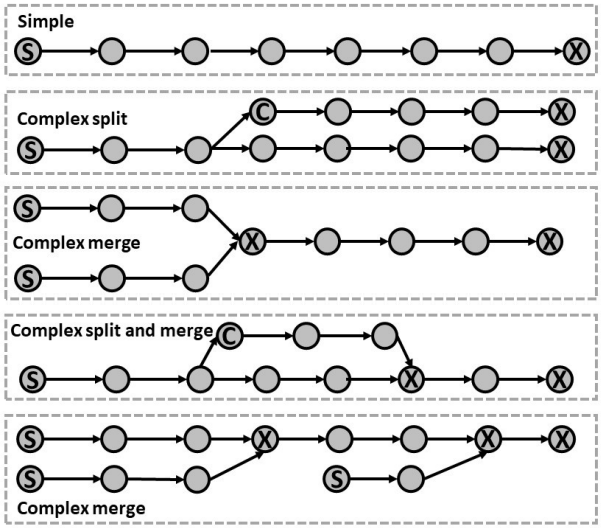

(b)

Figure 5.3: (a) Diagram showing a parent object (A) splitting into 3 child objects with assigned label numbers A1, A2 and A3. (b) Schematic showing examples of simple and complex objects that are dealt with by the labelling algorithm. 'S' marks the start of a parent object. 'C' marks the split of a child object and 'X' marks the end of an object. Merging objects end at the merge ('X') and start at their start ('S'). Splitting objects end at the end of the parent ('X') and start at the start of the parent ('S'). Complex events count as multiple thermals.

5.3 Lifetime of thermals

Thermal lifetime was estimated as the time difference between the first and last radar scan in which it was observed. If a thermal was detected in the first scan it may have existed before scanning started and if a thermal was present in the last scan it may have continued to exist after the last scan, therefore having an incomplete lifetime. There were a total of 32 complete thermals and 18 incomplete thermals identified out of a total of 50. Incomplete thermals are included in the subsequent analyses.

Figure 5.5(a) shows that there were more simple (red) thermals identified than complex thermals (blue). 34 out of 40 simple thermals had lifetimes less than 5 minutes.

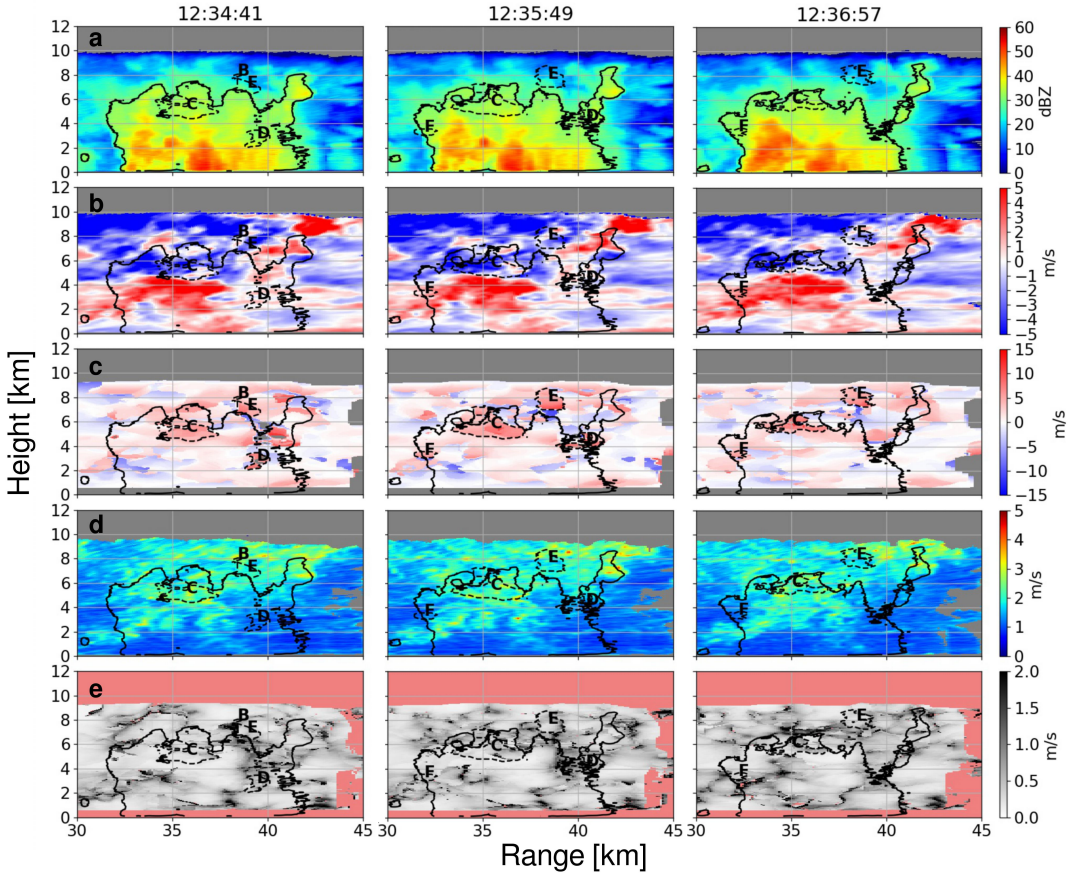

Figure 5.4: (a) Reflectivity, (b) horizontal velocity with mean velocity subtracted (red = away from radar), (c) vertical velocity, (d) spectrum width and (e) uncertainty in vertical velocity. Thermal median height indicated by label letter and object outline in dashed black. 30 dBZ contour in solid black. Example of a sequence of scans for 12:34 (first column), 12:35 (second column) and 12:37 (third column) from the DYMECS campaign on 25th August 2012. Restricted to 30-45 km range on the x-axis. Height is on the y-axis. Missing uncertainty values indicated by pale pink and missing values in panels (a)-(d) indicated by grey.

There were 6 simple thermals that lasted between 5 and 10 minutes. Complex thermal lifetimes were relatively uniformly distributed between 2 and 9 minutes.

The mean lifetime of all thermals was 3.8 minutes with a standard deviation of 2.2 minutes, although the minimum observable lifetime was 2 minutes and the shorter lifetime includes incomplete observations. There did not seem to be clear evidence of difference in lifetimes between simple and complex thermals. The large number of short lived simple thermals was likely due to sampling bias, incomplete observations and if a thermal was observed only twice, it cannot be complex by definition.

These lifetimes were within the range of reported lifetimes from observations and numerical simulations in the literature, which are on the order of minutes and up to 15 minutes (Blyth *et al.*, 2005; Sherwood *et al.*, 2013; Hernandez-Deckers and Sherwood, 2016; Moser and Lasher-Trapp, 2017). Peters *et al.* (2019) found thermals lasted on average 63 s and 72 s in non sheared and sheared model simulations respectively, which are notably different from prior literature.

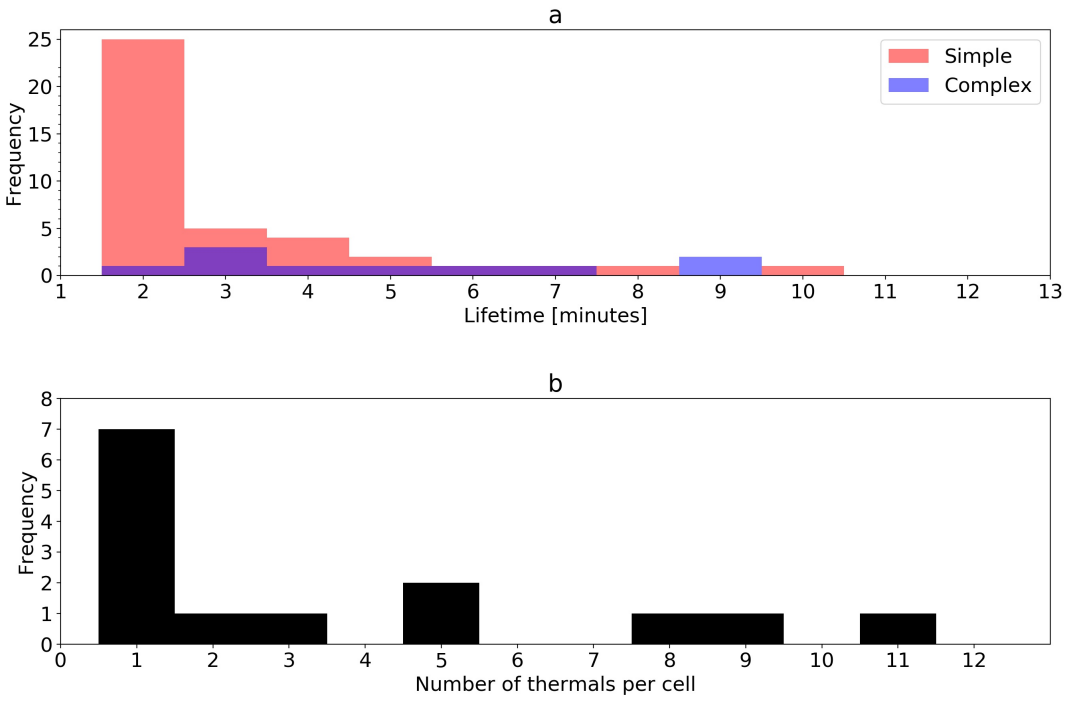

Figure 5.5: (a) Distribution of lifetime for simple (red) and complex (blue) thermals. (b) Distribution of number of thermals per cell for both simple and complex thermals.

5.4 Number of thermals per cell

For this purpose, a cell was defined as being bound by the 30 dBZ contour, which corresponds well to areas of surface rainfall and distinct convective regions within clouds. It is in these regions that strong updraughts are expected to exist. For instance, Nicol *et al.* (2015) found a clear relationship between the width of the updraught and the width of the 20 dBZ contour. Thermals were counted as belonging to a cell if they

overlapped the 30 dBZ contour or were located above. This accounted for times that a thermal could have been be ascending ahead of the cell top (top of 30 dBZ contour) or on the edge of cells, thus was not be completely inside the cell but associated with it.

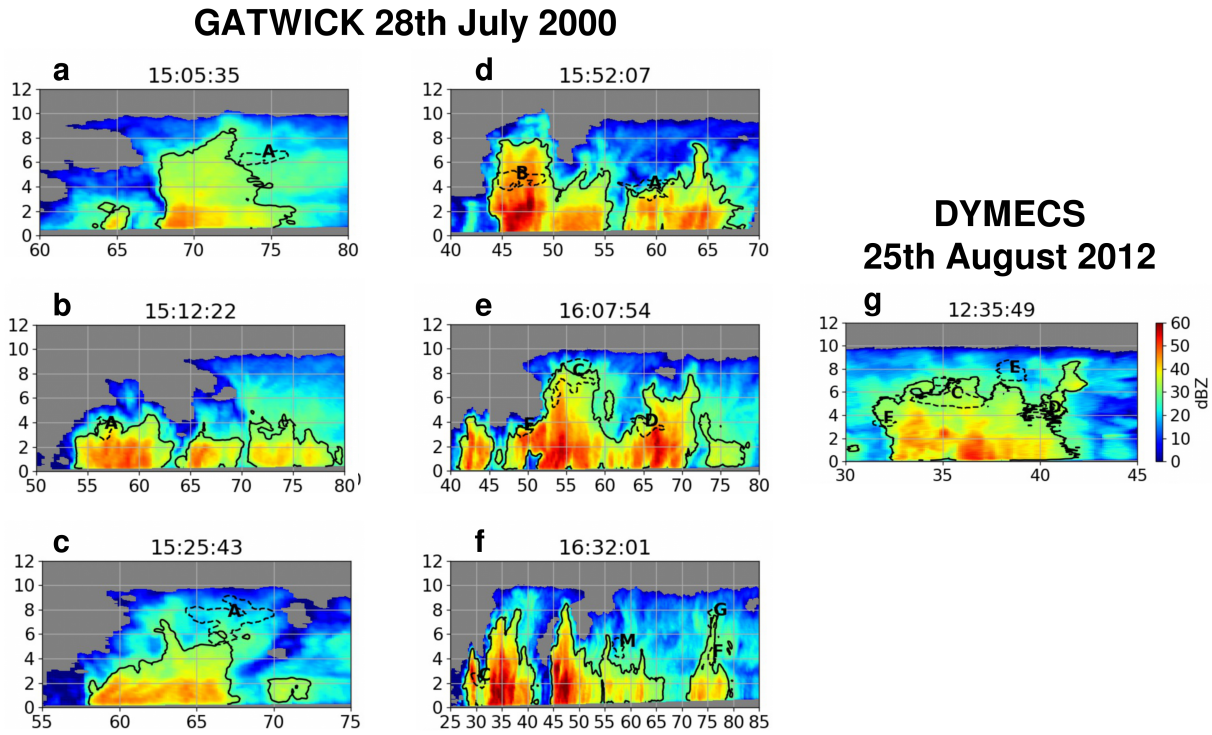

Figure 5.6: Examples of a single RHI scan with 30 dBZ contour in solid black, reflectivity and identified thermals shown by letters and dashed contour for scans within the scan times for each case shown in table 2.2. For the Gatwick cases on 28 July 2000 examples from (a) 15:05 in the 15:02-15:06 scans, (b) 15:12 in the 15:09-15:15 scans, (c) 15:25 in the 15:19-15:31 scans, (d) 15:52 in the 15:47-16:00, (e) 16:07 in the 16:05-16:17 scans, (f) 16:32 in the 16:23-16:51 scans and for the DYMECS case on 25 August 2012 (g) 12:35 in the 12:31-12:48 scans. Grey shading indicates no data. Height is on the y-axis and range on the x-axis.

Figure 5.6 shows examples of single RHI scans for selected scan times within the scan windows detailed in table 2.2. These panels show the clouds reflectivity with the 30 dBZ contour shown in solid black used to identify convective cells as described above. Identified thermals are shown by the given letters and dashed contours defining the outline. These examples show that clouds with multiple cells existed and each cell was in a different stage of life cycle. Examples of multiple cells can be seen in Figure

5.6(b), (d), (e) and (f). Within each cell and in some cases on the edges and above identified cells there were single or multiple thermals identified. In these examples some cells were decaying, some were reaching the mature stage and some were growing with high reflectivity ascending in the cloud. As cells grew, the thermals identified were observed ascending ahead of the 30 dBZ contour on multiple occasions. Animations of this process were produced but are not shown. For example in Figure 5.6(a) thermal A, in (b) thermal A, in (d) thermal A, in (e) thermal C, in (f) thermal M in one cell and thermals G and F in another cell and in (g) thermals C and E. On some occasions the thermals were located on the edges as the cells grew and in some cells the thermals were located within and above a stronger region of reflectivity such as shown in Figure 5.6(d) thermal B and in (e) thermal D.

Figure 5.5(b) details the number of thermals observed per cell for the duration that the cell was scanned. There was a tendency for a lower number of thermals per cell but in longer observed cloud systems with multiple cells, as shown in table 2.2, there tended to be more thermals per cell during the observation period. Due to the vertical velocity thresholds, slower thermals would not have been captured in these results. Nevertheless, the focus remained on strong vertical motion in convective cells.

Of the 50 thermals identified, there were 8 splits and 2 mergers that contributed to the complex object classification. This indicated that splitting was more common than merging over a thermal's lifetime. The cells that had a total of 21 thermals when combined belonged to the 28th July 2000 16:23 case. The thermals from this storm had a total of 3 splits occurring. This storm had 4 cells identified and had longest scanning time lasting 28 minutes.

5.5 Height of origin and termination

The start (dots) and end (crosses) of identified thermals for 3 selected scan periods from the DYMECS (25th August 2012) and Gatwick (28th July 2000) campaigns are indicated by colours shown in Figure 5.8(b). The 16:05 and 16:23 cases from 28th July 2000 and the 25th August 2012 case with their identified cells are indicated in

the legend. These cases were chosen as they had the longest scanning times which increased the probability of capturing the origin and termination of thermals. The arrows point from the start height and start time identified after scanning started to the corresponding end height and end time for each thermal. Grey arrows correspond to thermals that were not completely observed, that is they could have existed before scanning started or scanning ended.

By splitting each case into its individual cells, the net displacement and time evolution of identified thermals can be analysed to determine if thermals originated at higher or lower heights as time progressed. Some thermals in Figure 5.8(b) originated higher than a preceding thermal. For example, 28th July 2000 16:23 cell F thermals mostly originated higher than previous thermals, but a small number originated lower. Cell L for the same scan period had thermals that originated lower. Cells C and D had similar numbers of thermals originating higher and lower. On the other hand, 28th July 2000 16:05 cell E and 12:31 25th August 2012 cell H had thermals that mostly originated lower than prior thermals.

Thermals in the 28th July 2000 cases originated lower than those in the 25th August 2012 case, most likely due to the lower level of free convection (LFC), estimated to be 600 m height from the atmospheric sounding. Table 5.1 lists the LFC, freezing level and equilibrium level (EL) for the DYMECS and Gatwick cases and selected literature studies. In the 25th August 2012 case the LFC was estimated to be 1 km. Figure 5.8(b) shows that the 25th August 2012 origin heights were above 1 km height, and in the 28 July 2000 case there were some thermals with origin heights less than 1 km height. In both cases, thermals terminated before the EL, estimated to be 9 km height on 25th August 2012 and 9.5 km height on 28th July 2000. The freezing level was similar in both cases estimated to be 2 km height from the bright band seen in radar reflectivity. A majority of thermals existed above the freezing level in both cases, but in the 28th July 2000 clouds, 9 thermals existed below the freezing level from multiple clouds and cells.

In simulations of shallow stage, congestus stage and deep stage convection by Hernandez-Deckers and Sherwood (2016), most thermals were found to have originated

below 3 - 4 km height. As convection matured, thermals originated at higher heights as clouds grew. Succeeding thermals always originated at heights that were higher than the prior thermals, suggesting this mechanism is what causes convection to deepen, not the thermals travelling higher. Thermals were identified at all heights regardless of freezing level, but terminated lower than the EL and the maximum number originated between 1 km and 2 km height.

In shallow and congestus cumulus clouds, thermals were found to originate between 2 - 5 km height (Blyth *et al.*, 2005; Sherwood *et al.*, 2013; Moser and Lasher-Trapp, 2017). In these studies thermals originated above the LFC and the freezing level did not appear to have an impact on thermal location. Thermals ascended to near the EL and the highest freezing level was in Sherwood *et al.* (2013) where peak vertical velocities were found between 5-6 km height compared to the 7 km freezing level. Thermals were observed at various heights in clouds with depths of 3 km and bases near 5 km mean sea level (Damiani *et al.*, 2006). This indicated that thermals can be located at various heights in clouds independent of basic thermodynamic properties seen in atmospheric soundings.

Similar results were found in observations of thermals discussed in this section, suggesting that thermals can originate near cloud base and ascend but could also originate in the mid-levels and ascend. There are two possibilities for mid-level origin heights, firstly thermals do not originate in the mid-levels and this is a threshold effect which is a known caveat of this work. This means that they could have existed prior to reaching 4 m s^{-1} vertical velocity and could have originated lower in clouds, and once they had ascended somewhat, met the 4 m s^{-1} vertical velocity threshold to be identified at their (origin) height discussed in this section. Although this could occur, the focus of this work was on tracking significant vertical motion, hence the higher vertical velocity threshold. Secondly, thermals acquired additional buoyancy due to the freezing of liquid water and the release of latent heat. Further observations of in-cloud thermodynamics are required to investigate sources of buoyancy in different regions of clouds.

Figure 5.8(a) shows a distribution of net vertical displacement for all identified

Table 5.1: Level of free convection (LFC), freezing level and equilibrium level (EL) for the DYMECS and Gatwick cases and examples from selected literature studies.

Case	LFC	Freezing Level	EL
Gatwick (28th July 2000)	600 m	2.3 km	9.5 km
DYMECS (25th August 2012)	1 km	2 km	9 km
Hernandez-Deckers and Sherwood (2016)	1 km	4.8 km	12 km
Blyth *et al.* (2005)	650 m	5 km	11.5 km
Sherwood *et al.* (2013)	380 m	7 km	14.5 km
Moser and Lasher-Trapp (2017)	1.5 km	2.5 km	5 km
Damiani *et al.* (2006)	5.1 km	4.9 km	7.1 km

thermals. This was calculated by taking the difference between the height at the end of tracking and the height at the start of tracking. Most thermals had net vertical displacement equal to or less than 1.5 km. The largest displacements were between 3 km and 4 km, each by an individual thermal respectively. Thermals that had smaller displacements corresponded to the short lifetimes of the detected thermals which also tended to have lower vertical velocity. Most short lived thermals did not persist long enough to ascend large depths.

5.6 Size of thermals

Previous research from observations and numerical simulations has suggested thermals can have a range of physical sizes on the order of hundreds of metres up to 1 - 2 kilometres. Sherwood *et al.* (2013) and Hernandez-Deckers and Sherwood (2016) both determined size by fitting a sphere to a thermal object which was identified by maximum vertical velocity. The sphere was fitted by finding the radius that the average vertical velocity of the enclosed volume matched the previously estimated vertical velocity at each model output time. Romps and Charn (2015) tracked ascending cloudy regions that were connected in time. Then a stream function was calculated by averaging $\rho(w - w_{top})$ azimuthally around an axis through cloud top, where w_{top} was the vertical velocity of the cloud top and w was the vertical velocity enclosed in the azimuthal average. The thermal boundary was defined where the streamline was zero.

Blyth *et al.* (2005) and Damiani *et al.* (2006) determined thermal size from transects of vertical velocity taken during flights, and Damiani *et al.* (2006) was able to use dual Doppler measurements to estimate vortex ring diameters. In this section the equivalent diameter of a thermal was estimated by calculating the diameter of a circle that has the same area as enclosed by a thermal. A thermal was identified using a vertical velocity threshold of 4 m s^{-1} and a minimum area of 0.04 km ^{2}. Similar to the studies discussed, this assumed a circular shape enclosed the region of interest.

Figure 5.7(a) shows a distribution of mean equivalent diameter over thermal lifetime. The distribution had higher frequency between diameters of 0.5 and 1.5 km. Comparing to results from Peters *et al.* (2019), which used a similar method to Hernandez-Deckers and Sherwood (2016) to determine size, used idealised numerical simulations in a sheared environment and found that thermal radii had the highest frequencies between 0.5 km and 2 km. Soundings for the DYMECS and Gatwick cases showed minimal vertical wind shear. In shallow and congestus cumulus clouds, thermals were found to have radii between 250 m to 1 km (Blyth *et al.*, 2005; Sherwood *et al.*, 2013; Hernandez-Deckers and Sherwood, 2016; Moser and Lasher-Trapp, 2017). Thermals observed in the DYMECS and Gatwick clouds with smaller equivalent diameters were associated with pulses of vertical velocity ascending in clouds. Larger equivalent diameters tended to be associated with contiguous vertical velocity features but did have smaller pulses embedded within them. Equivalent diameters indicated that there were shorter lived thermals in the clouds observed and that a smaller number of larger updraughts were detected. Results show that the thermals observed in this chapter had similar sizes to those previously studied in the literature with varying cloud depths and stages of cloud growth.

Figure 5.7(b) shows mean equivalent diameter vs thermal lifetime for simple (black circles) and complex (black circles) thermals. Thermals that lasted between 2 and 5 minutes tended to have mean equivalent diameters between 500 m and 2.5 km, shown by the clustering of points in the lower left quadrant of Figure 5.7(b). These were due to pulses of vertical velocity that had small diameters and were short lived, observed in animations of vertical velocity and thermal tracking (not shown). Lifetime and

mean equivalent diameter were correlated with Pearson correlation of 0.75 with a p-value $< 10^{-3}$ shown in Figure 5.7(b). Excluding complex thermals, the correlation of lifetime and mean equivalent diameter for simple thermals was 0.64 with a p-value $< 10^{-3}$. This decrease could indicate that complex thermals tended to have a more linear relationship between lifetime and their mean equivalent diameter. There was one point that did not lie close to the line of best fit, shown at 11 minutes lifetime, which had a mean equivalent diameter of 1.5 km over its lifetime. This thermal was associated with a growing convective cell in the 16:23 28th July 2000 case and was located above the 30 dBZ contour. Further longer scanning periods of growing and mature convection are required to determine if there is difference between thermals in growing and mature convective cells.

There was no distinct separation in diameters between simple and complex thermals, but most complex thermals tended to be larger as indicated by the 7 black crosses above the black dashed line in Figure 5.7. Both simple and complex thermals had a range of diameters both increasing with lifetime. More samples could highlight the size separation between tracked thermals and larger more contiguous updraught features in clouds, which could be useful to relate to different time scales of updraught evolution in convection.

Thermals that had the largest vertical displacements became larger in size over time and regions of vertical velocity that grew to larger sizes were associated with strong reflectivity cores spanning ≈10 km horizontally, reached heights of 10 km and had reflectivities upwards of 60 dBZ (not shown) Rather than remaining as a smaller region of ascent (a thermal) the features appeared to grow into a larger updraught region as it ascended before shrinking in size near echo top. Although, associated with these larger vertical velocity features were physically smaller pulses of higher vertical velocity, which could be identified by using a higher vertical velocity threshold. This may indicate that within the larger updraught structures observed there existed thermal pulses throughout its lifetime, suggested to be thermal chains by Morrison *et al.* (2020) and Peters *et al.* (2020). Overall, longer lived thermals, which reach a higher altitude, will grow larger and therefore have a larger mean diameter.

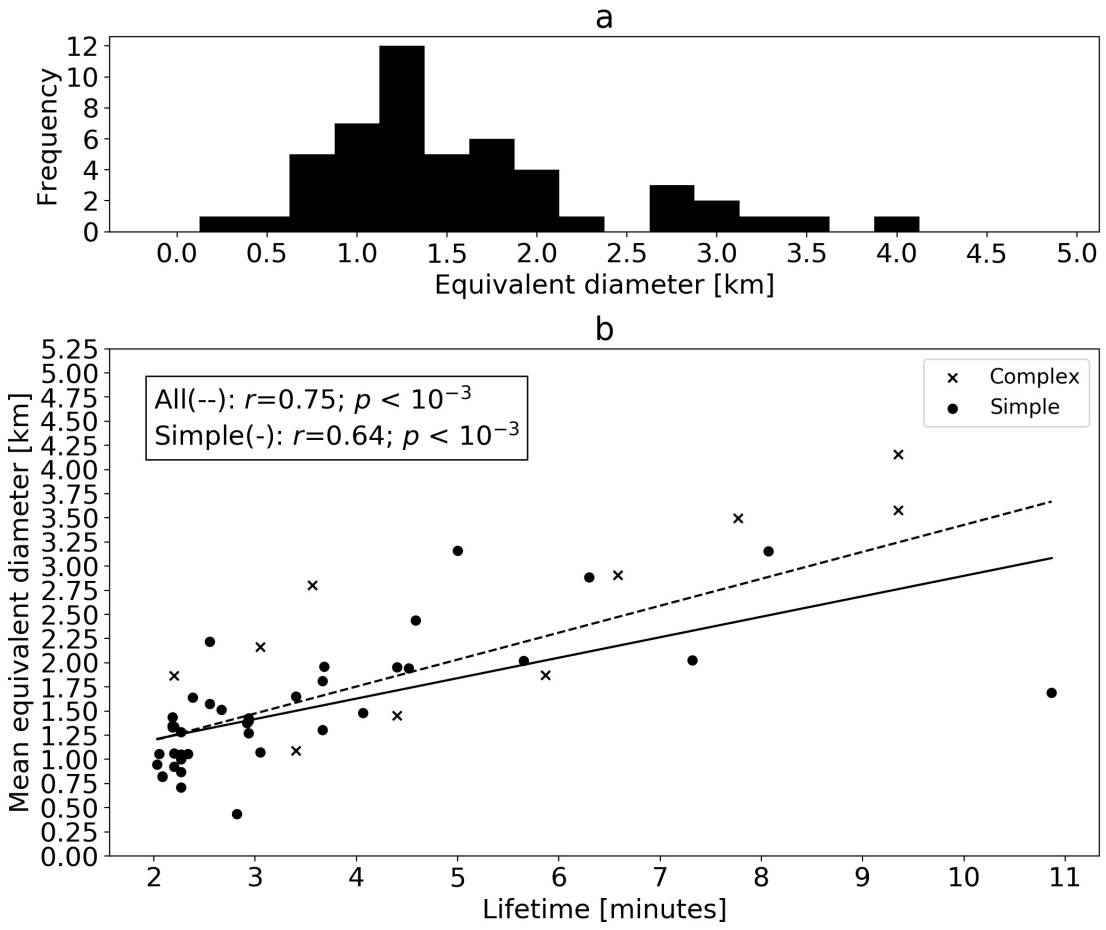

Figure 5.7: (a) Distribution of equivalent diameter in km, binned into 0.25 km bins. (b) Scatter plot of simple lifetime (black circles) and complex lifetime (black crosses) vs mean equivalent diameter over thermal lifetime. Lines of best fit for all (dashed black) and simple only (solid black) thermals.

Objects that had vertical displacements greater than 2 km tended to be larger than those that did not. They also tended to be associated with large and long-lived areas of high reflectivity. Objects that had smaller displacements, tended to be short-lived and ascended with developing reflectivity cores. This difference in size could point to a split between developing ascending cores and developed cores with larger regions of updraught.

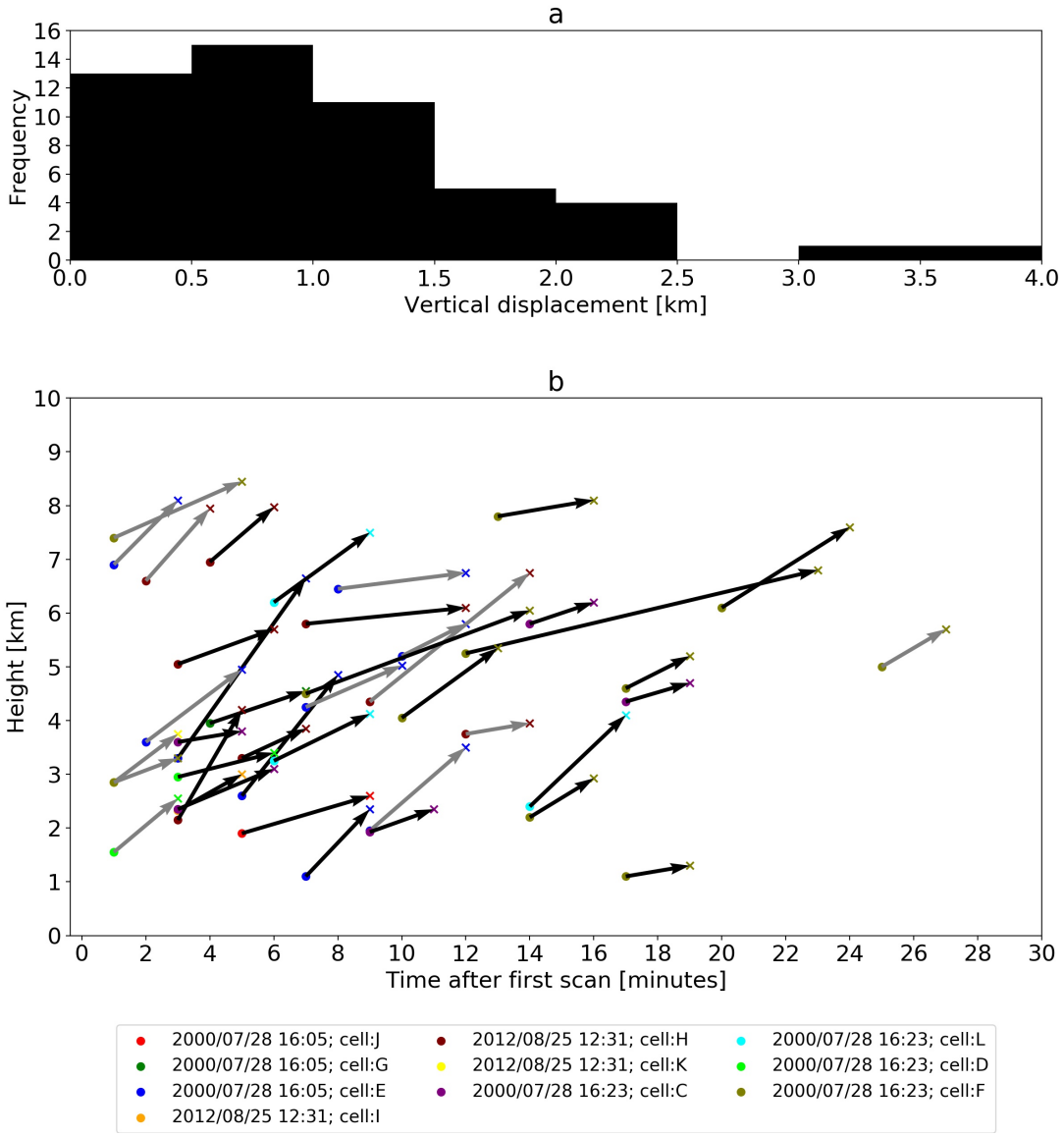

Figure 5.8: (a) Distribution of net vertical displacement of thermals over their lifetime. Binned by 0.5 km bins. (b) Initial thermal identification (dots) and end of thermal tracking (crosses) height and time for selected cases. Arrows point from start to end showing path in time and height. Cases and cells indicated by colour and are shown in the legend. Grey arrows indicate thermal may not have been observed for its true start or end.

5.7 Sensitivity to thresholds

To determine how sensitive the thermal identification and tracking was to the chosen thresholds, a sensitivity analysis was performed. Vertical velocity thresholds ranging

from 1 - 5 m s^{-1} with 1 m s^{-1} increments and area thresholds ranging from 0.04 - 2.04 km^2 with 0.08 km^2 increments were tested. As discussed above, these thresholds are similar to the radii and vertical velocity from the literature. Each combination of vertical velocity and area threshold was used to identify and track thermals to gain insight into how sensitive the number of identified thermals were to thresholds.

Figure 5.9 shows the total number of identified objects for each minimum area threshold and minimum vertical velocity threshold. The peak number of identified objects was at 3 m s^{-1} and between 0.04 and 0.44 km^{-2}, shown by the yellow in Figure 5.9. As the vertical velocity increased and decreased from 3 m s^{-1} and the area threshold increased the number of objects identified decreased, shown by the change from yellow to green colours in Figure 5.9. As the minimum area threshold increased fewer objects meet the required minimum area, indicating fewer large objects. There were more objects identified by going from 1 to 3 m s^{-1}, as large objects identified by 1 or 2 m s^{-1} thresholds were broken into multiple smaller objects at 3 m s^{-1}, i.e peaks of vertical velocity within larger vertical velocity regions. Then going from 3 to 5 m s^{-1} the number of objects decreased as the number of objects that met the larger vertical velocity criteria decreased. This pattern can be seen by the Gaussian shape of the total number of objects identified (green and yellow colours) in Figure 5.9. This shows that the most objects were identified at 3 m s^{-1} and met the small area threshold criteria, thus there were more 3 m s^{-1} vertical velocity regions across all clouds than there were with 5 m s^{-1} minimum vertical velocity.

At the fixed area threshold of 0.04 km^2 there was a increase of 20% in identified objects going from 4 m s^{-1} to 3 m s^{-1} vertical velocity threshold. Going from 5 m s^{-1} to 4 m s^{-1} there was an increase of 6% in identified objects. It can be seen in Figure 5.10b that as vertical velocity threshold increased up to 3 m s^{-1} the number of objects increased. Then the number of objects decreased from 3 to 5 m s^{-1} as there were fewer intense vertical velocity features. Figure 5.10a shows that as area threshold increased the number of objects identified generally decreased, but much less than a change in vertical velocity. This sensitivity analysis shows how the number of identified thermals changed due to the thresholds used. This indicates that most thermals in the clouds

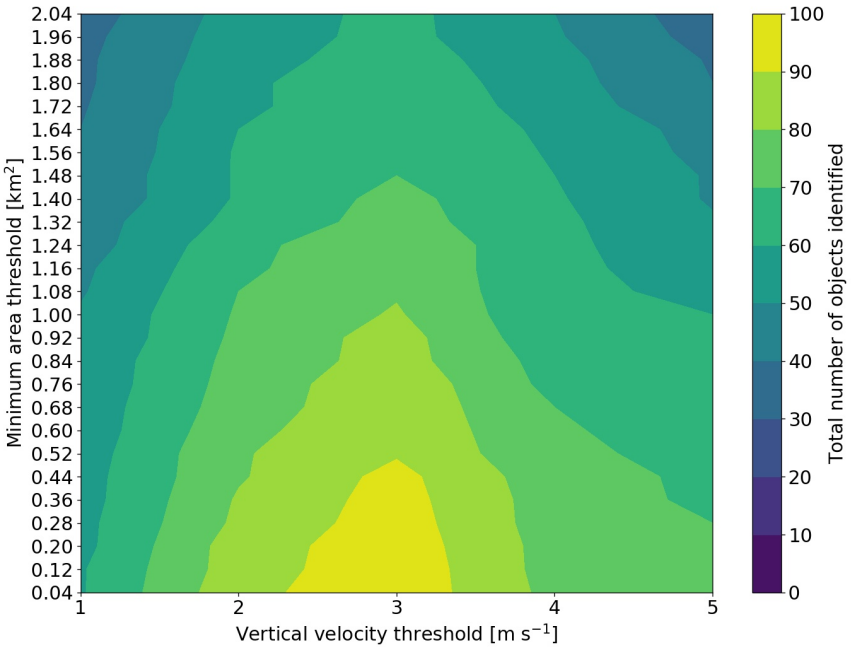

Figure 5.9: Total number of identified objects at each minimum area threshold and minimum vertical velocity thresholds.

observed had vertical velocities of 3 m s^{-1} and above. It does not indicate how the life time, sizes and origin height change based on different vertical velocity and area thresholds.

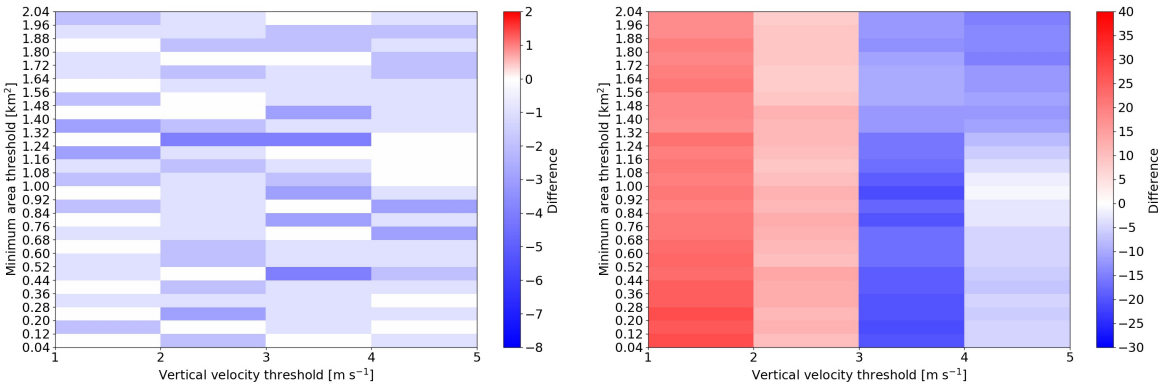

Figure 5.10: (a) Difference in thermal number between adjacent minimum area threshold bins, by taking the difference along the y-axis. (b) Difference in thermal number between minimum vertical velocity threshold bins, by taking the difference along the x-axis.

5.8 Summary

In this chapter some fundamental characteristics of thermals have been investigated in observations of deep convection. Thermals identified using scanning Doppler radar have shown that there were a small number per cell and 82% of total thermals lasted less than or equal to 5 minutes in lifetime. 60% of the total number of thermals had equivalent diameters less than or equal to 1.5 km, with the remainder reaching up to 4 km equivalent diameter. Mean equivalent diameter was shown to be correlated with lifetime indicating thermals that lived longer were larger. 80% of the total number of thermals had a net vertical displacement less than 1.5 km. In the observations presented in this chapter, there was no distinct signal in whether successive thermals originated higher or lower than preceding thermals in the same cell. Both scenarios appeared to occur in batches of sequences.

There were 8 thermals that had sizes over 2 km in equivalent diameter. There did not appear to be a difference in lifetime, diameter and displacement between complex and simple thermals. Although there were more simple thermals than complex. Splitting of thermals was more common than merging in the observations in this chapter. The sensitivity of object identification was tested to the thresholds used. It was found that object identification was more sensitive to vertical velocity threshold than area threshold. The results presented highlight that there were short lived thermals occurring in deep convection as clouds evolved. It is important to determine how these pulses of growth affect cloud evolution and whether they are important at certain stages of the clouds maturity.

There are some limitations with the work presented in this chapter. The CAMRa radar has a 10 cm wavelength which is less sensitive to small particles. Therefore it is not optimal for small liquid water cloud detection. This limits observations of growing cumulus clouds before cloud drops become big enough to be detectable. For example, Melnikov and Zrnic (2017) increased the detectability of weak echos on the Norman, Oklahoma KOUN radar. This allowed a much lower signal to noise ratio than typically used operationally, short pulses, more samples per volume and a high pulse repetition frequency. This meant that the S-band radar could observe echoes from

Bragg scattering in clear air which allowed the authors to observe thermals identified using insects trapped in the circulations. The purpose of this work was not to observe such thermals in this stage but to attempt to observe thermals in deep convective clouds.

The 300 m range resolution used in the DYMECS and Gatwick is not the highest range resolution CAMRa can obtain. The 300 m range resolution may not capture small thermals because the signal will be smoothed out by averaging over 4 gates to obtain the 300 m range resolution. Using the highest range resolution of 75 m may allow finer scale circulations to be observed in Doppler velocity.

Table 5.2 shows the pro's and con's of using the scanning strategy used during the DYMECS and Gatwick campaigns. The main limitations of this scanning strategy are that (1) it is not known where the exact core location is, (2) scans were taken through the assumed core location but this did not account for possible regions adjacent to the assumed core in an attempt to capture the correct core, (3) there was a lack of observations in the cross-beam direction, such that there was no information of the spatial extent of the core in the cross-beam direction and the time clouds were scanned for was short.

Pros	**Cons**
High temporal resolution due to shorter times for pairs of scans	Assumes core location
Automated	Could miss updraught core
	Missing cross-beam information
	Short observations of many clouds

Table 5.2: Pro's and con's of the continuous RHI scan method.

Finally, the scanning strategy used during DYMECS meant that there were numerous cells that were not observed long enough to be used in this work, but was optimal for the statistical study of the DYMECS radar scans (Nicol *et al.*, 2015; Stein *et al.*, 2015). The one case that was observed long enough (12:31 25th August 2012) was the scanning period used in this chapter. All other scanning periods were substantially shorter meaning that tracking of objects could not be achieved because there were not enough scans to track objects in. Therefore, a new scanning strategy is proposed in

the following chapter in an attempt to address some of these issues and to use longer scanning times targeting individual clouds.

Chapter 6

Thermals observed using 3D scans of deep convection

6.1 Motivation

Prior observations have been able to determine that vertical velocities are coherent in time, depth and along-beam horizontal extent (along the observation line of sight). Feist *et al.* (2019) found that turbulence was generally stronger in deep convection than in shallower shower clouds. Most of the clouds observed in their study internally contained weak turbulence which was approximately co-located with shear which can be observed in radar observations. Weak turbulence was also co-located with regions of buoyancy that cannot be observed with radar scans but may be inferred from the presence of accelerating vertical velocity. Stronger turbulence was found near the tops of deep clouds and was found to be strongly correlated with updraught strength. It was further found that turbulence was strongly correlated with gradients in vertical velocity, thus gradients in vertical velocity are important for generating turbulence rather than the updraughts' velocity itself. The spatial dimensions of updraughts were found to not be correlated with turbulence (Feist *et al.*, 2019).

A common theme in the literature is to use overshooting tops to estimate updraught width, as a proxy for storm intensity and for now-casting severe weather (lead times). In these studies, no retrieval of updraughts was done. Multiple authors note the importance to understand the kinematics of deep convection and overshooting tops related to updraughts and the importance of physical processes involved in storm evolution. Borque *et al.* (2020) noted pulses of updraughts due to changes in brightness temperature, derived from the temporal derivative of the 10.3 μm wavelength satellite band.

The authors hypothesised a strong cooling rate of cloud top temperature was related to strong updraughts and that minimum infra-red measurements from satellite were followed by hail a few minutes later. The authors also suggested that intense warming rates could be linked with updraught decay, because as the updraught weakens the cloud top descends somewhat, increasing the brightness temperature. At this point the vertical velocity is not sufficient enough to suspend hail, therefore it falls. These pulses lasted on the order of 5 - 6 minutes from which the duration of updraught life cycles was inferred.

Lightning Mapping Arrays (LMA) have shown that maximum lightning flash densities can occur in the overshooting top of deep convective clouds (Jurkovic *et al.*, 2015; MacGorman *et al.*, 2016) and that very high frequency source densities increased as the 18 or 30 dBZ echo tops ascended and maintained heights above the level of neutral buoyancy (MacGorman *et al.*, 2016). Overshooting tops also preceded jumps in lightning rates (Carey *et al.*, 2019; Borque *et al.*, 2020), hail (Jurkovic *et al.*, 2015; MacGorman *et al.*, 2016), tornado intensity and can be used to help the issuance of severe weather and tornado warnings (MacGorman *et al.*, 2016; Marion *et al.*, 2019).

A new scanning strategy, detailed below, was used to target reflectivity cores and take multiple scans within the region surrounding the most intense reflectivity core identified within convective clouds. Previously updraughts evolving as pulses or thermals have been observed in 2D radar scans, as presented in chapter 5. The following questions are addressed in this chapter;

1. Are thermal objects coherent in space and time using 3D radar scans of clouds?

2. Are eddy dissipation rate structures coherent in space time using 3D radar scans of clouds?

3. How do updraught pulses develop in individual convective cells and how do these relate to reflectivity, differential reflectivity and eddy dissipation rate?

4. How do updraughts develop in the region of overshooting tops?

6.2 Eddy dissipation rate retrieval

Turbulence in radar observations can be estimated from observations of Doppler spectrum width. When Doppler velocity is measured, the mean Doppler velocity is obtained from the mean of all the velocities observed within a sample volume and sampling time. The spectrum width also known as the Doppler spectrum variance (σ_v^2) is the variance of the Doppler velocity in time (i.e over a large number of pulses). Therefore, spectrum width includes the velocity variance due to turbulent motion of hydrometeors observed in a sample volume on scales smaller than the sample volume. There are also other contributions to the turbulent motion measured, thus σ_v^2 can be decomposed into a sum of these contributions which are statistically independent (Doviak and Zrnic, 1984):

$$\sigma_v^2 = \sigma_s^2 + \sigma_t^2 + \sigma_{TV}^2 + \sigma_\alpha^2 + \sigma_o^2 + \sigma_B^2, \tag{6.1}$$

where σ_v^2 has contributions from the radial wind shear across the sample volume σ_s^2, turbulence σ_t^2, the distributions of hydrometeor fall velocities σ_{TV}^2, radar antenna rotation σ_α^2, hydrometeor oscillations σ_o^2 and beam broadening σ_B^2.

To render estimates of turbulence more comparable for different beamwidths (and hence ranges), Feist *et al.* (2019) expressed results in terms of the equivalent eddy dissipation rate (EDR), ε, assuming inertial sub-range scaling. Given turbulent motion cannot be directly measured using σ_v^2, it must be inferred from σ_v^2 by accounting for all the contributions in equation 6.1. To do this, each contribution either needs to be subtracted from σ_v^2 or determined to be negligible compared to σ_t^2.

To determine stability of flow, the dimensionless Reynolds number (R_e) is used. R_e is the ratio of the inertial forces over the viscous forces. That is, forces due to momentum of the fluid and forces due to the viscosity of the different layers of fluid. R_e is given by dimensional analysis

$$R_e = \frac{inertial}{viscous} = \frac{(u \cdot \nabla)u}{\nu \nabla^2 u} \approx \frac{(U \cdot \frac{1}{L}) \cdot U}{\nu \cdot \frac{1}{L^2}} \approx \frac{UL}{\nu}, \tag{6.2}$$

where u is the flow velocity, ν is the viscosity of the fluid, L is the characteristic

length scale and U is the characteristic velocity. Flows become turbulent when R_e exceeds the critical Reynolds number (R_c), which is generally 10^3.

For flows with a high Reynolds number, such as convective clouds, turbulent structures can form in the flow rather than the flow remaining laminar. In an ideal system the largest energy-containing scales can be identified (Γ_L) these are typically of order 10 km for deep atmospheric convection. Kinetic energy generated at these scales can degrade to smaller-scales in the Richardson/Kolmogorov energy cascade. This is a downscale transfer of turbulent kinetic energy from Γ_L to smaller dissipation scales with energy converted by viscous forces. The scale at which viscosity and advection (inertia) have equal magnitude (Re = 1) is known as the Kolmogorov microscale (Γ_D) (Kolmogorov, 1941). Γ_D is a function of the fluid viscosity and the rate of eddy dissipation. The anisotropy of large scale eddies for fluids with very high Reynolds numbers is assumed to be lost in the Richardson energy cascade (Kolmogorov, 1941). This results in a range of isotropic eddy scales, known as the inertial sub-range, where the largest scale (Γ_0) exists between Γ_L and Γ_D. In this range, there are no mechanisms that can generate new energy, or dissipate energy. Energy is transferred downscale, at a rate equal to the eddy dissipation rate.

If the spatial scales of the radar sample volume are smaller than the largest scale of Γ_0, then σ_v^2 includes velocity variances from isotropic turbulence. σ_v^2 due to turbulence can be related to the eddy dissipation rate based on some key assumptions (Feist *et al.*, 2019):

1. Reflectivity is uniform throughout the sample volume.
2. Turbulence is homogeneous within the sample volume.
3. The largest scale of the sample volume is less than Γ_0.
4. The effect of turbulence is reflected in the motions of hydrometeors within the sample volume.

The above assumptions are met for radar observations using CAMRa. The scale to calculate shear at, the shear removal scale, was chosen to be 900 m. This scale must

be larger than the sample volume but less than Γ_0, assumed to be 1 km, relating to the scales of updraught circulations. The shear removal scale is the scale at which to remove variances from σ_v^2 due to turbulence outside of the inertial sub-range scales. Γ_0 was assumed to be constant, but could vary from cloud to cloud. If the shear removal scale was larger than Γ_0, variance from outside the inertial sub-range may be included in σ_t^2. Due to this scale, eddy dissipation rate was not retrieved directly to the cloud edges. CAMRa has a suitably high enough resolution to sample velocity variance from the inertial sub range. For the contributions in equation 6.1, Feist *et al.* (2019) found that:

1. The variance contribution due to ice aggregates is always negligibly small in the absence of hail.
2. The variance contribution due to hydrometeor fall speed (σ_{TV}^2) is negligible if observations are made at elevation angles less than 13.9°. If the freezing level is less than 1.5 km, σ_{TV}^2 is negligible at ranges greater than 6.1 km from the radar.
3. If wet hail is present but below the freezing level of 1.5 km, σ_{TV}^2 is negligible at ranges greater than 6.5 km.
4. If dry hail is present σ_{TV}^2 is negligible when elevation angles are less than 11.5°.
5. σ_α^2 is only significant with extreme scanning speeds (4.1 rad s^{-1}).
6. σ_B^2 is always negligible for radar capable of sampling within the inertial sub-range.
7. σ_o^2 was neglected, given its small contribution to retrievals.
8. σ_s^2 can be calculated from observations using the shear of radial wind and a statistical relationship between the shear along the beam and across the beam, derived in Feist *et al.* (2019).

The above findings hold true for the radar data in this chapter, therefore σ_{TV}^2 and σ_α^2 were negligible given RHI scanning speeds of $8{\times}10^{-3}$ rad s^{-1} were used. This leaves contributions from σ_t^2 and σ_s^2 to σ_v^2. σ_s^2 is necessary to remove given contributions

from radial wind shear across the sample volume are from outside the range of scales sampled by the radar.

All assumptions and parameters used for CAMRa and the DYMECS case hold true for the data in this chapter with only 3 parameter changes. The pulse pairs for radar scans using the bracket scan strategy was increased from 32 to 64 allowing lower values of spectrum width to be measured. The elevation scanning speed was increased from 0.4° s^{-1} to 0.5° s^{-1}, to maintain a small time difference between each RHI scan and each sequence of 4 scans. Finally, the range gate resolution used the observed 75 m rather than averaging over 4 gates to obtain 300 m, in an attempt to observe smaller scale features.

Radar scans used in Feist *et al.* (2019) and in this chapter were taken at elevation angles less than 15°. Results discussed above show that horizontal velocity fluctuations will dominate the Doppler velocity spectrum. Full details of the eddy dissipation rate retrieval are discussed in Feist *et al.* (2019). Of note, is that the method is beneficial to investigate turbulence in the context of larger scale process such as the cloud and updraught characteristics but not small scale processes such as microphysics and entrainment. Turbulence kinetic energy in clouds is primarily produced by shear and buoyancy associated with vertical motion. Values of which tend to be large near strong updraughts. Finally, observations of Doppler velocity and spectrum width are fed to the eddy dissipation rate retrieval algorithm to retrieve turbulence on a scan by scan basis.

Assuming horizontal homogeneity the turbulence kinetic energy in a flow is governed by the turbulent kinetic energy equation, which is obtained by using Reynolds averaging on the Navier-Stokes equation and multiplying by the horizontal velocity u. A full derivation is not provided in this thesis but can be found in Feist (2019). The final result to note for eddy dissipation retrievals is that assuming homogeneous, steady-state turbulence with a co-ordinate system that is aligned with the flow, the production of TKE by shear and buoyancy is balanced by the viscous dissipation given by

$$\varepsilon = -\overline{u'w'}\frac{\partial \overline{u}}{\partial z} + \frac{g}{\theta_0}\overline{w'\theta'}, \tag{6.3}$$

where $\frac{\partial \overline{u}}{\partial z}$ is the vertical gradient of horizontal velocity and $\frac{g}{\theta_0}\overline{w'\theta'}$ is the buoyancy. The shear production terms can be observed, as shown by flows in Doppler velocity but the buoyancy production is hard to observe or measure in convective clouds without in-situ measurement of temperature. Therefore it is inferred by the presence of strong updraughts, i.e buoyant air. Thus, where eddy dissipation rate structures are present with a lack of shear in the Doppler velocity, the dominant production mechanism implied is buoyancy.

6.3 New scanning strategy

The 4 consecutive RHI's used for DYMECS campaign were not designed to study updraught pulses. A new scanning strategy was designed to provide more suitable data for this purpose. This strategy combines considering pairs of scans at the same azimuth and scanning direction (up or down) as needed by the retrieval algorithm with four different azimuths designed to bracket the estimated reflectivity core location. Uncertainty in the estimated location of the updraught core is due to the resolution of the composite radar network that is used for tracking storms. The operational radar network has a resolution of 1 km thus the location of the core can be incorrect to this resolution. There is also a delay of 5 minutes for this data to be processed and ingested into the tracking algorithm. Assuming a 10 m s^{-1} storm motion over a time period of 5 minutes, a storm could move 3 km introducing further uncertainty to the core location due to error in the storm motion estimate. The tracking algorithm attempts to account for the storm motion by calculating motion vectors and advecting the estimated core location forward in time between operational network updates to update the azimuthal scanning direction issued to CAMRa (Stein *et al.*, 2015). The new strategy:

1. Accounted for uncertainty in the core location.

2. Increased the number of observations around the reflectivity core allowing thermals to be tracked in the core and in the regions of cloud surrounding the core yielding almost three dimensional observations of the core of the cloud.

3. Provided a level of redundancy as the whole four-azimuth sequence has to be adjusted periodically to maintain tracking of the core.

It is useful to have a level of redundancy from the extra scans because uncertainty in the core location from the cell advection algorithm and that from the operational radar network can be somewhat accounted for. For example, if a scan no longer targets the core due to uncertainty, it has an increased chance of being observed by one of the further surrounding scans. Thus, consistent observations of the same region of cloud can be maintained.

The distance between scans in a sequence of bracket scans can be chosen based on the uncertainty of the composite radar network data or chosen based on the physical size of the features of interest. Given the reported physical size of thermals from the literature discussed in chapters 1 and 5 having a minimum diameter of ≈500 m and the requirement for independent observations, a bracket of 500 m was chosen. A corresponding bracket in degrees azimuth ($\Delta\theta_{ST}$), shown in Figure 6.1 is calculated which is equal to ($\frac{500}{R}$), where R is the range from the radar. This yielded no beam overlap out to 100 km which is where the beamwidth due to beam broadening equals the azimuth step (500 m). This provided a 2 km swath which was appropriate to capture the physical size of updraughts. For a range larger than 100 km beams may slightly overlap, for example at 120 km the beamwidth is 568 m. With a 500 m step it takes less than one second at all ranges to move the radar to the next azimuth, minimising time between scans.

RHI scan commands are issued to the radar carrying out sequences of scans as depicted in Figures 6.1 and 6.2. The sequence is as follows:

1. Locate reflectivity core from composite radar network data.
2. Pass azimuth to scan scheduler to calculate required azimuth sequences to scan using the range of reflectivity core and core azimuth.
3. Execute scan A (red).
4. Execute scan B (green).

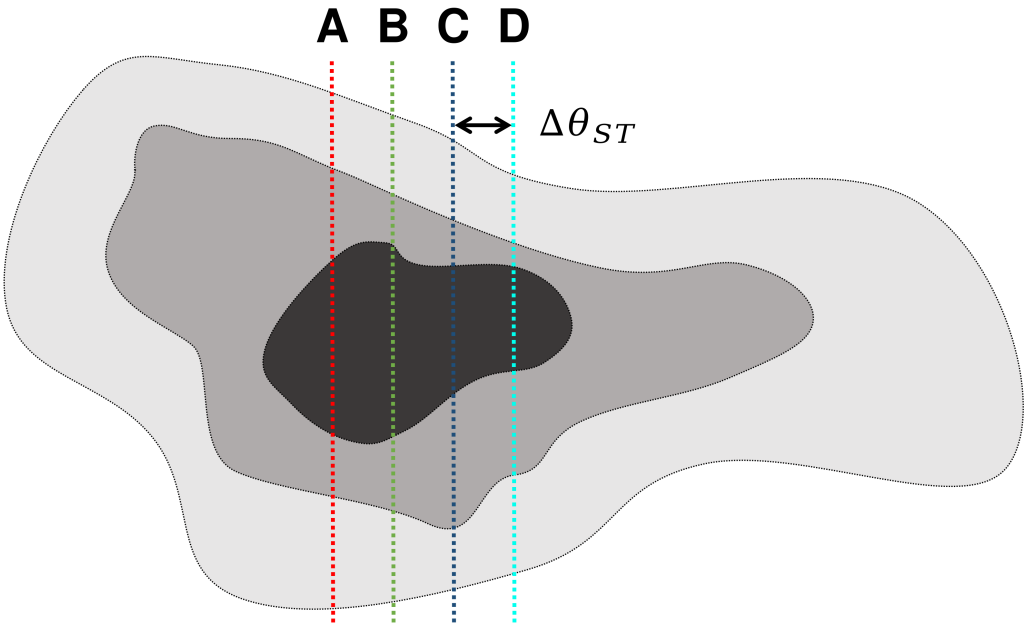

Figure 6.1: Plan view showing scan sequence through core of cloud. Red shows the first scan A, green shows the second scan B, dark blue shows the third scan C and cyan shows the fourth scan D. Each scan was separated by $\Delta\theta_{ST}$. Darker grey shading marks the convective core. Note that the parallel coloured lines converge to the point where the radar is located.

5. Execute scan C (dark blue).

6. Execute scan D (cyan). Each scan within a sequence is shown in Figure 6.2.

7. Repeat each scan to produce a sequence of 4 scans separated by azimuthal angle step ($\Delta\theta_{ST}$), calculated in step 2, until the cloud of interest is no longer tracked by the tracking algorithm feeding data to the scan scheduler.

For this sequence to be possible, the scan scheduler code was updated to integrate the new bracketing scanning strategy for prioritised storms for this thesis. This allowed the scan scheduler to automatically issue the new scan strategy commands to the radar whilst focusing on a storm of interest.

The time taken to move the radar from one azimuth to the next ($\Delta\theta_{ST}$) for each range is shown in Figure 6.3. Using an azimuthal slew rate of 2° s^{-1} it takes less than 1 s to move the radar beam 500 m horizontally at ranges greater than 30 km.

Table 6.1 shows the pro's and con's of using the bracket RHI scan strategy. It shows

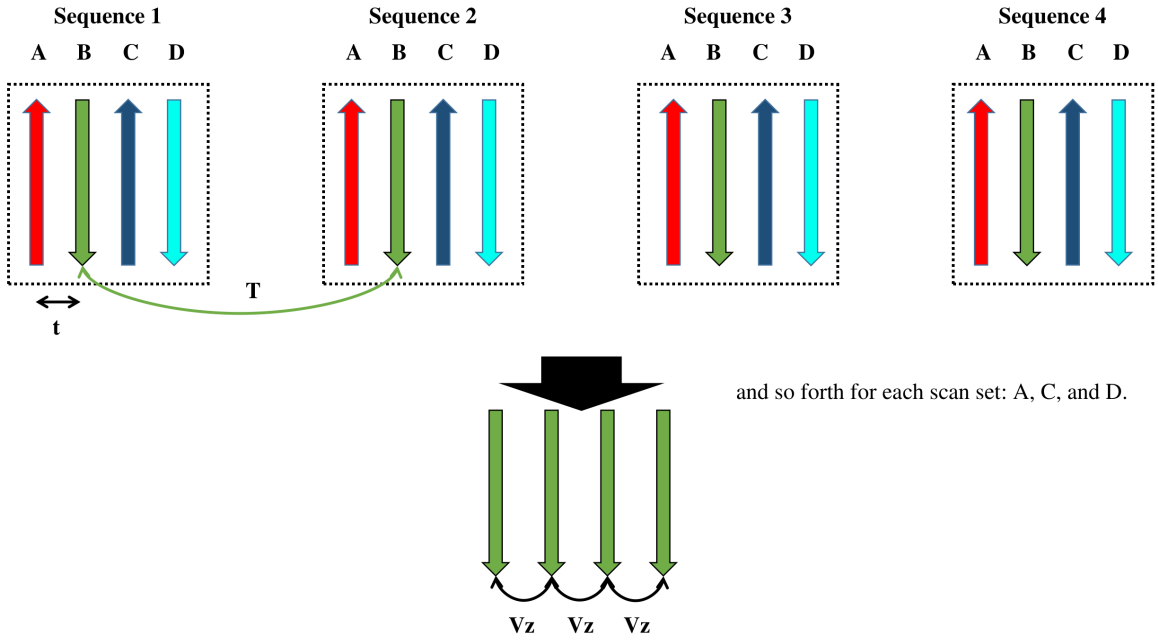

Figure 6.2: Sets of scan sequences shown inside dashed box. Arrows indicating scans within a sequence, with each colour corresponding to scan A (red), B (green), C (dark blue) and D (cyan). Each sequence was separated by 2 minutes (T) and each scan in a sequence was separated by 30 seconds (t). Vertical velocity (V_z) was derived from pairs of scans, for example scans through assumed reflectivity core (B) indicated in green.

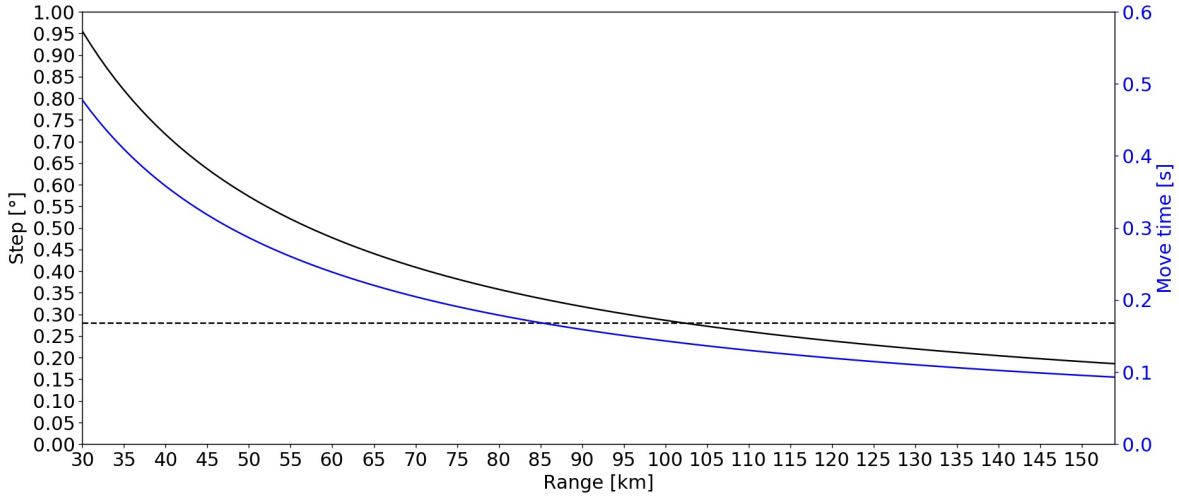

Figure 6.3: Azimuthal angle in degrees to move 500 m horizontally vs range (black). Time in seconds to move 500 m horizontally with a azimuthal scan velocity of 2° s^{-1} (blue). Dashed line is the beamwidth of CAMRa.

that the gain in observations by using the bracket scan strategy outweighs those of the continuous RHI scan strategy.

Pros	Cons
Increased chance of correctly scanning core	Longer time between core scans
Detection of lateral movement / shear across beam	Time between pairs could miss short lived thermals less than 2 minutes in lifetime
Extra spatial information about thermals and cloud	
Could reconstruct volume from 4 scans	
Average 2 scans with similar features	
3D view of cloud core, thermals and turbulence	
Observe coherent features across scans	

Table 6.1: Pro's and con's of the RHI bracket scan method.

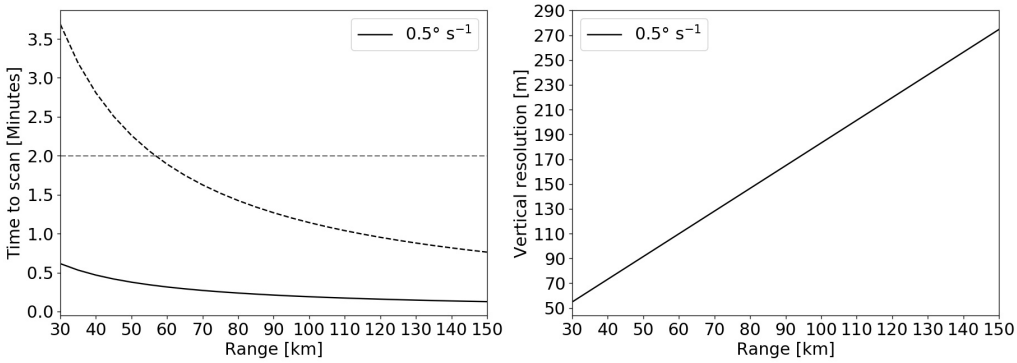

Figure 6.4: (left) Time in minutes taken to scan a single RHI (solid) and the time between corresponding pairs assumed to be in the same location (dashed). (right) Vertical resolution with range for 0.5° s^{-1} scanning rate. Grey dashed line (left panel) indicates shortest thermal lifetime. 64 pulse pairs, a PRF of 610 Hz and a maximum cloud depth of 10 km were used in the calculation.

Figure 6.4 (left) shows the time taken for a single RHI scan (solid) and the time between corresponding pairs assumed to be in the same location (dashed) assuming a maximum cloud depth of 10 km. Figure 6.4 (right) shows the scanning resolution vs range for the 0.5° s^{-1} scanning rate. The grey dashed line indicates the estimated shortest thermal lifetime of around 2 minutes. It was required that the time taken to obtain RHI scans used for tracking not exceed this across as much of the range as possible to be able to obtain enough temporal points to track thermals. A suitable elevation scanning rate would be 0.4° s^{-1} or 0.5° s^{-1} yielding a suitable temporal and vertical resolution for thermal tracking using 64 pulse pairs. To decrease scan time a 0.5° s^{-1} elevation scanning rate was used providing good temporal resolution between

corresponding pairs at ranges greater than about 60 km and reasonable temporal resolution at ranges between 40 - 60 km, but short lived structures may be missed at ranges less than 60 km with this scan setup.

Typical values of eddy dissipation rate in deep convection are 0.01 - 1 m^2 s^{-3}. Thus, 64 pulse pairs were chosen because it was not essential to increase the pulse pairs more than this to capture smaller spectrum width values. The spectrum width values obtained with more pulse pairs are considered insignificant when compared to typical values in deep convection (Matt Feist, personal communication). This also means the scanning rate does not have to decrease thus increasing the time between scans. A slightly faster scanning rate can be used whilst still maintaining a high vertical resolution.

Pairs of scans through the same region such as the example shown bt a set of 4 shown by the downwards green arrows in Figure 6.2 are used for vertical velocity retrievals. This means that the method discussed in chapter 4 was modified to use scans at times i and $i + 1$, rather than i and $i + 2$. In the new scan strategy, RHI scans were not alternating between upwards and downwards through the same region (up-down-up-down pattern), but either scanned upwards or downwards for a particular region as shown in Figure 6.2 by arrows of the same colour and direction.

6.4 24th September 2019 case study

Figure 6.5 shows the UK radar network composite at 1 hour increments between 0900 UTC and 1600 UTC. All following timestamps discussed are in UTC unless stated otherwise. Two large bands of showers can be seen moving north-eastwards across the UK between 0900 and 1200 associated with occluded fronts. Between 1100 and 1600 on-wards as a cold front passed over the UK located behind the occluded fronts, a line of convection with some discrete cells developed. The convective system located north-east of Chilbolton between 1400 and 1600 was the convective system scanned and used in this chapter between 1510 and 1540.

A zoomed in view of the convective system of interest is shown in Figure 6.6 between

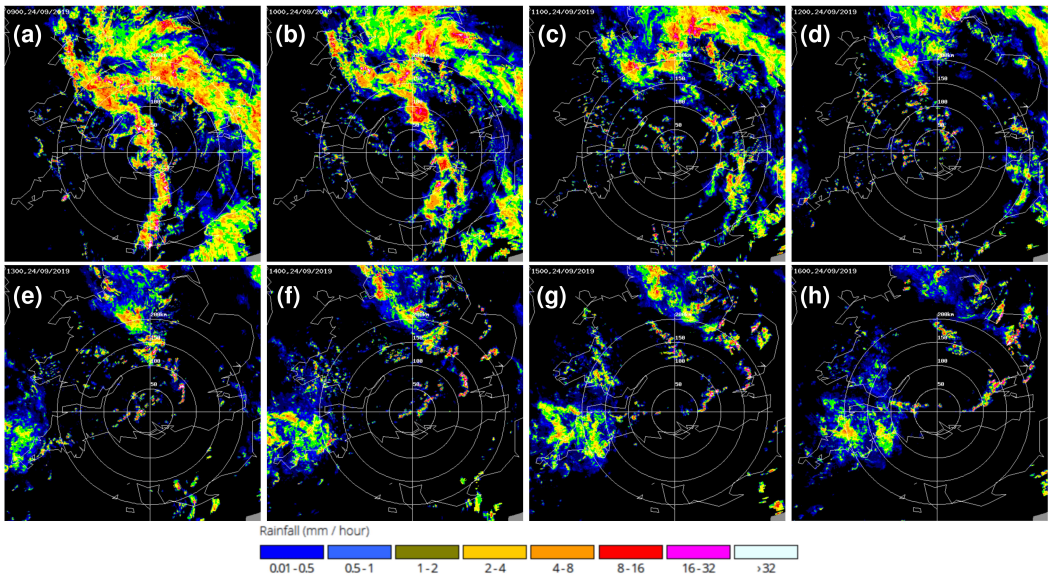

Figure 6.5: UK radar network composite provided by the Met Office showing the rainfall across the UK at (a) 0900, (b) 1000, (c) 1100, (d) 1200, (e) 1300, (f) 1400, (g) 1500 and (h) 1600. (a)-(h) show the larger scale system evolution throughout the day with the first band of rain between 0900 and 1300 and then a second band of rain with associated convective cells from 1100 to 1600 which contained more discrete convective cells passed over Chilbolton. Centred on Chilbolton with 50 km range circles.

1400 and 1600 in 10 minute increments. Scanning of this system with CAMRa started at 1510 and ended at 1540. At 1400 the system was seen to be composed of two separate convective cells indicated by the gap in high reflectivity. The low reflectivity between these two convective clouds indicates that they were part of a larger cloud system that contained individual convective cells. Multiple maxima of heavy rain can be seen shown by the red colours. At 1420 the system appeared to organise into a more distinct line with rainfall intensifying shown by the purple and white colours. The 'tail' of this cloud system was not focused on but is shown to highlight how the system developed in time. The region shown by the brightest (purple and white) colours was targeted by CAMRa as this was the most intense convective core. At 1500 three cores can be seen indicated by the distinct blobs of white and these persisted until 1520 until they joined into a larger area of rainfall. Some separation can still be seen at 15:30 on-wards as the core nearer the radar weakened and the following two cores remained intense. Further development can be seen on the north and north-east of the system that appeared to be associated with the environment the cloud of interest was in but was not scanned.

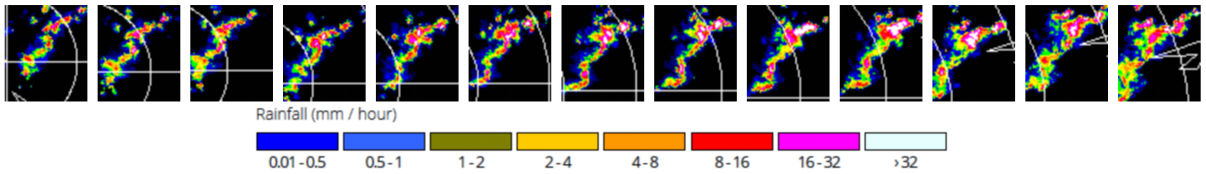

Figure 6.6: Zoomed in UK radar network composite provided by the Met Office showing the convective development and rainfall associated with the cells scanned for this chapter. First image was at 1400 and last image was at 1600 separated by 10 minute intervals showing the convective development leading up to scanning starting at 1510 and after scanning ended at 1540.

An example of a sequence of 4 scans taken using the bracketing strategy detailed are shown in Figure 6.7 for the 24th September 2019 case. The top 4 panels in Figure 6.7 show scans A, B, C and D with corresponding locations shown by the dashed coloured lines in the bottom panel on the radar network composite for 15:30. Lightning strikes are shown as yellow circles on the radar composite and strike label and time are annotated. Lightning observations were obtained from the Arrival Time Difference Network (ATDNet) which provides time and location information of a sferic. The uncertainty in location of a lightning strike over the UK is 1 - 2 km and the strength, polarity and type (inter-cloud, in-cloud, cloud-ground) cannot be determined (Met Office, 2019). This demonstrates how a convective cloud was scanned using the strategy and illustrates the scan sequence showing consistency in reflectivity through slices of cloud.

An example of a sequence of processed scans taken using the bracket strategy are shown in Figure 6.8. Reflectivity in dBZ (first panel) with 4 m s^{-1} vertical velocity contoured in solid black. Doppler velocity in m s^{-1} in second panel, spectrum width in m s^{-1} in third panel, ZDR in dB in fourth panel and EDR in m^2 s^{-3} in fifth panel. Timestamps and azimuths shown at top for the 24th September 2019 cloud case. This example shows the consistency of radar variables and retrieved variables across each of the scans and how features in each of the scans can be co-located.

There were two main updraughts present throughout the clouds lifetime, shown early on in their lifetime by the black contours in Figure 6.8 first row. Inflow into the cloud was from the west of the cloud and descended eastward to the base into the

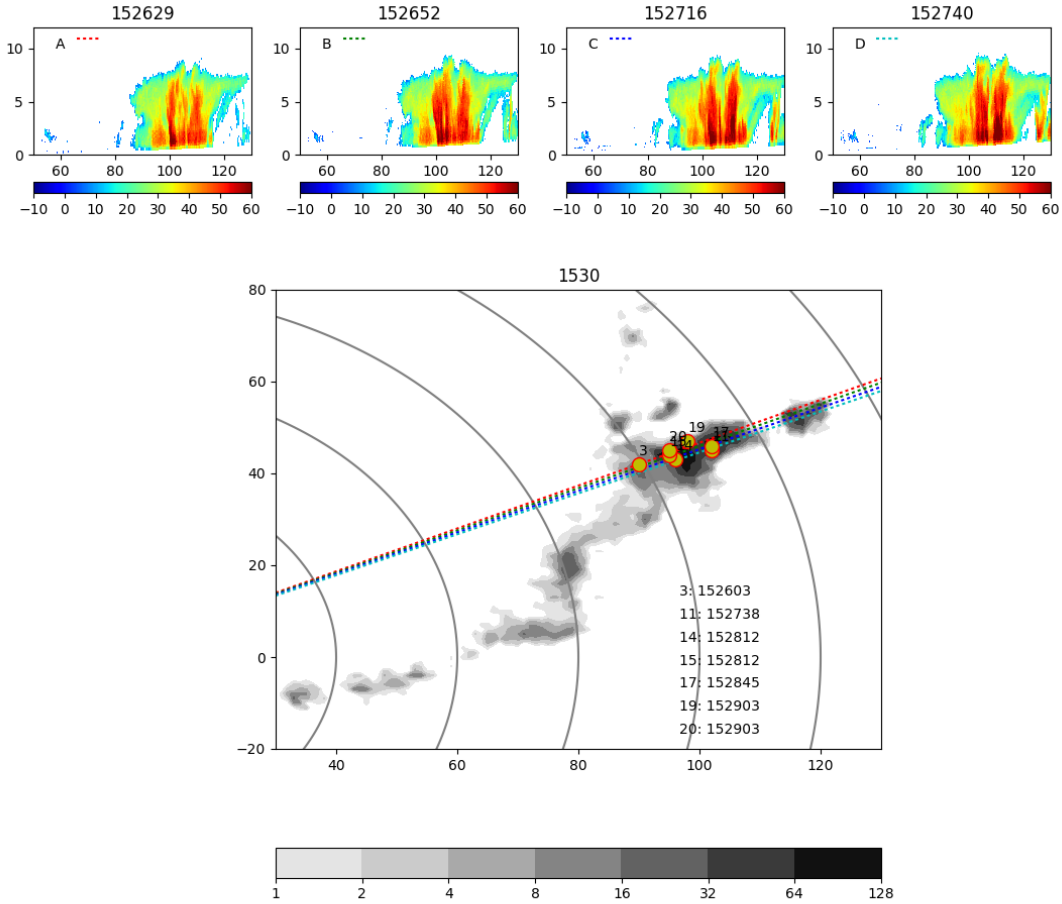

Figure 6.7: Example of a sequence of 4 RHI scans showing reflectivity in dBZ with timestamps shown (top) for the 24th September 2019 cloud case. UK composite radar image at 15:30 on 24th September 2019 (bottom) with rainfall rate in mm h^{-1} and dotted coloured lines corresponding to each scan (A, B, C and D) through cloud as defined by the bracket scan strategy. Lightning strikes from the Met Office ATDNet are shown as yellow circles, with strike label and time annotated. This scan was around the time of an overshooting top. Centred on Chilbolton Observatory with 20 km range circles and zoomed into 40 to 120 km range.

centre of the cloud, shown by the red slanting Doppler velocity in Figure 6.8 second row. Ascent was visible into the cloud top and curled around into the outflow shown by the strong red Doppler velocity across the top of the cloud from west to east. This type of flow structure is similar to that seen in squall line systems with a rear-inflow jet and a front-to-rear ascending flow. Generally with strong rear inflow the cloud system will bow and a notch of low or no radar reflectivity echo region can be seen behind the

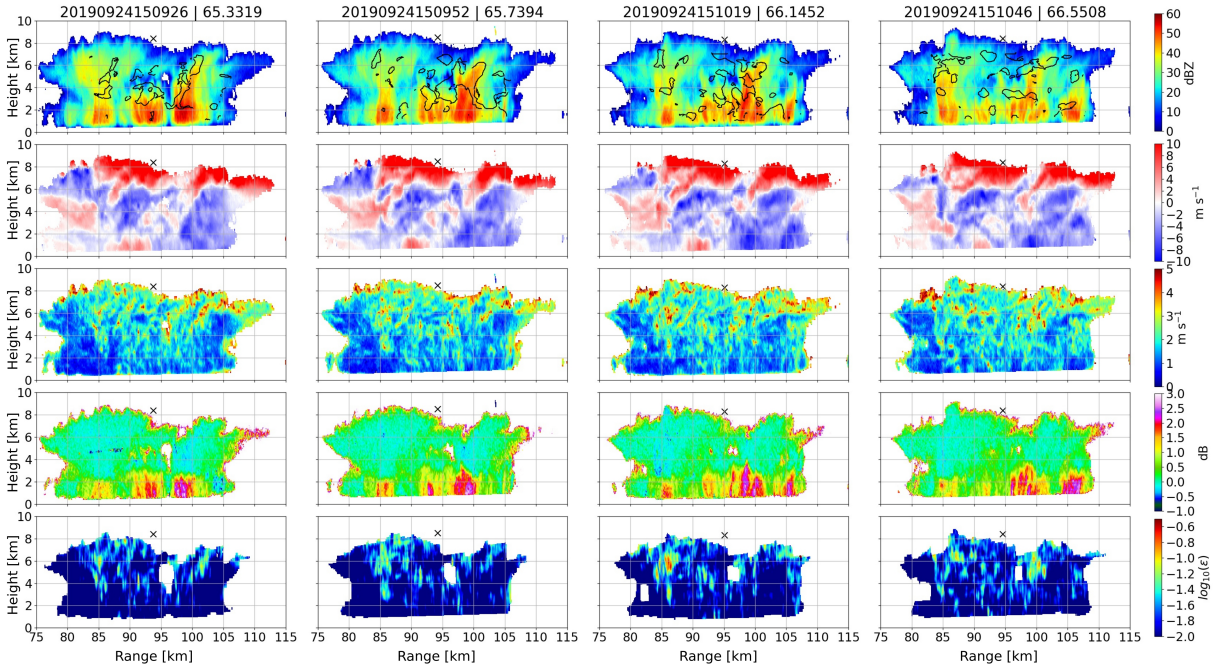

Figure 6.8: Example of processed data for a sequence of 4 RHI scans showing reflectivity in dBZ (first row) with 4 m s^{-1} vertical velocity contoured in solid black. Doppler velocity in m s^{-1} in second row, spectrum width in m s^{-1} in third row, ZDR in dB in fourth row and $log_{10}(\varepsilon)$ in the fifth row. Timestamps and azimuths (degrees) shown at top for the 24th September 2019 cloud case. Range is on the x-axis and height on the y-axis.

line of convection. The cloud system in this case did not exhibit a clear bowing but some potential bowing of the cloud with a low echo region can be seen at the rear of cell along the line-of-sight the radar. This bowing can be seen in the central convective cell in panels 7 to 9 in Figure 6.6 as the cloud formed an arc shape. This could explain the clear descending inflow seen in Doppler velocity observations. These main features are summarised by a schematic of the general composite flow in the cloud in Figure 6.9.

Further processing of specific scans from the scan sequences was required due to azimuth changes resulting from the core-tracking strategy during scanning. Azimuthal direction adjustment of scans during a sequence to maintain scans through the same region impacted the vertical velocity retrieval at 15:16, 15:26, 15:31 and 15:36. In some of the pairs of scans within the listed timestamps (timestamps refer to scan B), the azimuth difference between a corresponding scan at the current and prior time was 0.2°

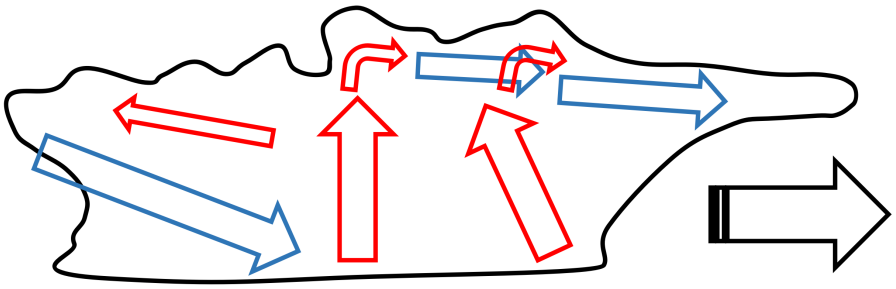

Figure 6.9: Composite schematic showing the dominant general flow in the cloud over the time scanned. Solid black outlines cloud and black arrow indicates cloud direction of movement. Red arrows indicating rising motion that was seen from two main distinct updrafts and some weaker slantwise ascent towards the rear of the cloud. Blue arrows indicate downwards flow into the cloud from the rear and outflow along the cloud top towards the front of the cloud.

or 0.4°.

Prior to carrying out these scans, it was not fully appreciated how sensitive the method was to matching objects in one scan to those in another scan when the scan is through a different region of cloud that exhibits a different Doppler velocity pattern that is significant enough such that the retrieval method cannot optimally retrieve vertical velocity. The tracking algorithm that advects the estimated core location forward in time to update the azimuthal scanning direction issued to CAMRa between operational network updates caused a jump to occur when the next scanning sequence was taken. To account for such azimuth shifts, interpolation was done by selecting scans in space with the nearest azimuths to those in the prior sequence and interpolating scans from the next sequence to azimuths of the previous sequence. This means that at 15:16 scan D is missing, at 15:26 scans A and B are missing, at 15:31 scans C and D are missing and at 15:36 scans A and B are missing. These scans were not used because they would not form a consistent sequence in time and space for vertical velocity retrieval because there were no azimuths near enough in the previous sequence to interpolate too allowing a consistent sequence to be formed. Vertical velocity was then retrieved from the new sequence including the interpolated scans. This will be taken into account when interpreting the results presented in this chapter, such that at the given times average composites and dimensions will not be representative of a complete set of 4 scans. Figures presented below show that even though select scans were missing,

consistency remained in time and space in the retrieved updraughts and is discussed below.

Due to the breaks in time in the data, object tracking may not be consistent with larger gaps in time and relating objects with themselves in successive scans may be inconsistent. Therefore the object tracking algorithm was not applied to avoid reporting inconsistent results such as misrepresentation of the number of identified objects. Although consistent updraught pulses were still identifiable visually, as shown below, updraughts were identified by applying the area and vertical velocity thresholds at each time allowing the estimation of properties. Updraught trajectories were estimated subjectively as shown in the following sections to compare ascent rates to retrieved vertical velocities.

To mitigate this issue in the future, the advection algorithm in the scanning scheduler on the Chilbolton systems could be updated by reducing the time between cell advection using calculated velocity vectors to estimate azimuth. Resulting in smaller increments of azimuth when estimating cell location in the periods where the system is waiting for updates from the operational radar network. Therefore creating a smoother transition when the operational radar network data become available and possibly helping to bridge this gap. Alternatively the tracking adjustment calculated could be checked to make sure it always equals the scan spacing and an extra 1 or 2 scans could be added to the sequence when adjusting.

6.5 Dimensions of coherent updraught and eddy dissipation rate structures

There have been no prior quasi 3D observations in the along-beam, cross-beam and depth dimensions of eddy dissipation rates in convective clouds. By inspecting the dimensions in all three planes: along-beam, cross-beam and depth, relationships of the three dimensional structure of updraughts and eddy dissipation rate structures in deep convection are obtained.

To find coherent updraught and EDR structures, thresholds of 4 m s^{-1} vertical

velocity and $\varepsilon = 0.02$ m^2 s^{-3} were applied to identify features in each scan. From this, a field was created counting at each grid point the number of scans the identified structure was present in. This resulted in a field of integers ranging from 0 to 4 for each sequence of 4 scans, termed the *count*. For a given sequence of scans the scan separation in degrees is given by $\Delta\theta$ and the scan separation at range R, ΔS_R, in metres can be calculated by $\Delta S_R = 2\pi R\frac{\Delta\theta}{360}$. The beam width at range R due to beam broadening is given by $\varphi_R = 2\pi R\frac{0.28}{360}$, where 0.28° is the beam width of CAMRa (φ_0). Using information about the scan separation and range of features from the radar the cross-beam width of an object at range R (W_R) is given by:

$$W_R = \varphi_R + ((count - 1)\Delta S_R \tag{6.4}$$

Such a scenario, demonstrated by 2 scans is shown in Figure 6.10 where the separation between two scan beams (ΔS_R) is shown and the beamwidth at range R (φ_R) is indicated. Clearly, object widths cannot be measured if the object is present in either the first (A) or last scan (D), as it likely extends further either side, so W_R is only meaningful if the object only appears in the centre two scans. On the other hand, a large W_R means that the object was observed in more scans so suggests that derived quantities are likely to be less uncertain.

For each identified coherent structure from a sequence of 4 scans, the cross-beam width was calculated. An example of a scan from a sequence at 15:30 is shown in Figure 6.11, where the cross-beam width of updraught features are shown in the top panel and EDR features in the bottom panel. Black contours show the reflectivity ranging from 10 to 60 dBZ in 10 dBZ increments. This example shows a coherent updraught feature that was located between 90 - 95 km range and 4 - 8 km height in the cloud which spanned up to 2.5 km width in its centre. On the edges its width varied between about 1 km and 1.6 km. This coherent updraught was located at the top of a cell with reflectivity upwards of 40 dBZ and extended into a 30 dBZ reflectivity region in the upper part of the cloud. Other smaller coherent updraught features are shown between 95 and 105 km range. EDR structures were seen between 90 and 105 km range with cross-beam widths varying from a about 500 m to 2.5 km in the upper regions of the

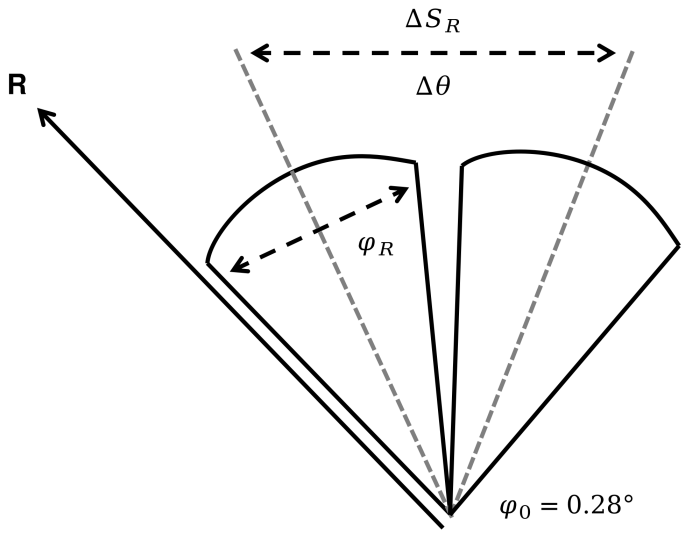

Figure 6.10: Diagram showing an example of 2 scans with beam axis shown by dashed grey line. Range R increases along scan and beam width of CAMRa (φ_0) is 0.28°. Beamwidth at range R is given by φ_R, and scan separation in degrees is $\Delta\theta$ and in metres between beam axes is ΔS_R. Angles are exaggerated.

cloud between 95 and 100 km. These coherent EDR features were present in more than one scan and extend throughout a large depth of the cloud.

6.5.1 Updraught dimensions

By aggregating dimensions of along-beam length, cross-beam width and depth for each updraught and EDR structure at each scan time, a scatter plot for each combination of dimensions was produced. Figure 6.12(a) shows the maximum along-beam length vs the minimum cross-beam width, (b) maximum along-beam length vs maximum depth and (c) minimum cross-beam width vs maximum depth for coherent updraught structures. The cross-beam width is referred to as minimum throughout this section and chapter due to the azimuthal limit of the scanning strategy. The azimuthal limit is insufficient to span the complete width of the structure. Red circles represent structures that were observed within the middle two scans only (B and C; B or C) and were therefore bound by the outer two scans (A and D).

Figure 6.12(a) shows that for the identified updraught structures the maximum along-beam length was about twice the minimum observable cross-beam width. There

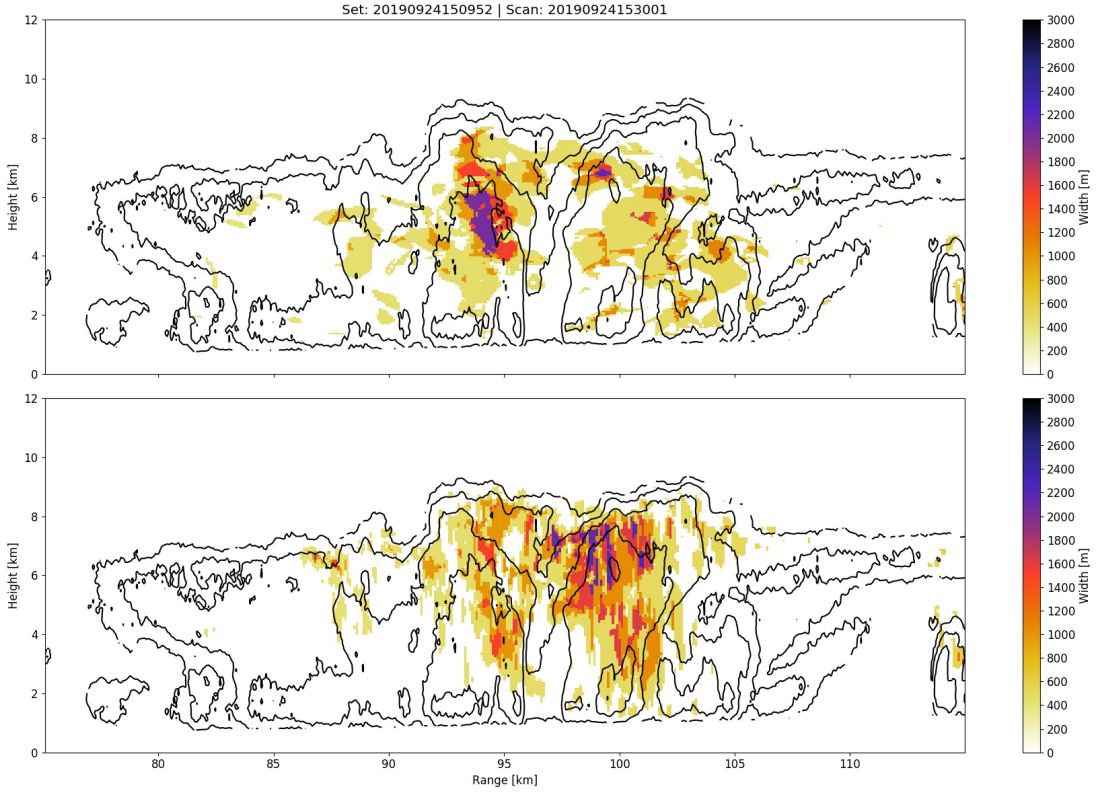

Figure 6.11: Example of coherent updraught (top) and EDR (bottom) structures for cell 2 (C2; detailed below) on 24th September 2019 at 15:30 using a sequence of 4 scans. Colours show varying cross-beam widths of structures located in different regions of cloud. Black contours show the reflectivity ranging from 10 to 60 dBZ in 10 dBZ increments.

appeared to be some relationship between these dimensions up to about 4 km maximum along-beam length, but due to the limitation on cross-beam scans (no more than 4 were done), as the maximum along-beam length increased the minimum cross-beam widths were generally between 2 - 3 km, near maximum possible values. This suggests that updraughts that were longer than 4 km were likely to be wider than 2.5 km. This does not suggest that 13 km length for example was wider than 7 km. However, it seems reasonable that the relationship between width and length appears to be truncated by the maximum observable width, so it seems likely that if more scans were used across the cloud the longer features would have proven to be wider.

Figure 6.13 shows the correlation matrix for each combination of updraught dimensions. A Pearson correlation for the cross-beam width and along-beam length dimensions had a value of 0.8, indicating a linear correlation. The maximum along-beam

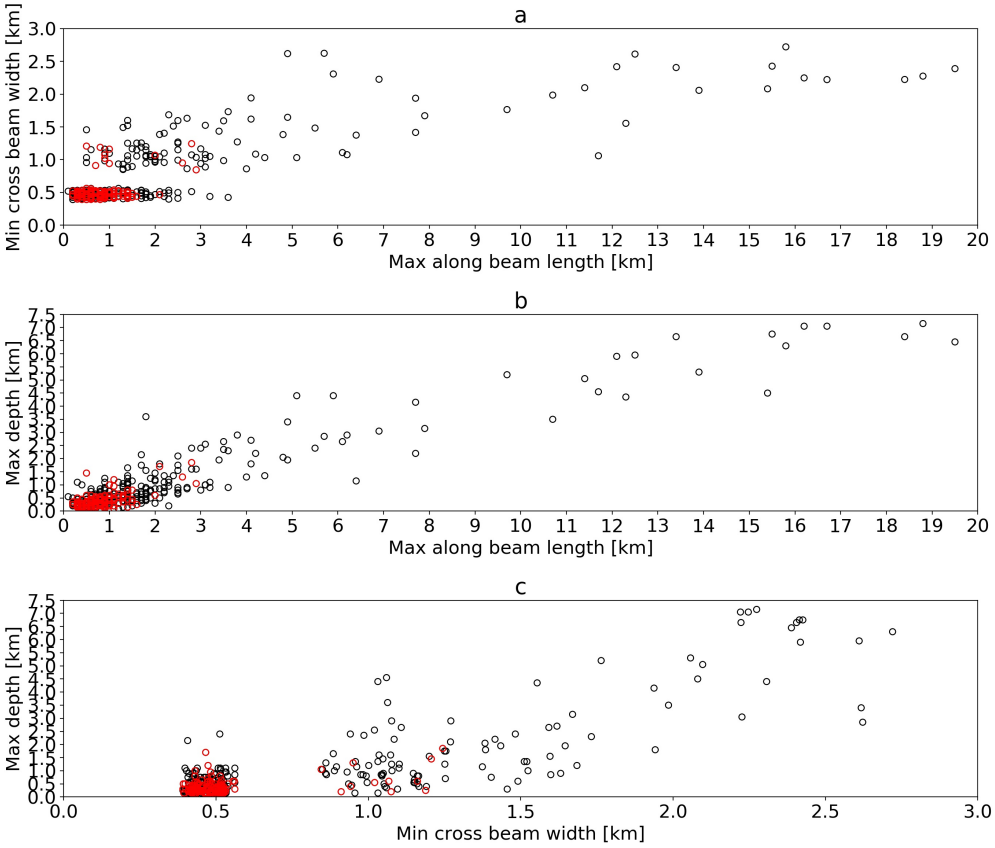

Figure 6.12: Scatter plots of (a) minimum cross-beam width vs maximum along-beam length. (b) maximum depth vs maximum along-beam length and (c) maximum depth vs minimum cross bream width for coherent updraughts at each scan time. Red circles show structures that were in either or both of the middle two scans only. Aggregated from each sequence of 4 scans (19 pairs of 4 scans) for the cloud scanned on 24th September 2019.

length vs the maximum depth is shown in Figure 6.12(b). This showed a much clearer relationship between these dimensions and that both dimensions increased somewhat linearly with a Pearson correlation of 0.94. Although, updraughts tended to be longer than they were deep after about 4 km depth and updraughts that extended in depth between 500 m and 4 km, tended to be twice as large in the along-beam direction as they were deep.

The minimum cross-beam width vs the maximum depth is shown in Figure 6.12(c). Note that this clearly shows clusters of data around roughly 0.4, 1.1 and 1.6, corresponding to appearing in 1, 2 and 3 beams in the scan sequence. The scatter in width

arises entirely from range. This showed that wider updraughts tended to be deeper and that narrow updraught structures tended to be shallow. These dimensions had a Pearson correlation of 0.83.

Combining all three dimensions it was determined that coherent updraught dimensions tended to increase in all dimensions. Updraughts were longer along the beam than they were wider across the beam, and that wider and longer updraughts had varied depths but smaller horizontal updraughts also remained small in depth. This could be hypothesised that due to the cloud being aligned along the wind and moving with the mean wind, updraughts developed preferentially in the along wind direction compared to the cross-wind direction. Updraught depth is likely to be constrained by the cloud depth, given structures within the cloud cannot be larger than the cloud itself, therefore depth is smaller than the length. There also appeared to be some clusters of dimensions, regardless of the clustering in the cross-beam width dimensions due to the data, but clustering of updraughts with small horizontal spatial extent along the beam of less than 2 km, across the beam of less than 1.5 km and with depths less than 2 km.

This showed that there were many small updraughts present at all times throughout the cloud and that there were fewer larger updraughts present within the cloud. Large along-beam lengths arise from the labelling of structures using a connected component algorithm in the along-beam direction and taking the maximum dimension. Nonetheless, visual inspection showed that large long structures also tended to be wide, but limited by the number of scans. An example is shown in Figure 6.13 where long structures were also wide shown by the red to purple colours indicating the maximum width observable with 4 scans. The correlation matrices in Figure 6.13 and Figure 6.15 are symmetric, therefore the correlation value of 1.0 for dimensions that correlation with themselves is redundant.

6.5.2 Eddy dissipation rate dimensions

Figure 6.14(a) shows the maximum along-beam length vs the minimum cross width width, (b) maximum along-beam length vs maximum depth and (c) minimum cross-beam width vs maximum depth for coherent EDR structures. The dimensions of

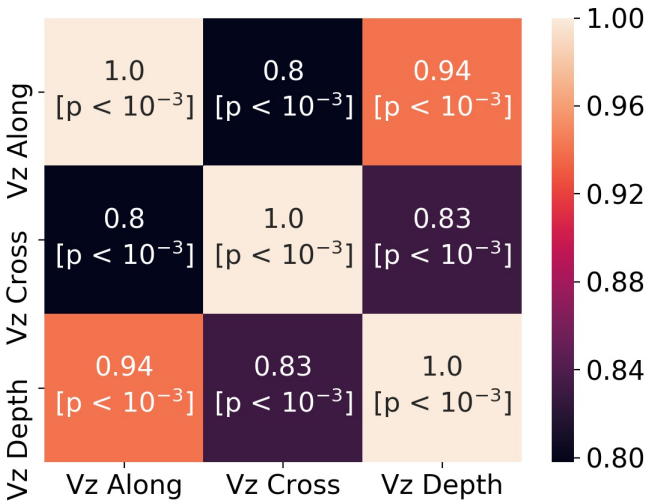

Figure 6.13: Correlation matrix for each combination of updraught dimension corresponding to Figure 6.12 with p-value in brackets.

EDR structures also showed clustering between small and large structures and that some relationship existed between each dimension. The maximum along-beam length of EDR structures that had lengths less than 3 km tended to be less than 2 km in width across the beam. There were some structures with large lengths extending between 6 and 20 km, which cannot be observed in the cross-beam direction. Given the linearity in dimensions less than 3 km and that the Pearson correlation was 0.74, shown in Figure 6.15, may suggest that if further observations in the cross-beam direction were obtained that the large along-beam lengths could correspond to large cross-beam lengths. Although this would depend if clouds were more elongated or circular. These dimensions also show that the EDR structures are somewhat circular horizontally.

Figure 6.14(b) shows the maximum along-beam length vs the maximum depth. This shows that the EDR structures tended to be deeper than they were long shown by the steep incline in the scatter points below 3 km along-beam length. EDR structures increased in depth up to 4.5 km whilst mostly remaining less than 2 km in length. There was a cluster of points between 1 km length and 2.5 km depth indicating more smaller structures than there were large. A sparser number of larger structures were seen with lengths generally larger than depths. The Pearson correlation for these dimensions was

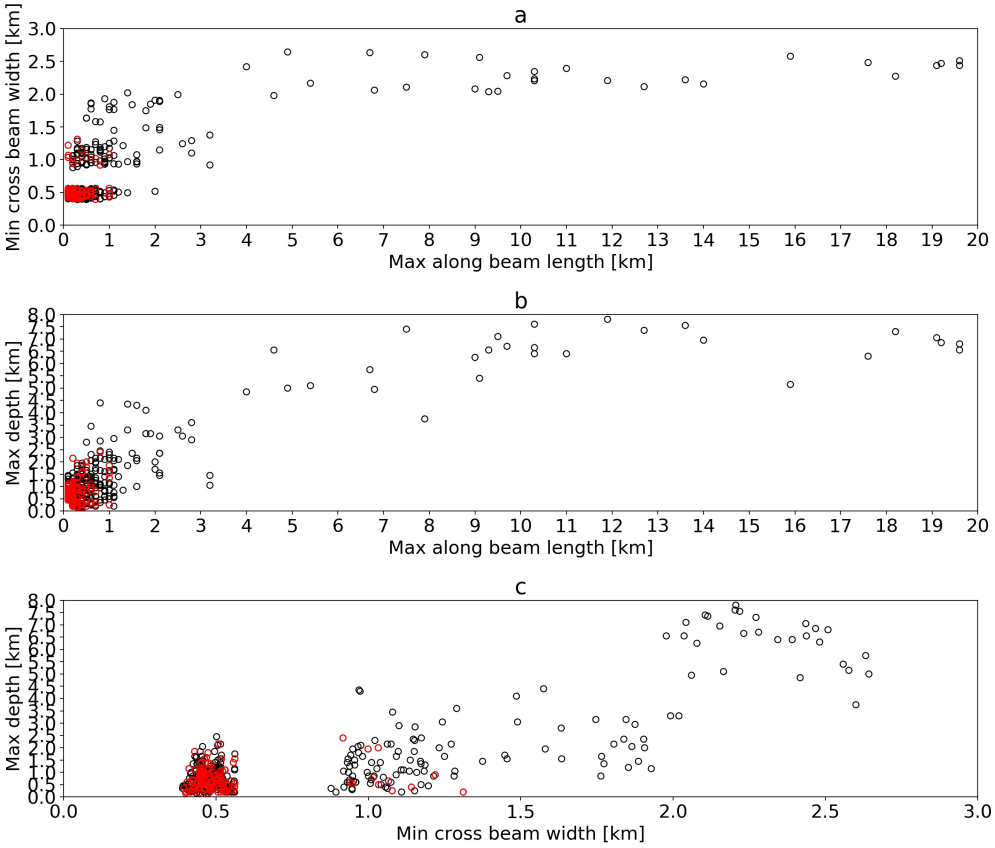

Figure 6.14: Scatter plots of (a) minimum cross-beam width vs maximum along-beam length. (b) maximum depth vs maximum along-beam length and (c) maximum depth vs minimum cross bream width for coherent EDR structures at each scan time. Red circles show structures that were either or both of the middle two scans only. Aggregated from each sequence of 4 scans (19 pairs of 4 scans) for the cloud scanned on 24th September 2019.

0.85, indicating a positive relationship between this pair of dimensions.

Figure 6.14(c) shows the minimum cross-beam width vs maximum depth. This figure showed a cluster of structures that were less than 2.5 km deep and less than 1 km wide. Again this is similar to the maximum along-beam length vs maximum depth in that structures were deeper than their horizontal extent. An increase in maximum depth was also be seen up to 7.5 km with an increase in cross-beam width from 0.5 km to just over 2.5 km. Gaps in the minimum cross-beam width dimension in Figure 6.14(c) are due to discretisation caused by the gaps between the sequence of 4 radar scans. The Pearson correlation for the minimum cross-beam width and maximum depth was

0.81. These results suggest that the horizontal dimensions were strongly correlated to the vertical extent. This could imply that such coherent EDR structures grew in all dimensions somewhat equally, but maintained a slightly larger extent vertically with a potentially cylindrical shape horizontally.

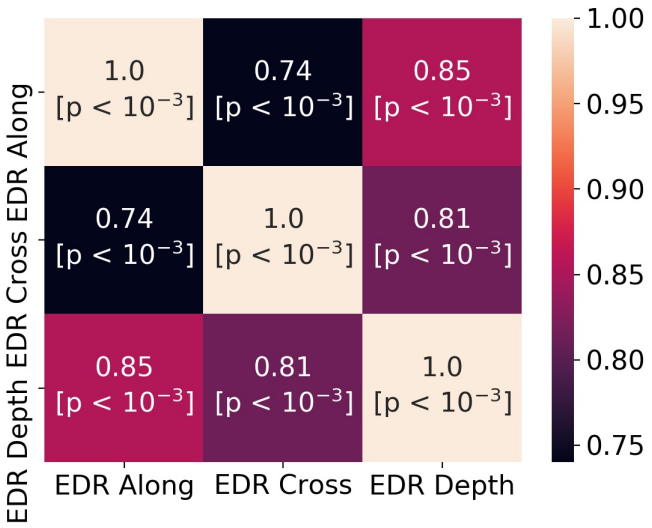

Figure 6.15: Correlation matrix for each combination of EDR dimension corresponding to Figure 6.14 with p-value in brackets.

Similar to along-beam updraught structures, EDR structures with large lengths were identified by connected component labelling to identify the full length of a structure. An alternative would be to find the length of individual structures based on their width such that for a given width its length and depth can be found, rather than structures extending in large lengths in the along-beam direction but only extending up to 3 km in the cross-beam direction. Visual inspection of figures similar to Figure 6.11 show that larger cross-beam widths tend to occur in the 'core' of long objects and that identifying objects by width threshold would result in similar length dimensions. The only two dimensions that were observed with certainty were the along-beam length and depth because full measurement was obtained, compared to the truncation in cross-beam width. Figure 6.12(b) shows that the along-beam length and depth for updraught dimensions generally follows a $y = ax + b$ relationship. Figure 6.14(b) shows that the along-beam length and depth for EDR dimensions could be represented by a

logarithmic curve.

6.6 Development of updraught pulses in individual cells

To investigate the development of coherent updraught pulses in the convective cells, composites of reflectivity, vertical velocity, differential reflectivity (ZDR) and EDR were produced by averaging each sequence of 4 radar scans taken using the bracket strategy together. Therefore, structures that were present and persistent in composite averages had a high probability of being present in more than one scan and up to all 4 scans, indicating coherent structures in the cross-beam direction, along-beam direction and depth. Such structures were consistent in space and can be determined to be consistent in time if they were present in each frame of the composite. This highlights the development of coherent structures within the cloud.

The cloud contained 3 distinct convective cells identifiable by eye as three regions of enhanced reflectivity greater than 30 dBZ and resembling columnar reflectivity towers. Each individual convective cell was isolated to investigate the development of coherent structures given each individual cell was in a different stage of its life cycle. This is subjective, but identified individual regions of cloud where substantial development occurred as seen by enhancements of reflectivity and increases in surface rainfall shown by reflectivity above 40 - 50 dBZ below the freezing level in the identified range boundaries.

Throughout the observation period each cell remained within the identified range boundaries due to the Lagrangian displacement. Cell 1 (C1) was identified between 82 and 88 km, cell 2 (C2) was identified between 88 and 96.5 km and cell 3 (C3) was identified between 96.5 and 105 km. These bounds and an example of average reflectivity (top panel) and vertical velocity (bottom) using a sequence of 4 scans are shown in Figure 6.16 for 15:09.

In the following figures for C1, C2 and C3, reflectivity, ZDR and EDR are shown with motion vectors from the Doppler velocity and vertical velocity superimposed for the observation period between 15:09 and 15:40 with timestamps shown. Coloured

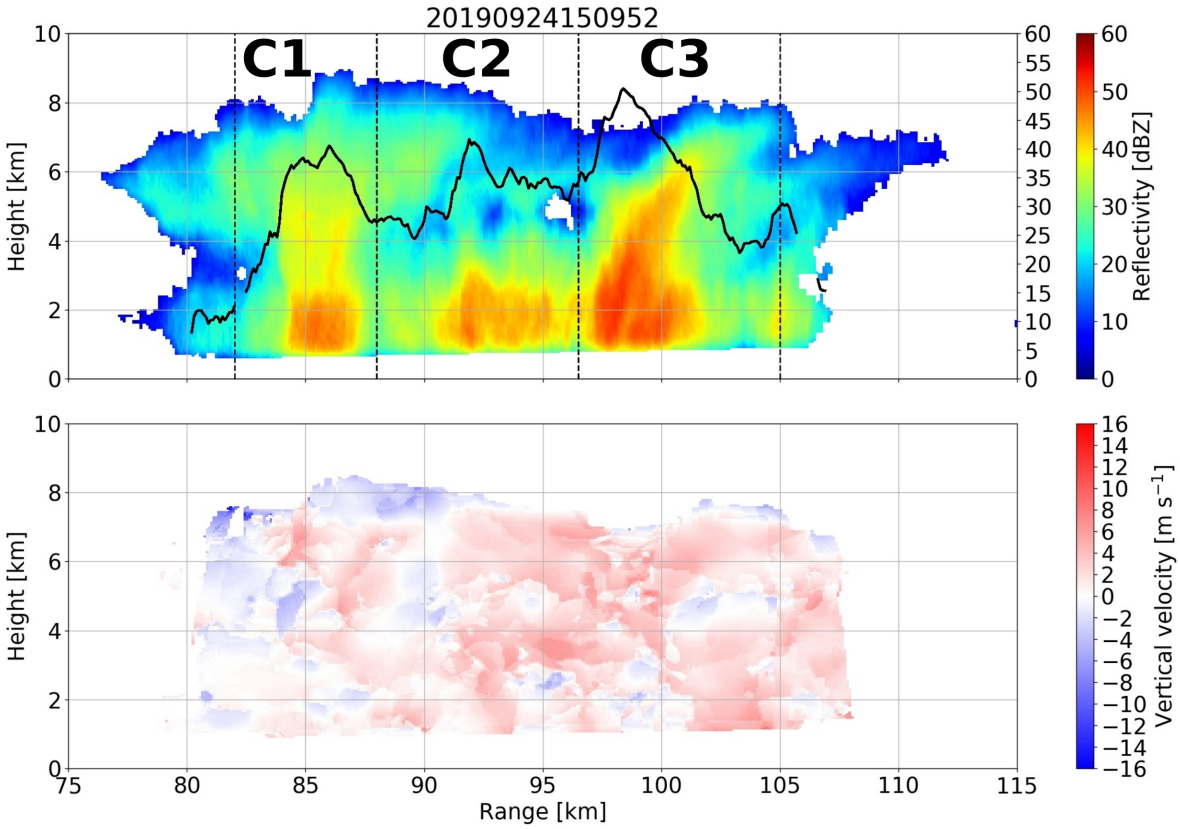

Figure 6.16: Example of composite reflectivity (top panel) and vertical velocity (bottom panel) for 15:09 24th September 2019. Solid black line is reflectivity at 3 km height. Dashed vertical black lines are bounds of individual cells with cells labelled.

contours for updraught velocities of 2 (grey), 4 (black), 6 (red) and 8 (magenta) m s^{-1} are added to show developing updraughts and locally strong updraught regions.

6.6.1 Cell 1

Cell 1 (C1) was located between 82 and 88 km range and is shown in Figure 6.17 between 15:09 and 15:20, Figure 6.18 between 15:20 and 15:30 and Figure 6.19 between 15:30 and 15:39. C1 decayed over the observation period and observations appear to have started near cell maturity or beginning of decay phase and ended when the cell had mostly decayed from being convective, leaving a low (20 - 25 dBZ) reflectivity region in the cloud. This example provides a contrast to cell 2 and cell 3 which were intensifying.

The reflectivity in the mid to upper regions of C1 above 3 km appeared to weaken

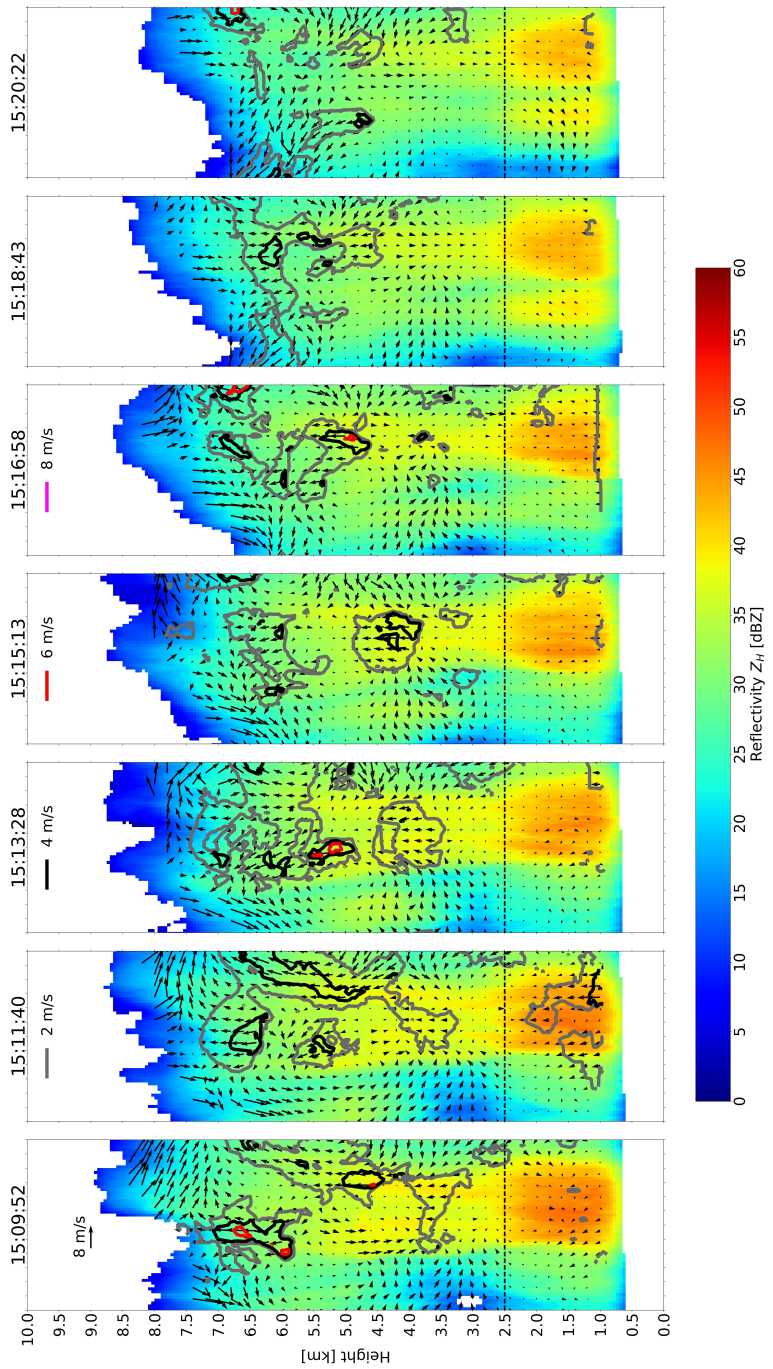

Figure 6.17: Reflectivity in dBZ for C1 between 15:09 and 15:20 isolated between ranges 82 km to 88 km at each time frame given by the timestamp. Tick marks on the x-axis and y-axis are separated by 500 m. Updraught contours are 2 (grey), 4 (black), 6 (red) and 8 m s^{-1} (magenta). Wind vectors show the in-cloud motion and are thinned to every 4th grid point. The length of an 8 m s^{-1} vector is shown in the first panel for scale. Dashed black line indicates 2.5 km freezing level from 12Z Camborne, UK sounding.

from about 40 dBZ over a period of 15 minutes to 20 - 25 dBZ, as shown in Figures 6.17 and 6.18. Maximum reflectivity below 3 km also weakened over the full observation period of 30 minutes. Associated with the reflectivity column were mostly blobs of 2 and 4 m s^{-1} updraughts between 3 and 7.5 km height with some small local regions of 6 m s^{-1} updraught seen in Figure 6.17. Over a period of 15 minutes the updraughts weakened as final remnants of updraught ascended, resided in the upper levels and decayed, shown in Figures 6.18 and 6.19.

After 15:20 downdraught became dominant below 5 km, descended slantwise from the west (upper left) to east (lower right). At about 2 km this downdraught met a weak updraught from a small pulse of development from the east side of the cell. Between 15:09 and 15:13 there appeared to be a counter clockwise vortex present between 4 and 6.5 km in the west of the cell. The ascending part of this circulation appeared to be distinct from the larger region of ascent to the east of it. This circulation weakened thereafter as the downdraught became dominant.

A second vortex circulation became present between 15:26 and 15:31 centred at 5 km, also counter clockwise rotating, seen in Figure 6.18. Associated with these vortex circulations was shear, seen by changes in horizontal Doppler velocity direction with height. Between 15:31 and 15:39 there was an increase in updraught centred at 6 km height in the west of the cell. This was short lived and above 6 km height whilst downdraught persisted below. Downdraughts were also present throughout each time frame, assumed to be penetrating into the upper cloud region from cloud top.

ZDR is shown in Figure 6.20 between 15:09 and 15:20, Figure 6.21 between 15:20 and 15:30 and Figure 6.22 between 15:30 and 15:39. Figure 6.20 shows higher ZDR signal below 2.5 km indicating precipitation when combined with the reflectivity.

The low reflectivity signal and ZDR of about 1 - 1.5 dB between 15:36 and 15:39 (Figure 6.22) near cloud top could be due to noise in a low SNR region. Figures 6.21 and 6.22 show ZDR of around 0.5 dB throughout the cloud as reflectivity decreased, located in a region of downdraught potentially indicating the presence of aggregates. EDR shown in Figure 6.23, was most prominent in C1 between 15:09 and 15:18, thereafter the signal weakened in the interior of the cloud with a slight increase at cloud top at

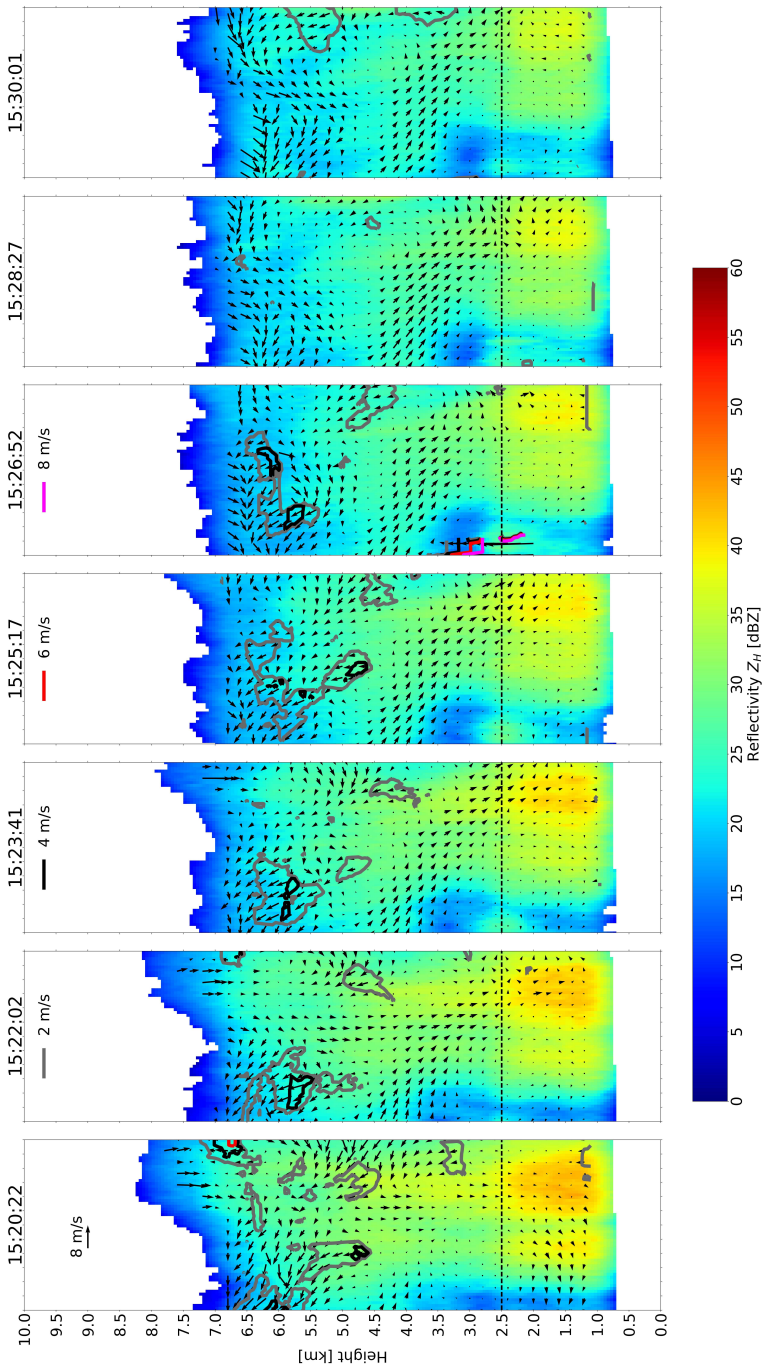

Figure 6.18: As in Figure 6.17 but for the time period 15:20 until 15:30.

15:28 (Figure 6.24) and a weak region at 3.5 km between 15:31 and 15:39 (Figure 6.25).

EDR structures tended to be vertically elongated with streaks of strong EDR and appeared to weaken over time as did the reflectivity. The streaks of EDR at 15:09 appeared to be located between 5 and 6.5 km height with strong upward motion that decreased in magnitude, seen in Figure 6.23. This flow also had a horizontal component

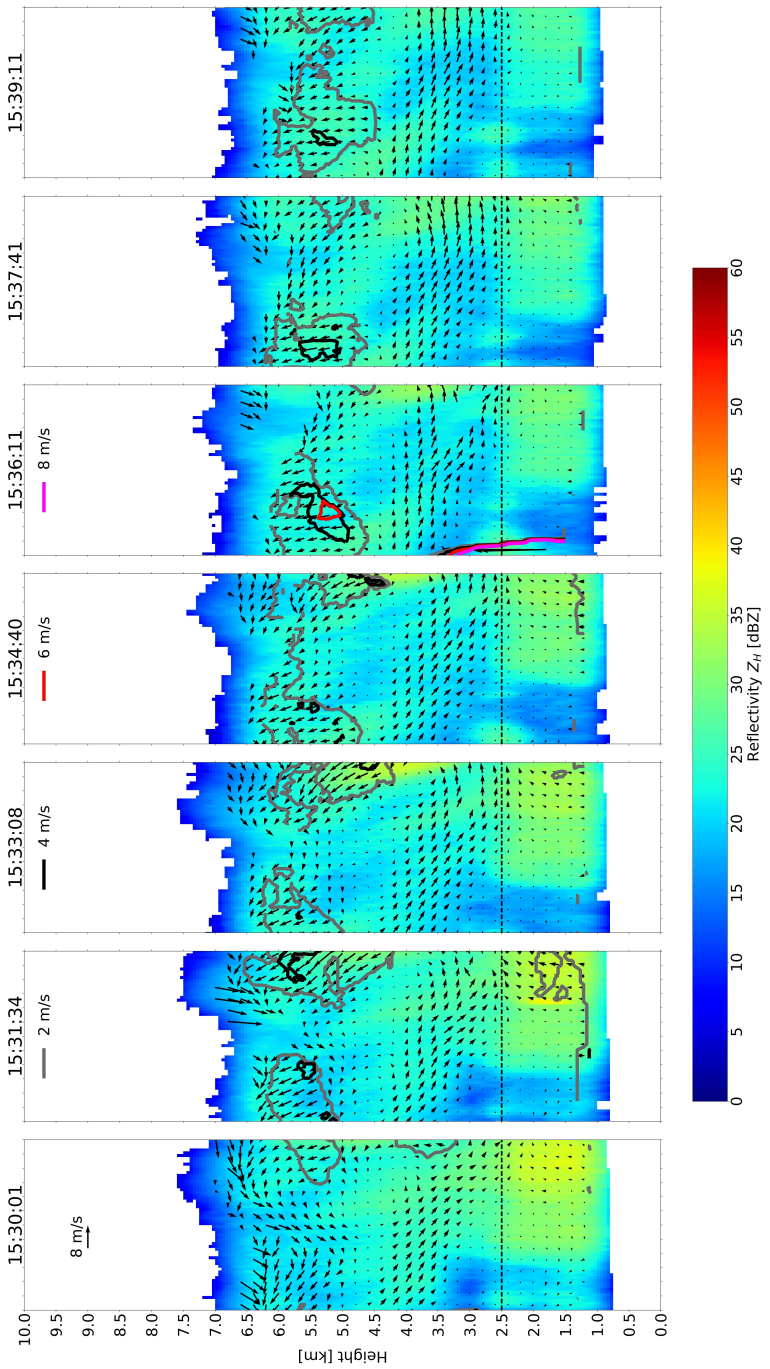

Figure 6.19: As in Figure 6.17 but for the time period 15:30 until 15:39.

to the west near the top of the EDR structure. The weaker EDR structure located at 4.5 to 5.5 km height was associated with downwards motion and resided to the east of the vortex.

At 15:11 and 15:13 this structure appeared to intensify as the vortex grew and became intense with EDR up to 0.1 m^2 s^{-3} in a 'core' with the upward part of the vortex

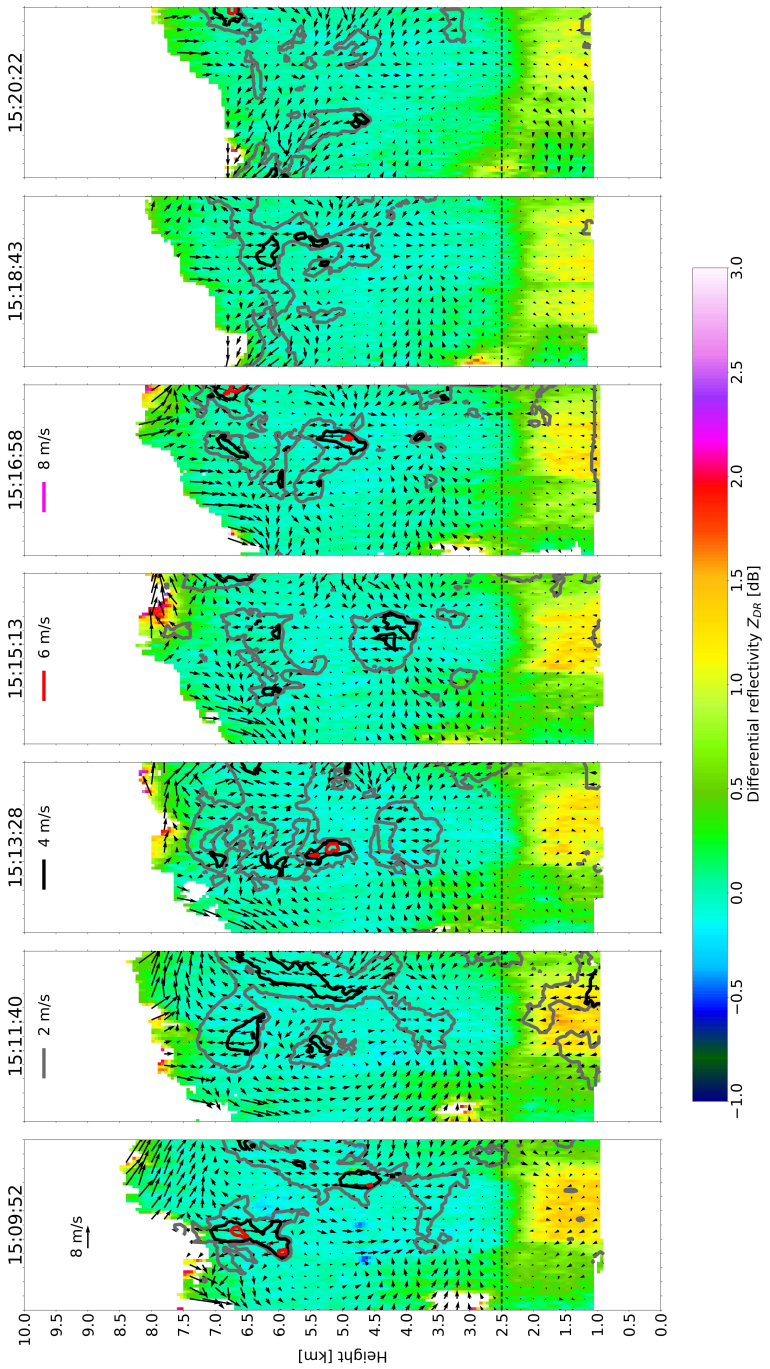

Figure 6.20: C1 as in Figure 6.17 but for Differential Reflectivity (ZDR) in dB between 15:09 and 15:20.

meeting the downward motion associated with the high reflectivity precipitation shaft. This structure then weakened over time as did the vortex circulation and a smaller EDR structure intensified between 15:15 and 15:16 associated with a downdraught located between ascent, a region of horizontal gradient in the vertical velocity.

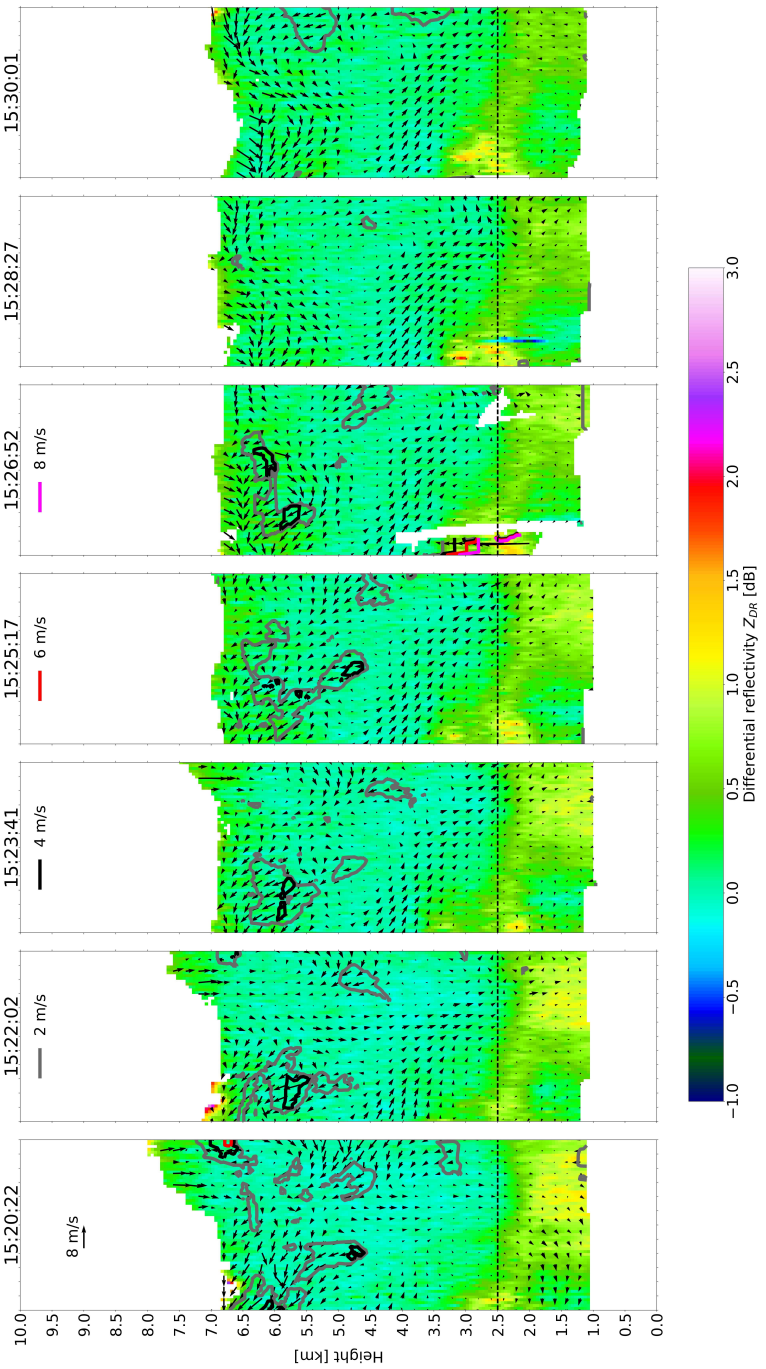

Figure 6.21: As in Figure 6.20 but for the time period between 15:20 and 15:30.

As the flow circulations within the cloud weakened and contain larger scale circulations, the EDR tended to decrease in magnitude and decay from 15:23 on-wards, clearly seen in Figures 6.24 and 6.25. EDR production in this case was therefore likely due to horizontal shear associated with vortical circulations.

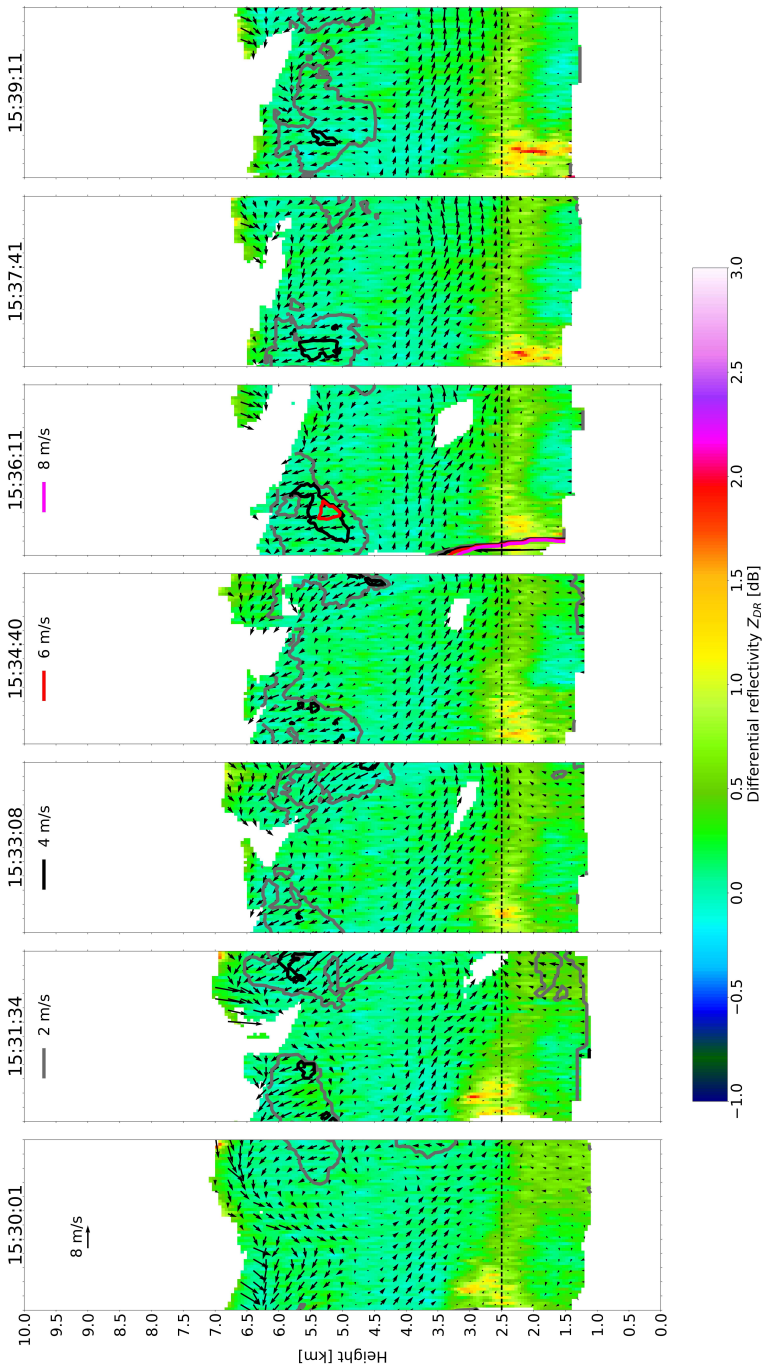

Figure 6.22: As in Figure 6.20 but for the time period between 15:30 and 15:39.

6.6.2 Cell 2

Cell 2 (C2) was located between 88 and 96.5 km range and is shown in Figure 6.26 between 15:09 and 15:20, Figure 6.27 between 15:20 and 15:30 and Figure 6.28 between 15:30 and 15:39. C2 had substantial echo top height, updraught, reflectivity

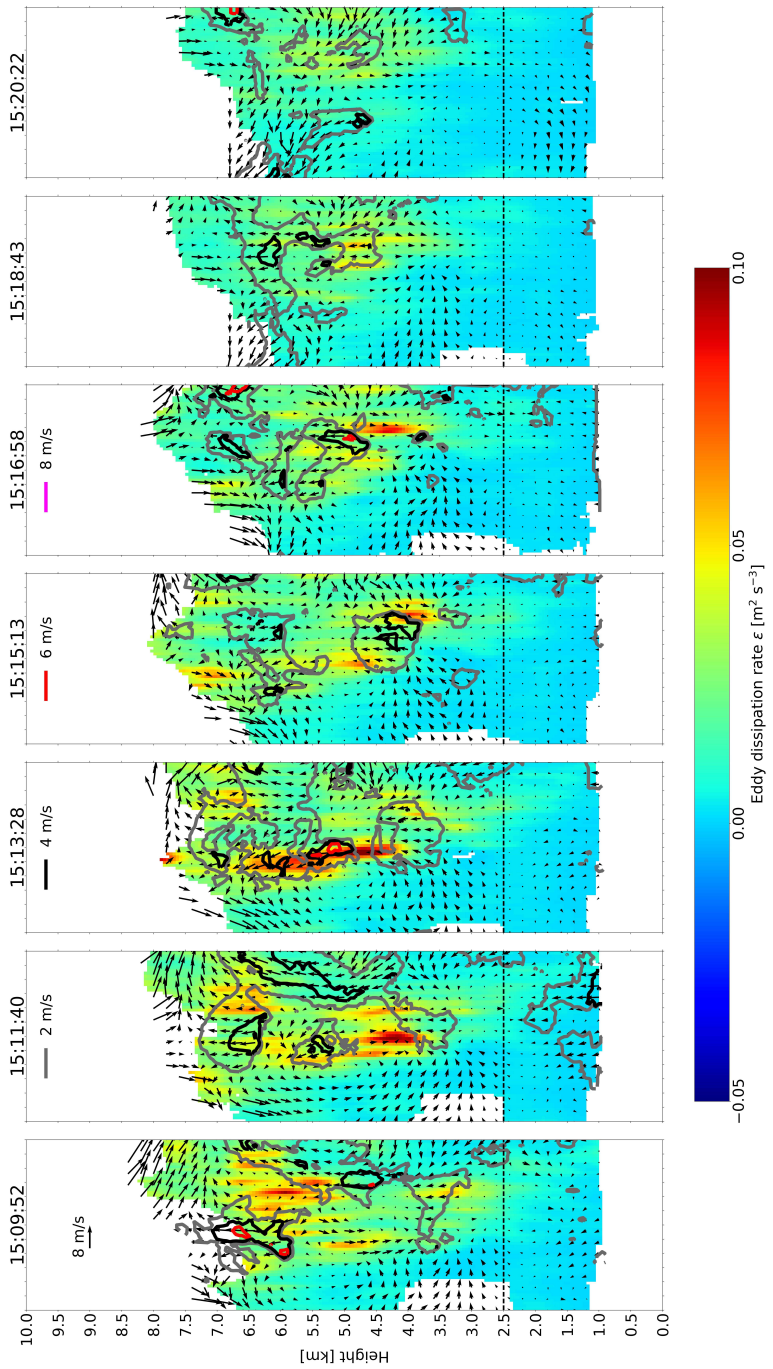

Figure 6.23: C1 as in Figure 6.17 but for Eddy Dissipation Rate (ε) in $m^2\ s^{-3}$ between 15:09 and 15:20.

and EDR development over the observation period. C2 had clear intensification from 15:09 to 15:30 at which point an overshooting top occurred, with updraughts ascending throughout this period. At 15:28 a second pulse of intensification appeared to have occurred with an increase in reflectivity, echo top height and increase in updraught

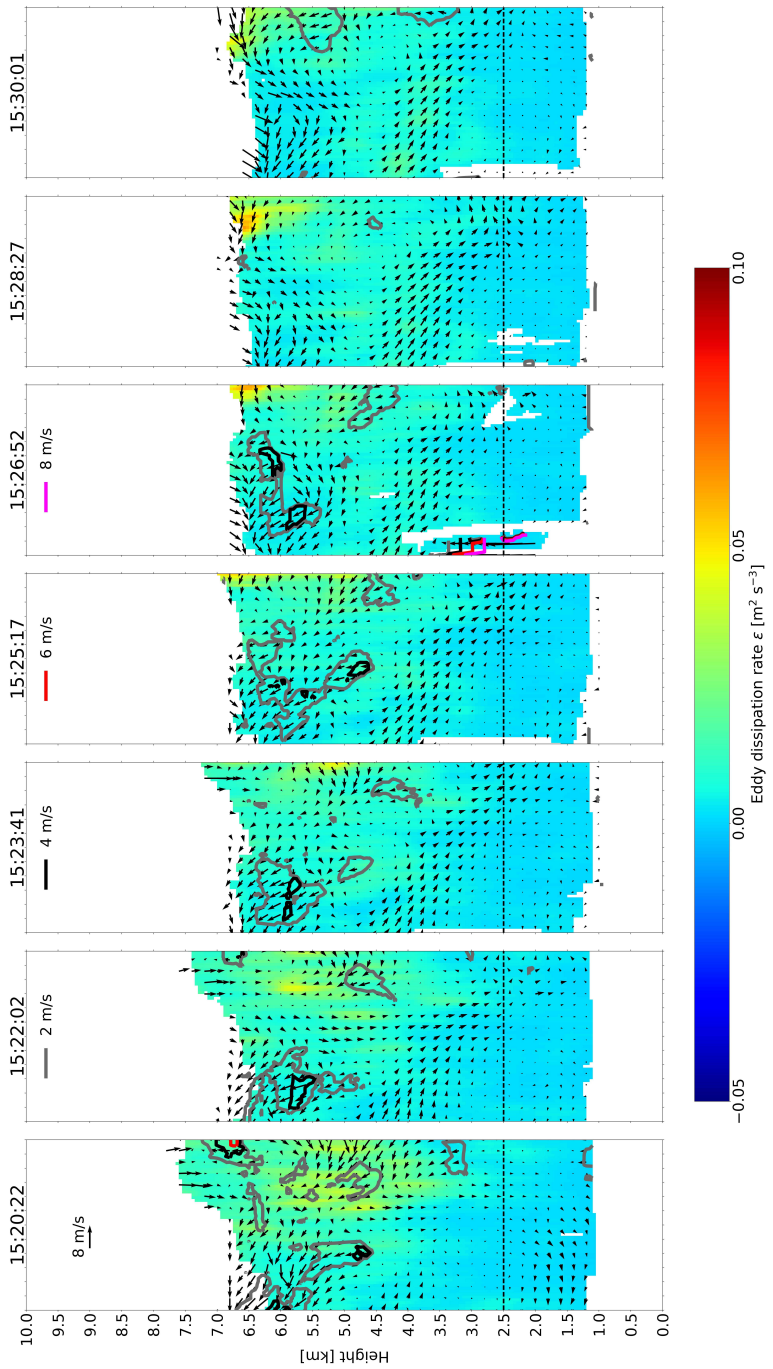

Figure 6.24: As in Figure 6.23 but for the time period between 15:20 and 15:30.

magnitude and spatial extent. From 15:33 on-wards C2 appeared to decay with decreasing reflectivity and remnants of 'fragments' of updraught.

Reflectivity in C2 increased from around 45 dBZ to 55 dBZ between 15:09 and 15:23. A reflectivity signal with magnitude between 40 - 45 dBZ also ascended from around 3 km up to 7.5 km whilst the 0 dBZ echo top maintained a stable height of

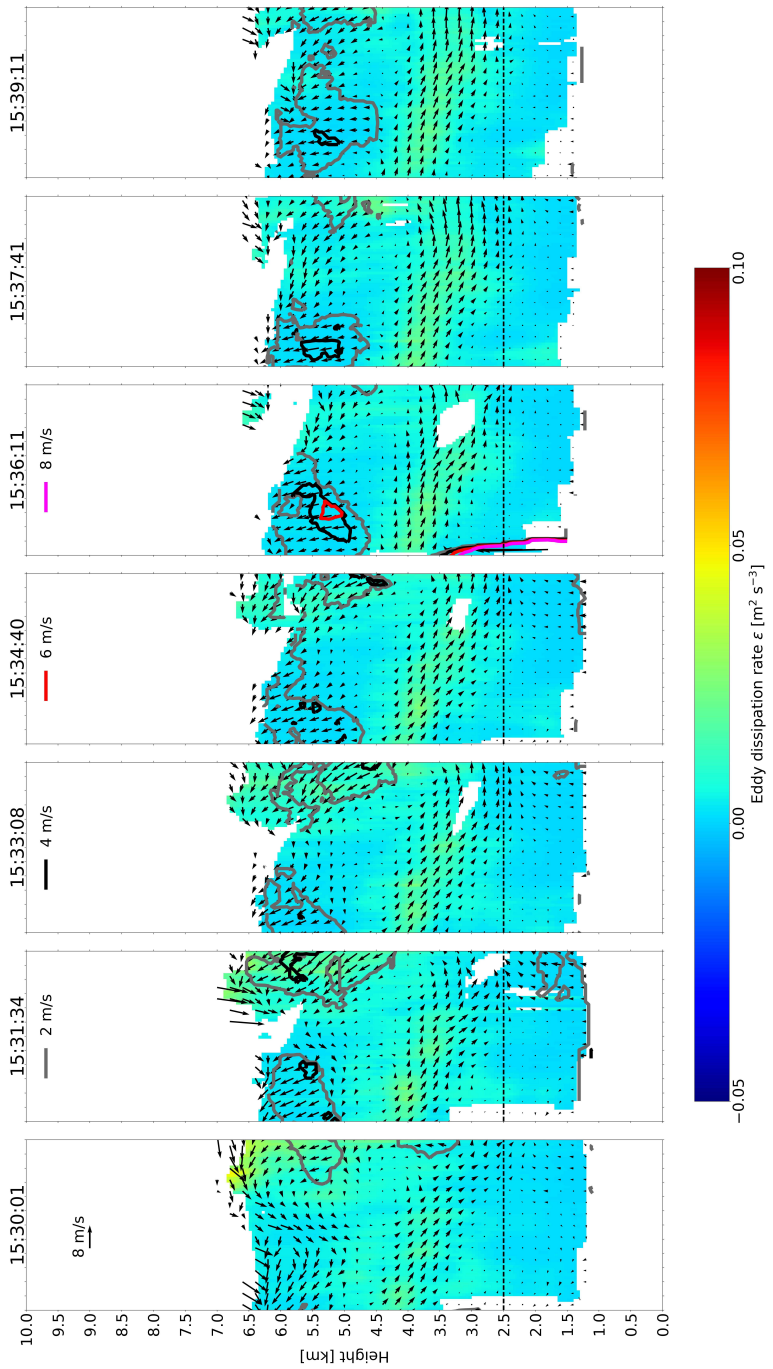

Figure 6.25: As in Figure 6.23 but for the time period between 15:20 and 15:30.

8.5 km. The high reflectivity values were indicative of heavy rain reaching the surface. Associated with the ascent of reflectivity were multiple updraught structures shown by the black and red contour lines indicating velocities of 4 and 6 m s^{-1}. These updraughts with blob-like structure appeared to ascend ahead of and within the ascending region of reflectivity above 3 km height. A clockwise vortical circulation was present

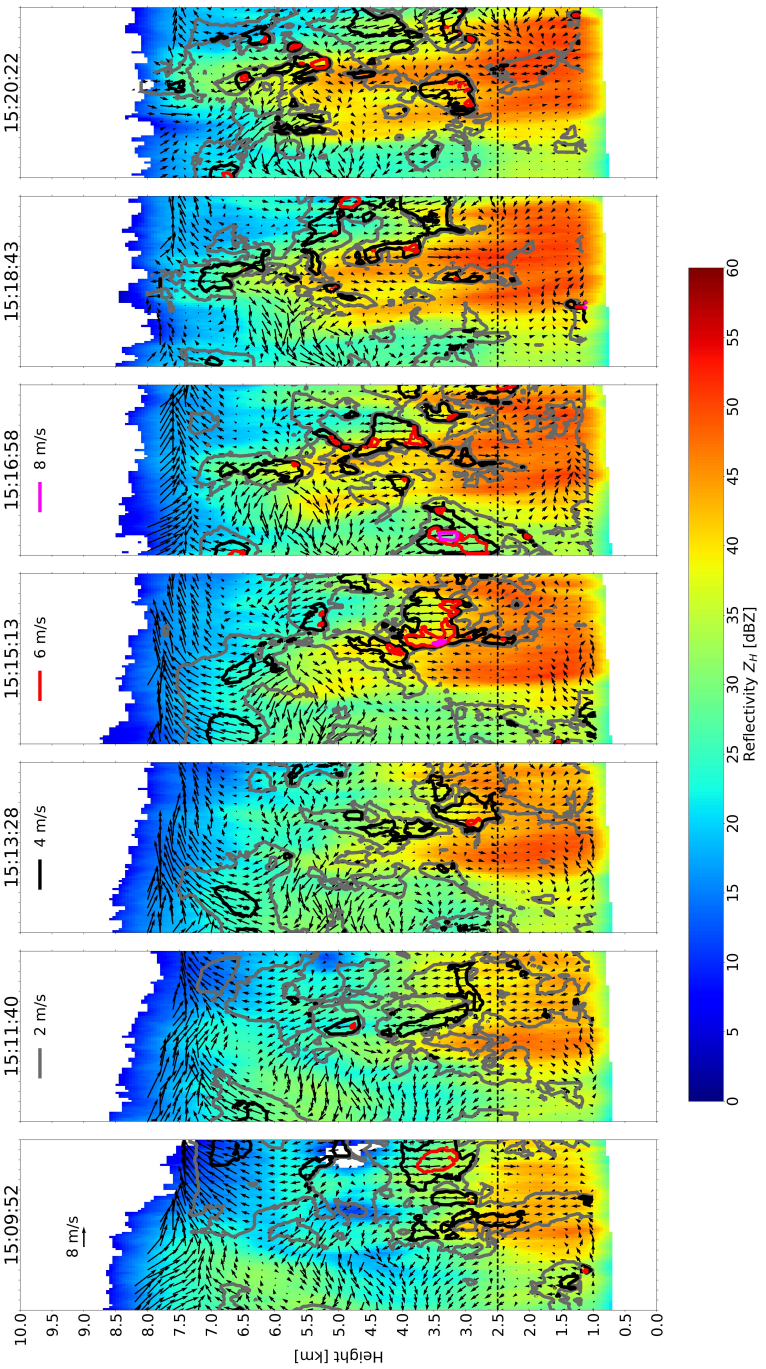

Figure 6.26: Reflectivity in dBZ for C2 between 15:09 and 15:20 isolated between ranges 88 km to 96.5 km at each time frame given by the timestamp. Tick marks on the x-axis and y-axis are separated by 500 m. Updraught contours are 2 (grey), 4 (black), 6 (red) and 8 m s^{-1} (magenta). Wind vectors show the in-cloud motion and are thinned to every 4th grid point. The length of an 8 m s^{-1} vector is shown in the first panel for scale. Dashed black line indicates 2.5 km freezing level from 12Z Camborne, UK sounding.

between 15:09 and 15:16, with a clear circulation pattern at 15:15, located between 5.5 and 7.5 km height, which then appeared to become distorted as an updraught pulse ascended into it at 15:16 on-wards. There were some local regions of downdraughts below updraughts co-located with reflectivity cores.

Between 15:23 and 15:26 there were multiple updraught structures that existed between 3 and 8 km height and up to 8.5 km height as the echo top began to overshoot, seen in Figure 6.27. At 15:30 a strong more vertically contiguous updraught was present that appeared to have formed from the separate structures at 15:28. This updraught extended 3 km in depth then became distorted at 15:31 and began to break down fairly quickly into separate updraughts. This consistent upwards flow appeared to have a downdraught associated with it that was present below the updraught centred at 4 km height and associated with a reflectivity streak. It is evident that the pulses of updraught formed into a contiguous feature and were associated with the overshooting top, as echo top height ascended between 15:23 and 15:31, seen in Figures 6.27 and 6.28. The reflectivity during this time did not appear to increase indicating surface rainfall intensity did not change as the cell was overshooting and updraught intensified. The atmospheric sounding shows a rapid decrease of dew point temperature with height indicating a layer of drier air between 3 to 6.5 km at heights the plume-like updraught was located. This drier air could aid evaporation at these heights. From 15:30 downdraught began to dominate heights below 3 km, flowing downwards into the reflectivity cells. Updraught blobs remained in the upper region of cloud as the overshooting top began to fall back to the quiescent echo top height of 8 km.

Given the uniqueness of the data set introduced in this chapter, it provided an opportunity to study individual convective cells in detail which experienced overshooting tops and lightning during their lifetime. The pulse like behaviour noted in MacGorman *et al.* (2016) and Borque *et al.* (2020) is similarly observed in cell 2 and cell 3 (discussed below). A clear pattern of propagation of multiple updraught pulses ascending across the time series was observed in C2 over time with a clear bottom left to upper right slope looking across the frames in Figures 6.26, 6.27 and 6.28. These structures then maintained a fairly consistent altitude. Furthermore, these structures were remarkably

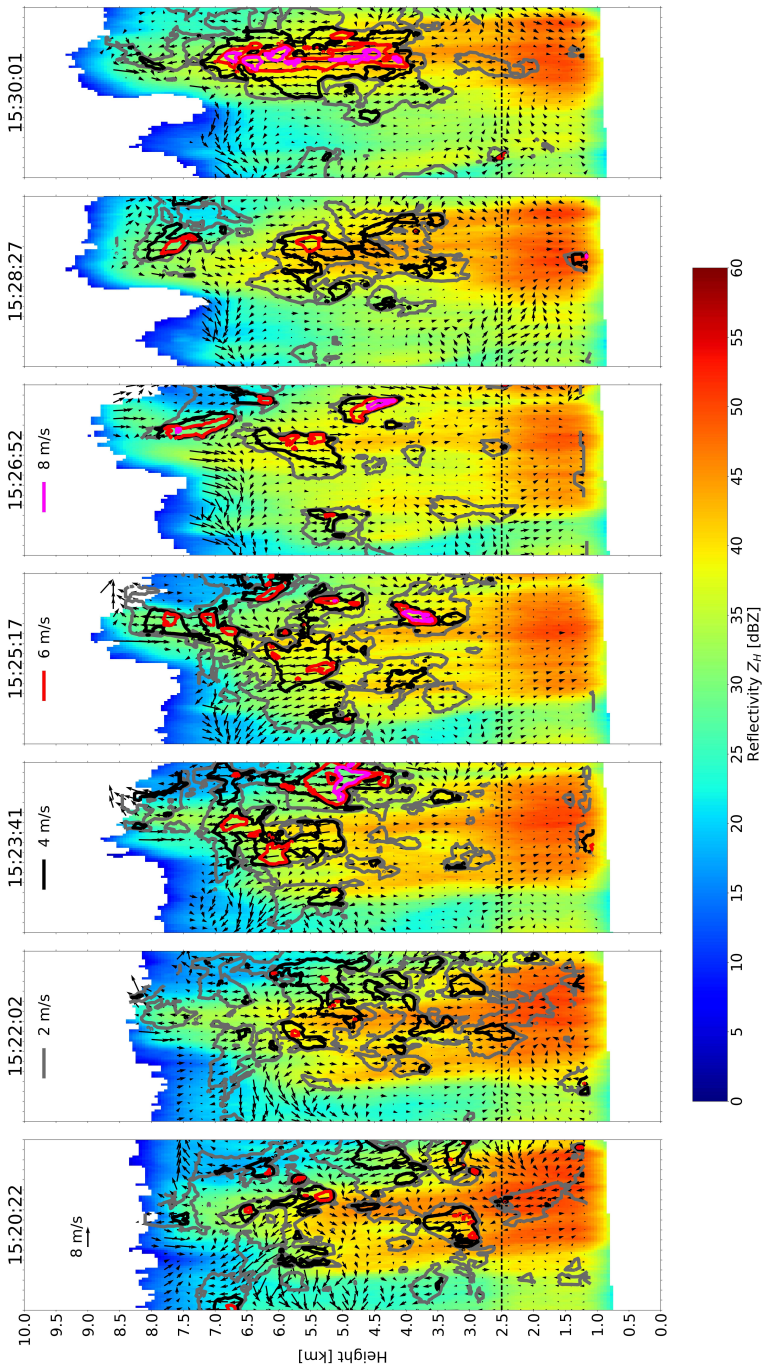

Figure 6.27: As in Figure 6.26 but for the time period between 15:20 and 15:30.

consistent in space, highlighted by the composite averaging because for an updraught to be present in the composite average it must be at least 4 m s^{-1} in each individual scan, and in time due to the frame to frame consistency. These are discussed more in section 6.7.1.

Figure 6.29 shows zoomed in UK radar composites of precipitation, similar to Fig-

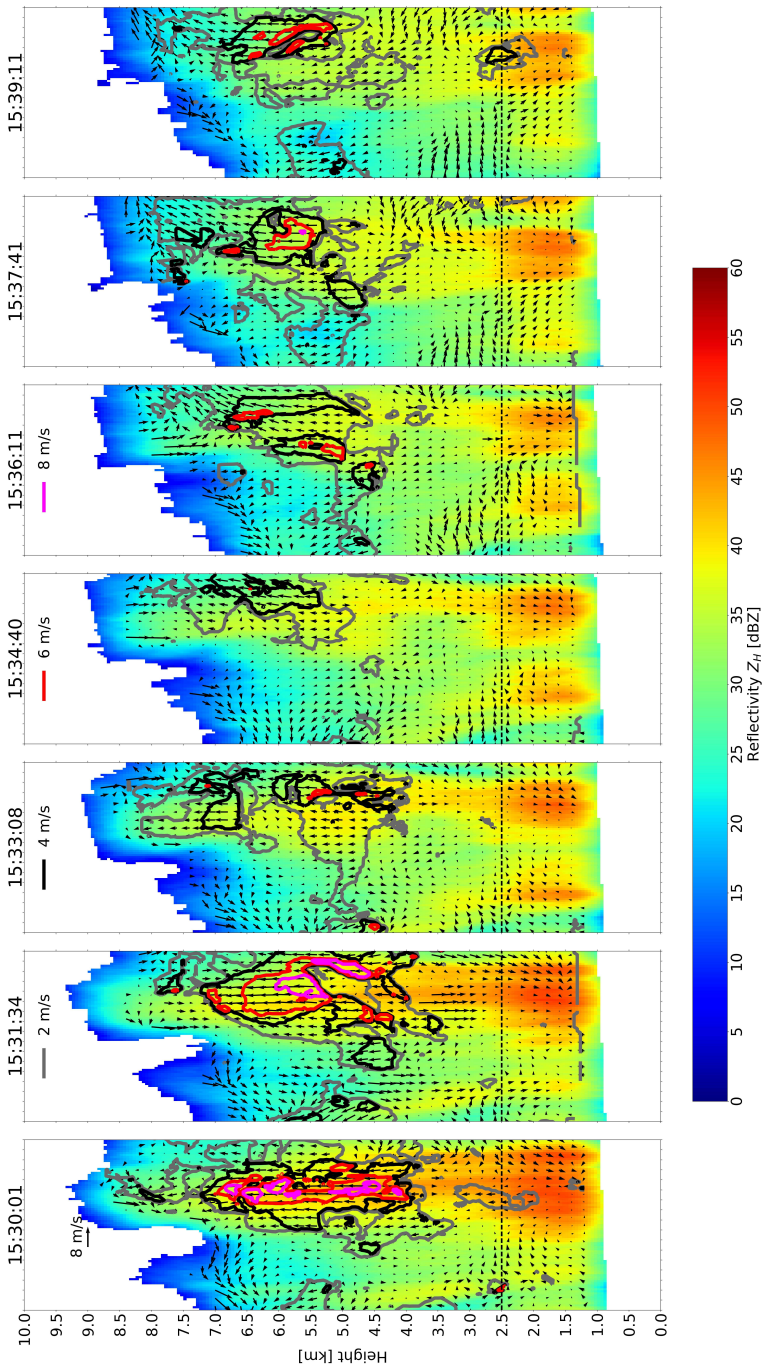

Figure 6.28: As in Figure 6.26 but for the time period between 15:30 and 15:39.

ure 6.7, but for times between 1510 and 1540 at 5 minute intervals. This shows how the number of lightning strikes measured by the Arrival Time Difference Network (ATD-Net) increased as the convective cell intensified and how they were mainly associated with the central cell, discussed as cell 2 below. The coloured lines, as shown in Figure 6.7 show that there were lightning strikes present as the convective cores were scanned

with CAMRa. Between 1525 and 1535 was when an overshooting top occurred in the central and farthest cell from the radar and at this time there were the most number of lightning strikes.

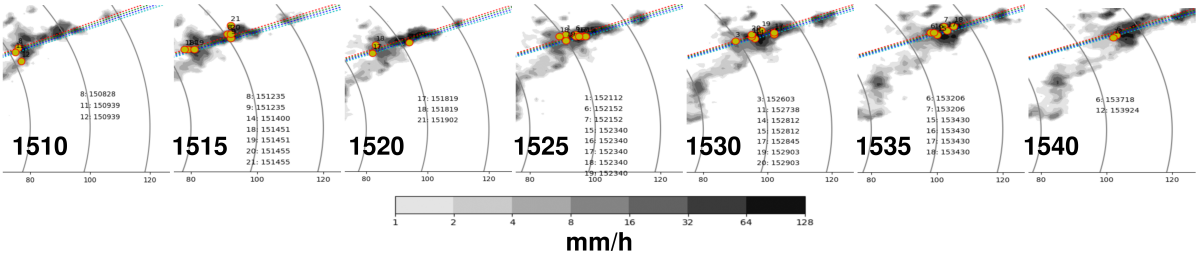

Figure 6.29: Zoomed in UK radar composite of precipitation (in grey scale) between 1510 and 1540 at 10 minute increments with lightning strikes from the Met Office ATDNet (yellow circles) overlaid and strike label number and time annotated. Shows how the number of lightning strikes changed over time and were distributed across the cloud scanned.

ZDR is shown in Figures 6.30, 6.31 and 6.32. ZDR signals indicated that there were some columns of ZDR with values between 1.5 - 2 dB that extended above the freezing level (black dashed line) up to 3 - 3.5 km height, seen in Figures 6.30 and 6.31. The ascent of the higher ZDR values appeared to be co-located with the ascent of the updraught structure between 15:09 and 15:18 located at 2 to 4 km height.

The freezing level at 12Z from the Camborne, UK sounding was located at 2.5 km height. This suggests that the ZDR values extending above 2.5 km height are ZDR columns containing large super-cooled liquid water drops and were co-located with the 50 - 55 dBZ reflectivity column. As the updraughts ascended away from the tops of the ZDR columns shown in Figures 6.31 and 6.32, there was no further advection of hydrometeors seen in the ZDR data. ZDR remained confined to the region below 2 km for the remainder of the observation period, shown in Figure 6.32.

There were some interesting EDR structures in C2, shown in Figures 6.33, 6.34 and 6.35. An EDR structure was present from 15:09 to 15:23 and appeared to grow vertically and horizontally and ascended from around 5 to 7.5 km height, shown in Figure 6.33. This structure appeared to increase in magnitude from 0.05 to 0.1 m^2 s^{-3} over 12 minutes with the EDR intensity mostly increasing between 15:16 and 15:20 when the flow associated with the structure was mostly horizontal and had increased in

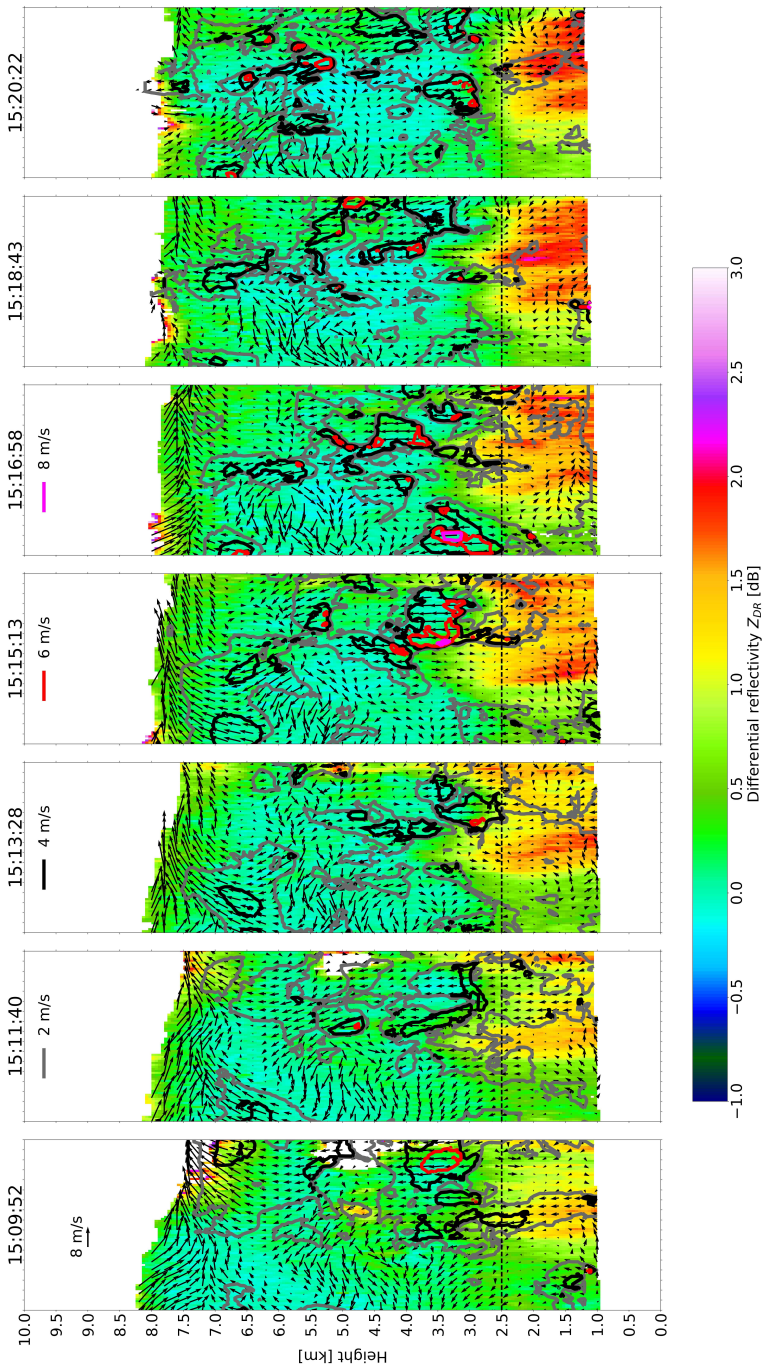

Figure 6.30: C2 as in Figure 6.26 but for Differential Reflectivity (ZDR) in dB between 15:09 and 15:20.

magnitude. This structure co-located with a region of flow with a rotational component also appeared to have an updraught pulse that ascended to the east of it which remained in the low EDR region.

There were no significant EDR signals in the lower regions C2 associated with

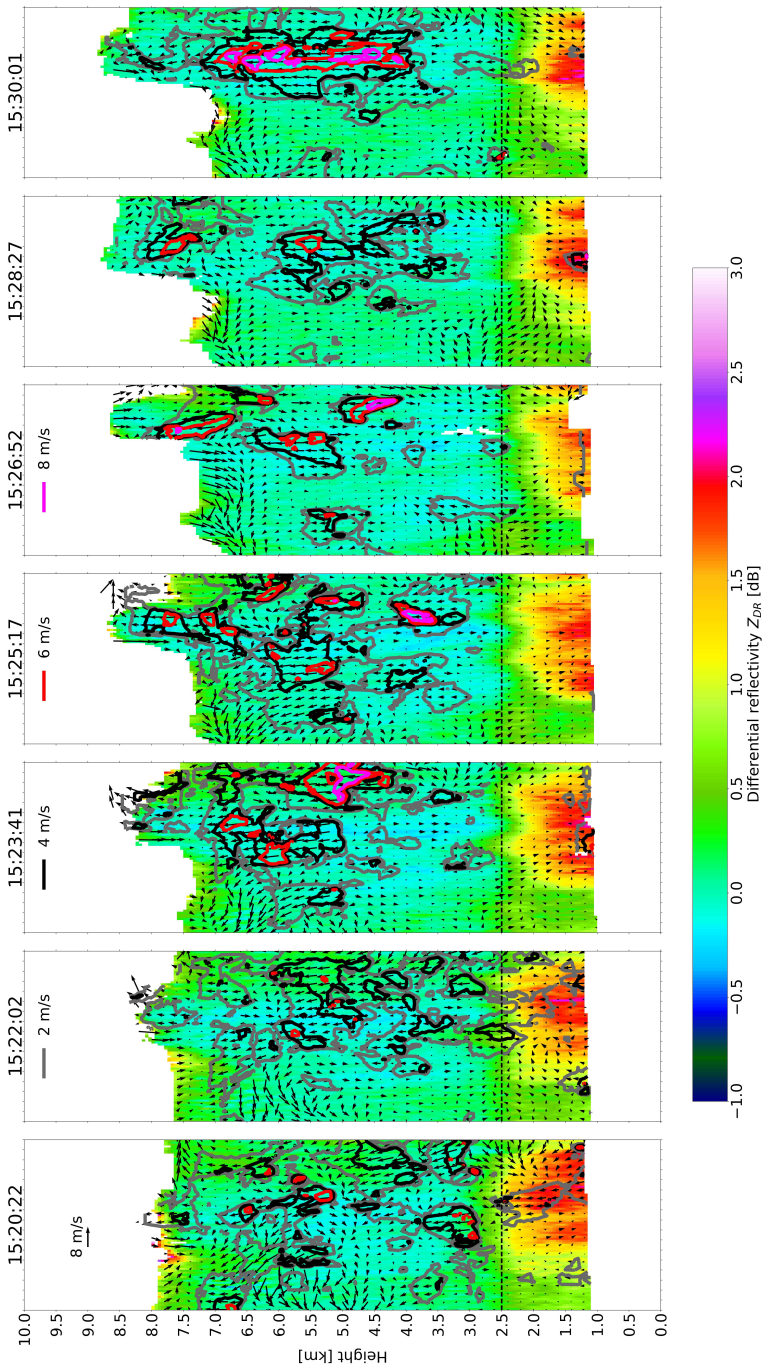

Figure 6.31: As in Figure 6.30 but for the time period between 15:20 and 15:30.

the rising pulses of updraught from the 3 km level seen in Figures 6.33 and 6.34. The structure appeared to rise into the echo top where it dissipated. This structure intensified due to the horizontal and vertical gradient in horizontal velocity across the region (not shown) creating a couplet of positive and negative vorticity. The mean magnitude of vertical shear, which is determined by differentiating the Doppler velocity

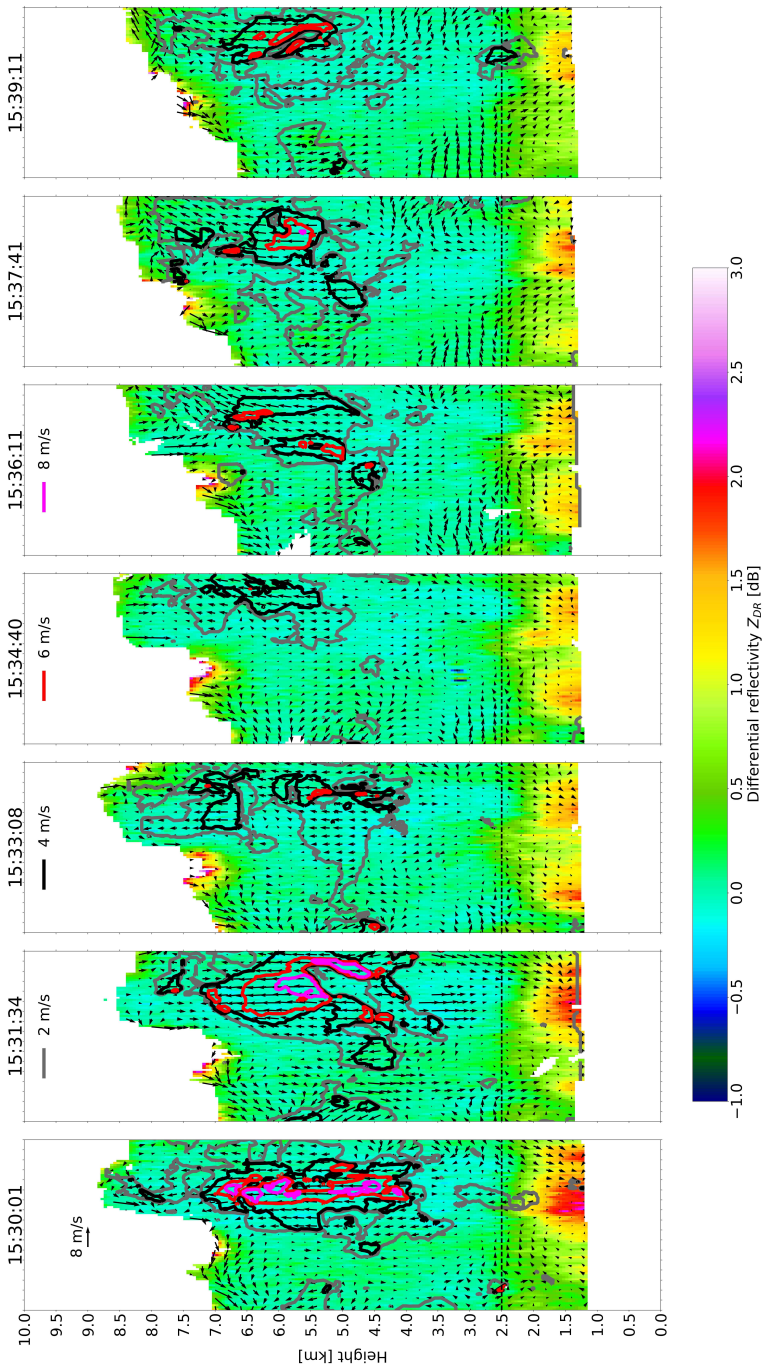

Figure 6.32: As in Figure 6.30 but for the time period between 15:30 and 15:39.

in the elevation direction, has been shown to be correlated with EDR above the updraft (Feist *et al.*, 2019). As the motion within the cell became more dominated by vertical flow due to the strengthening of updraughts and the presence of downdraughts, it appeared that the EDR weakened between 15:23 and 15:26, as the echo top began to overshoot seen in Figure 6.34. In this case EDR appeared to be produced by the shear

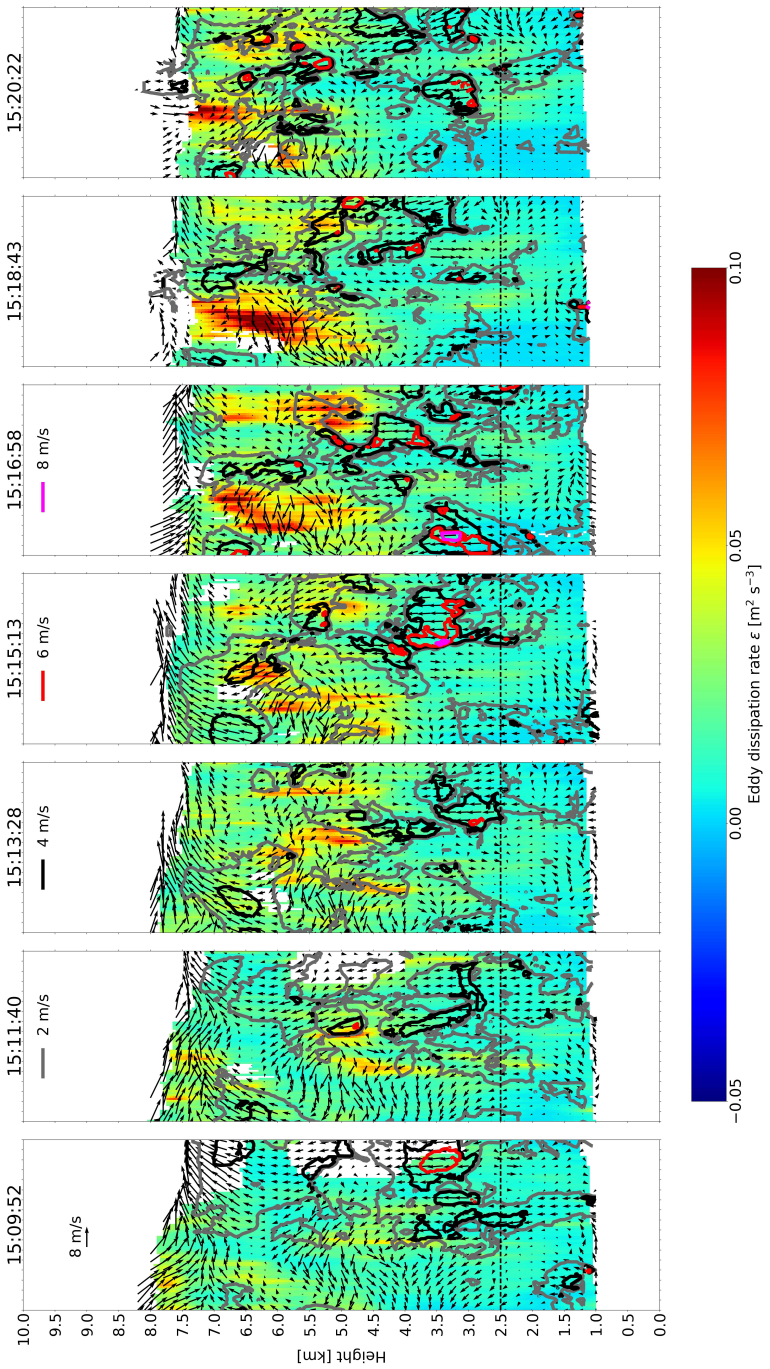

Figure 6.33: C2 as in Figure 6.26 but for Eddy Dissipation Rate (ε) in $m^2\ s^{-3}$ between 15:09 and 15:20.

component due to the vertical gradient of horizontal velocity which is important for the production of turbulent kinetic energy. The stretching and tilting term in equation 1.22 may be a dominant production of vorticity in this case due to the shear of horizontal velocity.

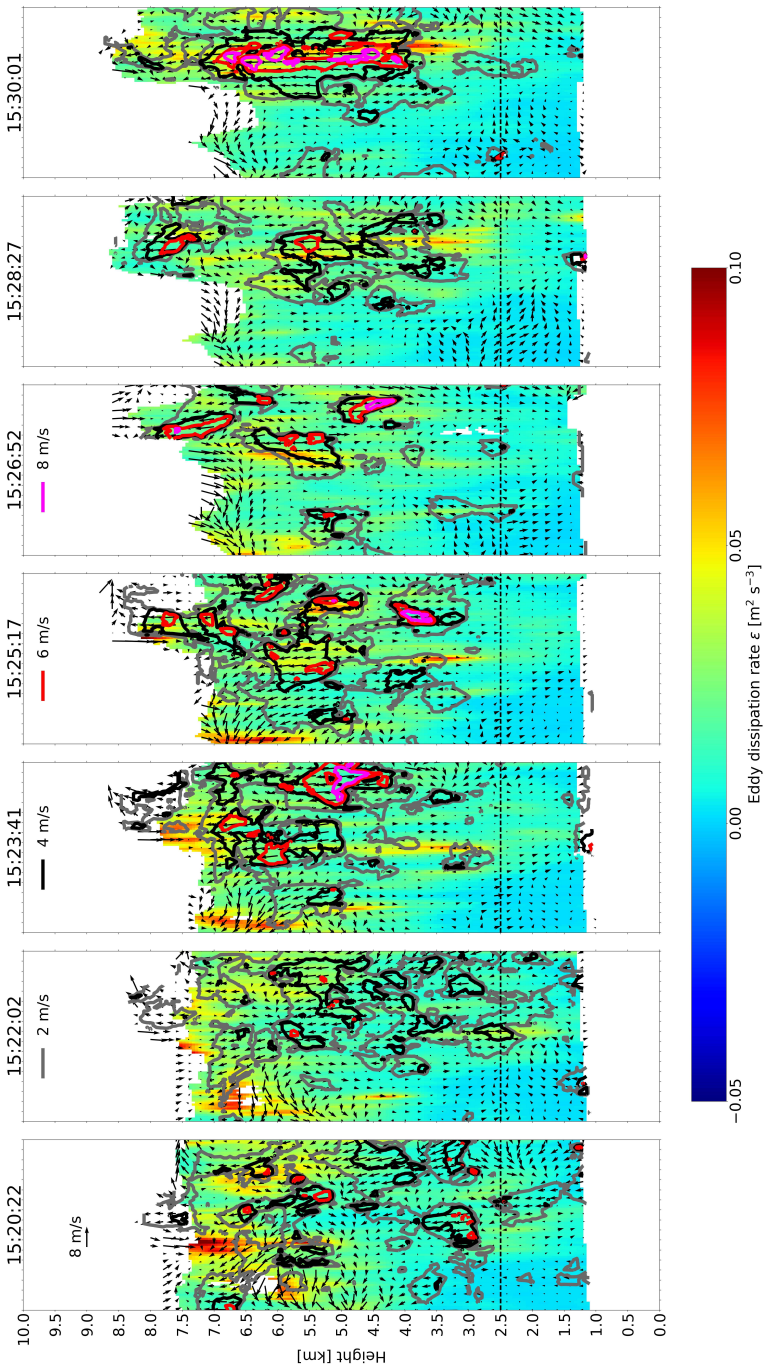

Figure 6.34: As in Figure 6.33 but for the time period between 15:20 and 15:30.

The EDR structure that was elongated between 15:26 and 15:33 was weaker in magnitude than the structure at 15:18, and was more narrow in horizontal extent but appeared to have larger vertical extent in the form of a column, seen in Figures 6.34 and 6.35. As updraught pulses appeared to combine to form a coherent updraught, the EDR structure was co-located with this updraught extending the depth of the

updraught flow. It appeared to be mostly centred with the strongest updraught velocities but as soon as the updraught became distorted and broke down into smaller blobs, the EDR structure also weakened. Horizontal shear was weaker in this region, therefore it is speculated that this EDR structure was less influenced by the shear component but more the buoyant component due to being co-located with updraught. The buoyancy component cannot be observed with radar and further in-cloud thermodynamic measurements would be required to measure temperature perturbations and location compared to updraughts and EDR structures. Buoyancy would indicate that the baroclinic production term in equation 1.22 is the main source of vorticity production.

EDR also appeared to be present in the overshooting top of C2 between 15:23 and 15:37. Between 15:34 and 15:39 (Figure 6.35) there were some smaller EDR structures at heights between 3 km and 7 km that were associated with downdraught and updraught with a horizontal component to the flow. Similarly, near 7 - 7.5 km height where the flow was moving diagonally there was an EDR structure present. These instances point to a dominant shear production component. Feist *et al.* (2019) also found that the 95th percentile of the horizontal gradient of vertical velocity was correlated with the 95th percentile of EDR, with a Pearson correlation value of 0.671 in deep convective clouds.

6.6.3 Cell 3

Cell 3 (C3) was located between 96.5 and 105 km range and is shown in Figure 6.36 between 15:09 and 15:20, Figure 6.37 between 15:20 and 15:30 and Figure 6.38 between 15:30 and 15:39. C3 was similar to C2 in that it was mature when scanning started, but then weakened for a short period of 6 minutes before it intensified again for a further 12 minutes. C3 also had an overshooting top and contained multiple updraught pulses.

At 15:09 there was an updraught present between 3 km and 6.5 km height that was formed of multiple updraught fragments of 4 m s^{-1} and greater, also co-located above a ZDR column seen in Figure 6.39. This updraught was associated with a reflectivity cell and was located in the upper region of C3 that was sheared to the east. At the

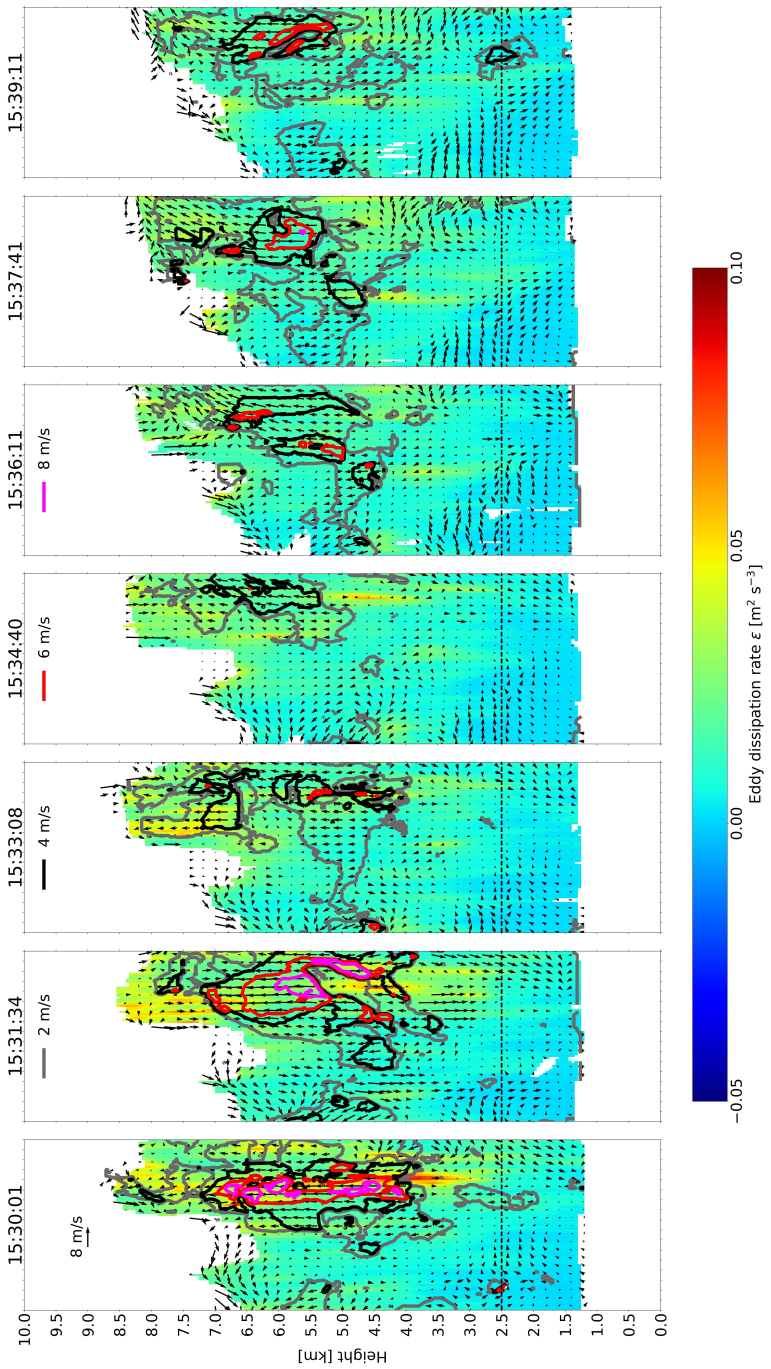

Figure 6.35: As in Figure 6.33 but for the time period between 15:30 and 15:39.

top of the 35 - 40 dBZ reflectivity and to the east of the updraught, as the updraught decayed there was a vortical circulation present between 5.5 and 7 km height. This clockwise circulation, again was associated with shear near the echo top, clearly evident in the flow and by the sheared reflectivity cell. As this reflectivity core began to decay at 15:15, the vortical circulation deformed but then returned with a clear circulation

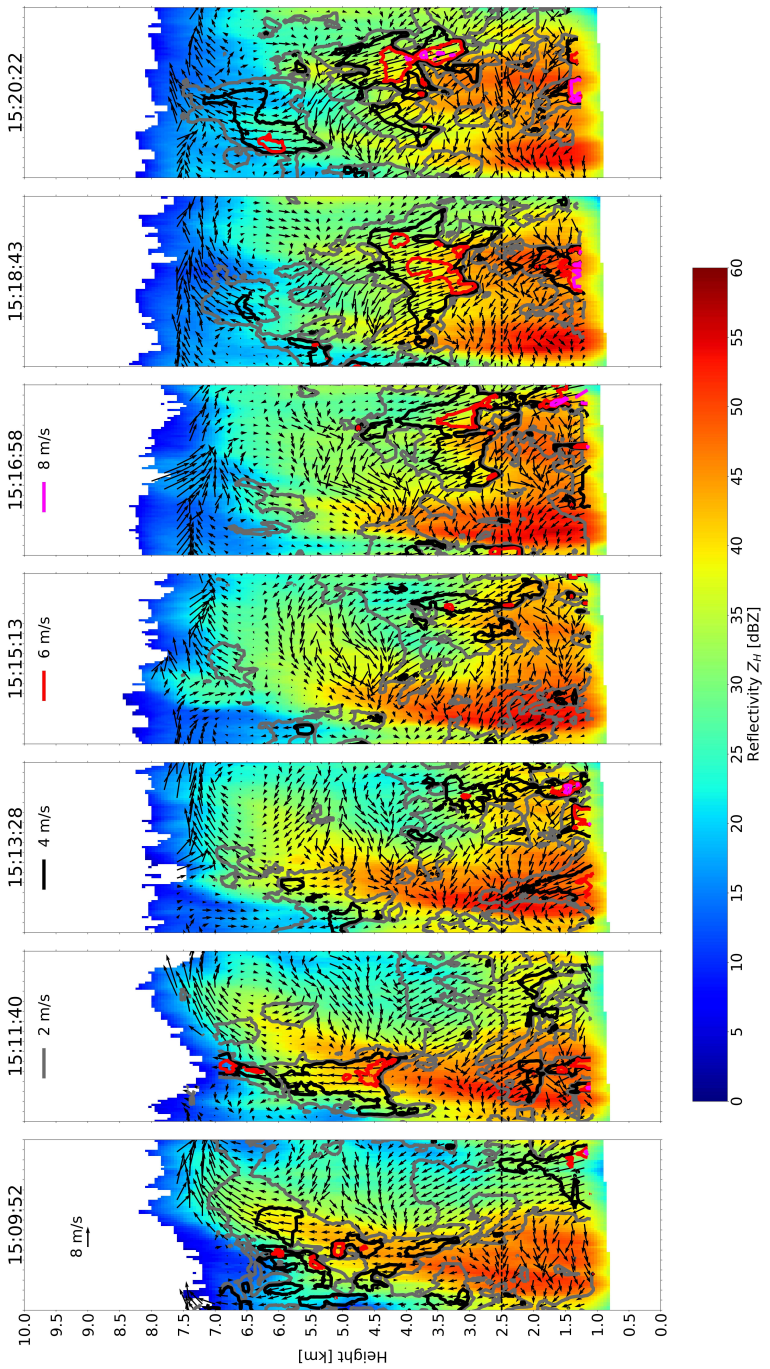

Figure 6.36: Reflectivity in dBZ for C3 between 15:09 and 15:20 isolated between ranges 96.5 km to 105 km at each time frame given by the timestamp. Tick marks on the x-axis and y-axis are separated by 500 m. Updraught contours are 2 (grey), 4 (black), 6 (red) and 8 m s^{-1} (magenta). Wind vectors show the in-cloud motion and are thinned to every 4th grid point. The length of an 8 m s^{-1} vector is shown in the first panel for scale. Dashed black line indicates 2.5 km freezing level from 12Z Camborne, UK sounding.

between 15:16 and 15:22, shown in Figures 6.36 and 6.37.

From 15:09 to 15:15 a region of fairly uniform upward motion can be seen in the east of the cell up to 4 km. By 15:15 a reflectivity core had intensified to the east of the decaying core. Co-located with this cell was an updraught structure that appeared to ascend ahead of the cell, rising at the top of the 35 - 40 dBZ reflectivity signal as blobs and in a region of developing ZDR signal forming a column above the freezing level seen in Figures 6.39 and 6.40.

As the updraught feature ascended from 2.5 km it grew in size, both horizontally and vertically, but then appeared to break down somewhat into smaller structures shown in Figure 6.36. Over this time period the ZDR column peaked in height, seen in Figure 6.40. This cell intensified over the following 15 minutes as multiple updraught pulses ascended through the 3 to 7.5 km height region of C3, seen throughout Figures 6.36, 6.37 and 6.38. At times these updraughts intensified, shown by the 6 (red) and 8 (magenta) m s^{-1} contours, as if having pulses of intensity. It is the development and ascent of this updraught structure that appeared to deform the vortical circulation above it. As updraught pulses ascended away from the top of the ZDR column, the ZDR column descended in height seen in Figure 6.41.

At 15:31 the echo top height of C3 peaked after overshooting from 15:26 to 15:31. From hereon the echo top descended between 500 m - 1 km back to the steady in time echo top (stable) height that existed prior to the overshoot, seen in Figure 6.28. The stable echo top height is similar to the tropopause height of 8 - 9 km seen as temperature begins to increase in the 12Z Camborne, UK sounding. A parcel lifted using this sounding adjusted for the surface and dew point temperature (20°C and 14°C respectively) at 15Z near the location of the clouds results in an equilibrium level of 8.6 km height. Reflectivity can be seen reaching this height in C2 and C3. From 15:31 on-wards the number of updraught structures had decreased in the cell and near the end of scanning there was one structure that resided at about 5 km height. Similarly to C2, there was a clear lower left to upper right (seen by looking across the frames as time progresses) ascent of updraught pulses seen in the frames, indicating C3 was developing through a series of ascending updraught pulses with some short bursts of

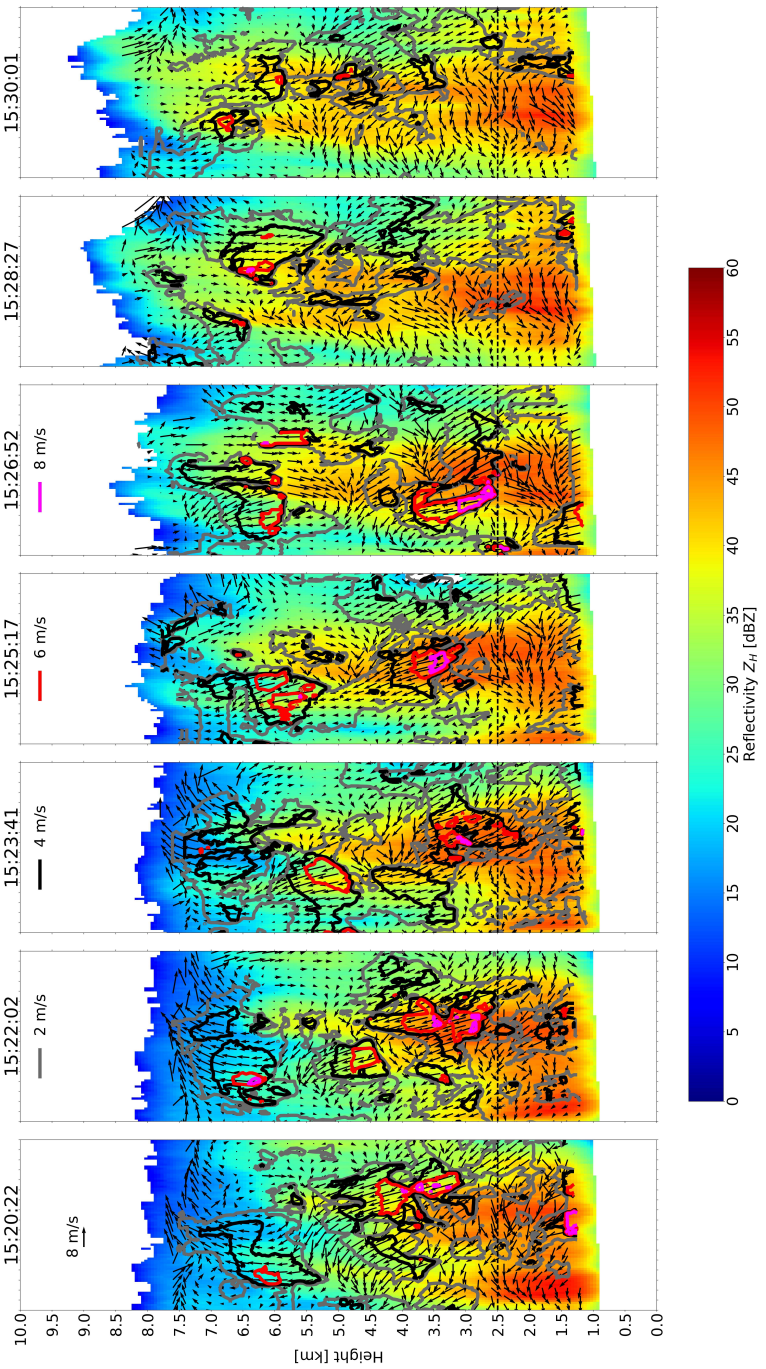

Figure 6.37: As in Figure 6.36 but for the time period between 15:20 and 15:30.

higher updraught velocities, further discussed in section 6.7.1.

Between 15:09 and 15:20 there was an EDR structure that had large vertical extent of 3 - 4 km and narrow horizontal extent, based on EDR values greater than 0.05 m^2 s^{-3} shown in Figure 6.42. This EDR structure did not appear to be associated with a strong updraught but rather downdraught and air motion that had a horizontal

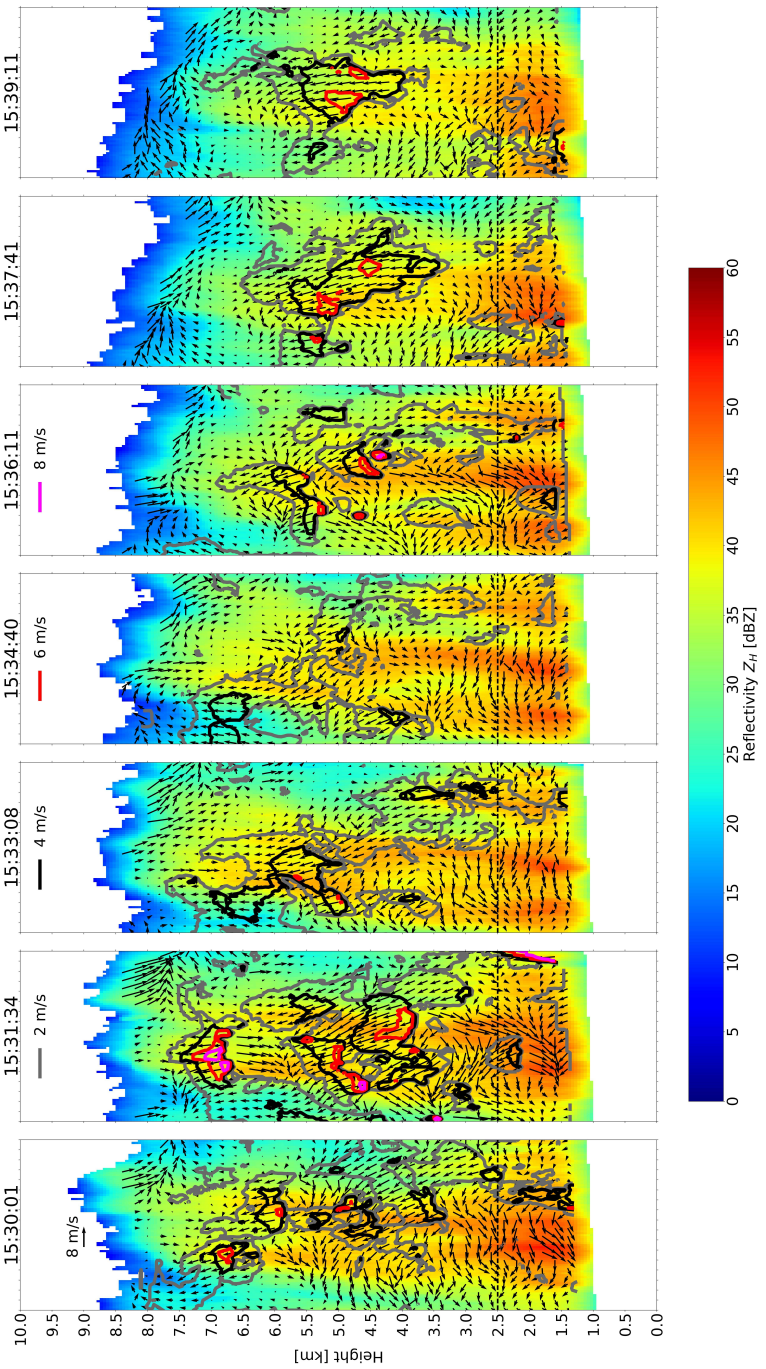

Figure 6.38: As in Figure 6.36 but for the time period between 15:30 and 15:39.

component. The magnitude of the EDR appeared to increase (shown by the stronger red colours) as the flow had more rotational component, as seen at 15:15 near 6 - 6.5 km height. Between 15:16 and 15:18 there was a slight weakening of EDR structures and a vortical circulation could be seen located near the echo top. As this vortical circulation was displaced by an ascending updraught, EDR structures began to grow

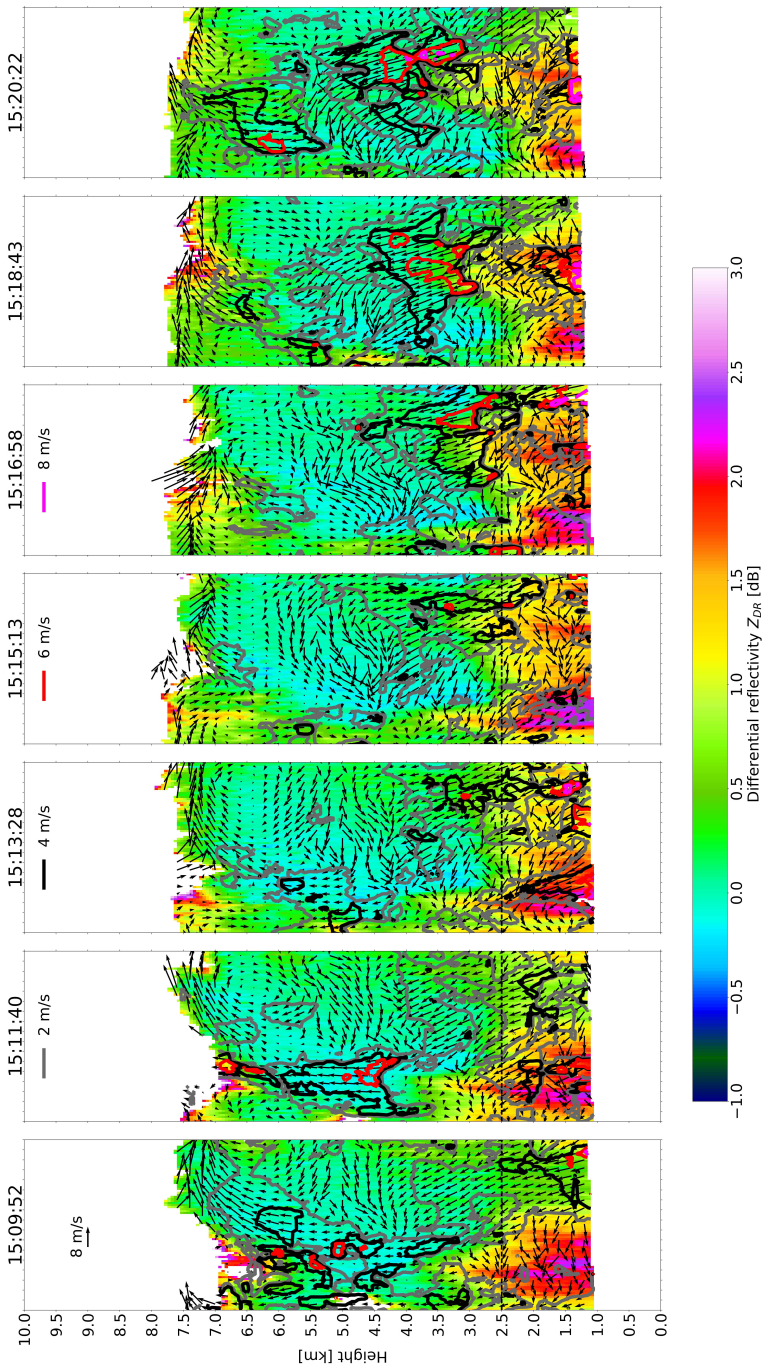

Figure 6.39: C3 as in Figure 6.36 but for Differential Reflectivity (ZDR) in dB between 15:09 and 15:20.

and intensify at 15:20. The strongest EDR structures appeared to be co-located with regions of strong vertical motion in the upper regions of clouds that contained some horizontal component of motion. This structure also appeared to be located in a region of decreasing updraught velocity shown by the motion vectors and the contour levels

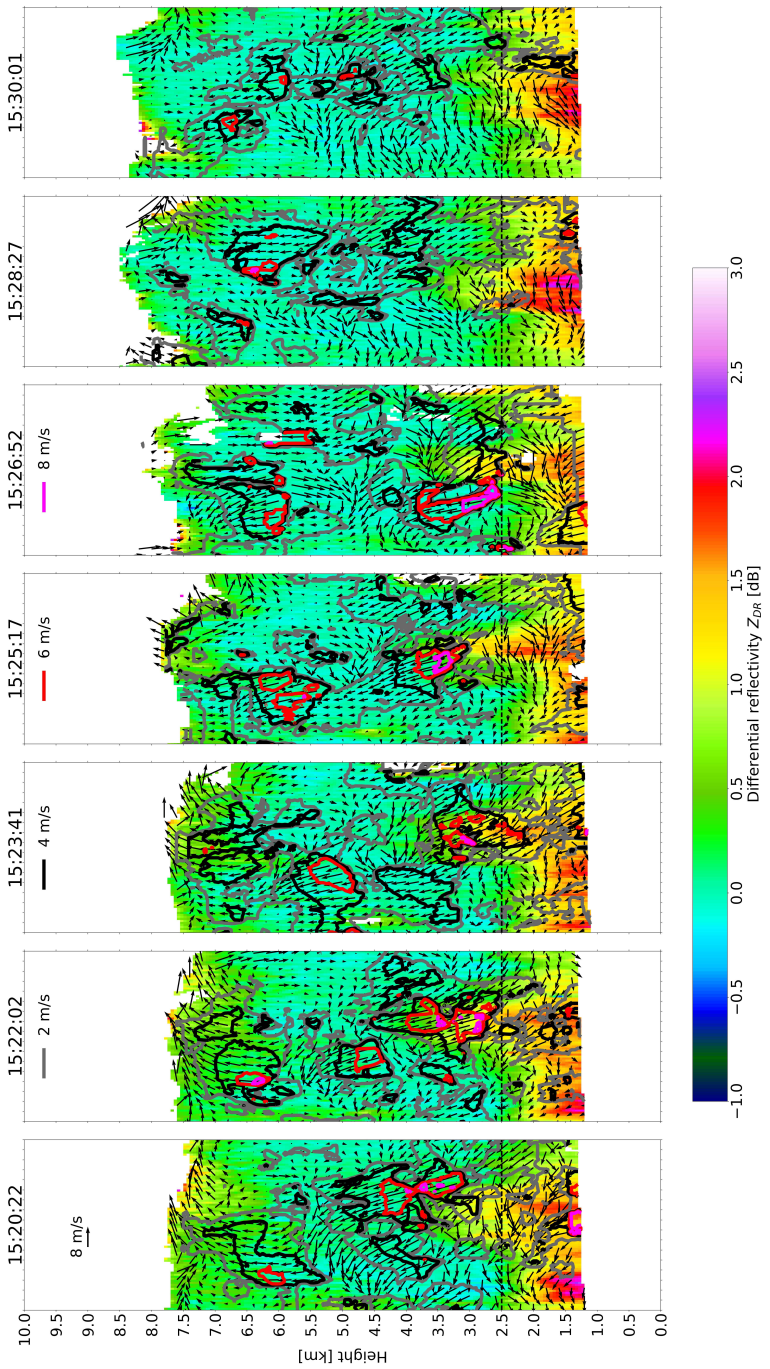

Figure 6.40: As in Figure 6.39 but for the time period between 15:20 and 15:30.

from 6 (red) to 4 (black) to 2 (grey) m s^{-1}, therefore a region where the vertical motion was slowing down.

There was an EDR structure located at 4 km height at 15:26 that intensified from 15:25 that was located above an ascending updraught with the similar pattern of decreasing vertical velocity upwards, seen in Figure 6.43. This updraught became dis-

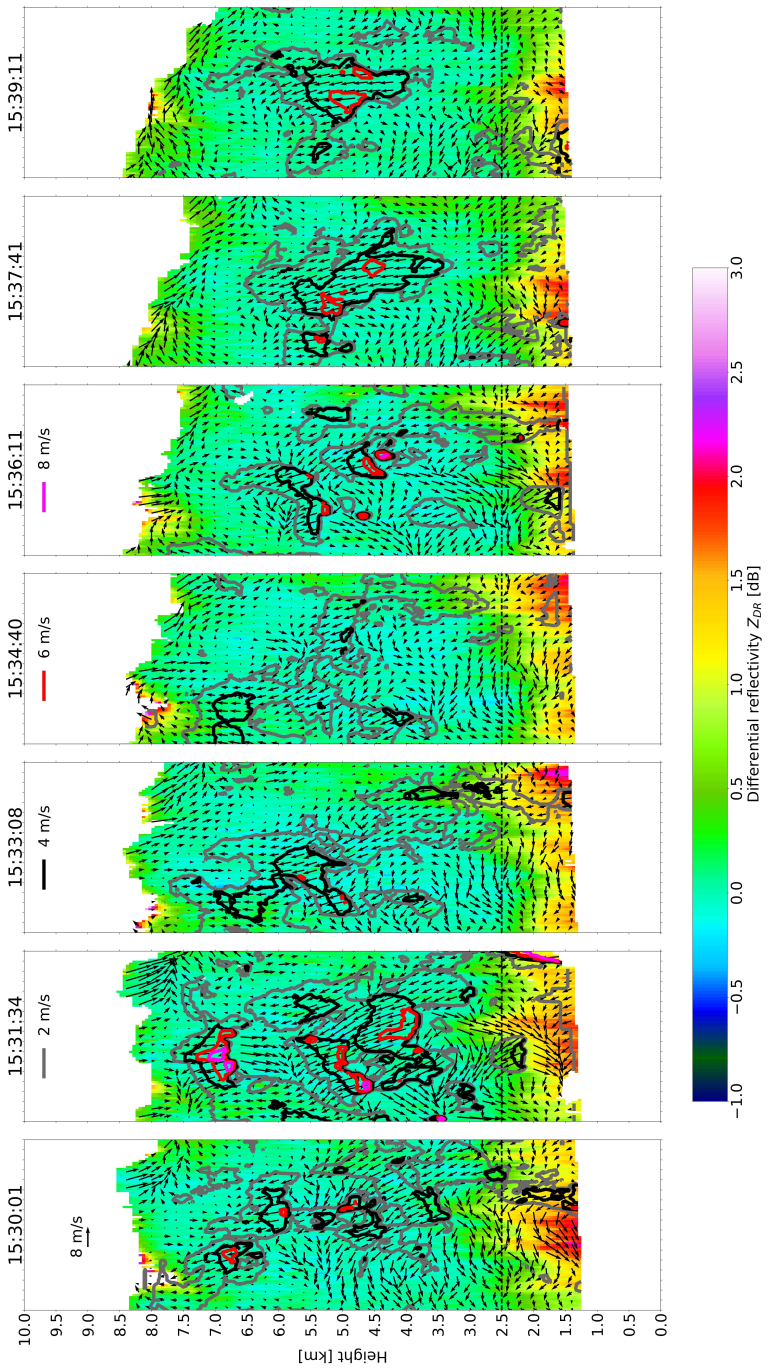

Figure 6.41: As in Figure 6.39 but for the time period between 15:30 and 15:39.

torted by some downwards and horizontal motion to take on the shape of a 'bean' at 15:26 centred at 3 km height. At 15:28 it appeared that the downdraught became dominant co-located with the EDR structure. Between 15:28 and 15:36 there were scattered updraught pulses which at 15:31 and 15:33 were co-located with strong EDR as the updraughts grew in size. These large EDR values were also associated with

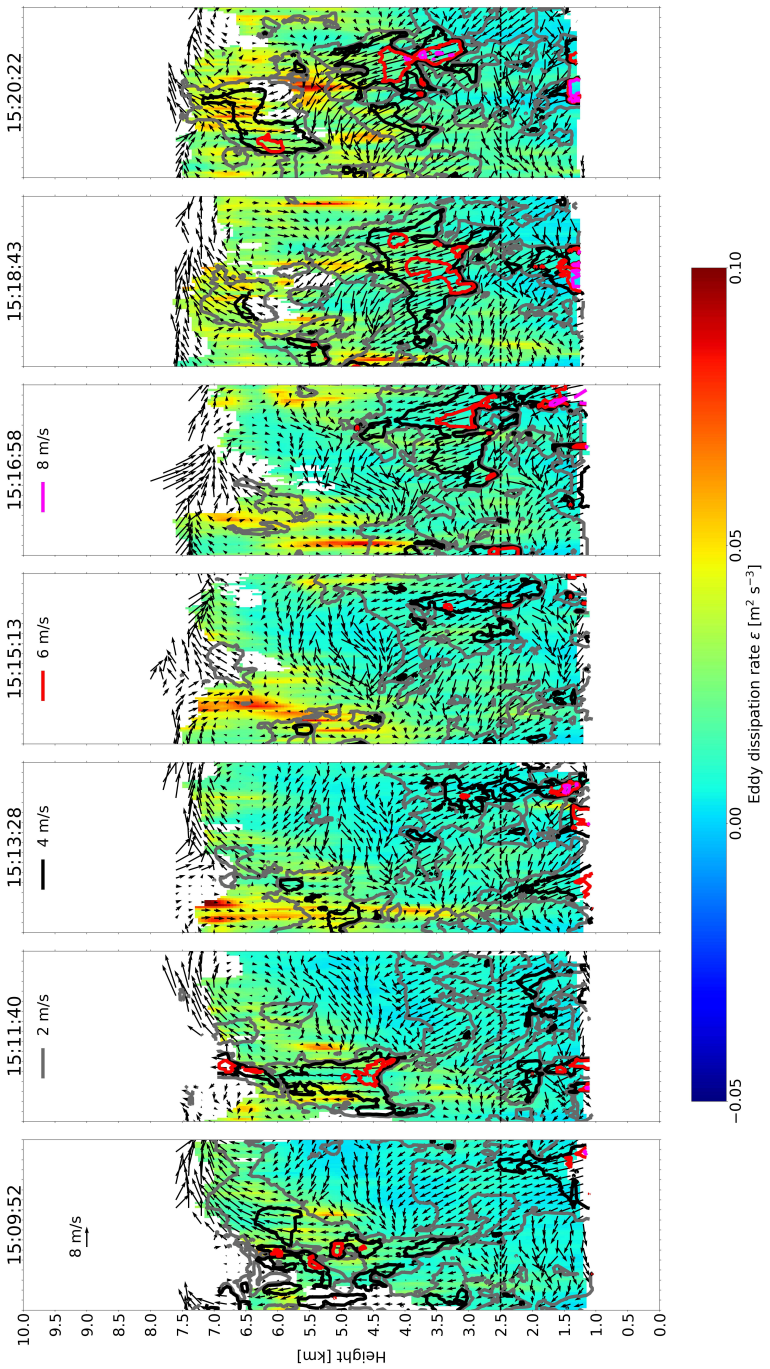

Figure 6.42: C3 as in Figure 6.36 but for Eddy Dissipation Rate (ε) in $m^2\ s^{-3}$ between 15:09 and 15:20.

downdraught, at 15:31 at 5 km height (Figure 6.44) a region where updraught meets downdraught and flow with a horizontal component and at 15:33 and 15:34 updraught with a horizontal component. At 15:33, a vortical circulation became present in C3 centred at 6 km height with strong EDR values located on the left side of the vortical

circulation. As the vortical circulation decayed from 15:36 until 15:39 the EDR also weakened.

Overshooting tops in C2 and C3 reached heights of about 9.5 km shown by the echo top height. A calculated maximum parcel level (MPL) for a parcel lifted from a 50 hPa deep mixed layer was 11 km. MPL is calculated by lifting a parcel from the equilibrium level until the negative area between the parcel trajectory and the environment temperature above the equilibrium level is equal to the CAPE (the positive area below the equilibrium level between the parcel trajectory and the environment temperature). This estimates the maximum height a parcel can ascend to after passing the equilibrium level (EL) because the parcel has some retained momentum after it becomes neutrally buoyant. The MPL is visually represented by an overshooting top above the cloud anvil. However, MPL is very sensitive to the choice of parcel properties. For example, taking the mean properties of a 30 hPa deep mixed layer results in an MPL of 9.6 km, much more similar to that observed. The CAPE for this parcel would be 419.8 J K^{-1} kg^{-1}. This indicates how sensitive parcel ascents are in forecast soundings or numerical weather prediction to estimated cloud depth, cloud base and cloud top height. There are multiple choices of types of parcels to use such as; surface, most unstable and mixed layer and each one can give a different result. Overshooting tops reached heights of 9.5 km in C2 and 9 km in C3, estimated from reflectivity, which are very similar to the calculated MPL. The updraught structure in C3 was weaker and less organised, which appeared to be why the overshoot in C3 did not reach as high as the overshoot in C2. Parcel calculations were done using the SHARPpy Sounding Toolkit (Blumberg *et al.*, 2017).

6.7 Discussion

6.7.1 Updraught pulses

Figures 6.45, 6.46 and 6.47 show composite images of the vertical velocity, EDR, reflectivity and Doppler velocity features of interest between 15:09 - 15:20, 15:20 - 15:30 and 15:30 - 15:39 respectively for C1. Similarly 6.48, 6.49 and 6.50 for C2 and 6.51, 6.52 and

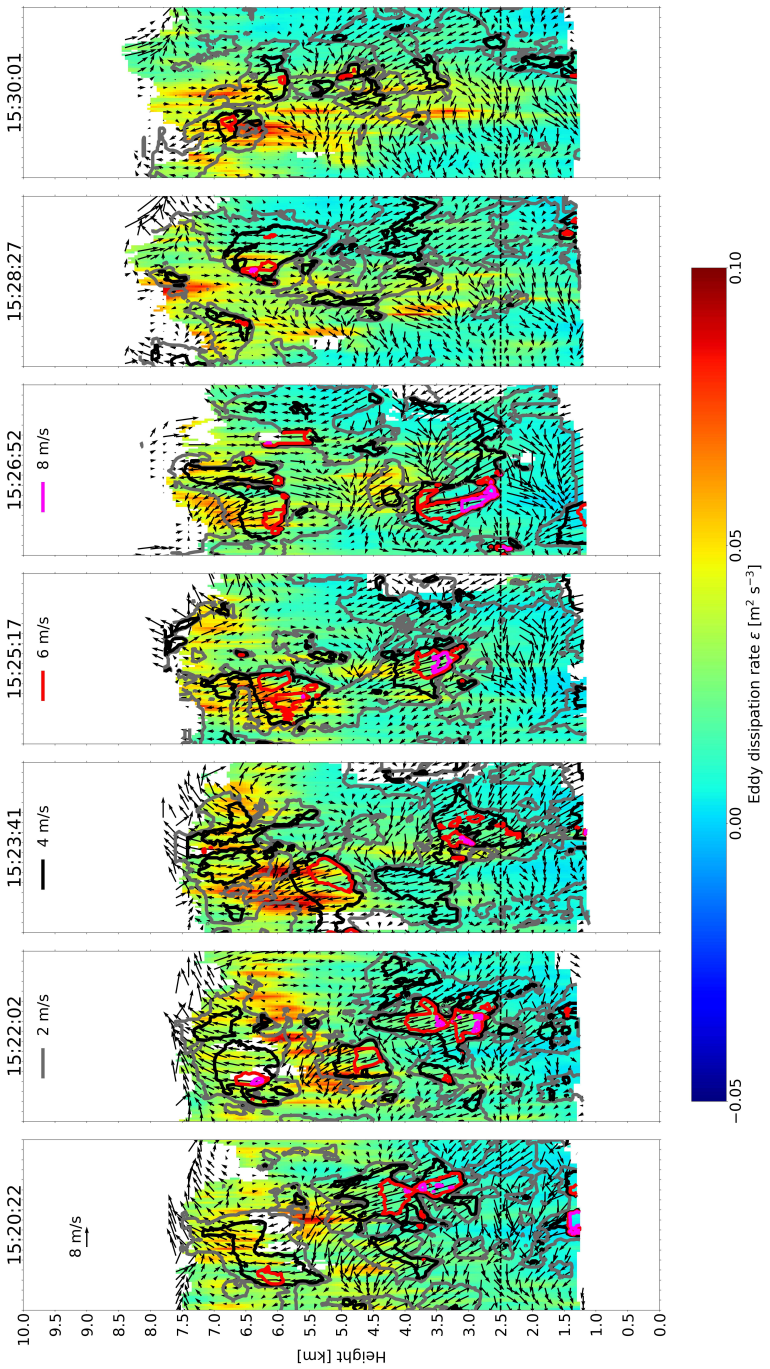

Figure 6.43: As in Figure 6.42 but for the time period between 15:20 and 15:30.

6.53 for C3. The terminology *composite* is used hereon to represent figures produced by averaging information from all 4 scans (as above in this chapter) and overlaying the vertical velocity, reflectivity, eddy dissipation rate and Doppler velocity for selected magnitudes. Reflectivity is plotted as filled contours with 5 dBZ in light grey, 20 dBZ in medium grey and 40 dBZ in dark grey highlighting the cloud and the convective

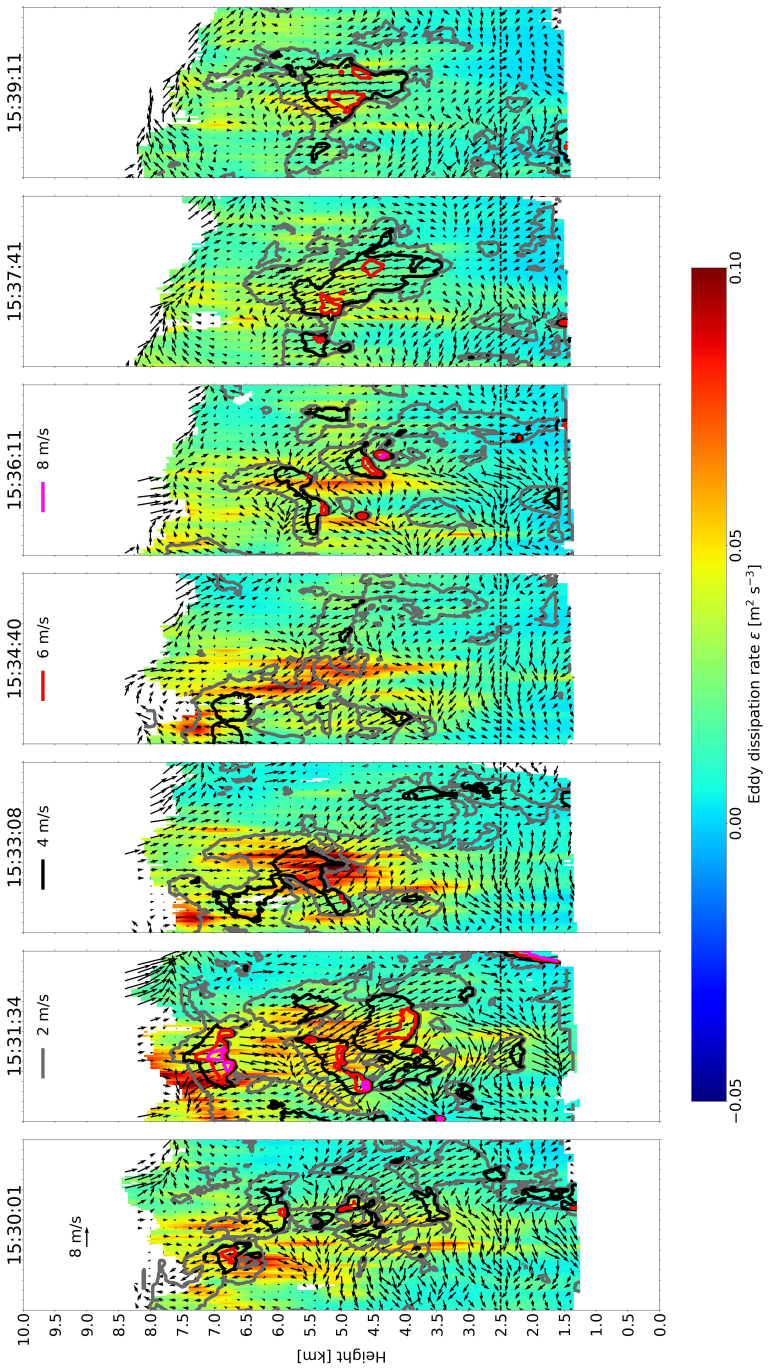

Figure 6.44: As in Figure 6.42 but for the time period between 15:30 and 15:39.

cell region. The 4 m s^{-1} vertical velocity is contoured in red and -2 m s^{-1} in blue. Due to downdraughts being weaker, a lower threshold was used. EDR structures with magnitudes greater than 0.05 m^2 s^{-3} are contoured in dark green. Doppler velocity of 1 m s^{-1} is contoured in solid black and -1 m s^{-1} is contoured in dashed black. For C3, Doppler velocity of -1 m s^{-1} is contoured in dashed black and -4 m s^{-1} is contoured in

solid black, due to C3 being predominantly located in motion towards the radar seen as slantwise ascent. Overlaps of the Doppler velocity contours with vertical velocity highlights regions of air being advected in the cells.

The composite figures along with the figures of reflectivity and EDR show how the vertical velocity and EDR structures were consistent in time across each frame for each cell. Furthermore, there was consistency of vertical velocity and EDR between each cell, with updraught pulses and EDR structures clearly seen ascending in each cell individually. The figures presented in this section have been subjectively analysed to highlight ascending updraught pulses in thick solid black lines, with a basic ascent rate calculated by subtracting the start height from the end height and dividing by the time between these points. This basic ascent rate estimate can be compared to the vertical velocity retrieval.

C1 had two updraught pulses identified. Pulse 1 between 15:09 and 15:16 had an ascent rate of 4.7 m s^{-1}, which was close to the retrieved vertical velocity region contoured of 4 m s^{-1}. A second pulse between 15:15 and 15:20 had an estimated ascent rate of 8.3 m s^{-1} which was twice the retrieved velocity, both shown in Figure 6.45. This mismatch between retrieved vertical velocity and estimated ascent rate could either be due to vertical velocity retrieval error or subjective measurement error of the trajectory.

As discussed above, this cell was decaying and the composite shows this as the 20 dBZ contours shrank in height as downdraughts dominated and the horizontal flow became more horizontally aligned. Taking into account the shift of frame of reference due to the Lagrangian displacement of the system, the updraughts in C1 moved with the system velocity which closely matched the mean Doppler velocity, especially at mid-levels. Consistency between the Doppler velocity patterns and vertical velocity was expected due to vertical velocity being retrieved from movement of Doppler velocity patterns. No further updraught trajectories were identified in Figures 6.46 and 6.47.

C2 as discussed was developing and 4 ascending updraught pulses were identified. Pulse 1 existed between 15:09 and 15:28 and had an estimated ascent rate of 4.2 m s^{-1} which was very close to the vertical velocity region contoured, shown in Figures 6.48

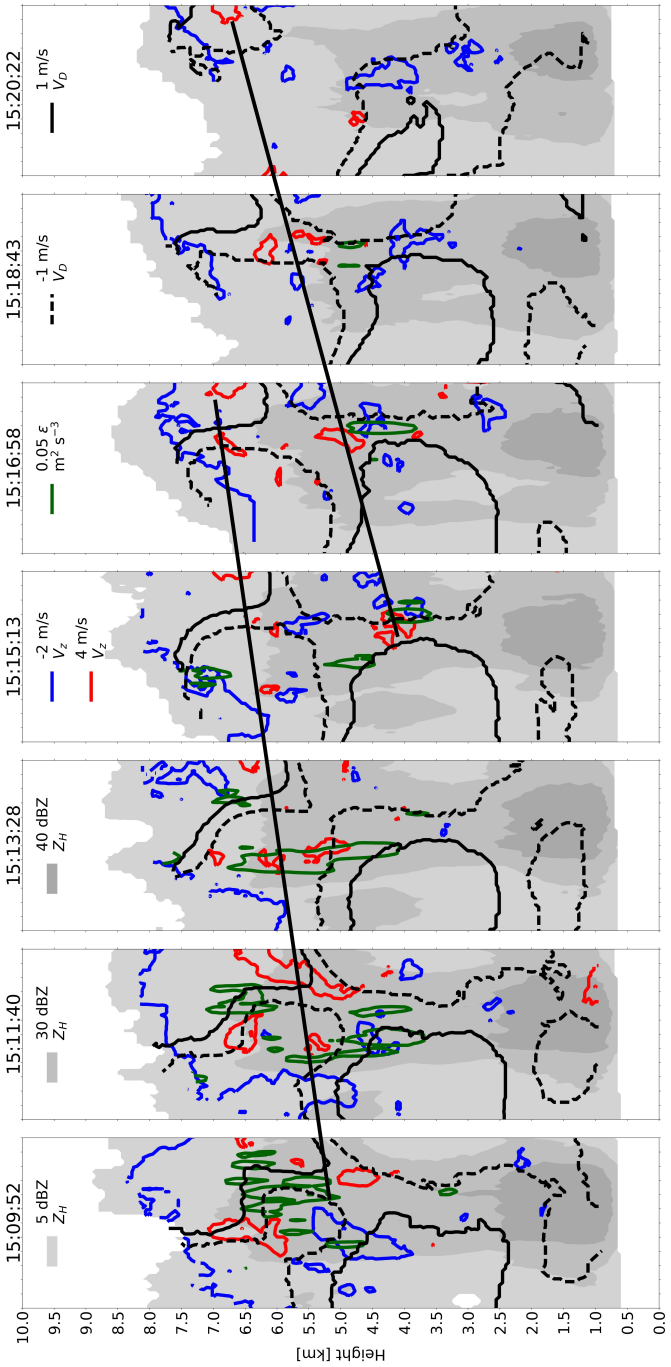

Figure 6.45: Composite of C1 of features of interest between 15:09 and 15:20. Reflectivity as filled contours with 5 dBZ in light grey, 20 dBZ in medium grey and 40 dBZ in dark grey. 4 m s^{-1} vertical velocity is contoured in red and -2 m s^{-1} in blue. EDR of 0.05 m^2 s^{-3} is contoured in dark green. Doppler velocity greater of 1 m s^{-1} is contoured in dashed black and -1 m s^{-1} is contoured in solid black. Estimated ascent trajectories are shown by solid black line.

and 6.49. In this cell the Doppler velocity contours clearly showed how the air was ascending and co-located with the updraught with 'blobs' of air seen ascending from

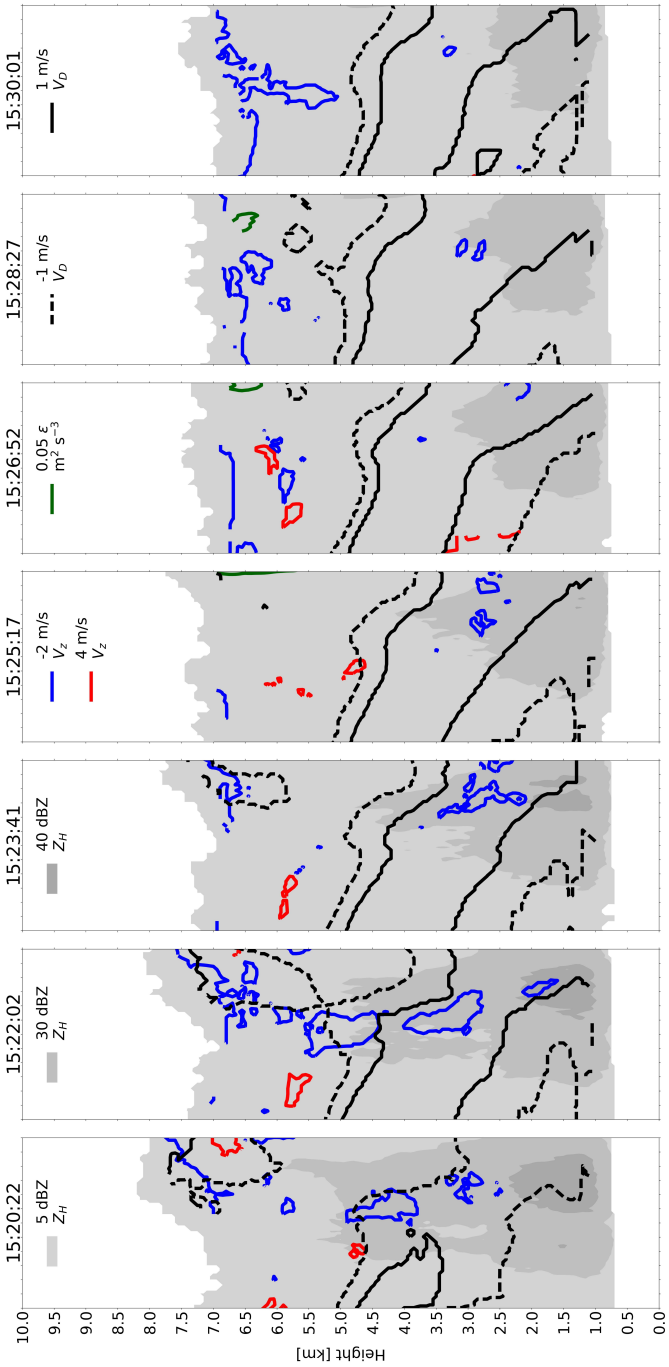

Figure 6.46: As in Figure 6.45 but for the time period between 15:20 and 15:30

.

the cloud base with each updraught pulse. A clear low-level inflow was seen from the west that eventually undercut the updraught. Note that scanning was approximately along the line of cells, but any motion lateral to the scans was very small.

Pulse 2 initiated at 15:13 and ascended until 15:26 and had an estimated ascent

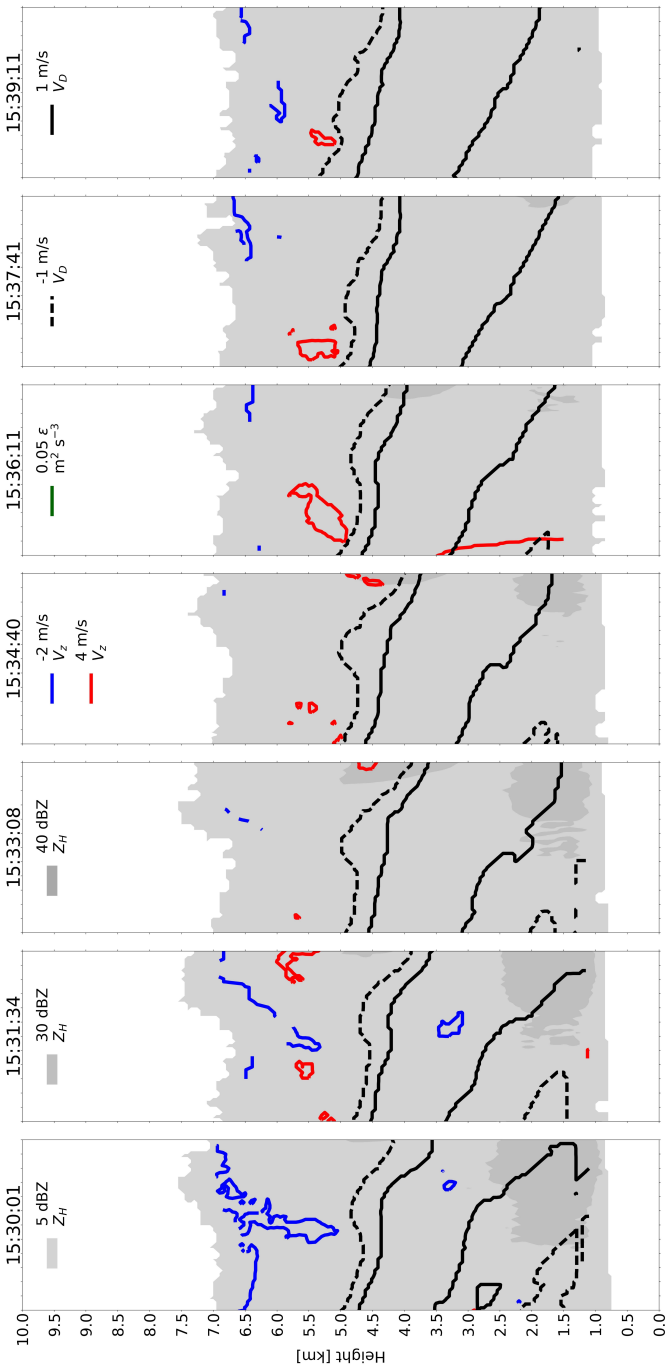

Figure 6.47: As in Figure 6.45 but for the time period between 15:30 and 15:39

.

rate of 3.7 m s^{-1}. Pulse 3 existed from 15:20 to 15:34, had an ascent rate of 3.6 m s^{-1} and was associated with stronger downdraught adjacent and below it, shown in Figure 6.49. Pulse 3 became more coherent than the prior pulses as the overshooting top occurred, but then quickly broke down into fragments of updraught. The Doppler

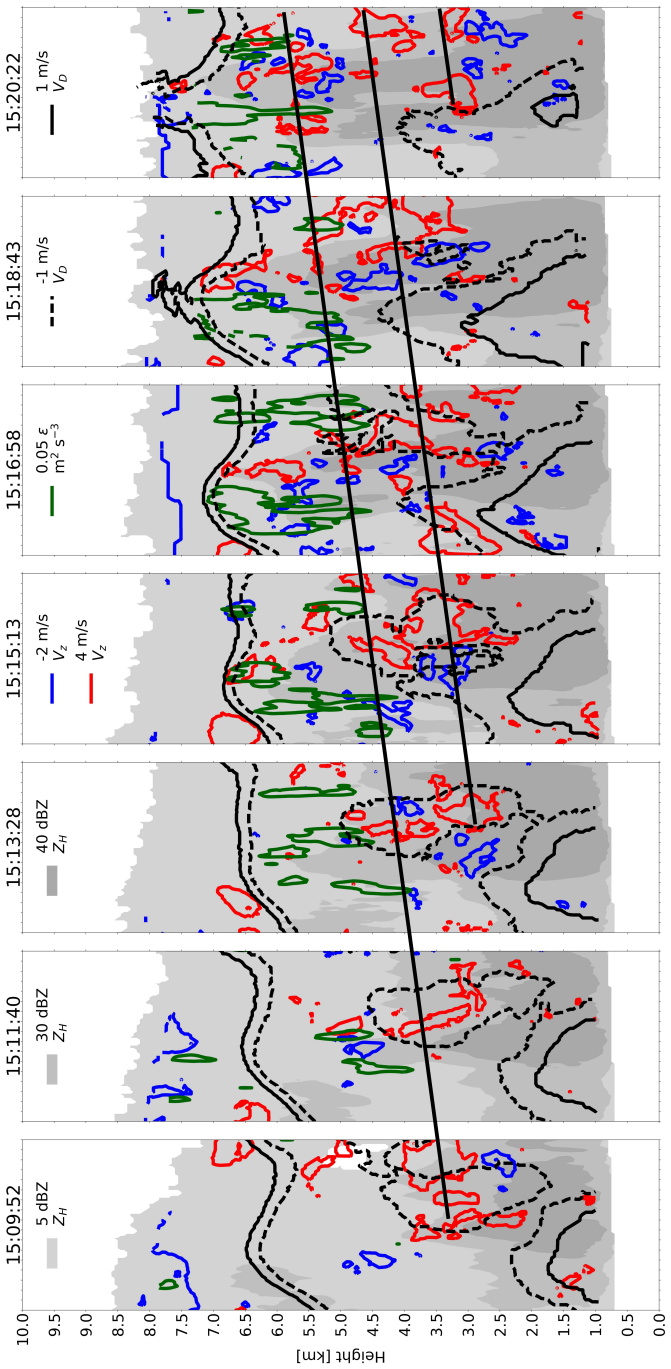

Figure 6.48: Composite of C2 of features of interest between 15:09 and 15:20. Reflectivity as filled contours with 5 dBZ in light grey, 20 dBZ in medium grey and 40 dBZ in dark grey. 4 m s^{-1} vertical velocity is contoured in red and -2 m s^{-1} in blue. EDR of 0.05 m^2 s^{-3} is contoured in dark green. Doppler velocity greater of 1 m s^{-1} is contoured in dashed black and -1 m s^{-1} is contoured in solid black. Estimated ascent trajectories are shown by solid black line.

velocity continued to ascend within this cell into the overshooting top which is shown by the 5 dBZ reflectivity filled contour overshooting the 8 - 8.5 km height. Pockets of

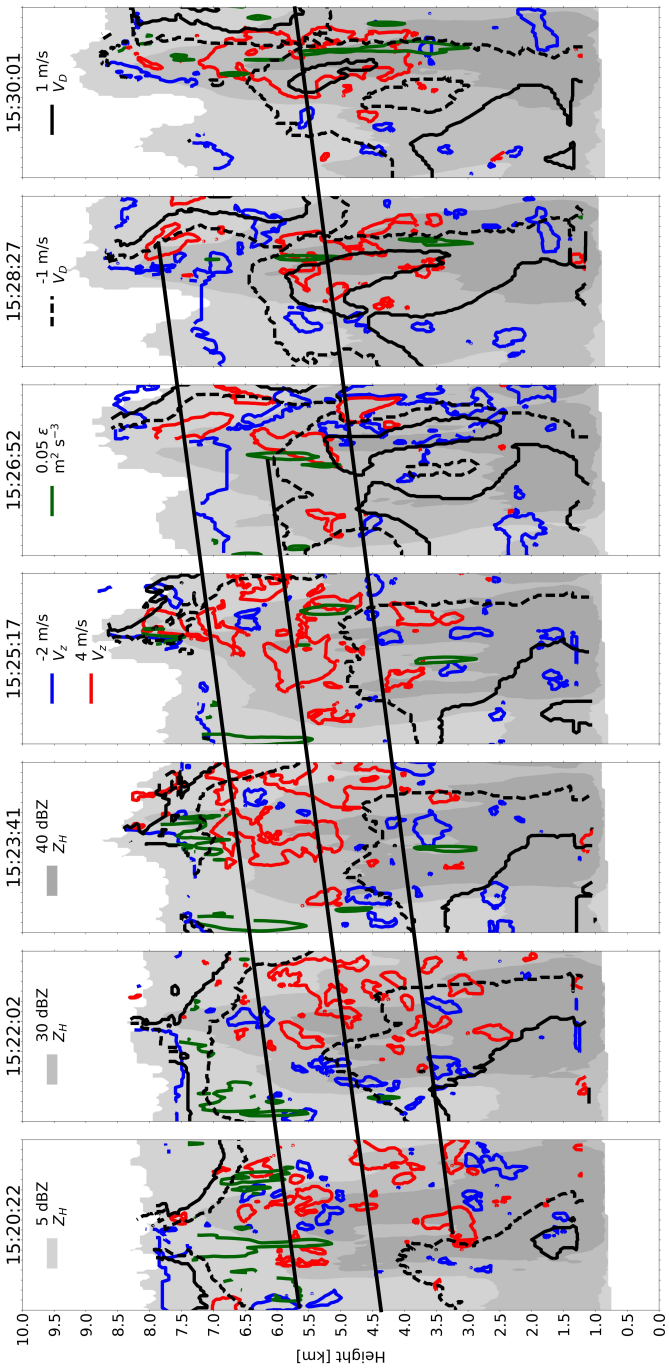

Figure 6.49: As in Figure 6.48 but for the time period between 15:20 and 15:30.

updraught ascended into the overshoot from the first two pulses seen in Figure 6.49.

Once the overshooting top began to decline there was a final updraught pulse between 15:36 and 15:39, which may have existed longer but is limited due to the scanning time, with an estimated ascent rate of 4.2 m s^{-1} shown in Figure 6.50. At 15:30 and 15:31 when the strongest updraught occurred and was vertically aligned, there was a

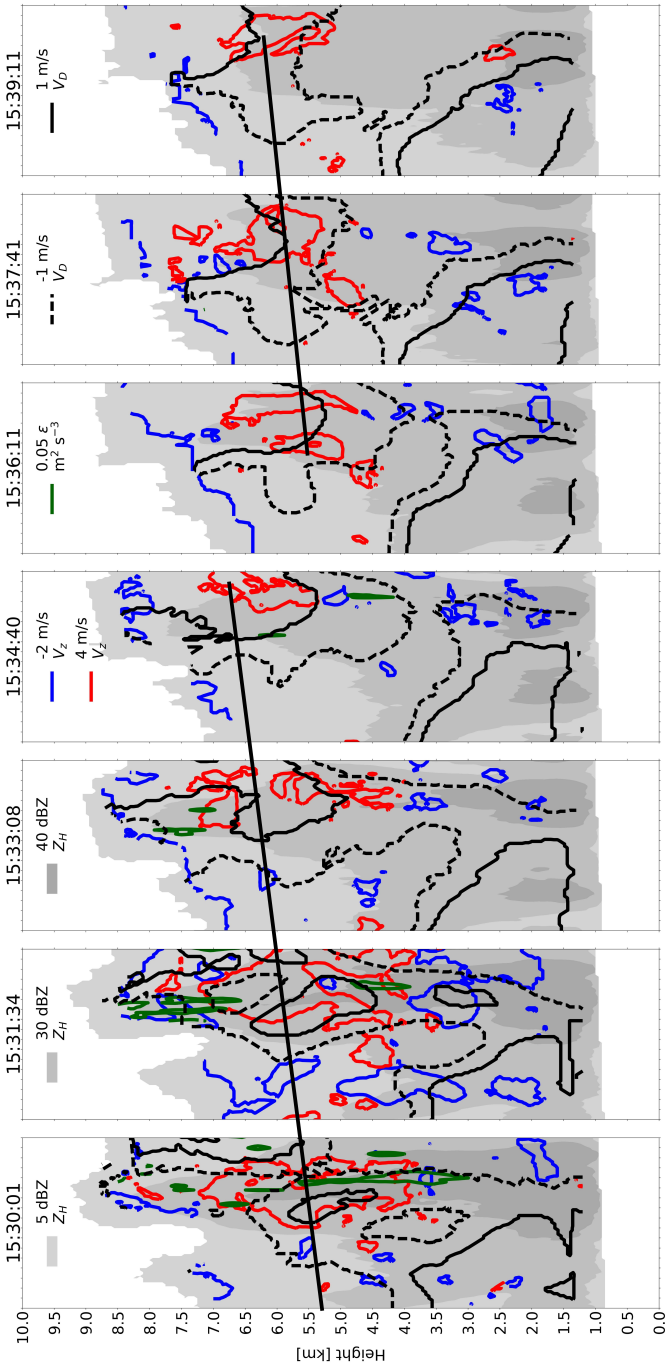

Figure 6.50: As in Figure 6.48 but for the time period between 15:30 and 15:39.

clear connected region of Doppler velocity showing air motion from the cloud base to echo top as the overshooting top reached its peak height.

C3 also underwent development during scanning and had 4 updraught pulses identified. The circulations appeared to be more variable in this cell as seen by the wind vectors having complex circulations and with multiple local regions of convergence.

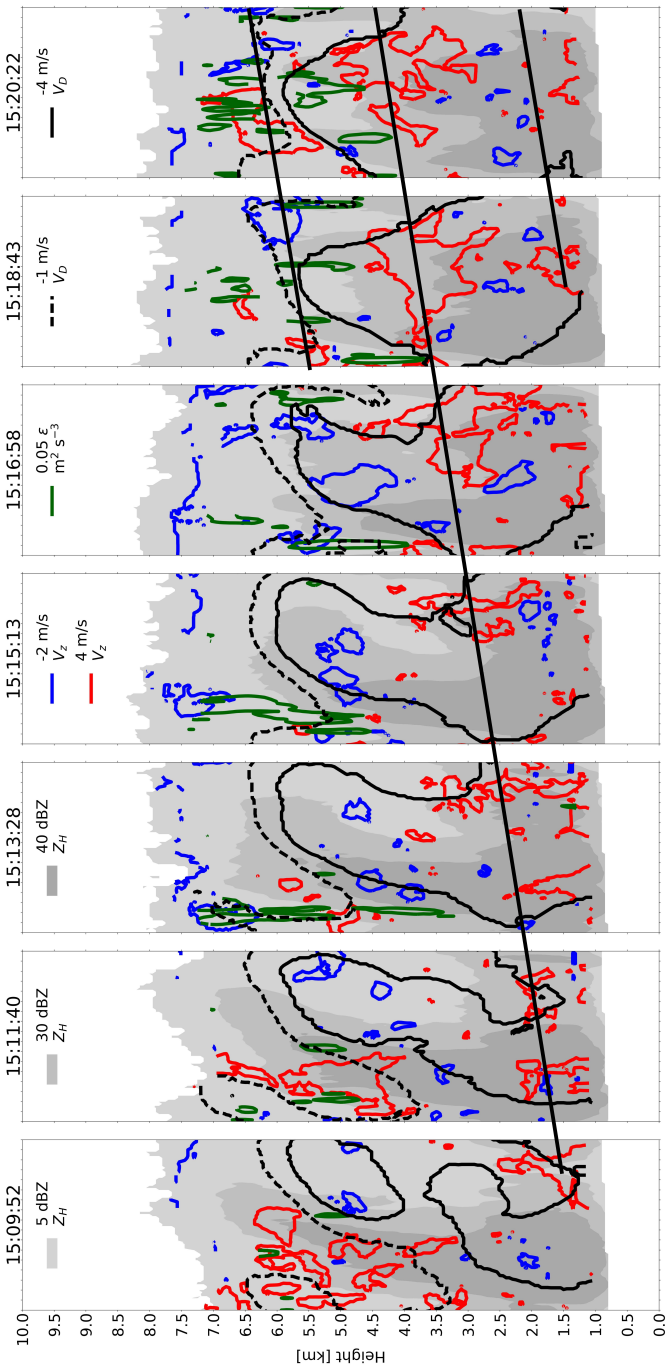

Figure 6.51: Composite of C3 of features of interest between 15:09 and 15:20. Reflectivity as filled contours with 5 dBZ in light grey, 20 dBZ in medium grey and 40 dBZ in dark grey. 4 m s^{-1} vertical velocity is contoured in red and -2 m s^{-1} in blue. EDR of 0.05 m^2 s^{-3} is contoured in dark green. Doppler velocity greater of 1 m s^{-1} is contoured in dashed black and -1 m s^{-1} is contoured in solid black. Estimated ascent trajectories are shown by solid black line.

Pulse 1 initiated near cloud base at 15:09 and ascended to cloud top by 15:31 with an estimated ascent rate of 4.5 m s^{-1}. This pulse can clearly be seen growing and

ascending into the overshooting top region in Figures 6.51 and 6.52. In comparison to C2, this updraught did not have a Doppler velocity signature bound by the 1 and -1 m s^{-1} contours. Rather it existed in a horizontal velocity region that had a horizontal component towards the radar as it ascended, therefore the -1 and -4 m s^{-1} highlight the ascending air with a component towards the radar in Doppler velocity. The Doppler velocity contours clearly show the vertical extent of the motion towards the radar aligned with updraughts, and extending from cloud base to echo top when the overshooting top occurred.

Pulse 2 was short lived and had an estimated ascent rate of 4.7 m s^{-1} and initiated at 15:18 at 5.5 km height and ascended to 7.5 km height at 15:25 (Figure 6.53). Pulse 3 identified at 15:18 until 15:34 (Figure 6.53) also ascended from cloud base like pulse 1 into the echo top and had an estimated ascent rate of 5.2 m s^{-1}. The final pulse observed during scanning ascended from 3 km height to 5 km height between 15:26 and 15:39 (Figure 6.53) and had a shallower ascent trajectory, with an estimated ascent rate of 2.6 m s^{-1}. In contrast to the overshooting top in C2, here the updraught was weaker and was located in motion towards the radar, shown by the Doppler velocity contours. Although the echo top height in C3 also reached near 9.5 km as in C2, C3's overshoot structure was less well defined than in C2. C2 had a column type appearance and C3 was wider and less distinct, when comparing by eye. C2's overshoot also persisted for longer than C3's, suggesting that the formation of a vertically aligned contiguous updraught produced a more distinct overshoot. In both C2 and C3, updraught pulse widths tended to be similar to the reflectively cell width as both were developing. In C3 the updraught pulses also appeared to of similar width to the width of the ZDR columns as they were ascending above the freezing layer.

Results presented in this chapter show that individual cells in a convective system observed from a fixed perspective, evolved via multiple pulses and that these results were capable of following the time and spatial evolution of such updraught pulses. Cloud thermals in Romps and Öktem (2015) were observed for an average of 9 minutes, which the authors state is contrary to the notion that moist convection comprises of steady state plumes. As shown in chapter 5 there were some short lived thermals

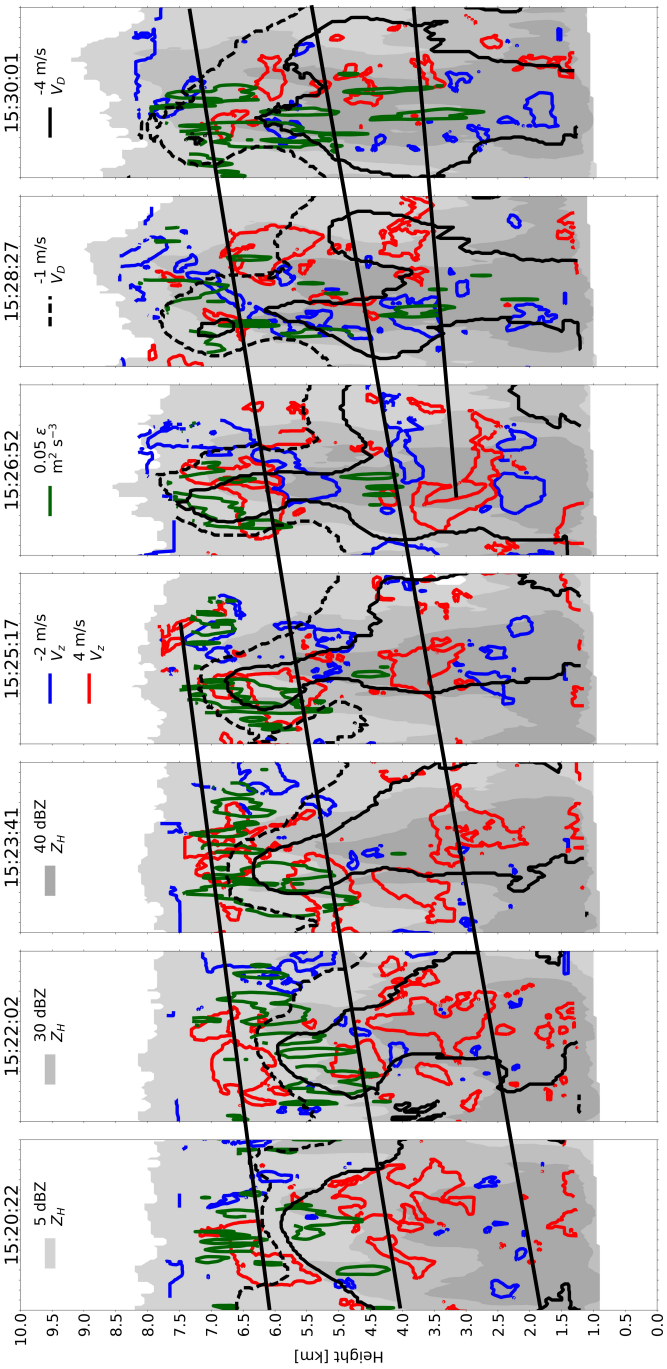

Figure 6.52: As in Figure 6.51 but for the time period between 15:20 and 15:30.

but there were also some longer lived larger thermals lasting between 8 and 11 minutes. Similarly, updraughts in individual cells presented in this chapter evolved as a sequence of short lived pulses, similar to Romps and Öktem (2015) observed by visual inspection of time lapse videos. Significant updraught pulses had lifetimes between 10 to 15 minutes. Damiani *et al.* (2006) also found evidence that clouds observed were

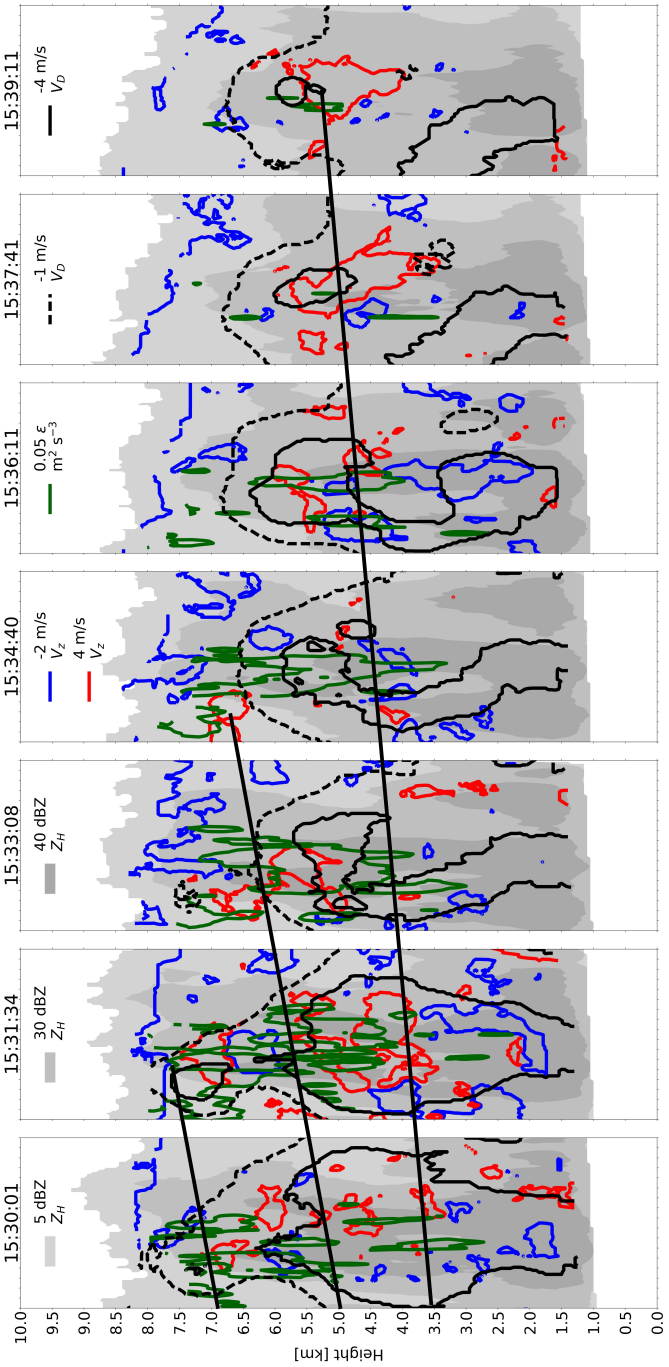

Figure 6.53: As in Figure 6.51 but for the time period between 15:30 and 15:39.

characterised as multi-thermal, rather than driven by a quasi-steady plume.

This chapter has shown that in individual convective cells there was substantial dynamical development occurring which may not be fully represented by the 0 dBZ or column weighted reflectivity in mature convective cells, implemented in a vertical velocity algorithm by Kumar *et al.* (2016). Based on observations in this chapter

updraught structures were seen to be co-located and evolving with the 30 - 40 dBZ reflectivity signal which ascended in cells. Using such signals may yield more information for retrieval of vertical velocity in mature convective cells relying on only reflectivity. One such simple approach would be the height change of the 30 or 40 dBZ echo top ($\frac{\Delta Z_{H,ETH}}{\Delta t}$). Although the column weighted reflectivity parameter will increase in such a scenario and Kumar *et al.* (2016) found that $\frac{dZ_H}{dt}$ of the 0 dBZ ETH correlated well with wind profiler column mean vertical velocities, selection of different reflectivity values may be more suitable in the mature phase. In C2 the 30 dBZ ETH followed a similar pattern to the pulsation of 99th percentile of updraught velocity. Similarly, Kumjian *et al.* (2014) found zero lag time between maximum updraught velocity and the 20 dBZ ETH in 2D simulations of deep convection. Finally, these analysis are only suitable for statistical evaluation, where as the vertical velocity retrieval in this thesis can be applied to individual and a large number of clouds to evaluate velocity, structure and time development of updraughts.

6.7.2 Downdraughts

Although this thesis primarily focuses on updraught structures, there were some strong downdraughts present within the observed clouds in this chapter and the DYMECS case presented in chapter 5. Figures 4.22 and 4.23 presented in chapter 4 show that strong downdraughts were retrieved from the observations. This section provides a short discussion on the downdraughts observed in the data used in this thesis. Figures 2.5 and 2.10 show similar dew point profiles indicating that the mid-levels were dry. Dry air in the mid-levels is favourable for the formation of downdraughts and may aid evaporative cooling of precipitation in this layer, further enhancing downdraughts. Downdraughts between -2 and -12 m s^{-1} were retrieved with similar 95th and 99th percentiles comparable to updraught velocities as shown by Figures 4.22 and 4.23. LeMone and Zipser (1980) measured downdraughts during GATE (discussed in chapter 1) and found a median downdraught velocity of -1.8 m s^{-1} with a maximum of -10 m s^{-1}. Byers and Braham (1949) found median downdraught velocities of around -5 to -6 m s^{-1} and similarly Knupp and Cotton (1985) discuss downdraughts from observations

and modelling studies of between -5 and -10 m s^{-1} in precipitating convection.

Strong downdraughts that reach the ground are usually termed gust fronts which produce convergence along the leading edge. Downdraughts can also spread out from strong convective storms such as Mesoscale Convective Systems to form cold pools. In severe storms with strong downdraughts, downbursts or microbursts can form which are fast moving downdraughts that descend to the surface, spread out to form straight line winds and are capable of causing damage due to the strength of the wind. If downdraughts do reach the surface and form a gust front, they can maintain convection and aid the formation of new convective cells due to low level convergence (Knupp and Cotton, 1985). Redelsperger and Lafore (1988) simulated a tropical squall line which consisted of a superposition of multiple convective elements in different stages of life cycle. New convective cells formed along the front of the system, fed by forced convergence due to the cold front. These new convective cells moved towards the rear of the storm as they became stronger and deeper. Precipitation is capable of feeding downdraughts due to water loading and evaporation.

Figure 2.6 and particularly Figure 6.6 shows that the DYMECS cloud system and the convective system presented in this chapter have a line structure. Figure 6.6 particularly shows convective cells developing and strengthening (white and purple colours) at the front or leading edge of the convective system. Over time these cells appeared to move towards the rear of the storm, shown by the white and purple colours moving from the front to rear along the line. Figure 6.28 shows that C2 reached maturity at around 15:31 and began decaying thereafter. Figure 6.38 shows C3 was reaching maturity and began to decay after C2. Similarly Figure 6.27 shows that as C2 was reaching maturity up to about 15:30, C3 in Figure 6.37 was still developing shown by the updraughts ascending from lower levels compared to the updraughts in C2 that were in the mid and upper levels during the same time period.

The retrieval of downdraughts, visible observation of downdraughts in the cells presented in this chapter and the inferred behaviour of the individual cells and cloud system could indicate that the downdraughts in this cloud system reached the surface to form a gust front, enhancing low level convergence and aiding the formation of

C3. During these time periods C1 at the rear of the cloud was clearly observed to be decaying with a slanted downdraught descending through the cell to cloud base. The downdraughts could also be the mechanism that produced the line of organisation of convection in these cases.

6.7.3 Vortical circulations

Observations of individual cells presented in this chapter showed updraughts ascending primarily as coherent pulses with lifetimes consistent with the ascent rate from at least near cloud base to near cloud top, but at times being more plume-like in structure in C2 associated with an overshooting top. In both updraught structure types, there were vortical circulations present above and slightly displaced to the side of the updraught.

As C1 decayed, a counter clockwise circulation was clearly visible dominating the region between 3.5 and 6 km height. As C2 developed, the first updraught identified had a clockwise circulation that was present above the updraught. This circulation was clearly defined and was located between 6 and 7.5 km height. As the updraught ascended the circulation was displaced to the east. While the updraught ascended into the echo top there were two clockwise vortical circulations either side of updraught also near echo top at 15:18. Note that the environment is clearly sheared along the beam, which may lead to preferential development of vorticity of one sign. Leading up to the overshooting top in C2, vertical motion became dominant with some small local regions of rotation generally to the west of the updraught in the mid-levels of the cloud. These circulations were not clearly visible like the larger more evident vortical circulations seen near cloud top. Near the end of scanning there existed a weak clockwise vortex around 3 km height which was short lived. Most vortical circulations were located in the mid and upper levels. There were still some strong updraughts present in C2 at end of scanning with counter clockwise circulation to the west of the updraught.

In C3, a very clear clockwise circulation was present near echo top and to the upper right of updraught, located near the anvil region at the start of scanning. This updraught was plume-like with pockets of stronger velocities. As this updraught weakened, so did the radius and strength of the clockwise circulation, leaving a weak clock-

wise circulation. Then as a new updraught below started intensifying, another clockwise circulation formed above this updraught in the mid and upper levels. A further updraught ascended and the overshooting top ascended with one or so small scale local circulations that were weak, located to the side of the updraught, again in the mid-levels. Similar to C2, when a strong updraught was present with an overshooting top there was no clear vortical circulation but some shorter lived clockwise circulations either side of the updraught. As the updraught weakened near end of scanning in C3, a larger clockwise circulation formed and was clearly evident, which then became displaced, weakened and shrank in size, apparently by the forming strong updraught below.

The circulations observed in the cells in this chapter show some similarity to those found in 3D model simulations of updraughts by Peters *et al.* (2020) (Figure 1.9 shown in Chapter 1). Updraughts in the simulations produced flow signatures representing thermals with vortical circulations. Time-height diagrams (not shown here but in their Figure 18) of the height of the maximum updraught velocity showed rising streaks of large horizontal maximum vertical velocity, with individual thermals, like the thermal chain structure (Peters *et al.*, 2020). This is similar to the ascent in time of the updraught pulses shown in the composite figures in section 6.7.1. As stated by the authors and discussed, a caveat of these simulations and those of prior studies is that a warm bubble was used to initiate convection. This is not representative of how convection may initiate in nature. Given this limitation, the flow structures obtained were similar to those in the observations shown in this chapter but circulations in these observations may be due to larger scale shear in clouds rather than induced by an ascending thermal due to the vertical gradient of horizontal velocity and the horizontal gradient of vertical velocity (term 2 in equation 1.21).

Vortical circulations appeared to be located in regions of vertical wind shear, visible in Doppler velocity, and through visual inspection appeared to interact with ascending updraughts. Peters *et al.* (2020) neglected vertical wind shear in their simulations but Peters *et al.* (2019) showed that thermals ascending in a sheared environments ascend with a fairly slantwise trajectory, in environments with moderate shear convection

generally deepened slower and that the termination heights of thermals were lower. Thermal chain structures were also evident in weakly sheared mid-latitude congestus (Moser and Lasher-Trapp, 2017) and tropical deep convection (Romps and Öktem, 2015; Hernandez-Deckers and Sherwood, 2016).

Wind shear in the cloud observed in this chapter appeared to be largest near echo tops, where the larger vortical circulations were present. The 12Z 24th September Camborne, UK sounding showed that the environment had little to no directional wind shear and that wind speed was fairly uniform with height at about 30 knots between 700 m and 8 km, increasing from 40 knots to 55 knots between 8 km and 10.4 km height, resulting in an environmental shear $\frac{\partial u_0}{\partial z}$ of 1.33×10^{-3} s^{-1}. This environmental shear is $\approx$2.5 times less than that used in Peters *et al.* (2019) simulations, therefore could explain why thermals identified in observations presented in this chapter did not terminate lower given environmental shear was much weaker. Doppler velocity shows directional wind shear associated with the cloud circulations, contributing to the $\frac{\partial u}{\partial z}$ component of vorticity normal to the plane.

This work is limited by the range the cloud was observed and the scale of the search box used, meaning that finer scale vortical circulations, such as those on the 40 m scale in Damiani *et al.* (2006) cannot be observed. Larger scale vortical circulations were also present in Damiani *et al.* (2006) on the order of 1.5 - 2 km in width and height. To observe finer scale vortical circulations, clouds nearer to the radar need to be observed and a smaller search box for retrieving vertical velocity would need to be used.

6.7.4 Microphysical implications in terms of polarimetric signals

The ZDR signal in C3 was stronger than in C2, seen by comparing Figure 6.39 with Figure 6.30. There appeared to be a ZDR column in C3 reaching heights of 3.5 - 4 km between 15:09 and 15:16 with ZDR signal of 0.5 - 1 dB with an updraught present above the ZDR column with a 4 m s^{-1} base at 4.5 km height. There was also a 0.5 dB ZDR signal extending the depth of the cloud. The higher ZDR signal near the cloud top, compared to near 0 dB signal in the bulk of C3 at these times is in a low reflectivity region and therefore a low SNR region. In embedded convection in a warm-

frontal cloud with the depth of convection less than in this case, Hogan *et al.* (2002) found that pristine ice crystals caused high ZDR signals. The pristine ice crystals were suggested to be produced by depositional growth which can occur near cloud top where aggregation may not have had time to occur. Hogan *et al.* (2002) found ZDR in the upper 500 m of ice clouds was larger than in the other regions of cloud. In their shallower convective cells, the authors also suggest that ice splinters produced by the Hallet-Mossop process were ejected from the top of ascending convective turrets. This is different for the cells observed in this chapter as they were already deep, mature and glaciated and no new cloud turrets ascended, therefore the Hallet-Mossop process was not likely. There were also no in-situ observations of ice concentrations.

In observations of over 400 deep convective storms with overshooting tops, Homeyer and Kumjian (2015) found that a common polarimetric feature was a near zero (0.1 - 0.3 dB) ZDR region in the upper levels of the convective core. The authors found that this signal was due to graupel in the overshooting top and hail in the middle of clouds. The near zero ZDR in overshooting tops in organised convection was found in regions of reflectivity ranging between 15 and 30 dBZ. Similar signals were seen in C2 and C3 with ZDR values between 0.1 - 0.5 dB in reflectivity regions between 15 - 30 dBZ near cloud top. Homeyer and Kumjian (2015) suggest that graupel in the overshooting top could be injected into the lower stratosphere from the downstream anvil and that this may be an efficient pathway for stratospheric water vapour. Given the strong updraught, overshooting top, the potential presence of graupel in the overshooting top and that lightning strikes increased in number between 15:25 and 15:30 could suggest that the updraught in C2 was associated with cloud electrification by aiding collisions of ice particles in the upper levels and separation of heavy and lighter crystals creating charge separation in the cloud.

At 15:13 an updraught began ascending in the east side of C3 at about 2 km height. This updraught appeared to be associated with a ZDR signal that was located and ascending below it. The updraught intensified from 15:16 on-wards and there were multiple pulses that ascended through C3 up to 7 km height. A similar scenario may have occurred for the earlier ZDR signal, but was not observed because observations

began near or at the end of this development. This updraught in C3 appeared to ascend from the lower right to upper left and originated below the freezing level compared to the updraughts in C2 during the observation period. Between 15:26 and 15:31 there appeared to be an increase in ZDR signal below the freezing level which then weakened from 15:31 on-wards. The 1.5 - 2 dB ZDR signal was indicative of large oblate particles, large raindrops which were co-located with the increase in reflectivity. Updraught ascent appeared to occur above the ZDR signal with updraught maxima at or near the top of the ZDR column.

Homeyer and Kumjian (2015) observed lower ZDR values with minimums located downstream and above ZDR columns features. These signals were also located in the range that the overshooting top occurred. In C3 local minima of negative ZDR signal can be seen between 15:13 and 15:18 above and to the east of the ZDR column clearly identified by the 1 - 2 dB ZDR signal. These minima are also located in a high reflectivity region, which could indicate that hail was present falling out of the updraught from 15:11. In C2, ZDR minima can be seen located in the range of the overshooting top, shown by the cyan colour in Figure 6.31.

In C2 the 1 dB ZDR column height peaked above the freezing level at 15:18, and the 30 and 40 dBZ ETH peaked 14 minutes later with the 99th percentile of vertical velocity when the overshooting top occurred. The 50 dBZ ETH also peaked at 15:18 when the ZDR strength and column height was maximum. In C2 the peaks and troughs of the 40 dBZ ETH followed a similar pattern to 99th percentile of vertical velocity oscillating in height over time at the same time as the 99th percentile of vertical velocity oscillated in strength. After 15:18 the area of high reflectivity below the freezing level increased shown by the widening of the reflectivity core indicating the area increase in surface rainfall.

In C3 the 1 dB ZDR column height was at a peak at the start of scanning (15:09), 15:18 and 15:23. The 30 and 40 dBZ ETH peaked in height 16 minutes after the 1 dB ZDR column height peak at 15:18 and 8 minutes after the 1 dB ZDR column height peak at 15:23. The overshooting top occurred 2 minutes before the 30 and 40 dBZ ETH peak. A peak in 99th percentile updraught velocity associated with updraught pulses

also occurred at the same time as the 30 and 40 dBZ ETH peaks. As the first ZDR column weakened and the updraught weakened and ascended away from the top of the ZDR column, the column height decreased and the reflectivity and ZDR below the freezing level increased in strength between 15:13 and 15:16. This could indicate large raindrops or hail falling out of the updraught as the column descended and surface reflectivity increased.

In ZDR column simulations by Kumjian *et al.* (2014) freezing drops and hail were located at the top of ZDR columns. When updraughts move away from the top, these hydrometeors can descend as they are no longer suspended by the updraught. At 15:16, a second ZDR column began to strengthen with a new updraught located above it, capping the column. When updraughts were located above ZDR columns, peaks in 99th percentile updraught velocity occurred ≈2 minutes before peak ZDR column height in both C2 and C3. This does not happen once updraughts have ascended away from the top of the ZDR column. The observations of these features in C2 and C3 match well with those simulated by Kumjian *et al.* (2014) and the found lag times. Finally, a basic ascent rate calculation of the 1 dB ZDR column height showed that the top of the column ascended at $\approx \frac{1}{2}$ 99th percentile of updraught velocity.

6.8 Summary

In this chapter a new scanning strategy was introduced and implemented to scan clouds using multiple RHI scans near the reflectivity core. This strategy provided high temporal resolution and information in the cross-beam direction of the radar scans. This yielded a 3D view of convective cloud cores to allow observations of the development of updraughts and EDR over time in different regions of clouds. This scanning strategy captured the consistency of updraught structures in the along-beam, cross-beam and depth directions in multiple convective cells.

Several coherent updraught regions were identified, remaining identifiable as they ascended from near cloud bottom to near cloud top. The mean ascent rate was comparable to the mean vertical velocity in the region. In most cases these were clearly

associated with enhancements to the reflectivity column originating from just below the peak ascent region. Some led to identifiable overshoot regions at cloud top. Weaker coherent downdraught regions were also identifiable.

Analysis of updraught dimensions found that both the along-beam lengths and cross-beam widths and along-beam length and depths were correlated. Updraughts tended to be longer than they were deep for the deepest updraughts, updraughts less than 4 km deep tended to be twice as big in the along-beam direction.

EDR structures that had along-beam lengths less than 3 km also tended to be less than 3 km in cross-beam width. EDR structures similarly showed high correlations between the three dimensions. EDR structures were deeper than they were long and most depths increased up to 4.5 km whilst lengths remained less than 3 km. The depth of EDR structures was larger than their cross-beam widths.

Composite observations of three individual cells within the scanned cloud showed that updraughts developed as a series of pulses throughout cell lifetimes, as shown by the frames and discussed above. These pulses were consistent in time and space across the bracket scans indicating that coherent updraught pulses ascended through the developing cells and at times formed into a contiguous plume-like structure and one such structure was associated with an overshooting top. These updraught pulses, appeared to originate at different heights within the cells and clear ascent trajectories could be identified as the updraughts rose into the cloud top. Updraughts that originated near cloud base appeared to be associated with ZDR columns and updraughts ascended above high ZDR signal reaching heights above the freezing level.

In contrast, as updraughts originated higher in the cells and were associated with the overshooting tops, the ZDR height did not increase. Updraught pulses tended to ascend ahead of the reflectivity column and were ascending ahead of the reflectivity tower in regions of about 35 - 40 dBZ. As overshooting tops occurred there was no increase in surface precipitation, and as the cells reached maturity updraughts resided in the mid to upper levels and decayed. EDR structures appeared to mostly be associated with shear in the cells, also shown by vortical circulations present at various stages of the cell growth and in the upper regions of cells. EDR structures did not appear

to be co-located with the strongest updraught velocities, but further observations of buoyancy are needed to investigate the buoyant production of EDR. Vortical structures existed near the top of the cells and became distorted by ascending updraughts, but then regained a clear vortical flow as updraughts decayed.

Further observations of many convective clouds would be required to investigate (1) the statistical properties of updraught pulses and (2) finer scale updraught circulations closer to the radar. Such observations would add completeness to the results presented in this chapter and to the various modelling studies discussed and in-situ observations using radar mounted on aircraft.

Chapter 7

Summary and future work

7.1 Updraught structures in deep convection

Updraughts have been and still are an important feature of interest and research in convective clouds. They have been studied for a long time using various measurement techniques from aircraft, satellite, radar and cameras and there exists a significant amount of literature on the simulation of convective clouds and their internal dynamics ranging from simple models to high resolution complex simulations at fine scales. Accurate measurements of updraughts at fine scales and in-cloud dynamics remain difficult due to aircraft limitations flying in strong updraughts and severe storms to take in-situ measurements and the capability of radar and satellite measurements to directly measure or estimate three-dimensional wind components in a large sample of deep convective clouds.

Many prior studies investigated updraught magnitude and size and some attempt to investigate the time and spatial evolution of updraught structures. Of particular interest in this thesis was the estimation of statistics of updraught structures evolving as a series of thermals or pulses. Such structures have been discussed since the 1950's but appear to have been subject to a resurgence in recent literature investigating updraughts evolving as a series of thermals in numerical simulations and some limited observational studies. The increase in model resolution and improvement of observational capabilities and measurement techniques appears to have highlighted that updraughts in shallow, growing and cumulus congestus clouds evolve as a series of pulses or thermals. This behaviour required investigating to determine how such updraught structures develop, their properties and how they impact cloud evolution and microphysics.

A small number of studies using radar observations and aircraft observations of deep convection have suggested that the updraught pulse structure exists in deep precipitating convection. No existing research specifically focused on investigating the time and spatial evolution and tracking of such structures in deep precipitating convection with low cloud bases, attempted to derive properties of updraught pulse structures in deep convective clouds and observe updraught pulse structures in 3D. This thesis

1. Observed thermals or updraught pulse structures in observations of precipitating deep convection.

2. Tracked updraught pulse structures in time to expanded upon observations of multi-thermal development briefly discussed by Damiani *et al.* (2006) and similarly hinted at by Hogan *et al.* (2008).

3. Estimated characteristics of thermals/updraught pulses in precipitating deep convection using radar observations.

4. Implemented a dedicated scanning strategy along with vertical velocity retrieval method to observe updraught structures in 3D in deep convection and determined what such structures look like at fine spatial scales and how they developed in time.

5. Analysed how coherent updraught pulses developed, interacted with the reflectivity signal, differential reflectivity signal and turbulence derived using an eddy dissipation rate retrieval technique from Feist *et al.* (2019).

Using the scanning strategy proposed in this thesis and the vertical velocity retrieval algorithm, developed based on Hogan *et al.* (2008), updraughts can be retrieved not only using the CAMRa research radar but any single steerable scanning Doppler radar capable of carrying out RHI scans measuring Doppler velocity. This means that a large volume of data can be collected on updraught structures in deep convection without relying on intense research campaigns, utilising aircraft or dual Doppler retrieval techniques. This could be useful for learning more about updraught structures

and in-cloud dynamics at fine scales to aid the development of numerical models at high resolutions.

7.2 Vertical velocity retrievals

A conventional integration method that vertically integrates horizontal divergence calculated from the along-beam Doppler velocity from single Doppler radars was investigated, but it was determined that the integration method would not be suitable for the purpose of this thesis. This was because (1) the integration method has assumptions about air density profiles and boundary conditions causing errors in vertical velocity estimates in columns, (2) vertical velocity retrievals tend to be columnar, (3) the integration method is very sensitive to scanning the core (in part inspiring the scan strategy section 7.4). In this thesis a vertical velocity retrieval algorithm was used that expanded upon the algorithm presented by Hogan *et al.* (2008). This algorithm retrieves vertical velocity by searching for similar features or patterns in Doppler velocity and determines the optimal cost value that corresponds to a features displacement, from which vertical velocity can be estimated. This method does not suffer from the caveats discussed that apply to the integration method. The vertical velocity retrieval method used in this thesis was applied to pairs of scans that were through the same region of cloud and various 'search box' sizes can be used to target the resolution of interest of the air motion to be retrieved. This method was found to work well when tested on idealised test cases, and applied to real observational data as presented in chapters 5 and 6 for retrieving vertical velocity fields consistent in space and time.

A method for estimating the uncertainty on vertical velocity retrievals was derived utilising the structure of the cost curve used in the vertical velocity retrieval process and spectrum width observations. Uncertainty estimates improve confidence in vertical velocity estimates and are useful to know when interpreting results. Statistics of vertical velocity uncertainty showed that uncertainty on the vertical velocity estimates was within reasonable values such that it was highly certain that retrievals of vertical velocity greater than 4 m s^{-1} were indeed updraught regions, with regards to typical

updraught velocities and thresholds used in this thesis. The method presented in this thesis provides a comprehensive way to estimate uncertainty for vertical velocity retrievals using radar observations.

7.3 Statistics of updraught structures in DYMECS and Gatwick cases

Chapter 5 presented results of thermal properties from a selection of deep convective clouds from the DYMECS and Gatwick campaigns that used a continuous RHI scanning strategy. These campaigns were useful to test the vertical velocity retrieval algorithm and provide a small sample of properties to analyse and inform choices for a future scanning strategy. Thermals were identified as upward moving thresholded regions of vertical velocity. Multiple thermals were observed and statistics derived showed that updraughts evolved as a series of short lived thermals with results indicating

1. Lifetimes were on the order of minutes, mostly between 2 and 5 minutes, with a small number of thermals lasting between 6 and 10 minutes.

2. Thermal splitting was more common than merging and there were more simple (non splitting and/or merging) thermals than complex (splitting and/or merging).

3. There were multiple thermals per convective cell.

4. Thermals generally ascended less than 1.5 km in height with a small number ascending between 1.5 km and up to 4 km in height.

5. Thermals mostly had equivalent diameters between 0.5 and 2 km with a small number of thermals having diameters between 2.5 and 4 km. Larger thermals lasted longer and thermal lifetime and mean equivalent diameter had a Pearson correlation of 0.75 for all thermals and 0.64 for simple only thermals.

These results give insight into the statistics of updraughts evolving as a series of pulses in deep convective clouds. Thus, providing new information on updraught characteristics in deep convection and built upon prior results in the literature from shallow, growing and cumulus congestus in observations and numerical simulations. Statistics presented in chapter 5 appeared to be similar to those reported in the literature from a range of numerical simulations and limited observations. The existing observations were somewhat unsuitable as they could not account for thermals moving across the line of sight, the 3D nature of thermals was unknown and observations of more longer lived and evolving thermals were wanted. Thus, further observations were required to specifically target convective cores for a longer scanning time and observe the 3D nature of updraught and turbulence structures to determine spatial coherency and observe development.

7.4 Scanning strategy

The DYMECS and Gatwick cases presented in chapter 5 used a scanning strategy that was designed for those campaigns, which was not entirely suitable for the work in chapter 6 and for observing updraught structures in 3D. Nevertheless, these cases were useful to develop the vertical velocity retrieval and thermal tracking algorithm which allowed the estimation of thermal properties in deep convective clouds from the DYMECS and Gatwick campaigns.

To further investigate updraught structures, a new scanning strategy was implemented that targeted convective cores using a bracketing technique allowing cross-beam observations of a 2 km swath separated by a relatively short time (30 s between each scan and < 2 minutes between corresponding scans of a sequence) and small horizontal distance (500 m) meaning that good temporal and spatial resolution was maintained. The radar parameters for the new 3D radar scans were modified somewhat from the DYMECS and Gatwick cases to increase the range gate resolution and increase the sensitivity to spectrum width. Feist (2019) also proposed changes to the scanning strategy used in DYMECS to simplify the eddy dissipation rate retrieval process, improve data

collection and produce more accurate eddy dissipation rate retrievals. Such changes to scanning strategy were introduced and refined in this thesis and implemented using the multi-scan bracket scanning strategy to collect measurements across cloud cores and results were presented in chapter 6. Furthermore, the range resolution of the radar was reduced from 300 m to 75 m for the results presented in chapter 6. Feist (2019) suggest that the 300 m restricted velocity surface fits to 300 m intervals when removing velocity variance contributions due to shear, but eddy dissipation rate was shown to be insensitive to this scale. Nonetheless, the increased resolution was utilised in this thesis to (1) allow retrieval of finer scale in-cloud dynamics and (2) increase resolution of eddy dissipation rate retrievals. Finally, the pulse pairs used by CAMRa were increased which allowed measurements of spectrum width to be made closer to the lower limit that is enforced by the Nyquist velocity of CAMRa, down to 0.6 m s^{-1} spectrum width rather than 0.9 m s^{-1} in the DYMECS case. This allowed a broader range of eddy dissipation rates to be retrieved.

Along with providing higher resolution and more spatial information, this strategy primarily accounts for shear across the beam which was not previously possible due to the singular scans. The bracket scans allow observations of clouds that may not be moving parallel to the radar beam from which the previous strategy may have struggled to maintain observations of reflectivity cores, and such scans are not optimal for applying the Nicol *et al.* (2015) vertical velocity retrieval to individual clouds. These scans also allow observations of structures moving from one beam to the next which is useful for analysing developing updraught structures. The bracket scan strategy allows the observation of coherent updraught and turbulent structures in convective clouds using a single Doppler radar.

7.5 Observations of updraught pulses using 3D scans of deep convection

The new scanning strategy allowed the observation of 3D reflectivity, Doppler velocity, differential reflectivity, vertical velocity estimates and eddy dissipation rate estimates

in an active deep convective cloud. Originally the bracket scanning strategy was to be applied to a large number of clouds. Unfortunately due to limited convective weather a statistical approach to observing a large number of updraught pulses in deep convective clouds in 3D was not possible. Nonetheless, the case presented in chapter 6 was investigated in detail given it provided unique observations of a deep convective cloud containing multiple cells, had two overshooting tops and had lightning associated with it. This in-depth study yielded 3D observations of updraught pulses and eddy dissipation rate structures, not previously observed with a single Doppler radar or studied in the literature.

Individual scans in a sequence were used to estimate the dimensions of coherent updraught and eddy dissipation rate structures. From this, relationships between the along-beam length, cross-beam width and depth dimensions were analysed. It was found that

1. Updraughts were approximately 2 times longer in the along-beam direction than they were deep and wide.

2. Larger updraughts in the along-beam direction were deeper and were linearly correlated with an r-value of 0.94.

3. There were more smaller updraught and eddy dissipation rate structures with a 'fragment' type structure.

4. Eddy dissipation rate structures with along-beam lengths less than 3 km had cross-beam widths less than 2 km.

5. Eddy dissipation rate structures depth and along-beam length increased almost linearly to 4.5 km depth then along-beam length significantly increased between 4.5 and 8 km depth.

Dimensions in the cross-beam direction were most likely limited by the measurement technique. Depth dimensions are hypothesised to be limited by the physical size of clouds, given the size of internal structures cannot be larger than the clouds themselves. Thus, structures were larger in the along-beam dimension than they were in the vertical

dimension. Alignment of the cloud with the mean wind may have caused preferential development of updraught structures in the along-beam direction, resulting in longer along-beam structures compared to across-beam or cross-wind dimensions.

Analysis of updraught structures in individual cells found that multiple updraught pulses were observed to be coherent in time and space, updraughts were evolving as a series of pulses and ascended through convective cells into the cloud top and overshooting top over time. These observations followed the time evolution of updraught structures, showed updraughts oscillating in velocity magnitude and expanded upon observations not possible by Damiani *et al.* (2006) of multi-thermal evolution. Observations of the multi-thermal nature in individual convective cells were more comprehensive in this thesis due to being able to track convective cells for a period of time, observe spatial extent, develop an understanding of how updraught pulses and how the clouds and microphysics (inferred from dual-polarization measurements) were developing over time. This provided a more complete picture of updraught development than aircraft observations sampling flight legs, in-cloud radar sampling limited regions and cameras observing clouds externally.

One particular updraught in a cell formed into a larger vertically contiguous structure, which could be interpreted or termed as plume-like, as the cloud top was overshooting but this did not occur in the other cell. As clouds were overshooting and updraughts intensified, surface precipitation did not appear to increase. Furthermore, updraught structures were co-located in range with differential reflectivity column signatures and updraught structures and maxima were located above differential reflectivity columns above the freezing level, which ascended in height over time. As updraught pulses ascended towards the mid-levels, differential reflectivity columns began to descend below the freezing level as the updraught structure and core moved away from the top of the differential reflectivity column. This indicated that the updraught structures were lofting large liquid particles above the freezing level to produce ZDR column signatures. Large raindrops then descended to the surface as the updraughts ascended away from the top of the ZDR columns or hydrometeors were large enough such that their terminal velocity was greater than the updraught velocity.

Multiple vortical structures were observed near the top of convective cells which became distorted as updraught pulses ascended into the region, but regained clear circulations as updraughts weakened. Eddy dissipation rate structures mostly appeared to be associated with these vortical circulations indicating that they were generated by shear. There were less and weaker eddy dissipation rate structures associated with strong vertical velocities, indicating that observations of in-cloud buoyancy are required to investigate the buoyant and shear production terms of turbulent kinetic energy individually. Most eddy dissipation rate structures were 'streaky' in appearance and were observed in each of the scans and were located near cloud tops in regions with horizontal flow and the inward branch of a vortical circulation.

7.6 Limitations

7.6.1 Observations

There are some limitations associated with this work regarding the observations, vertical velocity retrieval process and eddy dissipation rate retrieval. Such retrieval processes rely on the original Doppler velocity and spectrum width as input and although steps are taken to ensure the integrity of this data from the radar, errors can still exist. Furthermore, the retrieval methods are associated with assumptions and caveats further adding to the uncertainty in the results and that the true vertical velocity and eddy dissipation rate cannot be known. Observations of convection and thermal properties were limited in sample size therefore it is difficult to confidently report statistics without further acquiring a large sample size. Therefore the statistics of properties presented in chapter 5 represent what is possible to investigate by tracking thermals in deep convection and the statistics based on the limited sample size help give an example of the characteristics of thermal structures in observations of deep convection. Observations were also limited in time in that clouds were only scanned for a portion of their lifetime and thus the full evolution of updraughts was not observed. Although, the new scan strategy did improve observations of updraught lifetime in chapter 6. Selection of clouds to scan was limited by manual choice from a list provided ranked

by maximum rain rate and area. This process and observer subjectivity of what is an 'intense' developing cloud and which cloud will continue to develop can limit selection of clouds with potential for continued development.

Improvements targeting clouds early on in their lifetime and remaining to track a particular cloud over its lifetime are required. Potential cloud candidates could be selected by their growth rates of radar reflectivity (i.e change in maximum reflectivity or maximum echo top height over X minutes) and satellite observations (i.e change in cloud top height over X minutes) and ranking clouds by such criteria. Faster growing clouds will be ranked higher (i.e above the 90/95th percentile) and so should be prioritised because they would be deemed more 'intense' relative to other clouds. This will help select developing convective clouds potentially providing a more complete evolution of updraught structures.

The results presented in chapter 6 were of a cloud that was a substantial distance from the radar. Observing clouds closer to the radar will provide (1) the ability to track clouds for longer if they are moving away from the radar because the range will be in favour, or towards and then away for the radar (i.e. west to east in westerly flow) and (2) higher resolution observations because beam broadening will be less and a smaller search box can be used to retrieve vertical velocity closer to the radar. A suggested minimum range is 60 km given at 60 km range the time between corresponding scans is 2 minutes which maintains good temporal resolution, maximum elevation angle would be 10° for a 10 km deep cloud which is suitable for the eddy dissipation rate retrieval which requires elevation angles less than 13.9° for rain and less than 11.5° if hail is present due to hydrometeor fall speed contributions. At 60 km the beamwidth is ≈300 m compared to 500 m at 100 km range. The search box to retrieve vertical velocity in this thesis was based on the size of the features visually observed in Doppler velocity measurements and that used by Hogan *et al.* (2008). The search box size can further be refined to use smaller dimensions with observations closer to the radar which will allow finer scale circulations to be retrieved and thus estimates of fine updraught circulations and in-cloud dynamics.

Vortical circulations retrieved in chapter 6 were on the order of kilometres, but

vortical circulations on the order of hundreds of metres have been reported in the literature. Such circulations could potentially be retrieved using CAMRa, given it has the required horizontal and vertical resolution, but with refinement of the search box size. Larger search boxes will smooth out such signals. Refinement of the search box size would also allow retrieval closer to the cloud edges. Further improvements can be made to the vertical velocity retrieval algorithm, these are discussed in future work.

7.6.2 Updraught identification

Sensitivity analysis showed that the number of structures identified depends on the vertical velocity threshold. Using fixed thresholds is less than ideal when attempting to track developing structures because they can be below or drop below a fixed threshold during their lifetime. Implementing a method that uses a sequential threshold such that objects are tracked from lower to higher vertical velocity thresholds and related to each other may improve tracking structures earlier on in their lifetime and near the end of their lifetime when they decay, rather than objects 'dropping out' of tracking. A watershed algorithm which is a region based method that segments regions by treating a field as having ridges and valleys could be used. The watershed description comes metaphorically by thinking in terms of a geological watershed or topographical feature with mountains and valleys. By applying the watershed algorithm, a field of vertical velocity would be treated as a topographical map with maxima representing peaks, which then decrease into the basins. Using the geological metaphor, water would pour into the valleys or catchments. In the basin, where local minimum exist, water would collect but water from other regions is not allowed to mix so is separated by a boundary. This results in multiple segmented regions, each found by starting with a seed point and filling outwards. This is different from typical threshold based flood-fill algorithms that only fill up until the boundary of the chosen threshold.

Updraught or object identification could be extended to 3D using the multi-scan strategy and scans collected in this thesis, rather than applying object tracking to each scan individually. A basic approach to this was shown in chapter 6, by finding coherent updraught and eddy dissipation rate structures across the 4 scans after each

object had been identified in each scan individually. Rather than applying object identification individually it could be applied in 3D space across each of the scans, assuming stationarity of objects in time given the time difference between the first and last scan. This may result in a more coherent and consistent 3D object tracking of updraught structures than applied to individual scans. Aside from object tracking, the vertical velocity retrieval itself could be improved by applying it across each scan taken using the bracket scan strategy and also comparing with retrievals from the prior time step. Therefore, applying consistency in space and time to build a more physically consistent variational retrieval method.

7.6.3 Eddy dissipation rate retrieval

Limitations of the eddy dissipation rate retrieval method and using CAMRa are discussed in Feist (2019). It is assumed that CAMRa can sample the velocity variance from the inertial sub-range turbulence. This is possible because CAMRa has a sufficiently high resolution but this assumption was not tested in this thesis or in the work of Feist (2019). The shear removal scale (Γ_0) was assumed to be 900 m, but this can change from cloud to cloud and can vary within clouds. Such variability was tested by Feist (2019) and it was found that eddy dissipation rates were insensitive to the chosen scale. The eddy dissipation rate retrieval algorithm was applied 'as-is' to the RHI scans in this thesis in the confidence that the assumptions discussed in chapter 6 and its applicability to the CAMRa radar are suitable, as discussed in detail in Feist (2019).

7.7 Future work

The work in this thesis can be extended with further field campaigns, improvements to radar scans, usage of large eddy simulations, additional observations and improvements to the vertical velocity retrieval and tracking algorithm (discussed above).

7.7.1 Evaluation

Validation of the vertical velocity retrievals would add further confidence to this work and the algorithm. Vertical velocity retrievals can be validated using in-situ measurements from aircraft at different locations within clouds, vertically pointing wind profilers observing the same vertical profile of cloud (Kollias *et al.*, 2001; Collis *et al.*, 2013; Kumar *et al.*, 2016; North *et al.*, 2017), using another radar retrieval from a different viewing angle, and combining multiple radars to compare to a dual Doppler variational retrieval (Gao *et al.*, 2006; North *et al.*, 2017). By collecting larger samples of vertical velocity using the method in this thesis, comparison to the Nicol *et al.* (2015) vertical velocity algorithm could be done and measurements from wind profilers or in-situ to try and validate which vertical velocity method is closer to the truth. Validation studies would answer the question of: *how accurate are radar retrieved vertical velocities from CAMRa using the method in this thesis?* Statistics such as root mean square error, biases or potentially a statistical relationship between 'true' (in-situ and/or wind profiler) velocities and radar retrieved velocities could be found, further improving vertical velocity retrievals from single Doppler radar.

7.7.2 Complete life cycle

Development of updraughts could also be extended by tracking initial thermals in the boundary layer for surface based convective initiation. By applying a similar method as Melnikov and Zrnic (2017) to a mobile radar such as the National Centre for Atmospheric Research (NCAS) X-band mobile radar or an operational network radar. Thermal pulses could be tracked from the boundary layer up until cloud formation from which the NCAS X-band radar could be used to observe clouds in early development and take Doppler velocity measurements prior to a reflectivity signal being present in S or C-band from rainfall. Once rainfall is present at X-band (9.3 GHz), CAMRa at S-band and the operational C-band (6 GHz) radars can all be used to observe the cloud. This would provide a more complete life cycle of convective initiation, growth and decay from which the in-cloud dynamics can be observed from the earliest

stages of surface based initiation in the boundary layer. With radars that are scanning in RHI mode and measuring Doppler velocity, vertical velocities can be retrieved at different resolutions using the X-band, S-band and C-band radars, although the operational C-band would most likely scan in PPI mode.

Radar observations could further be enhanced by satellite observations of cloud, cloud top height, brightness temperature and potentially space borne radar. Some studies also used lightning mapping arrays, discussed in chapter 1. Having such a comprehensive collection of instruments would allow observations of in-cloud dynamics and microphysics, lightning and external observations of cloud from satellite. This would help combine findings of in-cloud dynamics from studies using only radar with those estimated from satellite. Therefore allowing a full picture of convective and updraught evolution to be produced by observing clouds with multiple instruments and viewing angles. Potential research questions for this future work are:

1. *How do updraughts structures evolve over their full lifetime from production to decay?*

2. *Can we observe updraughts originating in the boundary layer and forming pulses during cloud formation up until deep convection?*

3. *Using large sample sizes, what does an 'average' or 'composite' updraught look like?*

4. *Can relationships between satellite derived and radar retrieved vertical velocities be obtained?*

7.7.3 Improved statistics

Collecting a larger number of radar observations, especially closer to the radar will (1) increase the sample size for collecting statistics of updraught structures at fine scales and (2) allow retrieval of structures at fine scales because they are closer to the radar and a finer scale search box can be used in the vertical velocity retrieval algorithm. A dynamic search box size could be used that varies based on the range from the radar

rather than using a fixed search box size at all ranges. This would allow finer scales to be retrieved where possible and would relax to larger scales at greater range from the radar. Increased samples would be useful for statistics on the timescale or frequency of updraught pulses and 3D reconstruction of updraught structures across many deep convective clouds. Potential research questions are:

1. *How many updraught pulses occur during a convective cells lifetime?*
2. *What is the pulsation time frequency, is it regular or irregular?*
3. *What processes determine updraught pulsation frequency?*
4. *Do updraughts observed at fine scales in deep convection have small scale vortical circulations associated with them?*
5. *What does an average updraught pulse look like?*
6. *Which updraught structure contributes to cloud evolution more; plumes, thermals or thermal-chains? Why?*

7.7.4 Better physics

In the results presented in chapter 6, eddy dissipation rate structures mostly appeared to be associated with shear flow and not with strong updraughts. In-cloud measurements of thermodynamics, such as temperature, would be useful to determine the buoyancy production of turbulent kinetic energy and how this might be associated with location and magnitude of eddy dissipation rate retrieved with radar to provide further insight into the ratio of buoyancy and shear production of turbulent kinetic energy. Measurements of particle types at different heights within clouds and temperatures would be useful to determine where ice, liquid and super-cooled liquid particles are located compared to updraught pulses and whether (1) variations of buoyancy can be seen in temperature measurements or (2) phase changes of liquid to ice releasing latent heat causing local perturbations in the thermodynamic profile and whether this has an impact on updraught intensity as they ascend above the freezing level, especially updraughts co-located with differential reflectivity columns.

Large eddy simulations could be used to understand the physics occurring on scales smaller than those observable. Convective clouds and updraughts can be simulated in large eddy simulations to determine the development and structure of updraughts and if they display similar structures under similar circumstances to those observed. If updraught structures are similar to those observed, then large eddy simulations simulations can be used to investigate small scale processes such as turbulence and potentially entrainment and how they impact updraught pulse structures and vice versa. Conversely, if updraught structures simulated do not represent those observed, then analysis is required to determine why that is and what factors determine the structure of updraughts and whether such factors need to be further understood. To supplement in-situ observations, large eddy simulations can be used to determine how turbulence is advected in clouds and to evaluate vertical velocity retrievals by treating vertical velocity in large eddy simulations as truth.

As discussed in chapter 1, in numerical simulations using the Met Office Unified Model rainfall features can look realistic when compared to radar observations but the model cannot produce the initial convective plume, can initiate convection at the wrong time and showers are usually under-resolved which leads to evolution at the wrong scales (Clark *et al.*, 2016). Large peaks in rainfall rates, too fewer large cells occur and cells can be too intense (Lean *et al.*, 2008). In 1 km simulations cells were too far apart and in 200 m simulations storms were not large enough (Hanley *et al.*, 2015). Large eddy simulations could be used to perform an in-depth study of how the updraught structures observed in this thesis affect how quickly or slowly clouds evolve and how much rainfall occurs. Rather than using statistical analysis such as domain averaged rainfall, individual clouds in simulations can be studied to find out how they evolve in time depending on updraught structure. This could help further knowledge on the initiation and timing of convective clouds and amount of rainfall, of which is difficult to accurately forecast, still seen in weather forecasts today. Potential research questions are:

1. *Do simulated clouds with updraught pulses evolve on similar timescales to those observed?*

2. *Do simulated clouds with updraught pulses produce similar rainfall amounts to those observed?*

3. *Can buoyancy production be observed to impact updraught intensity and produce eddy dissipation rate structures?*

4. *How is turbulence being advected in deep convection?*

7.7.5 WesCon

As part of improving numerical modelling of convection across the range scales of 1 to 100 km, the 'Parametrising Convection' (ParaCon) project is a 5 year project that aims to explore new ideas of convection parametrization and integrate these new findings with high resolution simulations. The project has 5 components: (1) triggering convection, (2) fluid dynamics of convective flow, (3) mass flux and beyond, (4) convection-dynamics coupling and 5) turbulent approaches for the grey zone. Whilst this project is heavily focused on modelling, frameworks for the formulation of convection schemes and numerical methods within parametrizations, a future campaign has been proposed specifically focusing on observations. This observational campaign called 'Wessex Summer Convection Experiment' (WesCon) (Barrett *et al.*, 2021) will be a field campaign carried out over the Wessex region of the UK collecting detailed observations of summertime convection.

Of relevance to extending the work presented in this thesis, WesCon will be able to utilise the bracket scanning strategy used to collect observations in chapter 6 and apply the vertical velocity retrieval algorithm. The project will further investigate what updraught and turbulent dynamical structures look like at fine spacial scales, how they develop over time and how the structures are represented in $O(100$ m) and $O(1$ km) scale models. Results in chapter 6 show that updraughts can evolve as a series of pulses. Updraughts in convection permitting models tend to be coherent extending from near cloud base to cloud top but resemble bubble-like cores at higher resolutions (Varble *et al.*, 2014). Thus, further knowledge of updraughts structures is required because if such structures are incorrect in models then this can be related to the rep-

resentation of turbulence and entrainment. The observations of updraught structures can also be compared to high resolution model simulations to evaluate how models are representing fine scale in-cloud dynamics of updraughts and eddy dissipation rate (turbulence). The FAAM research aircraft will also provide in-cloud measurements of thermodynamics with the hope to obtain buoyancy measurements to determine when and where the buoyancy and shear terms of turbulence dominate and how turbulence is advected. Furthermore, WesCon will investigate how cloud microphysical properties vary between turbulent and non-turbulent regions, observe the 3D structure of turbulence and updraughts, clouds and precipitation (with examples of this shown in chapter 6) using CAMRa and the Wardon Hill radar located in Dorset, UK. A new X-Band (9 GHz/3 cm) radar will be mounted on the CAMRa dish which is capable of increased sensitivity to clouds and has a spatial resolution of 150 m at 100 km range. Combining the X-Band and S-Band CAMRa radar it may be possible to track updraught development very early on in clouds using the X-band radar when signals are not detectable by the S-Band radar, up to maturation in the X and S-band radars, and then decay, providing unique long lifetime observations of the full updraught development cycle. Aircraft observations will be used to evaluate turbulence and vertical velocity retrievals from CAMRa (such as those presented in this thesis) and evaluate high resolution models, such as those from the ParaCon project.

Bibliography

Arakawa, A. (2004). REVIEW ARTICLE - The Cumulus Parameterization Problem: Past, Present, and Future. *J. Climate*, **17**, 2493–2525.

Arakawa, A. and Jung, J. H. (2011). Multiscale modeling of the moist-convective atmosphere A review. *Atmos. Res.*, **102**, 263–285.

Arakawa, A. and Schubert, W. H. (1974). Interaction of a Cumulus Cloud Ensemble with the Large-Scale Environment, Part I. *J. Atmos. Sci.*, **31**, 674–700.

Barrett, P., Abel, S., Lean, H., Price, J., Stein, T., Stirling, A., and Darlington, T. (2021). WesCon 2023: Wessex UK Summertime Convection Field Campaign. EGU General Assembly 2021, EGU21-2357.

Battan, L. J. (1975). Doppler Radar Observations of a Hailstorm. *J. Appl. Meteorol.*, **14**, 98–108.

Blumberg, W. G., Halbert, K. T., Supinie, T. A., Marsh, P. T., Thompson, R. L., and Hart, J. A. (2017). SHARPpy: An Open Source Sounding Analysis Toolkit for the Atmospheric Sciences. *Bull. Amer. Meteor. Soc.*, **98**, 16251636.

Blyth, A. and Latham, J. (1993). Development of ice and precipitation in New Mexican summertime cumulus clouds. *Q. J. R. Meteorol. Soc.*, **119**, 91–120.

Blyth, A., Cooper, W. A., and Jensen, J. B. (1988). A study of the source of entrained air in Montana Cumuli. *J. Atmos. Sci.*, **45**, 3944–3964.

Blyth, A. M., Lasher-Trapp, S. G., and Cooper, W. A. (2005). A study of thermals in cumulus clouds. *Q. J. R. Meteorol. Soc.*, **131**, 1171–1190.

Bony, S. and Stevens, B. (2012). WCRP Grand Challenge Number 4: Clouds, Circulation and Climate sensitivity: How the interactions between clouds, greenhouse gases and aerosols affect temperature and precipitation in a changing climate. *White paper*, pages 1–7.

Borque, P., Vidal, L., Rugna, M., Lang, T. L., Nicora, M. G., and Nesbitt, S. W. (2020). Distinctive Signals in 1-min Observations of Overshooting Tops and Lightning Activity in a Severe Supercell Thunderstorm. *J. Geophys. Res.*, **125**, 1–19.

Bousquet, O., Tabary, P., and Chatelet, J. P. D. (2008). Operational multiple-Doppler wind retrieval inferred from long-range radial velocity measurements. *J. Appl. Meteorol. Clim.*, **47**, 2929–2945.

Browning, K. A. and Wexler, R. (1968). The Determination of Kinematic Properties of a Wind Field using Doppler Radar. *J. Appl. Meteorol.*, **7**, 105–113.

Bryan, G. H. and Fritsch, J. M. (2002). A benchmark simulation for moist nonhydrostatic numerical models. *Mon. Wea. Rev.*, **130**, 2917–2928.

Byers, H. R. and Braham, R. R. (1949). *US Weather Bur.* U.S. Government Printing Office.

Carey, L. D., Schultz, E. V., Schultz, C. J., Deierling, W., Petersen, W. A., Bain, A. L., and Pickering, K. E. (2019). An Evaluation of Relationships between Radar-Inferred Kinematic and Microphysical Parameters and Lightning Flash Rates in Alabama Storms. *Atmosphere*, **10**, 1–36.

Carpenter, L. R. J., Droegmeier, K. K., and Blyth, A. M. (1998). Entrainment and Detrainment in Numerically Simulated Cumulus Congestus Clouds. Part I: General Results. *J. Atmos. Sci.*, **55**, 34173432.

Clark, P., Roberts, N., Lean, H., Ballard, S., and Charlton-Perez, C. (2016). Convection-permitting models: a step-change in rainfall forecasting. *Meteorol. Appl.*, **23**, 165–181.

Collis, S., Protat, A., May, P. T., and Williams, C. (2013). Statistics of updraft velocities from TWP-ICE including verification with profiling measurements. *J. Appl. Meteorol. Clim.*, **52**, 1909–1922.

Cotton, W. R., Bryan, G. H., and Heever, S. C. V. D. (2011). Cumulonimbus Clouds and Severe Convective Storms. In D. H. R. Dmowska and H. T. Rossby, editors, *Storm and Cloud Dynamics Second Edition*, pages 315–454. Academic Press.

Damiani, R. and Vali, G. (2007). Evidence for tilted toroidal circulations in Cumulus. *J. Atmos. Sci.*, **64**, 2045–2060.

Damiani, R., Vali, G., and Haimov, S. (2006). The structure of thermal in Cumulus from airborne dual-Doppler radar observations. *J. Atmos. Sci.*, **63**, 1432–1450.

Donner, L. J., O'Brien, T. A., Rieger, D., Vogel, B., and Cooke, W. F. (2016). Are atmospheric updrafts a key to unlocking climate forcing and sensitivity? *Atmos. Chem. Phys.*, **16**, 12983–12992.

Doviak, R. J. and Zrnic, D. S. (1984). *Doppler Radar and Weather Observations*. Academic Press Inc. (LONDON) LTD.

Emanuel, K. A. (1994). *Atmospheric Convection*, page 580. Oxford University Press.

Feist, M. (2019). *A Statistical Approach to Evaluate the Parametrisation of Turbulence in Convection-Permitting Models using Radar-Retrieved Eddy Dissipation Rates*. Ph.D. thesis, Department of Meteorology, University of Reading.

Feist, M., Westbrook, C., Clark, P., Stein, T., Lean, H., and Stirling, A. (2019). Statistics of convective cloud turbulence from a comprehensive turbulence retrieval method for radar observations. *Quart. J. Roy. Meteor. Soc.*, **145**, 727–744.

French, J. R., Vali, G., and Kelly, R. D. (1999). Evolution of small cumulus clouds in Florida: observations of pulsating growth. *Atmos. Res.*, **52**, 143–165.

Fritsch, J. M. and Chappell, C. F. (1980). Numerical Prediction of Convectively Driven Mesoscale Pressure Systems. Part I: Convective Parameterization. *J. Atmos. Sci.*, **37**, 1722–1733.

Gao, J., Xue, M., Lee, S. Y., Shapiro, A., Xu, Q., and Droegemeier, K. K. (2006). A three dimensional variational single Doppler velocity retrieval method with simple conservation equation constraint. *Meteorol. Atmos. Phys.*, **94**, 11–26.

Goddard, J. W. D., Eastment, J. D., and Thurai, M. (1994). The Chilbolton Advanced Meteorological Radar: a tool for multidisciplinary atmospheric research. *IEE Electronics and Communications Engineering Journal*, **6-2**, 77–86.

Gregory, D. and Rowntree, P. R. (1990). A Mass Flux Convection Scheme with Representation of Cloud Ensemble Characteristics and Stability-Dependent Closure. *Mon. Wea. Rev.*, **118**, 1483–1505.

Gu, J. F., Plant, R. S., Holloway, C. E., Jones, T. R., Stirling, A., Clark, P. A., Woolnough, S. J., and Webb, T. L. (2020a). Evaluation of the Bulk Mass Flux Formulation Using Large-Eddy Simulations. *J. Atmos. Sci.*, **77**, 2115–2137.

Gu, J. F., Plant, R. S., Holloway, C. E., and Muetzelfeldt, M. R. (2020b). Pressure Drag for Shallow Cumulus Clouds: From Thermals to the Cloud Ensemble. *Geophys. Res. Lett.*, **47**, 1–10.

Hallett, J. and Mossop, S. C. (1974). Production of secondary ice particles during the riming process. *Nature*, **249**, 26–28.

Hanley, K. E., Plant, R. S., Stein, T. H. M., Hogan, R. J., Nicol, J. C., Lean, H. W., Halliwell, C., and Clark, P. A. (2015). Mixing-length controls on high-resolution simulations of convective storms. *Q. J. R. Meteorol. Soc.*, **141**, 272–284.

Hannah, W. M. (2017). Entrainment versus dilution in tropical deep convection. *J. Atmos. Sci.*, **74**, 3725–3747.

Hernandez-Deckers, D. and Sherwood, S. C. (2016). A numerical investigation of Cumulus thermals. *J. Atmos. Sci.*, **73**, 4117–4136.

Hernandez-Deckers, D. and Sherwood, S. C. (2018). On the roles of entrainment in the fate of Cumulus thermals. *J. Atmos. Sci.*, **75**, 3911–3924.

Hill, M. J. M. (1894). On a spherical vortex. *Philos. Trans. Roy. Soc.*, **185A**, 213–245.

Hogan, R. J., Field, P. R., Illingworth, A. J., Cotton, R. J., and Choularton, T. W. (2002). Properties of embedded convection in warm-frontal mixed-phase cloud from aircraft and polarimetric radar. *Quart. J. Roy. Meteor. Soc.*, **128**, 451–476.

Hogan, R. J., Illingworth, A. J., and Halladay, K. (2008). Estimating mass and momentum fluxes in a line of cumulonimbus using a single high-resolution Doppler radar. *Q. J. R. Meteorol. Soc.*, **134**, 1127–1141.

Homeyer, C. R. and Kumjian, M. R. (2015). Microphysical Characteristics of Overshooting Convection from Polarimetric Radar Observations. *Amer. Meteor. Soc.*, **72**, 870–891.

Jensen, P. and Genio, A. D. D. (2006). Factors limiting convective cloud-top height at the ARM Nauru Island climate research facility. *J. Climate*, **19**, 2105–2117.

Jurkovic, P. M., Mahovic, N. S., and Pocakal, D. (2015). Lightning, overshooting top and hail characteristics for strong convective storms in Central Europe. *Atmos. Res.*, **161**, 153–168.

Kain, J. S. and Fritsch, M. (1990). A one-dimensional entraining/detraining plume model and its applications in convective parametrization. *J. Atmos. Sci.*, **47**, 2784–2802.

Keller, V. W. and Sax, R. I. (1981). Microphysical development of a pulsating cumulus tower: A case study. *Quart. J. Roy. Meteor. Soc.*, **107**, 679–697.

Klaassen, G. P. and Clark, T. L. (1985). Dynamics of the Cloud-Environment Interface and Entrainment in Small Cumuli: Two-Dimensional Simulations in the Absence of Ambient Shear. *J. Atmos. Sci.*, **42**, 26212642.

Knupp, K. R. and Cotton, W. R. (1985). Convective Cloud Downdraft Structure: An Interpretive Survey. *Rev. Geophys.*, **23**, 183–215.

Kollias, P., Albrecht, B. A., Lhermitte, R., and Savtchenko, A. (2001). Radar observations of updrafts, downdrafts and turbulence in fair-weather cumuli. *J. Atmos. Sci.*, **58**, 1750–1766.

Kolmogorov, A. (1941). Dissipation of energy in the locally isotropic turbulence. *Dokl. Akad. Nauk. SSSR*, **32**, 16–18.

Kumar, V., Protat, A., Jakob, C., Williams, C., Rauniyar, S., Stephens, G., and May, P. (2016). The Estimation of Convective Mass Flux from Radar Reflectivities. *J. Appl. Meteorol. Clim.*, **55**, 1239–1257.

Kumjian, M. R., Khain, A. P., Benmoshe, N., Ilotoviz, E., Ryzhkov, A. V., and Phillips, V. T. J. (2014). The Anatomy and Physics of ZDR Columns: Investigating a Polarimetric Radar Signature with a Spectral Bin Microphysical Model. *J. Appl. Meteorol. Clim.*, **53**(7), 1820–1843.

Lean, H. W., Clark, P. A., Dixon, M., Roberts, N. M., Fitch, A., Forbes, R., and Halliwell, C. (2008). Characteristics of High-Resolution Versions of the Met Office Unified Model for Forecasting Convection over the United Kingdom. *Mon. Wea. Rev.*, **136**, 3408–3424.

LeMone, M. A. and Zipser, E. J. (1980). Cumulonimbus Vertical Velocity Events in GATE. Part 1.: Diameter, Intensity and Mass Flux. *J. Atmos. Sci.*, **37**, 2444–2457.

Leon, D. C., French, J. R., Lasher-Trapp, S., Blyth, A. M., Abel, S. J., Ballard, S., Barrett, A., Bennett, L. J., Bower, K., Brooks, B., Brown, P., Charlton-Perez, C., Choularton, T., Clark, P., Collier, C., Crosier, J., Cui, Z., Dey, S., Dufton, D., Eagle, C., Flynn, M. J., Gallagher, M., Halliwell, C., Hanley, K., Hawkness-Smith, L., Huang, Y., Kelly, G., Kitchen, M., Korolev, A., Lean, H., Liu, Z., Marsham, J., Moser, D., Nicol, J., Norton, E. G., Plummer, D., Price, J., Ricketts, H., Roberts, N., Rosenberg, P. D., Simonin, D., Taylor, J. W., Warren, R., Williams, P. I., and Young, G. (2016). The Convective Precipitation Experiment (COPE). *Bull. Amer. Meteor. Soc.*, pages 1003–1020.

Levine, J. (1959). Spherical vortex theory of bubble-like motion in cumulus clouds. *J. Appl. Meteorol.*, **16**, 653–662.

MacGorman, D. R., Elliot, M. S., and DiGangi, E. (2016). Electrical discharges in the overshooting tops of thunderstorms. *J. Geophys. Res.*, **122**, 2929–2957.

Macura, W. K. (2019). 'Antialiasing' From MathWorld–A Wolfram Web Resource.

Marion, G. R., Trapp, R. J., and Nesbitt, S. W. (2019). Using Overshooting Top Area to Discriminate Potential for Large, Intense Tornadoes. *Geophys. Res. Lett.*, **46**, 12520–12526.

Marshall, J. S. and Palmer, W. M. (1948). The distribution of raindrops with size. *J. Meteorol.*, **5**, 165–166.

Matejka, T. and Bartels, D. (1998). The Accuracy of Vertical Air Velocities from Doppler Radar Data. *Mon. Wea. Rev.*, **126**, 92–117.

Melnikov, V. and Zrnic, D. (2017). Observations of convective thermals with weather radar. *J. Atmos. Ocean. Tech.*, **34**, 1585–1590.

Met Office (2019). Lightning strike location data. https://www.metoffice.gov.uk/binaries/content/assets/metofficegovuk/pdf /data/adtnet_data_sheet.pdf.

Morrison, H. (2017). An Analytic Description of the Structure and Evolution of Growing Deep Cumulus Updrafts. *J. Atmos. Sci.*, **74**, 809–834.

Morrison, H. (2019). What is the basic structural unit of cumulus convection, and why does it matter? Convection Parametrization: Progress and Challenges 2019.

Morrison, H. and Peters, J. M. (2018). Theoretical expressions for the ascent rate of moist deep convective thermals. *J. Atmos. Sci.*, **75**, 1699–1719.

Morrison, H., Peters, J. M., Varble, A. C., Hannah, W. M., and Giangrande, S. E. (2020). Thermal Chains and Entrainment in Cumulus Updrafts. Part I: Theoretical Description. *J. Atmos. Sci.*, **77**, 3637–3660.

Moser, D. H. and Lasher-Trapp, S. (2017). The influence of successive thermal on entrainment and dilution in a simulated Cumulus Congestus. *J. Atmos. Sci.*, **74**, 375–392.

Musil, D. J., Sand, W. R., and Schleusener, R. A. (1973). Analysis of Data from T-28 Aircraft Penetrations of a Colorado Hailstorm. *J. Appl. Meteorol.*, **12**, 1364–1370.

Nicol, J. C., R. H., Stein, T., Hanley, K., Clark, P., Halliwell, C., Lean, H., and Plant, R. (2015). Convective updraught evaluation in high-resolution NWP simulations using single-Doppler radar measurements. *Quart. J. Roy. Meteor. Soc.*, **141**, 3177–3198.

North, K., Kollias, P., Giangrande, S., Collis, S., and Potvin, C. (2017). Vertical Air Motion Retrievals in Deep Convective Clouds using the ARM Scanning Radar Network in Oklahoma during MC3E. *Atmos. Meas. Tech. Discuss.*, **10**, 2785–2806.

Peters, J. M., Morrison, H., , Varble, A. C., Hannah, W. M., and Giangrande, S. E. (2020). Thermal Chains and Entrainment in Cumulus Updrafts. Part II: Analysis of Idealized Simulations. *J. Atmos. Sci.*, **77**, 3661–3681.

Peters, M. J., Hannah, W., and Morrison, H. (2019). The Influence of Vertical Wind Shear on Moist Thermals. *J. Atmos. Sci.*, **76**, 1645–1659.

Picca, J. C. and Ryzhkov, A. V. (2010). Z_{DR} columns as a predictive tool for hail growth and storm evolution. In *25th Conference on Severe Local Storms Abstracts*, volume 2010.

Plant, B. (2009). Convective cloud lifecycles Lunchtime Seminar. http://www.met.rdg.ac.uk/ sws00rsp/research/tracking/dept_seminar09.pdf.

Protat, A. and Zawadzki, I. (1999). A Variational Method for Real-Time Retrieval of Three Dimensional Wind Field from Multiple-Doppler Bistatic Radar Network Data. *J. Atmos. Ocean. Tech.*, **16**, 753–760.

Ray, P. S., Ziegler, C. L., and Bumgarner, W. (1980). Single and Multiple Doppler Radar Observations of tornadic Storms. *Amer. Meteor. Soc.*, **108**, 1607–1625.

Raymond, D. J. and Blyth, A. M. (1989). Precipitation development in a New Mexico thunderstorm. *Quart. J. Roy. Meteor. Soc.*, **115**, 1397–1423.

Redelsperger, J. and Lafore, J. (1988). A Three-Dimensional Simulation of a Tropical Squall Line: Convective Organization and Thermodynamic Vertical Transport. *J. Atmos. Sci.*, **45**, 1334–1356.

Romps, D. M. and Charn, A. B. (2015). Sticky Thermals: Evidence for a dominant balance between buoyancy and drag in cloud updrafts. *J. Atmos. Sci.*, **72**, 2890–2901.

Romps, D. M. and Öktem, R. (2015). Stereo photogrammetry reveals substantial drag on cloud thermals. *Geophys. Res. Lett.*, **42**, 5051–5057.

Sand, W. R. (1976). Observations in Hailstorms Using the T-28 Aircraft System. *J. Appl. Meteorol.*, **15**, 641–650.

Scorer, R. S. (1957). Experiments on convection of isolated masses of buoyant fluid. *J. Fluid Mech.*, **2**, 583–594.

Scorer, R. S. and Ludlam, F. H. (1953). Bubble theory of penetrative convection. *Q. J. R. Meteorol. Soc.*, **79**, 94–103.

Sherwood, S. C., Hernandez-Deckers, D., Colin, M., and Robinson, F. (2013). Slippery thermals and the Cumulus entrainment paradox. *J. Atmos. Sci.*, **70**, 2426–2442.

Simpson, J. and Wiggert, V. (1969). Models of precipitating cumulus towers. *Mon. Wea. Rev.*, **97**, 471–489.

Snyder, J. C., Ryzhkov, A. V., Kumjian, M. R., Khain, A. P., and Picca, J. (2015). A ZDR Column Detection Algorithm to Examine Convective Storm Updrafts. *Weather. Forecast.*, **30**(6), 1819–1844.

Stein, T., Hogan, R., Hanley, K., Nicol, J., Lean, H., Plant, R., Clark, P., and Halliwell, C. (2014). The Three-Dimensional Morphology of Simulated and Observed Convective Storms over Southern England. *Mon. Wea. Rev.*, **142**, 3264–3283.

Stein, T., Hogan, R., Clark, P., Halliwell, C., Hanley, K., Lean, H., Nicol, J., and Plant, R. (2015). The DYMECS Project: A Statistical Approach for the Evaluation of Convective Storms in High-Resolution NWP Models. *Bull. Amer. Meteor. Soc.*, **96**, 939–951.

Stirling, A. J. and Stratton, R. A. (2012). Entrainment processes in the diurnal cycle of deep convection. *Q. J. R. Meteorol. Soc.*, **138**, 1135–1149.

Taylor, J. W., Choularton, T. W., Blyth, A. M., Liu, Z., Bower, K. N., Crosier, J., Gallagher, M. W., Williams, P. I., Dorsey, J. R., Flynn, M. J., Bennet, L. J., Huang, Y., French, J., Korolev, A., and Brown, P. R. A. (2016). Observations of cloud microphysics and ice formation during COPE. *Atmos. Chem. Phys.*, **16**, 799–826.

Tiedtke, M. (1989). A comprehensive mass flux scheme for cumulus parametrization in large scale models. *Mon. Wea. Rev.*, **117**, 1779–1800.

Turner, J. S. (1969). Buoyant plumes and thermals. *Annu. Rev. Fluid Mech.*, **1**, 29–44.

Ulbrich, C. W. (1983). Natural variations in the analytical form of the raindrop size distribution. *J. Appl. Meteorol. Clim.*, **22**, 1764–1775.

Varble, A., Zipser, E. J., Fridlind, A. M., Zhu, P., Ackerman, A. S., Chaboureau, J., Collis, S., Fan, J., Hill, A., and Shipway, B. (2014). Evaluation of cloud-resolving and limited area model intercomparison simulations using TWP-ICE observations: 1. Deep convective updraft properties. *J. Geophys. Res. Atmos.*, **119**, 13891–13918.

Warren, R. A. and Protat, A. (2019). Should Interpolation of Radar Reflectivity be Performed in Z or dBZ. *J. Atmos. Ocean. Tech.*, **36**, 1143–1156.

Whitall, M. (2019). A New Generalised Mass-flux Convection Scheme for the Met Office Unified Model. Convection Parametrization: Progress and Challenges 2019.

Woodward, B. (1959). The motion in and around isolated thermals. *Q. J. R. Meteorol. Soc.*, **85**, 144–151.

Yang, J., Wang, Z., Heymsfield, A. J., and French, J. (2016). Characteristics of vertical air motion in isolated convective clouds. *Atmos. Chem. Phys.*, **16**, 10159–10173.

Yano, J. I. (2014). Basic convective element: bubble or plume? A historical review. *Atmos. Chem. Phys.*, **14**, 7019–7030.

Yuter, S. E. and Houze, R. A. J. (1995). Three-Dimensional kinematic and microphysical evolution of Florida cumulonimbus. Part III: Vertical mass transport, mass divergence, and synthesis. *Mon. Wea. Rev.*, **123**, 1964–1983.

Zhao, M. (2014). An Investigation of the Connections among convection, clouds and climate sensitivity in a global climate model. *J. Climate*, **27**, 1845–1862.